Syntheses and applications of tungsten oxide-based nanocrystals

Dissertation

zur Erlangung des Grades

"Doktor der Naturwissenschaften"

im Promotionsfach Chemie

am Fachbereich Chemie, Pharmazie, Geographie und Geowissenschaften

der Johannes Gutenberg-Universität Mainz

René Dören

geb. in Dernbach (Westerwaldkreis)

Mainz, 2021

JOHANNES GUTENBERG UNIVERSITÄT MAINZ

JG|U

Dekanin: [redacted]

Erster Berichterstatter: [redacted]

Zweite Berichterstatterin: [redacted]

Tag der mündlichen Prüfung: 11.01.2022

Declaration:

The presented dissertation has been prepared between May 2018 and November 2021 under the supervision of [redacted] at the Department Chemistry of the Johannes Gutenberg-University Mainz.

I hereby declare that I wrote the presented dissertation independently and without outside help. All used references and resources are completely indicated.

Erklärung:

Die vorliegende Arbeit wurde in der Zeit Mai 2018 bis November 2021 unter der Betreuung von [redacted] im Department Chemie der Johannes Gutenberg-Universität Mainz durchgeführt.

Hiermit erkläre ich, dass die vorliegende Arbeit selbstständig verfasst und keine anderen als die angegebenen Quellen und Hilfsmittel verwendet wurden. Alle Stellen, die wörtlich oder sinngemäß aus Quellen übernommen wurden, sind als solche gekennzeichnet.

Mainz, November 2021

René Dören

I. Acknowledgements

[redacted]

II. List of Publications

[redacted]

III. Abstract

The art of nanocrystal synthesis has been the focus of interest for many years and many researchers. Finding the "right" synthesis for a desired product can be time consuming and very frustrating. Often, syntheses suffer from low reproducibility and comparability when different preparative methods are used.

Therefore, the main objective of this work was to find suitable ways to synthesize nanocrystals of various reduced tungsten oxides, tungsten bronzes and metal tungstates. For tungsten oxides, a synthesis was developed starting from ammonium metatungstate and a combination of oleic acid and oleylamine, which acts both, as solvent and protective surfactant. The simultaneous development of WO_{3-x} nanorods of Magnéli type and hexagonal ammonium tungstate bronzes was observed. The selectivity was analyzed by varying the reaction parameters, e.g., precursor concentration, heating rate and solvent ratio. An unintended quantitative chemical reaction of the solvents towards their condensation product oleyl oleamide was observed and its effect for suppressing ammonium bronze formation was further investigated. A strong absorption of near-infrared light by the anisotropic nanorods and nanocrystals due to localized surface plasmon resonance was observed. It was also found that the maximum of the resonance can be tuned by changing the aspect ratio of the respective nanocrystals synthetically.

WO_{3-x} nanorods catalyze the oxidation of sulfides to sulfoxides with the cheap and green oxidant H_2O_2. The selectivity in the formation of sulfoxides compared to sulfones is high with reaction times of less than one hour. An advantage of WO_{3-x} nanorods is the low overoxidation to sulfones. The catalytic oxidation of a wide range of sulfides with different chemical structure and the reusability of the catalyst was demonstrated.

As this work progressed, it became apparent that impurities of iron in oleic acid (from the container material) can strongly impact the size and phase selectivity of the nanorod synthesis. A more detailed investigation of this process led to the formation of iron tungstate nanocrystals, which crystallize in the ferberite structure. At the same time, the use of oleyl oleamide led to the formation of a potentially new ferrotungstate phase. The basic structural analysis of this phase was based on a known, related magnesium tungstate phase of still unknown structure, which can be prepared in a similar way.

Synthesis and applications have been investigated for cesium-tungsten bronzes. These nanocrystals have a hexagonal and/or pyrochlore-like cubic crystal structure. The formation of the phases depends on the cesium-tungsten ratio, the heating rate and excess of oleylamine during synthesis. Cubic cesium-tungsten bronzes showed promising haloperoxidase-like properties, which were detected by a phenol red assay. Strong biofilm inhibition of the nosocomial bacterium *Pseudomonas aeruginosa* up to 35 % and strong suppression of the growth of the fungus *Fusarium graminearum* up to 54 % were observed

for both WO_{3-x} nanorods and cubic cesium-tungsten bronzes. In addition, a significant reduction of mycelium was observed with WO_{3-x} nanorods, while cubic cesium-tungsten bronze showed a smaller but comparable effect. Mixed hexagonal/cubic cesium-tungsten bronzes, on the other hand, showed an influence on bacterial growth of *Staphylococcus aureus*, *Pseudomonas aeruginosa* and *Phaeobacter gallaeciensis* under infrared light. Compared to non-irradiated samples, a reduction in bacterial growth of up to 30 % was observed. This effect could be attributed to hyperthermia, which in turn is due to the strong plasmonic absorption of these nanocrystals in the red to near infrared range of light.

In a final project, the influence of transition metals in steel on the biofilm formation of bacteria was investigated. In addition to iron, steel contains other metals such as tungsten, manganese, copper, cobalt and zinc. Steel promotes the proliferation and biofilm formation of the bacterium *Phaeobacter gallaeciensis* significantly compared to glass and polymer surfaces. The study of metal salts showed that primarily iron and secondarily manganese have a positive effect on bacterial biofilm formation, as they serve as a nutrient for bacteria. Following these results, different (transition-) metal tungstate nanocrystals were tested for their effect on bacterial growth and biofilm formation. In contrast to manganese salts, the manganese tungstate nanocrystals with hübnerite structure significantly reduced biofilm formation by up to 40 % while increasing the number of planktonic cells in the supernatant. The same effect was observed with *Pseudomonas aeruginosa* and cannot be due to haloperoxidase properties of the nanocrystals. Iron tungstate nanocrystals with ferberite structure showed a similar but less intense influence. The effect could be due to the fact that the surfaces of the iron and manganese tungstate nanocrystals mimic nutrients and cause dispersion of the biofilm by binding relevant siderophores.

IV. Kurzzusammenfassung

Die Kunst der Nanokristall-Synthese steht seit vielen Jahren im Zentrum des Interesses vieler Forscher. Es kann zeitraubend und sehr frustrierend sein, die „richtige“ Synthese für ein gewünschtes Produkt zu finden. Die Synthesen leiden oft unter geringer Reproduzierbarkeit und Vergleichbarkeit, wenn verschiedene Herstellungsmethoden verwendet werden.

Daher war ein Ziel dieser Arbeit, geeignete Wege zur Synthese von Nanokristallen verschiedener reduzierter Wolframoxide, Wolframbronzen und Metall-Wolframate zu finden. Für Wolframoxide wurde eine Synthese ausgehend von Ammoniummetawolframat und einer Kombination aus Ölsäure und Oleylamin entwickelt, die sowohl als Lösungsmittel als auch als schützendes Tensid fungieren. Dabei bildeten sich gleichzeitig WO_{3-x}-Nanostäbchen vom Magnéli-Typ und hexagonale Ammoniumwolframat-Bronzen. Die Selektivität der Reaktion wurde durch Variation der Reaktionsparameter, z.B. der Konzentration der Vorstufe, der Heizrate und des Lösungsmittelverhältnisses analysiert. Bei den Reaktionen trat unbeabsichtigt die quantitative Reaktion der beiden Lösungsmittel zu ihrem Kondensationsprodukt Oleyl-Oleamid auf und die Auswirkung dieser Kondensation zur Unterdrückung der Bildung von Ammoniumbronzen wurde weiterverfolgt. Alle Nanostäbchen und Nanokristalle der reduzierten Wolframoxide und -bronzen zeigen eine starke Absorption im nahen Infrarotbereich die auf die Anregung lokalisierter Oberflächenplasmonen zurückgeht. Das Resonanzmaximum lässt sich durch synthesebedingte Veränderung des Aspektverhältnisses der jeweiligen Nanokristalle einstellen.

WO_{3-x}-Nanostäbchen katalysieren die Oxidation von Sulfiden zu Sulfoxiden mit dem billigen und vergleichsweise umweltverträglichen Oxidationsmittel H_2O_2. Die Selektivität bei der Bildung von Sulfoxiden im Vergleich zu Sulfonen ist hoch, die Reaktionszeiten betragen weniger als eine Stunde. Ein Vorteil der Katalyse mit WO_{3-x}-Nanostäbchen ist die geringe Überoxidation zu Sulfonen. Die katalytische Oxidation ist für eine breiten Palette von Sulfiden mit unterschiedlicher chemischer Struktur möglich und der Katalysator kann wiederverwendet werden.

Eisenverunreinigungen in Ölsäure (eingetragen über das Behältermaterial) beeinflussen die Größe und Phasenselektivität der Nanostäbchensynthese. Eine genauere Untersuchung dieses Prozesses führte zur Bildung von Eisenwolframat-Nanokristallen, die in der Ferberitstruktur kristallisieren. Gleichzeitig führte die Verwendung von Oleyl-Oleamid zur Bildung einer neuen Eisenwolframatphase, deren Struktur der Struktur einer bekannten Magnesiumwolframatphase ähnelt. Die Struktur des neuen Eisenwolframats konnte jedoch bisher weder aus Röntgen-Pulverdaten noch aus Einkristall-Elektronenbeugungsdaten gelöst werden.

Neben Wolframbronzen vom Magneli-Typ wurde die Synthese und mögliche Anwendungen Cäsium-Wolframbronzen untersucht. Nanokristalle von Alkalimetall-Wolframbronzen haben eine hexagonale und/oder kubische pyrochlor-analoge Kristallstruktur. Die Bildung der Phasen hängt sowohl vom Cäsium-Wolfram-Verhältnis als auch von der Heizrate und dem Überschuss an Oleylamin während der Synthese ab. Kubische Cäsium-Wolframbronzen zeigten vielversprechende katalytische Aktivität für oxidativen Halogenierung (d.h. die Haloperoxidase-Reaktion), die mit Hilfe eines Phenolrot-Enzymassays nachgewiesen wurde. Sowohl für WO_{3-x}-Nanostäbchen als auch für kubische Cäsium-Wolframbronzen wurde eine starke Hemmung des Biofilmbildung des nosokomialen Bakteriums *Pseudomonas aeruginosa* um bis zu 35 % sowie eine starke Unterdrückung des Wachstums des Pilzes *Fusarium graminearum* um bis zu 54 % beobachtet. Darüber hinaus zeigten WO_{3-x}-Nanostäbchen eine signifikante Reduzierung des Myzels, während die kubische Cäsium-Wolframbronze eine geringere, aber vergleichbare Wirkung zeigte. Gemischte hexagonale/kubische Cäsium-Wolframbronzen hingegen zeigten unter Infrarotlicht einen Einfluss auf das Bakterienwachstum von *Staphylococcus aureus*, *Pseudomonas aeruginosa* und *Phaeobacter gallaeciensis*. Im Vergleich zu nicht bestrahlten Proben wurde eine Verringerung des Bakterienwachstums um bis zu 30 % festgestellt. Dieser Effekt könnte auf die Erwärmung der Bakterien (Hyperthermie) zurückzuführen sein, die wiederum auf die starke plasmonische Absorption dieser Nanokristalle im roten bis nahen infraroten Bereich des Lichts bedingt ist.

Im letzten Projekt der Arbeit wurde der Einfluss von Übergangsmetallen in Stahl auf die Biofilmbildung von Bakterien untersucht. Stahl enthält neben Eisen weitere Metalle wie Wolfram, Mangan, Kupfer, Kobalt und Zink. Stahl fördert die Biofilmbildung des Bakteriums *Phaeobacter gallaeciensis* deutlich im Vergleich zu Glas- und Polymeroberflächen. Die Untersuchung der Metallsalze ergab, dass vor allem Eisen und in zweiter Linie Mangan eine verstärkende Wirkung auf die Biofilmbildung haben, da sie den Bakterien als Nährstoff dienen. Daher wurde die Wirkung verschiedener Übergangsmetallwolframat-Nanokristalle auf das Bakterienwachstum und die Biofilmbildung von *Phaeobacter gallaeciensis* getestet. Im Gegensatz zu Mangansalzen verringerten Manganwolframat-Nanokristalle mit Hübnerit-Struktur die Biofilmbildung um bis zu 40 % und erhöhten gleichzeitig die Anzahl der planktonischen Zellen im Überstand. Der gleiche Effekt wurde bei *Pseudomonas aeruginosa* beobachtet, kann nicht auf die Haloperoxidase-Eigenschaften der Manganwolframat-Nanokristalle zurückgeführt werden. Eisenwolframat-Nanokristalle mit Ferberitstruktur zeigten einen ähnlichen, aber weniger starken Einfluss für beide Arten von Bakterien. Die Wirkung könnte darauf zurückzuführen sein, dass die Oberflächen der Eisen- und Manganwolframat-Nanokristalle Nährstoffe imitieren und durch Bindung relevanter Siderophore eine Dispersion des Biofilms bewirken.

V. Table of Contents

I. Acknowledgements VII

II. List of Publications IX

III. Abstract X

IV. Kurzzusammenfassung XII

V. Table of Contents XIV

1. Introduction 1

1.1 Crystal growth theory 2

1.1.1 Classical nucleation and the LaMer Model 2

1.1.2 Nonclassical nucleation 4

1.1.3 Influence of solvents and ligands/surfactants 4

1.2 Tungsten Oxides 5

1.2.1 Magnéli-Type tungsten sub-oxides and tungsten bronzes 6

1.2.2 Wolframite group 7

1.2.3 Localized surface plasmon resonance 8

1.3 References 9

Authorship Contributions Chapter 2 12

2. Gram-Scale Selective Synthesis of WO_{3-x} Nanorods and $(NH_4)_xWO_3$ Ammonium Tungsten Bronzes with Tunable Plasmonic Properties 13

2.1 Abstract 13

2.2 Introduction 14

2.3 Results and discussion 16

2.3.1 Competing Formation of WO_{3-x} Nanorods and $(NH_4)_xWO_3$ Bronzes 16

2.3.2 ^{1}H-NMR Study of Surfactant Reactions during WO_{3-x} Nanocrystal Formation and Role of Surfactant on Phase Selection 24

2.3.3 Mechanistic Study of WO_{3-x} and h-ATB Formation via Oriented Attachment 26

2.3.4 Surface Ligands and Composition of h-ATB Nanocrystals from Temperature-Dependent Solid-State MAS ^{1}H-NMR / PXRD Studies 28

2.3.5 Localized Surface Plasmon Resonances Study of WO_{3-x} and h-ATB 31
2.4 Conclusions 33
2.5 Experimental section 34
2.5.1 Characterization 35
2.6 References 37
Authorship Contributions Chapter 3 43
3. Magneli-Type Tungsten Oxide Nanorods as Catalysts for the Selective Oxidation of Organic Sulfides 44
3.1 Abstract 44
3.2 Introduction 45
3.3 Results and discussion 47
3.3.1 Evaluation of Reaction Parameters for *in situ* Oxidation of Thioanisole 47
3.3.2 Sulfide Screening 53
3.3.3 Nanoparticle Screening 55
3.4 Conclusions 57
3.5 Experimental section 58
3.5.1 Characterization 59
3.6 References 60
Authorship Contributions Chapter 4 64
4. Exploiting the effect of impurities for the controlled synthesis iron tungsten oxide nanocrystals 65
4.1 Abstract 65
4.2 Introduction 66
4.3 Results and discussion 67
4.4 Conclusions 75
4.5 Experimental section 76
4.5.1 Characterization 77
4.6 References 77
Authorship Contributions Chapter 5 82

5. Cesium tungsten bronze nanocrystals with enzyme-like activity prevent the formation of bacterial biofilms and inhibit fungal colonization 83
5.1 Abstract 83
5.2 Introduction 84
5.3 Results and discussion 86
5.3.1 Synthesis of hexagonal and pyrochlore-type alkali metal tungsten bronzes 86
5.3.2 Haloperoxidase properties 90
5.3.3 Biological properties of tungsten oxide NRs and tungsten bronze NCs 92
5.4 Conclusions 97
5.5 Experimental section 98
5.5.1 Characterization 100
5.6 References 101
Authorship Contributions Chapter 6 107
6. Antimicrobial activity of metal tungstate nanocrystals prevents bacterial biofilm formation 108
6.1 Abstract 108
6.2 Introduction 109
6.3 Results and discussion 111
6.3.1 Low-carbon steel affects marine bacterial BF formation 111
6.3.2 Metal ions affect bacterial BF formation 112
6.3.3 Synthesis and structural properties of (transition)metal tungstate nanocrystals 114
6.3.4 $MnWO_4$ and $FeWO_4$ nanocrystals do not affect bacterial growth but inhibit BF formation in *P. gallaeciensis* and *P. aeruginosa* 114
6.4 Conclusions 117
6.5 Experimental section 118
6.5.1 Characterization 119
6.6 References 120
7. Conclusions 125
8. Appendix 130
8.1 Supporting Information for Chapter 2 131
8.1.1 Author Contributions 131

8.1.2 Effect of Surfactant Concentration 156
8.2 Supporting Information for Chapter 3 158
8.2.1 Author Contributions 158
8.2.2 ^{1}H-NMR characterization 165
8.2.3 References 192
8.3 Supporting Information for Chapter 4 193
8.3.1 Author Contributions 193
8.4 Supporting Information for Chapter 5 204
8.4.1 Author Contributions 204
8.5 Supporting Information for Chapter 6 218
8.5.1 Author Contributions 218
8.5.2 $ZnWO_4$ NCs show antibacterial and antifungal effects 228
8.5.3 References 230
8.6 List of Figures 231
8.7 List of Tables 243
8.8 List of Abbreviations 245

1. Introduction

1.1 Crystal growth theory

1.1.1 Classical nucleation and the LaMer Model

A mechanism or model for crystal growth was first described by LaMer in 1950 for the formation of monodisperse hydrosols based on sulfur in solution.[1] This model has been reused many times and was greatly expanded thereafter.[2] As a general approach, his process starts with the decomposition of a precursor, forming molecular units (monomers) of undefined size. These monomers are attributed with a distinct solubility in the respective solvent. The different steps of the nucleation process can be observed by following the concentration *c* of the monomer over time as shown in Figure 1.1a.

With more of precursor decomposing over time (often associated with thermal decomposition by heating), first a saturation c_S is reached, closely followed by supersaturation *S* (step I). In supersaturated solutions the monomers start to form nuclei. Once a critical saturation concentration c_{crit} is achieved, these nuclei can stabilize (step II). The free energy ΔG_N of nuclei formation according to Eq. 1.1 depends on surface energy γ and lattice energy ΔG_v and is graphically illustrated in Figure 1.1b. The stability of nuclei is thereby dependent on their size expressed by the radius *r*.

$$\Delta G_N = 4\pi r^2\gamma + \frac{4}{3}\pi r^3\gamma\Delta G_v \tag{1.1}$$

For small nuclei the destabilizing surface energy is higher and overcomes the lattice energy that is on the other hand stabilizing the nuclei. Once a critical radius r_{crit} is reached, the lattice energy is predominant, and the nuclei become stable. Only nuclei reaching the critical radius are growing towards stable crystals. The critical radius as shown in Figure 1.1b is expressed by the ratio of surface to lattice energy (Eq. 1.2).[3]

$$r_{crit} = \frac{-2\gamma}{\Delta G_v} = \frac{-2\gamma V_m}{RTln(S)} \tag{1.2}$$

As the concentration drops below the critical supersaturation no more stable nuclei will form. The nuclei that reached the critical radius start to grow to crystals using free monomers until the concentration reaches the saturation again. As smaller crystals have a higher surface to volume ratio, those crystals grow faster compared to bigger crystals. Because of this, the size distribution becomes narrower, thus it is called size focusing effect (step III). Once the saturation is reached again, the so-called Ostwald ripening (step IV) begins. In contrary to the size focusing, smaller crystals now start to dissolve faster than bigger crystals when the monomer concentration drops below the saturation. As crystals with smaller surface to volume ratio have a higher stabilizing lattice energy, those crystals are more likely to

grow using the monomer source based on the dissolving smaller crystals. As a result, the size distribution becomes less narrow again.[4]

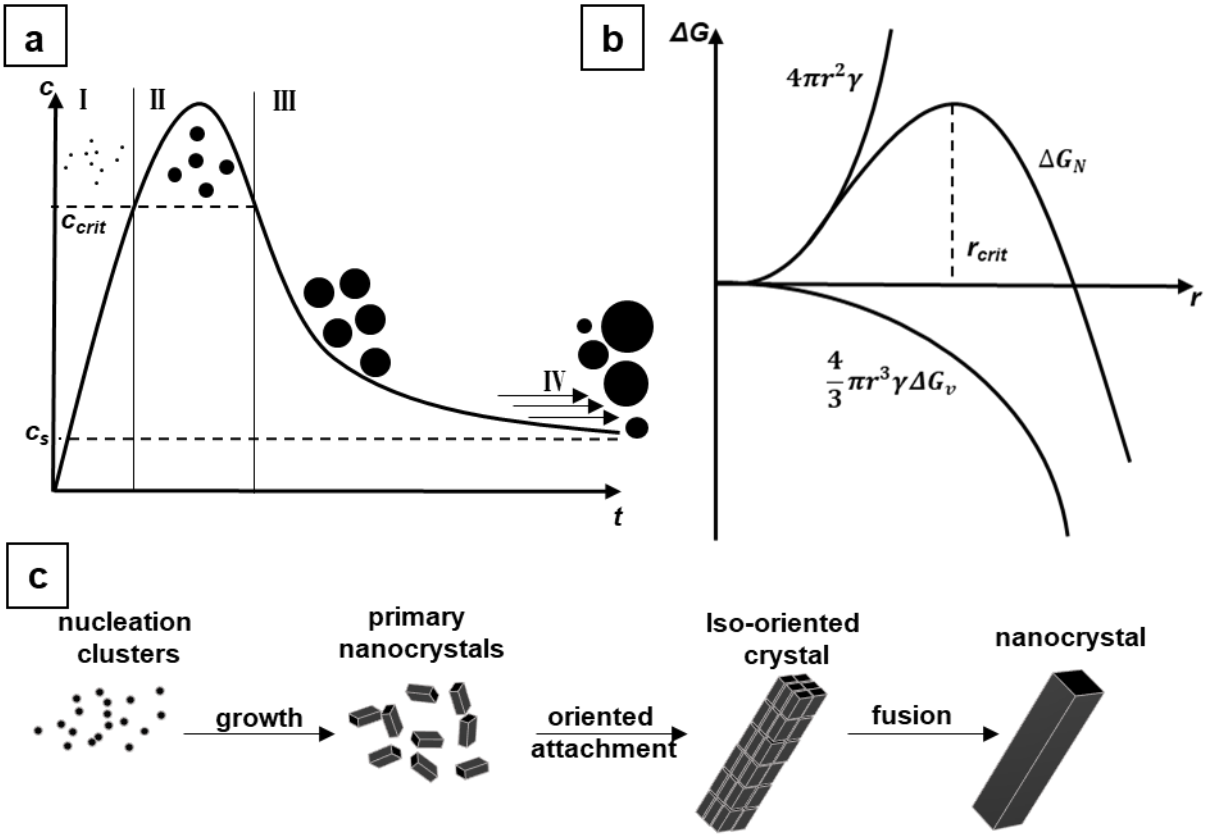

Figure 1.1. a) Nucleation curve according to LaMer[1], b) dependance of the r_{crit}. on surface and lattice energy c) Process of oriented attachment towards uniform nanocrystals according to the nonclassical nucleation theory. Inspired from [4] and [5].

Many nanocrystal (**NC**) syntheses utilize the concept described above for an efficient crystal design. Different reaction methods have been developed to synthesize NCs. Prominent examples are the hydro- and solvothermal synthesis, often associated with synthesis under pressure (e.g. in an autoclave) in (non)aqueous media,[2] as well as thermal decomposition synthesis, often performed at high temperatures (100-350 °C) with high boiling solvents. Additionally, special precursor application forms such as hot injection, where a liquid precursor or a solution is added at high temperature, can be used.[4]

For metal oxide NCs respective salts or complexes are frequently used as precursors. Those compounds typically decompose at elevated temperature to form the monomers. Knowledge of the different steps of the LaMer model is essential to get monodisperse NCs of the desired size, therefor Ostwald ripening should be avoided. Thus, the reaction must be stopped during the size focusing step. Examples of reaction parameters that influence the steps of the LaMer model are the heating rate, stirring speed, maximum temperature, and its holding time. Each of those parameters can influence different and even multiple steps of the model at the same time, thus have to be developed specifically for each NC

synthesis.[6] Solvents, ligands and additives that can influence the synthesis are discussed in the section below.

1.1.2 Nonclassical nucleation

In recent years, the nonclassical nucleation model has gained more interest. As an alternative to the classical nucleation theory, nonclassical nucleation describes the growth of NCs by so-called oriented attachment of smaller particles or clusters.[5,7] A schematic representation of this process is shown in Figure 1.1c. The growth species are described to be similar to the nuclei of the classical nucleation theory. Those primary NCs can aggregate and align, in contrast to the classical nucleation theory. By fusion of the those iso-oriented crystals the formation of a new single crystal can be observed.[5]

Tungsten oxide NCs have been described to undergo nonclassical nucleation. This involves the formation of polyoxotungstate species as pre-nucleation clusters.[8,9]

Surface active substances can stabilize primary NCs and induce oriented aggregation, therefore enabling fusion to single crystals.[5,10]

1.1.3 Influence of solvents and ligands/surfactants

A more in-depth look in the influence of a crucial parameter in NC synthesis, the choice of solvents and surfactants, is given in the following chapter. Especially the choice of solvent has a crucial impact on the synthesis, as it limits the solubility of monomers as well as the maximum reaction temperature and is able to interact with the monomer and nuclei during the synthesis. Many syntheses are carried out in water, due to its excellent dissolving capacities for metal salts and the ability to adjust the pH value, and thus ion concentrations, freely. To improve the limiting boiling point of 100 °C, reactions can be performed under pressure using autoclaves, the so called hydrothermal syntheses.[2]

Thermal decomposition syntheses typically use high boiling organic solvents such as 1-octadecene, oleic acid, oleylamine and tri-n-octyl amine.[6,11–14] These solvents possess boiling points of >300 °C and allow a wide range of syntheses options. Some of these solvents carry functional groups that can play an essential role in synthesis control.[13,14] Oleic acid (**OAc**) and oleylamine (**OAm**) are prototypes of aliphatic, functional solvents, carrying a carboxy group and a primary amine group respectively. These groups interact with nuclei surfaces during growth and can prevent certain crystal surfaces from growing by minimizing their surface energy due to stabilization. Thus, this effect strongly depends on the type and density of active surface centers on a crystal facete. For example, OAc can stabilize surfaces with high density of unsaturated, cationic metal atoms. OAm often coordinates less dense surfaces and shows higher tendency to coordinate anionic oxygen-rich surfaces. Additionally, OAm is used in noble metal NC synthesis and is discussed to exhibit reducing properties towards oxidized transition metals.[11] OAc

and OAm are often used as a couple making the exact choice of the deployed ratio essential.[9,14] Additionally, their salts can be used as additives in the reaction synthesis, e.g. sodium oleate is added in iron oxide synthesis.[13]

During the synthesis, OAc and OAm undergo in situ acid base reaction according to Eq. 1.3.[9,15] Their ionic counterparts have different coordination properties compared to the free acid/base. Hence, the formation of aliphatic ions regulates the nanocrystal formation as well. Upon heating to temperatures > ~150 °C oleyl oleamide (**OAd**) is formed by condensation (Eq. 1.4). As the nucleation and growth for metal oxide nanoparticles often proceeds at higher temperatures, OAd may act as surface active species.[9,16–18]

$$R - CH_2NH_2 + HOOC - R \rightarrow R - CH_2NH_3^+ + {}^+OOC - R \quad (1.3)$$

$$R - CH_2NH_3^+ + {}^+OOC - R \rightarrow R - CH_2NHOC - R \quad (1.4)$$

The anionic counterpart of the used precursor can also affect the synthesis. For example the commonly used iron oleate complex formed by iron(III)chloride and sodium oleate[19] releases oleate upon decomposition, which can exert surface active properties.

1.2 Tungsten Oxides

Tungsten(VI) is the most stable oxidization state of the 5d transition metal tungsten, possessing the electron configuration $[Xe]4f_{14}5d_06s_0$. Thus, no valence electrons are present. In most tungsten oxide structures, tungsten is coordinated octahedrally by six oxygen atoms and these octahedra are linked by sharing corners or edges. Tungsten(IV) forms a range of oxides, with monoclinic γ-structure being the thermodynamically most stable structure. Upon heating, the monoclinic structure undergoes phase transitions towards orthorhombic (β-WO_3, T>330 °C to 740 °C) and tetragonal (α-WO_3,T>740 °C) crystal structures.[20,21] Another monoclinic phase (ε-WO_3) can be observed below -43 °C and a triclinic phase (δ-WO_3) between -43 and 17 °C.[22] All WO_3 structures mentioned above derive form the cubic ReO_3 structure, which is a 3D network of corner sharing octahedra. The main difference is the tilting angle between the corner sharing octahedra. The ideal cubic structure is not stable in pure WO_3. By insertion of cations such as H^+, Li^+ and Na^+ the cubic structure can be stabilized at ambident temperature, resulting in a perovskite-like structure.[23] Figure 1.2a shows the monoclinic γ-structure of WO_3.

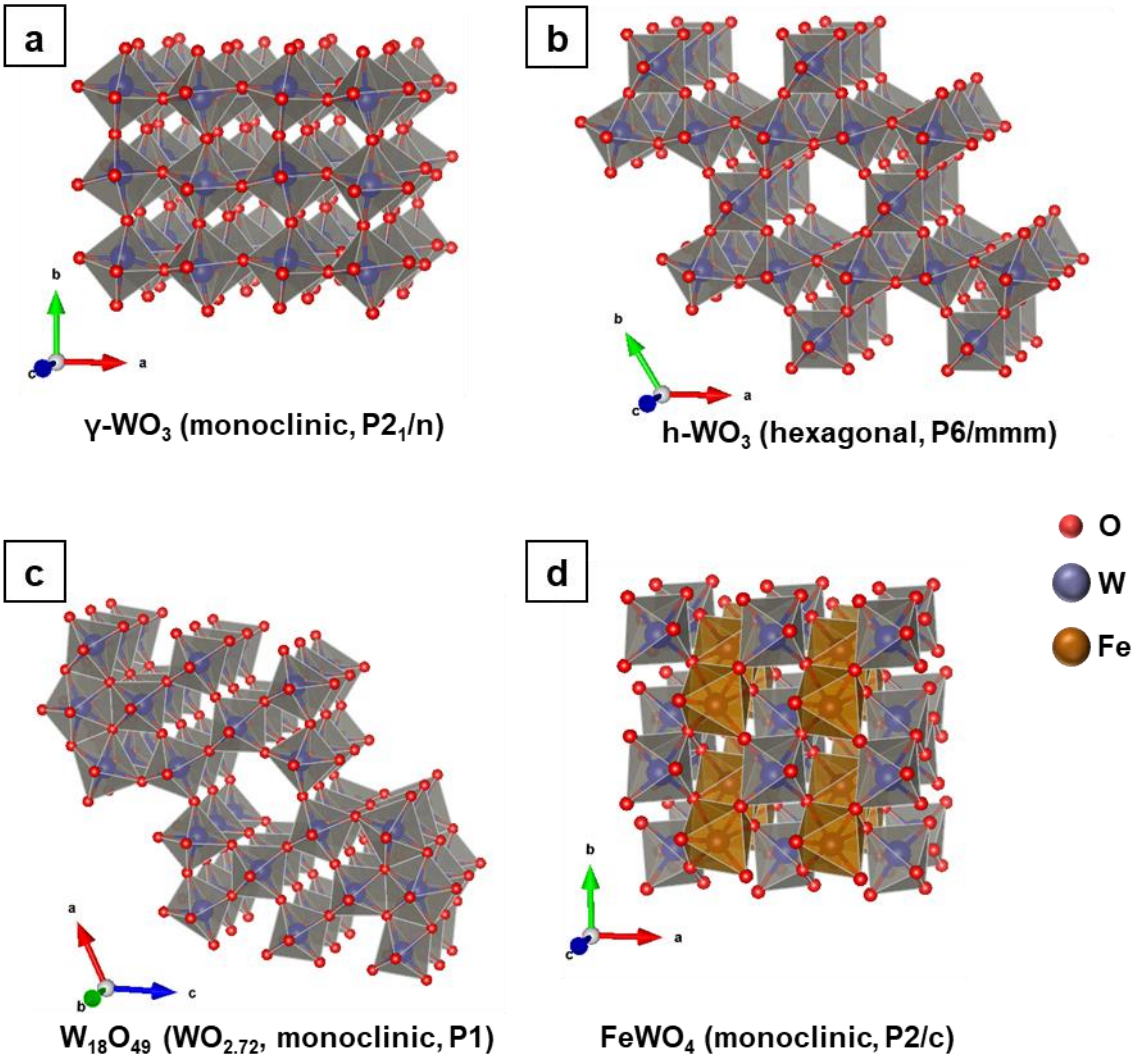

Figure 1.2. Crystal structure of a) γ-WO_3 with monoclinic space group $P2_1/n$ and b) h-WO_3 with hexagonal space group $P6/mmm$, c) $W_{18}O_{49}$ ($WO_{2.72}$) Magnéli sub-oxide with monoclinic space group $P1$ and d) the iron tungstate $FeWO_4$ (Ferberite) with monoclinic space group $P2/c$. Structures visualized using VESTA 3.6.5.

Moreover, the hexagonal structure h-WO_3 is prominent. It can be obtained by dehydration of WO_3*1/3H_2O, which is based on tungstic acid (H_2WO_4).[24] It is stable at room temperature und undergoes phase transition towards the monoclinic phase at T>400 °C. It is showing the specific feature of hexagonal channels formed by six corner-sharing WO_6 octahedra (Figure 1.2b).

1.2.1 Magnéli-Type tungsten sub-oxides and tungsten bronzes

Pure tungsten oxides have the possibility to form sub-stochiometric oxide structures with certain stable compositions in the range of WO_x ($2.625 \leq x \leq 2.92$) if synthesized in a reducing environment.[25,26] The WO_6 octahedra are partially edge sharing due to their oxygen deficiency. The first one to describe such tungsten (and molybdenum) oxide structures was Arne Magnéli, based on the dislocation of atoms

compared to the ReO_3 structure, thus these sub-oxides are often referred as magnéli-phases.[27–29]
To compensate the additional positive charge or lack of oxygen, the W^{6+} cations are partially reduced. This reduction results in additional charge carrier concentration and can lead to metallic behavior.[30] A very prominent and thermodynamically stable structure is $W_{18}O_{49}$ ($WO_{2.72}$), a monoclinic sub-oxide that is a common product of many tungsten oxide NC synthesis (Figure 1.2c).[30] The particles mainly form rod-like structures or nanowires that can have a length ranging from a few nanometers to several micrometers, depending on the synthesis. The growth direction being typically along [010]. These particles have high crystallinity only along their growth direction, which follows the W-O-W bond from stacked, edge-sharing WO_6-ocatahedra.

The hexagonal channels of h-WO_3 hold, similar to the perovskite type cubic tungsten oxides, the possibility to intercalate monovalent cations such as alkali metals with a general formula M_xWO_3 ($M=K^+$, Rb^+, Cs^+, NH_4^+, In^+, $0\leq x\leq 1$).[31–33] Similar to the sub-oxides of tungsten, partial reduction of these hexagonal tungsten oxides is observed. Such structures are known under the general term 'tungsten bronzes' due to their potential metallic behavior. Next to the hexagonal structure, tungsten bronzes are also known to form tetragonal, orthorhombic and cubic (pyrochlore) structures.[34]
Many reduced tungsten oxides display an intense blue coloring and are often found under the term '*tungsten blue oxides*'.[35,36] This appearance is associated with fluorescent properties, as well as localized surface plasmon resonance.[37,38]

1.2.2 Wolframite group

Besides the tungsten sub-oxides and bronzes, several (transition)-metal tungsten oxides are known, one of the most common structure being wolframite. This structure consists of a M^{2+} metal cation with an WO_4^{2-} (tungstate) anion, where all metals are coordinated octahedrally.[39] The monoclinic wolframite group can be viewed as layers of edge sharing octahedra of one metal, which are linked to similar layers of the other metal via corner of the octahedra.[40] The name wolframite group is based on the mineral $(Fe,Mn)WO_4$ covering all possible Fe:Mn ratios. The pure iron tungstate is called ferberite ($FeWO_4$, Figure 1.2d)[40], the analogue manganese counterpart hübnerite ($MnWO_4$).[39] Other prominent examples sharing this structure are $CoWO_4$, $ZnWO_4$, $MgWO_4$ and $NiWO_4$.[41,42]
$MnWO_4$, $FeWO_4$, $CoWO_4$ and $NiWO_4$ are paramagnetic and exhibit an antiferromagnetic ordering at Neel-temperatures T_N of 13.5 K, 76 K, 55 K and 67 K respectively.[39,41,43–45]

1.2.3 Localized surface plasmon resonance

Metal NCs convey an electromagnetic wave oscillating on the surface if conducting band electrons are excited by photons with certain frequencies. Such evanescent waves are called localized surfaces plasmon and their resonance energy is depending on different factors. Intrinsic properties of the material such as permittivity, but also refraction index of the surrounding medium, as well as size and morphology of the respective nanoparticle affect the energy of surface plasmons. Noble metal NCs (Ag, Au) are prototypes for the investigation of localized surface plasmon resonance (**LSPR**) as they are stable at ambient conditions and easily synthesized. Their LSPR band is often within the range of visible light, thus colloidal suspensions of these particles are colored.[46]

The two most investigated morphologies are spherical and elongated gold NCs. Spherical NCs reveal only one band, whereas the LSPR of elongated NCs is divided into a transversal (short axis) and a longitudinal (long axis) band. Figure 1.3 illustrates the resulting absorption spectra of both particle types. The resonance of longitudinal and transversal absorption is strongly depending on the aspect ratio (**AR)** of the particles, with the longitudinal being more intense and shifted to higher wavelength.[38,46]

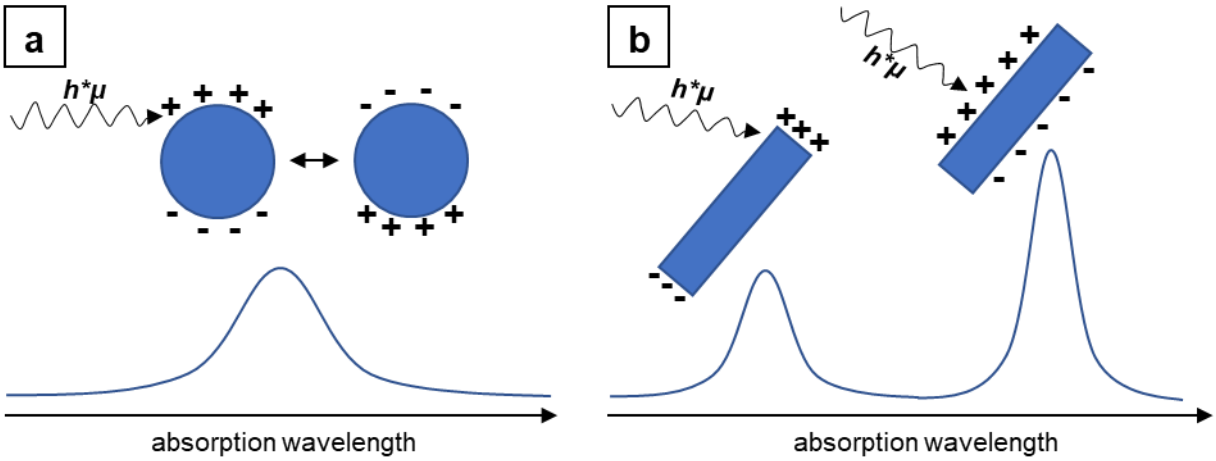

Figure 1.3. Localized surface plasmon resonance and resulting absorption spectra of a) spherical and b) rod-like nanocrystals. Inspired by [46].

1.3 References

1 V. K. LaMer and R. H. Dinegar, *J. Am. Chem. Soc.*, 1950, **72**, 4847–4854.

2 N. T. K. Thanh, N. Maclean and S. Mahiddine, *Chem. Rev.*, 2014, **114**, 7610–7630.

3 J. Park, J. Joo, S. G. Kwon, Y. Jang and T. Hyeon, *Angew. Chem. Int. Ed.*, 2007, **46**, 4630–4660.

4 S. G. Kwon and T. Hyeon, *Small*, 2011, **7**, 2685–2702.

5 M. Niederberger and H. Cölfen, *Phys. Chem. Chem. Phys.*, 2006, **8**, 3271–3287.

6 J. van Embden, A. S. R. Chesman and J. J. Jasieniak, *Chem. Mater.*, 2015, **27**, 2246–2285.

7 R. L. Penn and J. F. Banfield, *Science*, 1998, **281**, 969–971.

8 M. Juelsholt, T. Lindahl Christiansen and K. M. Ø. Jensen, *J. Phys. Chem. C*, 2019, **123**, 5110–5119.

9 R. Dören, B. Leibauer, M. A. Lange, E. Schechtel, L. Prädel, M. Panthöfer, M. Mondeshki and W. Tremel, *Nanoscale*, 2021, **13**, 8146–8162.

10 J. Polleux, M. Antonietti and M. Niederberger, *J. Mater. Chem.*, 2006, **16**, 3969–3975.

11 Z. Xu, C. Shen, Y. Hou, H. Gao and S. Sun, *Chem. Mater.*, 2009, **21**, 1778–1780.

12 S. Mourdikoudis and L. M. Liz-Marzán, *Chem. Mater.*, 2013, **25**, 1465–1476.

13 Z. Zhou, X. Zhu, D. Wu, Q. Chen, D. Huang, C. Sun, J. Xin, K. Ni and J. Gao, *Chem. Mater.*, 2015, **27**, 3505–3515.

14 C.-T. Dinh, T.-D. Nguyen, F. Kleitz and T.-O. Do, *ACS Nano*, 2009, **3**, 3737–3743.

15 C. Cara, A. Musinu, V. Mameli, A. Ardu, D. Niznansky, J. Bursik, M. A. Scorciapino, G. Manzo and C. Cannas, *Cryst. Growth Des.*, 2015, **15**, 2364–2372.

16 M. B. Mohamed, K. M. AbouZeid, V. Abdelsayed, A. A. Aljarash and M. S. El-Shall, *ACS Nano*, 2010, **4**, 2766–2772.

17 V. Perner, T. Rath, F. Pirolt, O. Glatter, K. Wewerka, I. Letofsky-Papst, P. Zach, M. Hobisch, B. Kunert and G. Trimmel, *New J. Chem.*, 2019, **43**, 356–363.

18 E. Hassanabadi, M. Latifi, A. F. Gualdrón-Reyes, S. Masi, S. J. Yoon, M. Poyatos, B. Julián-López and I. Mora-Seró, *Nanoscale*, 2020, **12**, 14194–14203.

19 J. Park, K. An, Y. Hwang, J.-G. Park, H.-J. Noh, J.-Y. Kim, J.-H. Park, N.-M. Hwang and T. Hyeon, *Nat. Mater.*, 2004, **3**, 891–895.

20 T. Vogt, P. M. Woodward and B. A. Hunter, *J. Solid State Chem.*, 1999, **144**, 209–215.

21 H. Zheng, J. Z. Ou, M. S. Strano, R. B. Kaner, A. Mitchell and K. Kalantar-zadeh, *Adv. Funct. Mater.*, 2011, **21**, 2175–2196.

22 E. K. H. Salje, S. Rehmann, F. Pobell, D. Morris, K. S. Knight, T. Herrmannsdörfer and M. T. Dove, *J. Phys.: Condens. Matter*, 1997, **9**, 6563–6577.

23 A. Hjelm, C. G. Granqvist and J. M. Wills, *Phys. Rev. B*, 1996, **54**, 2436–2445.

24 B. Gerand, G. Nowogrocki, J. Guenot and M. Figlarz, *J. Solid State Chem.*, 1979, **29**, 429–434.

25 D. B. Migas, V. L. Shaposhnikov and V. E. Borisenko, *J. Appl. Phys.*, 2010, **108**, 93714.

26 R. Pickering and R. Tilley, *J. Solid State Chem.*, 1976, **16**, 247–255.

27 A. Magneli, *Pure Appl. Chem.*, 1978, **50**, 1261–1271.

28 A. Magnéli, *Acta Crystallogr.*, 1953, **6**, 495–500.

29 A. Magnéli, *Nature*, 1950, **165**, 356–357.

30 K. Viswanathan, K. Brandt and E. Salje, *J. Solid State Chem.*, 1981, **36**, 45–51.

31 A. Magnéli, A. I. Virtanen, J. Olsen and N. A. Sörensen, *Acta Chem. Scand.*, 1953, **7**, 315–324.

32 P. G. Dickens, A. C. Halliwell, D. J. Murphy and M. S. Whittingham, *Trans. Faraday Soc.*, 1971, **67**, 794–800.

33 A. B. Swanson and J. S. Anderson, *Mater. Res. Bull.*, 1968, **3**, 149–152.

34 K. P. Reis, A. Ramanan and M. S. Whittingham, *J. Solid State Chem.*, 1992, **96**, 31–47.

35 H.-J. Lunk, B. Ziemer, M. Salmen and D. Heidemann, *Int. J. Refract. Hard Met.*, 1993, **12**, 17–26.

36 H.-J. Lunk, M. Salmen and D. Heidemann, *Int. J. Refract. Hard Met.*, 1998, **16**, 23–30.

37 A. Yella, M. N. Tahir, S. Meuer, R. Zentel, R. Berger, M. Panthöfer and W. Tremel, *J. Am. Chem. Soc.*, 2009, **131**, 17566–17575.

38 K. Manthiram and A. P. Alivisatos, *J. Am. Chem. Soc.*, 2012, **134**, 3995–3998.

39 H. Weitzel, *Z. Kristallogr. – Cryst. Mater.*, 1970, **131**, 289–313.

40 H. Cid-Dresdner and C. Escobar, *Z. Kristallogr. – Cryst. Mater.*, 1968, **127**, 61–72.

41 C. Wilkinson and M. J. Sprague, *Z. Kristallogr. – Cryst. Mater.*, 1977, **145**, 96–107.

42 R. C. Pullar, S. Farrah and N. M. Alford, *J. Eur. Ceram. Soc.*, 2007, **27**, 1059–1063.

43 H. Weitzel and H. Langhof, *J. Magn. Magn. Mater.*, 1977, **4**, 265–274.

44 H. A. Obermayer, H. Dachs and H. Schröcke, *Solid State Com.*, 1973, **12**, 779–784.

45 R. Guillen and J. R. Regnard, *Phys. Chem. Miner.*, 1985, **12**, 246–254.

46 L. M. Liz-Marzán, *Langmuir*, 2006, **22**, 32–41.

The following chapter 2 is reproduced from Nanoscale, 2021, 13, 8146-8162, DOI: 10.1039/d0nr09055g with permission from the Royal Society of Chemistry.

Authorship Contributions Chapter 2

Conception and design of the study:

[redacted]

Preparation of samples and acquisition of data:

[redacted] – preparation of samples

[redacted] – TEM measurements

[redacted] – PXRD measurements

[redacted] – NMR measurements

[redacted] – UV-Vis-NIR measurements

[redacted] – XPS measurements

[redacted] – ζ-potential measurements

Analysis and interpretation of data:

[redacted] – PXRD diffraction and refinements

[redacted] – TEM images

[redacted] – NMR spectroscopy

[redacted] – UV-Vis-NIR spectroscopy, ζ-potential

[redacted] – XPS spectroscopy

Drafting of the manuscript:

[redacted]

Revising the manuscript critically for important intellectual content:

[redacted]

Preparation of figures:

[redacted]

2. Gram-Scale Selective Synthesis of WO_{3-x} Nanorods and $(NH_4)_xWO_3$ Ammonium Tungsten Bronzes with Tunable Plasmonic Properties

2.1 Abstract

Localized surface plasmon resonance properties in unconventional materials like metal oxides or chalcogenide semiconductors have been studied for use in signal detection and analysis in biomedicine and photocatalysis. We devised a selective synthesis of the tungsten oxides WO_{3-x} and $(NH_4)_xWO_3$ with tunable plasmonic properties. We selectively synthesized WO_{3-x} nanorods with different aspect ratios and hexagonal tungsten bronzes $(NH_4)_xWO_3$ as truncated nanocubes starting from ammonium metatungstate $(NH_4)_6H_2W_{12}O_{40} \bullet xH_2O$. Both particles form from the same nuclei at temperatures >200°C; monomer concentration and surfactant ratio are essential variables for phase selection. $(NH_4)_xWO_3$ was the preferred reaction product only for fast heating rates (25 K/min), slow stirring speeds (~150 rpm) and high precursor concentrations. A proton nuclear magnetic resonance (^{1}H-NMR) spectroscopic study of the reaction mechanism revealed that oleyl oleamide, formed from oleic acid and oleylamine upon heating, is a key factor for the selective formation of WO_{3-x} nanorods. Since oleic acid and oleylamine are standard surfactants for the wet chemical synthesis of many metal and oxide nanoparticles, the finding that oleyl oleamide acts as chemically active reagent above 250°C may have implications for many nanoparticle syntheses. Oriented attachment of polyoxotungstate anions is proposed as a model to rationalize phase selectivity. Magic angle spinning (MAS) ^{1}H-NMR and powder X-ray diffraction (PXRD) studies of the bronze after annealing under (non)inert conditions revealed an oxidative phase transition. WO_{3-x} and $(NH_4)_xWO_3$ show a strong plasmon absorption for near infra-red light between 800 and 3300 nm. The maxima of the plasmon bands shift systematically with the nanocrystal aspect ratio.

2.2 Introduction

The tungsten-oxygen system is of technological importance in view of the application of tungsten metal and its compounds. Tungsten oxides are the starting point for the extraction of tungsten metal at elevated temperatures. Magnéli unraveled the conditions under which the binary phases of the tungsten-oxygen system are stable.[1,2] Besides different phases of WO_3[3,4] a number of sub-stoichiometric oxides WO_x ($2.625 \leq x \leq 2.92$) have been described. They are ordered line phases with precise stoichiometries $WO_{2.625}$ ($W_{32}O_{84}$),[55] $WO_{2.67}$ (W_3O_8)[6], $WO_{2.72}$ ($W_{18}O_{49}$),[7] $WO_{2.76}$ ($W_{17}O_{47}$),[8] $WO_{2.90}$ ($W_{20}O_{58}$)[1,2], $WO_{2.92}$ ($W_{25}O_{73}$)[9] (general formula W_nO_{3n-2})[10] whose structures are derived from the ReO_3 structure type. Characteristic features of their structures are WO_7 pentagonal bipyramids surrounded by five edge-sharing W–O octahedra.[8] In the ternary Nb-W-O phases the 7-coordinated position is occupied by the Nb atoms with larger atomic radius.[11]

The family of tungsten oxide structures can be described in terms of ordered one- or two-dimensional crystallographic shears, which are the principal sources of their structural complexity. The electrical and optical properties in bulk WO_{3-x} ($0 < x < 1$) are dominated by the oxygen deficiency. The associated gradual reduction of the tungsten atoms and the concomitant increase of the 5d band occupancy leads to a change of the optical and electrical properties.[12,13] Bulk WO_{3-x} undergoes a metal−insulator transition at $x = 0.1$, which has been established by temperature-dependent conductivity studies,[7,14] reflectivity measurements of the bulk plasma frequency, and X-ray photoelectron spectroscopy (XPS).[15]

Different from the sub-stoichiometric oxides, tungsten bronzes, originally described by Hägg,[16] are non-stoichiometric compounds of general formula A_xWO_3 ($0 < x < 1$), depending on the crystal phase.[17] The A cation comprises a range of choices including protons, alkali or alkaline earth metals and ammonium. Additionally, phosphate tungsten bronzes are known.[18] Structurally, the tungsten bronzes can be viewed as molecular sieve-like WO_3 open frameworks of cubic (pyrochlore), tetragonal, orthorhombic or hexagonal structure, depending on the nature of the metal cation and its fractional occupancy in the structure channels.[19–21] The cation occupancy determines the oxidation state of tungsten and thus the structural,[22] electrical,[23] magnetic,[12] electrochromic[24–26] or superconducting[19,27,2819YPERLI] properties of the bronzes. Tungsten (and molybdenum) bronzes can undergo charge density wave transitions.[18] Since minor variations in composition, temperature, or pressure can lead to dramatic changes in the physical properties, these “tungsten bronzes” serve as prototype model compounds in studies of electronic instabilities.[18] Tungsten bronzes as well as sub-stoichiometric oxides can show an intensive blue color and are often referred as ‘tungsten blue oxides’.[29] The redox properties of partially reduced tungsten oxides make them very promising candidates for a range of potential applications in photocatalysis,[30–33] photoelectrochemical water splitting,[34,35] for thermoelectrics,[36,37] in catalysis,[38,39] as anode material in Li-ion batteries,[40] for gas sensing,[41] in electrochromic layers,[42] as starting material for making WS_2 nanotubes,[43,44] in plasmonics,[45–47] or for antibacterial coatings,[48,49] because tungsten oxides are stable

under a wide range of conditions, and their band gaps in the red/infrared range are ideal for the absorption of visible light.

Tungsten bronzes and sub-stoichiometric oxides suffer from low electronic and ionic diffusion rates in the bulk, a problem that can be cured by reducing the dimensions to the nanoscale in order to minimize the diffusion length. This requires colloidally stable nanocrystals with tailored morphology, size and adjustable surface chemistry. Nanocrystals are compatible with small electron/ion diffusion coefficients[50] and high reactivities due to smaller diffusion paths and larger surface areas.[51] On the other hand, small particles may have undesired and unintended surface effects and lower crystallinity. Therefore, every application has an optimum nanocrystal size for maximum performance. However, such a size-dependent analysis is only possible for highly uniform and non-aggregated samples. Different plasmonic tungsten oxide nanoparticles have been reported, including WO_{3-x},[47,52–54] $(NH_4)_xWO_3$,[55] Na_xWO_3,[56] K_xWO_3,[57] and Cs_xWO_3.[58]

Although both the preparation of WO_{3-x} nanorods and hexagonal bronzes has been described before, their formation mechanism is still not well understood. This lack of understanding of molecular processes makes many of the surfactant-assisted protocols poorly reproducible and prevents the preparation of nanoparticles in large quantities. Thermal decomposition of labile molecular precursors is an appealing route for the synthesis of monodisperse nanocrystals. Still, the apparent simplicity of the synthesis is counterbalanced by a complex interplay of reaction variables that determine the final particle size, composition and morphology. Tungsten oxides and bronzes are formed in solution via polycondensation reactions, in the course of which large polyoxometalate clusters are formed. These clusters are molecularly defined polyanions whose stability range is determined by chemical variables such as solvent (which also acts as ligand), pH, electrochemical potential, temperature, organic ligands, and counter ions. Mixed oxides are prepared by the addition of other polyoxometalates as precursors.[59] Polyoxoanions may be viewed as prenucleation clusters for tungsten oxide formation in a variety of processes. The influence of the starting compounds, the formation sequence of polytungstate polyanions by polycondensation, the role of the solvent as well as the capping agents are still unclear.

Several *in situ* methods are available for tracking structural changes in solution.[60] Small angle scattering provides information about the size and shape of solution species, phase analysis is possible with powder X-ray powder diffraction (PXRD). A serious disadvantage here is that the samples must be crystalline, and a new phase can only be detected after its “birth”. Using X-ray total scattering with pair distribution analysis, the structure formation can be monitored starting from clusters in solution *via* molecular or amorphous intermediates to the crystalline final product even under hydro/solvothermal conditions.[61–63] However, the role of the organic ligands remains unresolved due to their small scattering contribution. We therefore performed a kinetic analysis of the formation of Magneli-type WO_{3-x} nanorods starting from ammonium meta-tungstate $(NH_4)_6H_2W_{12}O_{40} \bullet xH_2O$ (AMT) in a mixture of oleic acid (HOAc) and

oleylamine (OAm) using *ex situ* transmission electron microscopy (TEM)[64] and proton nuclear magnetic reseonance spectroscopy (^{1}H-NMR)[65] snapshots after given times and temperatures. Questions to be answered were (i) the formation mechanisms of Magneli-type WO_{3-x} phases, (ii) the formation of intermediates or the competing hexagonal ammonium tungsten bronze (h-ATB) phase, (iii) possible reactions between the capping agents HOAc and OAm and (iv) reaction control by surface-bound ligands.[66,67] Finding optimum conditions is a crucial task where synthetic variables (e.g., surfactants, precursor concentration, heating rate and stirring speed) are involved that are relevant as well in upscaling processes. Surfactants proved to be a synthetic key variable. ^{1}H-NMR revealed the formation of oleyl oleamide (OAd) by condensation of the HOAc and OAm in a primary step, which has an impact on the growth species and on product selectivity. We propose a reaction mechanism based on nonclassical nucleation and mesocrystal formation *via* oriented attachment.[68,69] Temperature related studies of metastable structures such as hexagonal tungsten oxides can provide useful information about stability and composition and intermediate products that could open pathways to potential applications.[70,71] By solid state ^{1}H-NMR spectroscopy and PXRD we were able to analyze the role of the NH_4^+ cation situated in channels of the bronze structure and the adsorption of water on the crystallite surfaces. The WO_{3-x} nanorods and $(NH_4)_xWO_3$ nanocrystals showed a strong plasmonic absorption above 800 nm. By a systematic investigation of the plasmonic absorption for different particle sizes, we demonstrate the relation between aspect ratio and plasmonic properties that have been addressed mainly theoretically in literature.[46] As our synthesis model yields reproducible, tailored nanocrystals on a large-scale from readily available and cheap chemicals, our findings could be very interesting for various applications.

2.3 Results and discussion

2.3.1 Competing Formation of WO_{3-x} Nanorods and $(NH_4)_xWO_3$ Bronzes

The decomposition of ammonium metatungstate (**AMT)** in a mixture of oleic acid (**HOAc)** and oleylamine (**OAm)** led to formation of WO_{3-x} nanorods and hexagonal ammonium tungsten bronze $(NH_4)_xWO_3$ (h-**ATB)**. We observed a strong dependence on the concentration of the AMT precursor. The nucleation and growth of nanocrystals is described by a set of coupled time-dependent equations that govern the dynamics of monomer concentration, nucleation rate, and particle size distribution. Relevant experimental variables are the surfactant ratio, heating rate, aging time, reaction temperature and precursor concentration.[72–75] We performed a systematic variation and evaluation of several variables to provide detailed information for this specific synthesis. Reactions for the investigation of WO_{3-x} nanorod formation were labeled **NR-X** and for the hexagonal bronze $(NH_4)_xWO_3$ **ATB-X**. Figure 2.1a gives an schematic overview for the most significant parameters and Table 2.1 provides detailed information about the relevant reactions analyzed in this paper.

In our standard experiments, the total amount of the HOAc and OAm surfactants was fixed at 40 mmol (1:1 for standard conditions) for different concentrations of the AMT precursor (multiples of 0.12 mmol, i.e. 1.43 mmol tungsten). AMT was chosen because of its availability and low costs compared to the frequently used tungsten precursors WCl_6[53,55], $W(CO)_6$[52,76], $W(OEt)_6$[46,47] and WCl_4[58,77]. Starting from the 'standard synthesis' (**NR-1**), TEM images of the particles (Figure 2.2a) show rod-like structures. The size of the crystals was calculated to be ~77.7 nm*7.6 nm (Table 2.2). The PXRD pattern (Figure 2.2e) was compatible with the monoclinic Magnéli structure of $WO_{2.72}$ (or $W_{18}O_{49}$). As a structural analysis is generally non-trivial for low-dimensional, nonstoichiometric metal oxides we use the generalized formula WO_{3-x} for theses nanorods. The presence of only two reflections indicates a preferred orientation along [010], as see often for these nanorods.[52,53] High resolution transmission electron microscopy (HR-TEM, Figure 2.3a, b) verified a *d* spacing of 3.8 nm along [010]. No other crystallographic planes are observed, underlining the preferred orientation of the nanorods in accord with the results obtained from PXRD.

Table 2.1. Overview of syntheses for nanorods (**NR-X**), h-ATB (**ATB-X**), with oleyl oleamide (**Amide-X**) with reaction conditions and estimated ratio of WO_{3-x} and h-ATB. Complete table: Table S8.1.1 (c) purified particles.

Particle Label	**HOAc:OAm:ODE / mmol**	**n(AMT) / mmol**	**Heating Rate / K/min**	**Stirring speed / rpm**	**% h-ATB (compared to WO_{3-x})**
NR-1	20:20:0	0.12	5	500	<2
NR-4	30:10:0	0.12	5	500	<2
NR-8	10:30:0	0.12	5	500	<2
NR-14	20:20:0	0.36	2,5	800	~50:50
ATB-1	20:20:0	0.24	5	500	40-80
ATB-2(c)	20:20:0	0.36	5	500	80-90(>90)
ATB-7	20:20:0	0.24	10	500	70-90
ATB-8	20:20:0	0.24	2.5	500	<10
ATB-9	20:20:0	0.24	10	0	>90
ATB-11	20:20:0	0.24	10	1000	<20
ATB-13(c)	40:40:0	0.48	25	150	>95 (>98)
ATB-15(c)	20:20:0	0.36	25	150	>95 (>98)
Amide-2	20 mmol amide[a]	0.36	5	500	<10
Amide-3	20 mmol amide[a]	0.24	25	150	>90

a. oleyl oleamide (OAd) synthesized hydrothermally without purification.

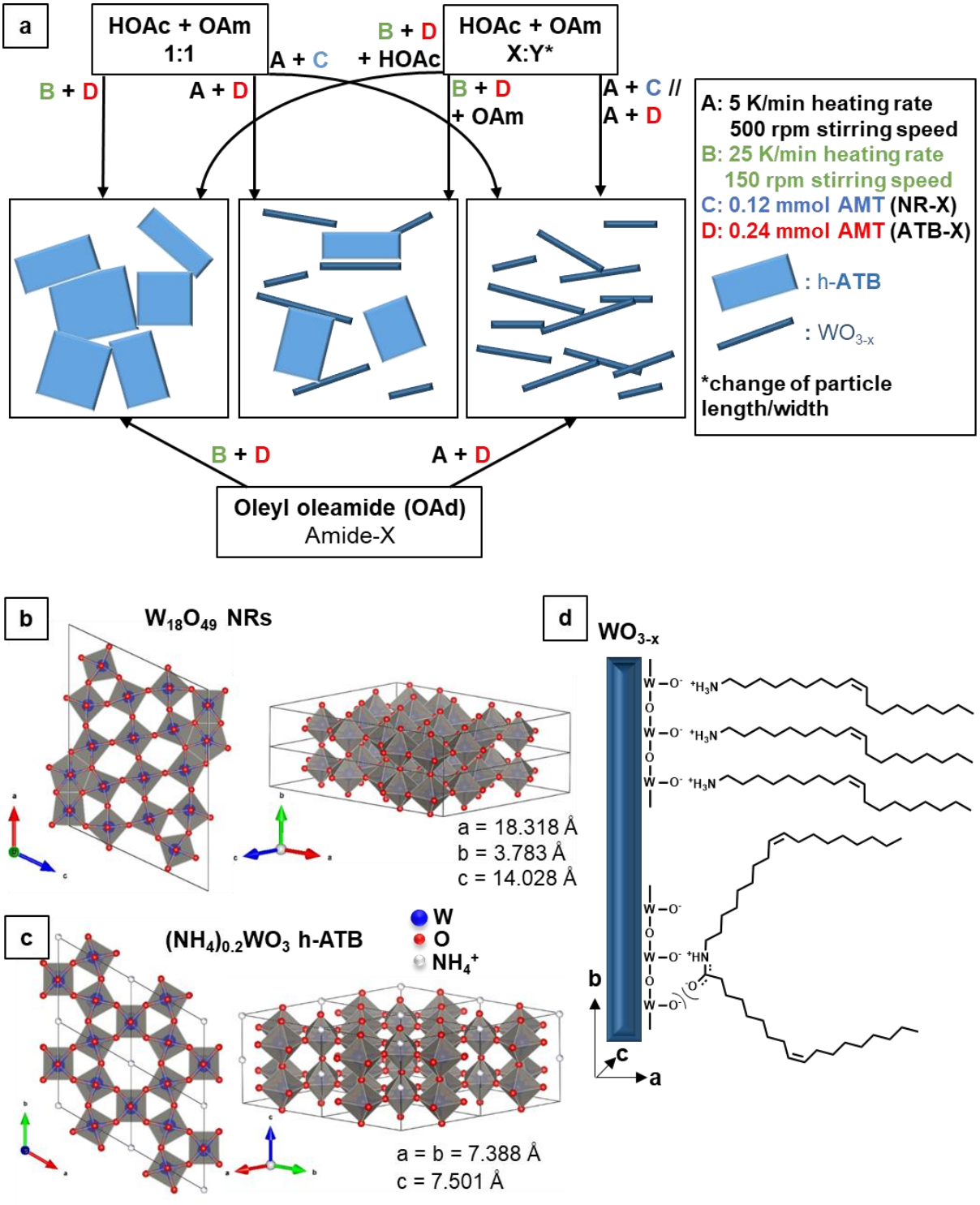

Figure 2.1. a) Overview scheme showing the reaction conditions leading to the formation of WO_{3-x} nanorods and h-ATB. b) Crystal structure of $W_{18}O_{49}$ (P2/m) (COD-ID: 1001678) and c) $(NH_4)_{0.2}WO_3$ ($P6_3$) according to the refinement of **ATB-13c** (Figure S8.1.2). d) Surface coordination of OAm and OAd for O^--terminated WO_{3-x} nanorods indicating steric effects of the ligands and resonance structure of OAd.

It is only possible to compare the combined intensities of both reflections with that of the unique 200 reflection of h-ATB ($Q = 1.966$ Å^{-1}). We used this semiquantitative method to estimate the purity of the

h-ATB phase (with respect to the WO_{3-x} side product) in different reaction setups (Table 2.1).

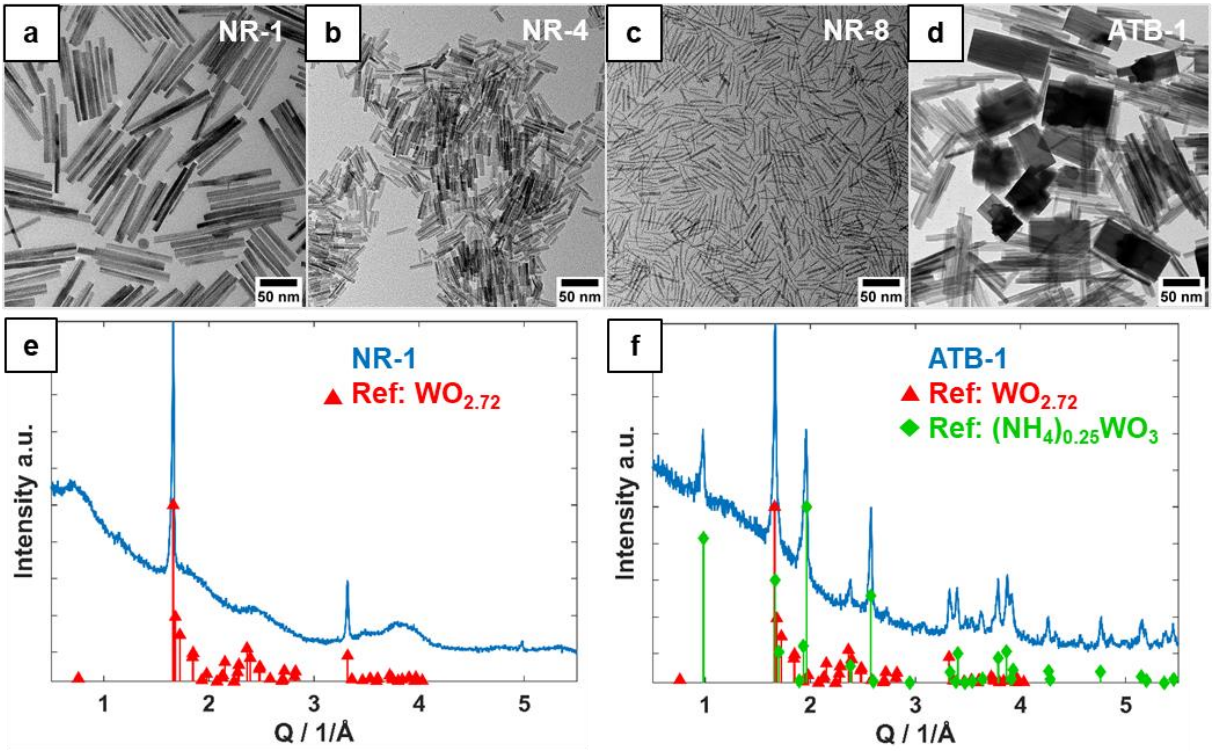

Figure 2.2. a) TEM image of WO_{3-x} nanorods obtained from the standard synthesis **NR-1** (T =350 °C, t = 30 min, heating rate = 5 °/min, HOAc/OAm = 20:20 mmol, AMT = 0.12 mmol), b) with HOAc/OAm ratio of 30:10 mmol (**NR-4**), c) with HOAc/OAm ratio of 10:30 mmol (**NR-8**), d) of a mixture of h-ATB and WO_{3-x} nanorods obtained from a synthesis with 0.24 mmol AMT (**ATB-1**) e) PXRD-diffractogram of **NR-1** (similar to **NR-4** and **NR-8**) with $WO_{2.72}$ Reference (COD, Entry No.: 96-152-8167). and f) PXRD-diffractogram of **ATB-1** with additional $(NH_4)_{0.25}WO_3$ Reference (ICDD, PDF Entry No.: 01-073-1084).

Table 2.2. Particle sizes including length, width, aspect ratio and number of particles of WO_{3-x} nanorods for selected syntheses. The corresponding histograms are provided in Figure S8.1.1.

Particle label	length / nm	width / nm	aspect ratio	NPs measured
NR-1	77.7±23.1	7.6±2.3	10.6±3.4	453
NR-4	25.2±8.4	5.5±1.7	4.8±1.5	400
NR-8	30.1±8.1	2.5±0.6	12.5±4.3	100
ATB-13	112.3±33.2	49.6±16.9	2.4±0.9	203

Additionally, we observed a poor solubility of h-ATB in non-polar solvents (e.g., chloroform). This indicates a lack of extensive HOAc or OAm surface binding. The solubility was used successfully for the purification of h-ATB by repeated dissolving the WO_{3-x} nanorods in $CHCl_3$ and separation of the supernatant from h-ATB by centrifugation. PXRD patterns in Figure 2.4 show, how the purification procedure affects the h-ATB content for a synthesis with 0.36 mmol AMT (**ATB-2**), that shows

significantly higher h-ATB content, after five cycles of purification (**ATB-2c**). We observed a significant reduction of the overlapping 010/002 reflections ~17 % towards the unique 200 reflection of h-ATB. As the poorly resolved X-ray data for WO_{3-x} ($WO_{2.72}$) (due to (i) the small particle size (only ~5 unit cells) in two dimensions, (ii) the structural disorder (Figure 2.1b) and (iii) the strongly preferred orientation allowed only a Pawley refinement (Figure S8.1.2a), we cannot give a reliable information on product purity. Table S8.1.2 compiles the lattice parameters and anisotropic crystallite size for the nanorods in direction a, b and c.

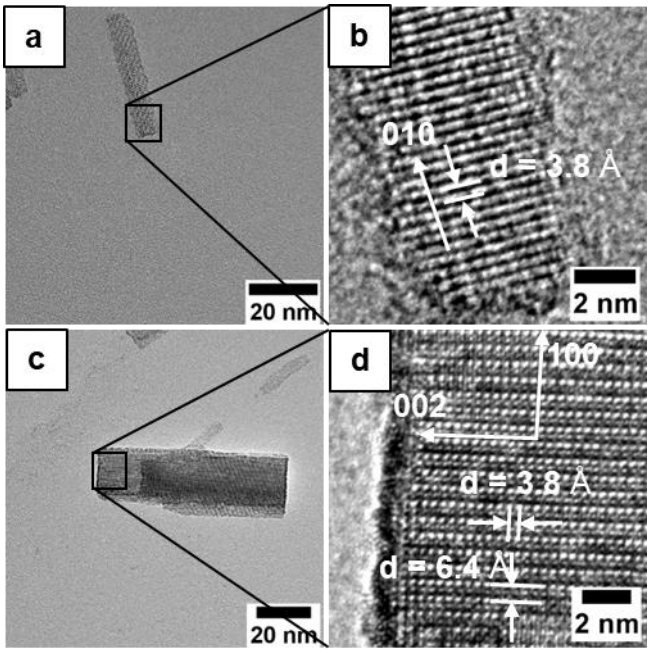

Figure 2.3. TEM and HR-TEM images of a, b) $WO_{2.72}$ NRs and c, d) h-ATB particles. Images taken from sample **NR-14**, containing both, NRs and h-ATB particles.

A kinetic analysis of the **ATB-1** reaction using TEM was performed to get information regarding the reaction mechanism. A ~200 µL sample was taken in a standard reaction containing twice the amount of AMT precursor at temperatures of 200, 250, 275, 300, 325 and 350 °C and after 5 min, 30 min, and 60 min dwelling time at 350 °C. The corresponding TEM images (Figure S8.1.3) revealed a sudden formation of h-ATB between 250 and 275 °C. Rod-like structures of ~150 nm evolved throughout the synthesis, starting at 200 °C (or even below). At 250 °C the larger structures had decomposed and small rods had formed. These rods appear to be the in the early stages of particle growth right after nucleation, and they are in the size range of polyoxotungstates (i.e. 1-3 nm wide and 3-22 nm long).[61,63,78]

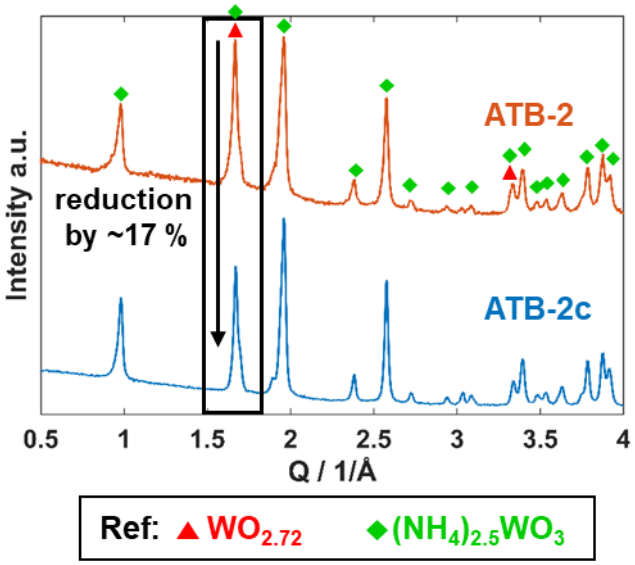

Figure 2.4. PXRD patterns of particles synthesized according to standard synthesis with 3-fold AMT (0.36 mmol) concentration before (**ATB-2**) and after (**ATB-2c**) purification (five times) with chloroform.

Such polyoxotungstates have been identified as paratungstates or α-Keggin like clusters under comparable conditions by *in-situ* diffraction.[63] As soon as the temperature exceeds 250 °C, burst nucleation of h-ATB is observed together with a growth of nanorods. As no other growth species were observed at 250 °C, these polyoxotungstates could serve as seeds for both, nanorod and h-ATB growth. Additionally, the AMT precursor could decompose completely above 250 °C,[79] leading to the burst growth of h-ATB due to a high monomer concentration. The nanorods kept growing until the temperature reached 350 °C, whereas no change occurred for h-ATB after reaching 300 °C. After 5 min at 350 °C no further change occurred at all, and the synthesis seems complete. We assume that besides precursor concentration the surfactant ratio, heating rate and stirring speed are fundamental variables affecting this system.

As we observed a significant difference in solubility of nanorods and h-ATB, we checked if the concentration and ratio of HOAc and OAm as surfactant have an impact on WO_{3-x} and h-ATB formation. In a mixture of HOAc and OAm the amine serves as Lewis base that deprotonates the acid HOAc according to the acid-base equilibrium (Eq. 2.1)).

$$RCOOH + RCNH_2 = RCOO^- + RCNH_3^+. \quad (2.1)$$

As excess of acid/amine leads to free, non-ionic surfactants, we performed a series of experiments with different ratios of HOAc and OAm with 0.12 and 0.24 mmol AMT loading.

For lower AMT concentrations we observed a decreasing nanocrystal length for an HOAc excess (Figure S8.1.4a-c, Figure 2.2c for **NR-4**). The nanocrystals were uniform in size for HOAc/OAm ratios

of 22.5:17.5 mmol (**NR-2**) and 25:15 mmol (**NR-3**). This uniformity decreased with increasing HOAc/OAm ratios of 30:10 mmol (**NR-4**) and 40:0 mmol (**NR-5**). This indicates that the HOAc content affects the length of the nanocrystals significantly. Changing the OAm concentration (and thus the HOAc/OAm ratio) in the same manner (Figure S8.1.4d-f, **NR-6**, **NR7** and **NR9**, respective, Figure 2.2c **NR-8**) leads to a decreasing diameter of the nanorods. A summary of the particle shape descriptors for **NR-1**, **NR-4** and **NR-8** (Figure 2.2a-c) is compiled in Table 2.2, the respective histograms are shown in Figure S8.1.1. We observe a reduction of the average particle length for high HOAc concentrations from 77.7 to 25.2 nm (**NR-1** → **NR-4**), whereas the length decreases only slightly from 7.6 to 5.5 nm. For higher OAm concentration (**NR-8**), the average length is also reduced (30.1 nm for NR-8), but the width is reduced even more significantly (7.6 to 2.5 nm). Checking the aspect ratio, i.e., length to width ratio, for different particles (10.6, 4.8 and 12.5 for **NR-1**, **NR-4** and **NR-8**), it becomes clear that excess HOAc has a higher impact on particle length than on particle width, whereas OAm mainly reduces the width of each particle. Additionally, several of **NR-8** particles appear bent, as their diameters of only 1-2 nm corresponds only to the width of a single $WO_{2.72}$ unit cell (Figure 2.1b). Thus, shear-forces from stirring might already be sufficient to cleave these particles, thereby reducing the particle length. Anisotropic crystallite sizes from Pawley refinements (Table S8.1.2) are in comparable with the size measured from TEM.

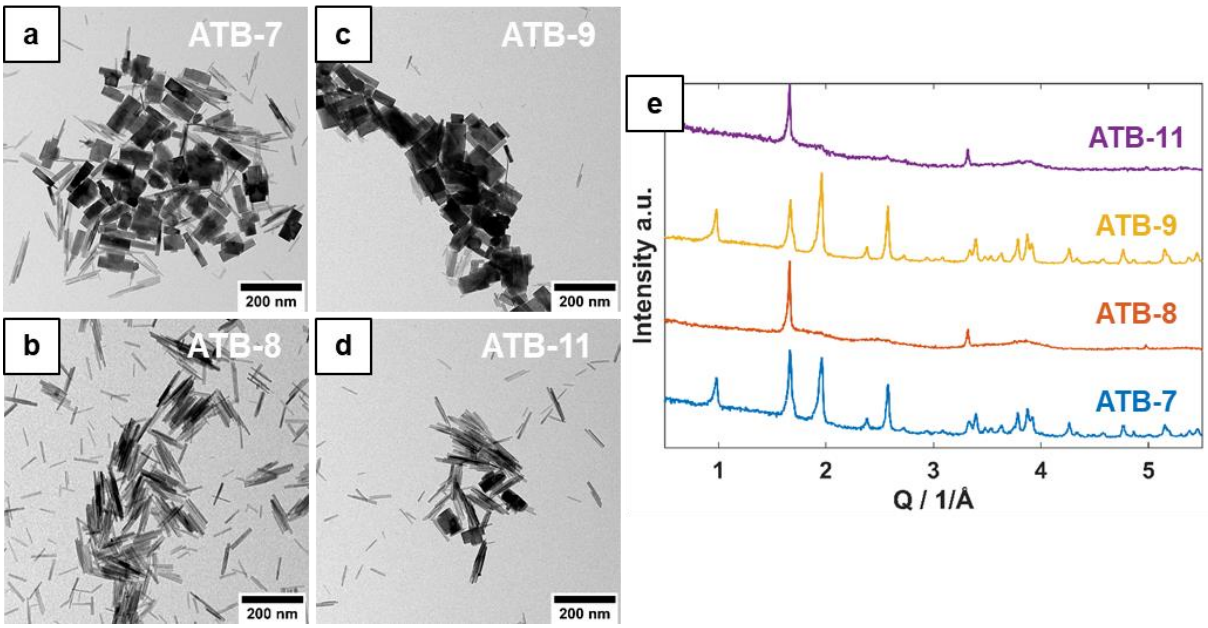

Figure 2.5. TEM images of WO_{3-x} / h-ATB particles from varied ATB-1 synthesis (fixed: 20:20 mmol HOAc/OAm, 0.24 mmol AMT, 350 °C for 30 min) with a) 10 °C/min (**ATB-7**), b) 2.5 °C/min heating rate (**ATB-8**), c) ~0 rpm and 10 °C/min (**ATB-9**), d) ~1000 rpm stirring speed and 10 °C/min (**ATB-11**) and e) corresponding PXRD-patterns for **ATB-7**, **ATB-8**, **ATB-9**, and **ATB-11**.

Different HOAc/OAm ratios were tested with twice the amount of AMT precursor regarding their influence on h-ATB formation (TEM and PXRD in Figure S8.1.4). For HOAc/OAm ratios of

22.5:17.5 mmol (**ATB-3**) and 17.5:22.5 mmol (**ATB-5**) we observed a reduced formation of h-ATB. Pure WO_{3-x} nanorods (almost no h-ATB contamination) were formed for surfactant ratios HOAc/OAm = 25:15 mmol (**ATB-4**) and 15:25 mmol (**ATB-6**).

In TEM images we observed that higher yields of h-ATB were obtained for a faster heating rate of 10 K/min (**ATB-7,** Figure 2.5a), whereas only WO_{3-x} nanorods were formed for a low heating rate of 2.5 K/min (**ATB-8,** Figure 2.5b). When the heating rate was kept at 10 K/min without stirring, excess h-ATB was formed (stirring speed of 0 rpm, **ATB-9,** Figure 2.5c), whereas WO_{3-x} nanorods were formed for a high stirring speed of 1000 rpm (only traces of h-ATB, **ATB-11,** Figure 2.5d). The PXRD patterns of those particles (Figure 2.5e) clearly show the effect of these different parameters. Variation of the heating rate (2.5 K/min, **NR-10** and 10 K/min, **NR-11**) without excess amount of AMT precursor had no effect on the final product (Figure S8.1.4g, h).

Optimized conditions for h-ATB formation comprise a stirring speed of 150 rpm (to prevent a boiling delay) and high heating rate of 25°K/min with an HOAc/OAm ratio of 20:20 mmol (**ATB-12**). These conditions allow the synthesis of gram scale sample batches. Twice the concentration of all components (**ATB-13**) allowed to increase the yield of h-ATB (approx. 1.2 g, ~90 %) per batch. The synthesis of even larger batches of h-ATB may be possible by reducing the amount of the WO_{3-x} side product. For 0.12 mmol AMT, an optimized single-batch synthesis yielded mainly h-ATB (~70 % **ATB-14**). For 0.36 mmol AMT the highest content of h-ATB (~95 % **ATB-15**) was found. Based on purified **ATB-13** particles (**ATB-13c**), we performed a Rietveld refinement for h-ATB only (Figure S8.1.2b) with crystallite size of ~60 nm (Table S8.1.2) and preferred orientation along [002]. Optimum refinements were obtained in space group $P6_3$ (instead of $P6_3/mcm$ as proposed by Schultz et al. for $K_{0.26}WO_3$.[80])

Upscaling the synthesis of WO_{3-x} nanorod was possible by setting the stirring speed to 800 rpm and the heating rate to 1 K/min (**NR-15**). However, increasing the volume by doubling the amount of AMT led to reduced mixing and thus to the formation of small amounts h-ATB as side product. Still, we could prepare gram amounts (approx. 1.2 g, ~90 % yield) of nearly phase pure WO_{3-x} nanorods by doubling the amount of the reactants (**NR-16**). TEM images and PXRD patterns of several upscaled synthesis are found in Figure S8.1.6.

To further investigate the effect of the surface-active species on h-ATB formation, we performed two types of synthesis (Figure S8.1.7) using identical conditions as for **ATB-12** with HOAc:OAm ratios of 15:25 mmol (**ATB-16**) and 25:15 mmol (**ATB-17**). h-ATB is main product again (with traces of WO_{3-x}) for excess HOAc. Using excess OAm resulted in the formation of much less h-ATB. In addition, the aspect ratio of the h-ATB nanocrystals increased (i.e., they were elongated). This indicates a structural relationship between WO_{3-x} and h-ATB.

XPS spectra of WO_{3-x} (**NR-1**) and h-ATB (**ATB-15c**) particles were measured to verify the presence of tungsten in reduced oxidation states and the nature of nitrogen species. Figure S8.1.8 (a-d for **NR-1**, e-

f for **ATB-15c**) shows overview spectra and the O1s, N1s and W4f core levels, matching closely values reported in ref. [54,55]. The W4f spectra show typical 4f7/2 (35.8 eV) and 4f5/2 (38.0 eV) doublets for W^{6+}, as well as shoulders at lower binding energies (34.4 eV and 36.6 eV) indicating the presence of W^{5+}. We calculated the W^{5+}/ W^{6+} ratio to be higher for WO_{3-x} than for h-ATB (~27 % and ~20 %). The N1s peaks are very weak for both, WO_{3-x} and h-ATB. Both spectra show signals at 401.9 eV for ammonium species and slight shoulders at 400.0 eV indicating presence of organic nitrogen, which is more pronounced for WO_{3-x} nanorods.

2.3.2 ^{1}H-NMR Study of Surfactant Reactions during WO_{3-x} Nanocrystal Formation and Role of Surfactant on Phase Selection

The surface-active species HOAc and OAm play a crucial role in the proposed reaction model. Therefore, further study of their behavior in the course of the reaction is essential. During nanoparticle synthesis an amide may be formed from HOAc and OAm (Eq. 2.2, Figure S8.1.9) by elimination of water at elevated temperatures.[65,81–83]

$$RCOO^- + RCNH_3^+ = RCONCR + H_2O \quad (2.2)$$

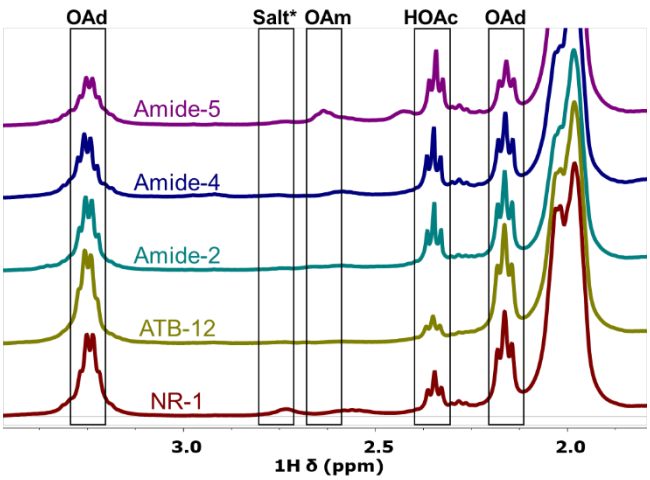

Figure 2.6. ^{1}H-NMR spectra of final reaction solution (30 min at 350 °C, 1:1 HOAc/OAm) for **NR-1**, **ATB-12**, **Amide-2**, **Amide-4** and **Amide-5** particles. Areas shown for α-H shifts of HOAc, OAm and OAd as well as oleylammonium oleate salt*. HOAc and OAm form OAd quantitatively before cleavage at the final heating step (Figure S8.1.10).

By studying the kinetics of the standard reaction (**NR-1**) using solution ^{1}H-NMR (Figure S8.1.10a) we could demonstrate the formation of the ion pair oleylammonium oleate (the ammonium salt of oleic acid and oleylamine) immediately after mixing HOAc and OAm. Condensation of this ionic pair at elevated temperature (T > 100 °C) led to the formation of oleyl oleamide (**OAd**). Complete conversion was

achieved with a heating rate of 5 K/min after 30 min at 350 °C, a conversion of 90 % to the amide was already reached at 275 °C. We observed no significant change for the condensation reaction in the absence of AMT (Figure S8.1.10b), i.e., AMT and tungsten oxide particle growth do not affect amide formation. At the end of the reaction, free (unbound) HOAc was observed only in the reaction mixture containing AMT, indicating that a cleavage of the amide OAd to oleic acid and oleylamine occurred during the final heating/annealing step (possibly catalyzed by acidic surface groups of the WO_{3-x} nanorods).[84] Figure 2.6 presents ^{1}H-NMR spectra of different reaction solutions after the reaction was complete. All of them show traces of HOAc (or $^-$OAc, probably stabilized by NH_4^+), whereas h-ATB (**ATB-12**) shows significantly less HOAc. This implies that the $OAmH^+$ counterpart stabilizes the negatively charged WO_{3-x} particle surfaces, improving the solubility of WO_{3-x} in the non-polar solvent. We conducted a control experiment, where **NR-1** particles were dissolved in 6.7 M sodium deuteroxide in D_2O (as tungsten oxides tend to form water-soluble tungstates (WO_4^{2-}) in highly basic environment).[85] Only free OAm and OAd (~3:1) were detected by ^{1}H and ^{1}H COSY NMR experiments after extracting the resulting solution with $CDCl_3$ (Figure S8.1.11a, b). The extract of the acidified aqueous solution with DCl showed no traces of HOAc.

WO_{3-x} nanorods should have less surface sites than h-ATB due to their lower crystallinity along the [001] and [100] directions (Figure 2.1b, c), i.e., electrostatic repulsion originating from the resonance structure of OAd will affect h-ATB to a higher extent (Figure 2.1d). As a result, WO_{3-x} NRs are functionalized to a higher extent than h-ATB, which explains their enhanced solubility.

For comparison, we synthesized pure OAd under (hydro-) thermal conditions[81] in quantitative yield without any additional solvent and used it without further purification to replace the HOAc/OAm couple in the particle synthesis (Figure S8.1.12). A synthesis under standard conditions (**NR-1**: T =350 °C, t = 30 min, heating rate = 5 °/min, AMT = 0.12 mmol) in the presence of OAd (**Amide-1**) and a threefold amount of AMT (**Amide-2**) yielded almost exclusively WO_{3-x} nanorods, whereas the HOAc/OAm couple under **Amide-2** conditions yielded 80-90 % h-ATB (**ATB-2**). Under optimized conditions for h-ATB formation according to **ATB-12**, h-ATB was the main product again (>90 %, **Amide-3**). We found significant amounts of HOAc in the final reaction solution of **Amide-2** (Figure 2.6) underlining the cleavage of OAd by WO_{3-x} nanorods.

In view of cost reduction, we recycled the reaction solutions (under **NR-1** conditions) to improve the yields. As the components are mainly unreacted AMT (or decomposition products) and OAd (as well as traces of HOAc) the resulting WO_{3-x} particles (**Amide-4**) are comparable in size with **NR-2** particles (100% yield with respect to the amount of AMT used for the second cycle). By adding a small amount of OAm we could synthesize WO_{3-x} particles comparable to those obtained from **NR-1** under standard conditions (**Amide-5**) and h-ATB using **ATB-12** conditions (**Amide-6**). Yields were close to 100 %.

TEM images and PXRD patterns of reactions using OAd (**Amide-1** - **Amide-6)** are compiled in Figure S8.1.12.

2.3.3 Mechanistic Study of WO_{3-x} and h-ATB Formation via Oriented Attachment

Although tungsten oxide nanoparticles have been reported repeatedly in the past, only a few articles were concerned with their nucleation and growth behavior. Polleux et al[53] found indications for nonclassical nucleation by oriented attachment during crystallization. Saha et al[61] and Juelsholt et al[63] investigated intermediate species during h-ATB growth by *in situ* X-ray total scattering. It has been found that nucleation can undergo several steps including formation of polyoxotungstates and a pyrochlore intermediate (depending on the solvent used for the synthesis). Based on the published results and our experimental data in this paper we propose a mechanism for the phase selectivity resulting from the effect of different surfactants and reaction conditions.

From the TEM kinetics of **ATB-1** we learned that only rod like polyoxotungstates were formed at 250 °C. Therefore, we assume that those polyoxotungstates serve as nuclei for both WO_{3-x} and h-ATB. The polyoxotungstates could form larger structures by oriented attachment along their short and long axes. Depending on the reaction conditions, either oriented attachment along the long or short axis could be favored, as illustrated in the overview in Figure 2.7a. For high AMT concentration with respect to the surfactant, more polyoxotungstates are formed and oriented attachment along the long axis to form h-ATB is statistically more likely. As excess HOAc or OAm led only to the formation of nanorods, we suppose that both surfactants must prevent the oriented attachment to h-ATB by blocking the surfaces of the growth species in the direction of the long axis. As the aspect ratio increases with increasing OAm content (eg. **NR-8**), the width of those particles is not significantly larger than the width of the polyoxotungstates from the TEM kinetics (~1.5-2.5 nm). Therefore, we suppose that amines can functionalize these surfaces during growth. This explanation is supported by the negative ζ potential (-35 mV) for **NR-1** particles, indicating O^- termination of those surfaces. For higher HOAc concentrations (excess HOAc) the aspect ratio decreased significantly. This indicates a blockage of oriented attachment along the short axis. We suppose that NH_4^+ cations must be present at the surfaces to induce oriented attachment and a subsequent phase transition to h-ATB. In this case HOAc would bind as oleate counterion, whereas analogously OAm^+ cations would compete for surface sites. Therefore, excess of both surfactants prevents h-ATB formation. Only for a 1:1 ratio of HOAc:OAm the formation of the ionic pair leads to less surface coordination and more h-ATB formation, because oriented attachment is not favored in any direction (i.e., on any surface).

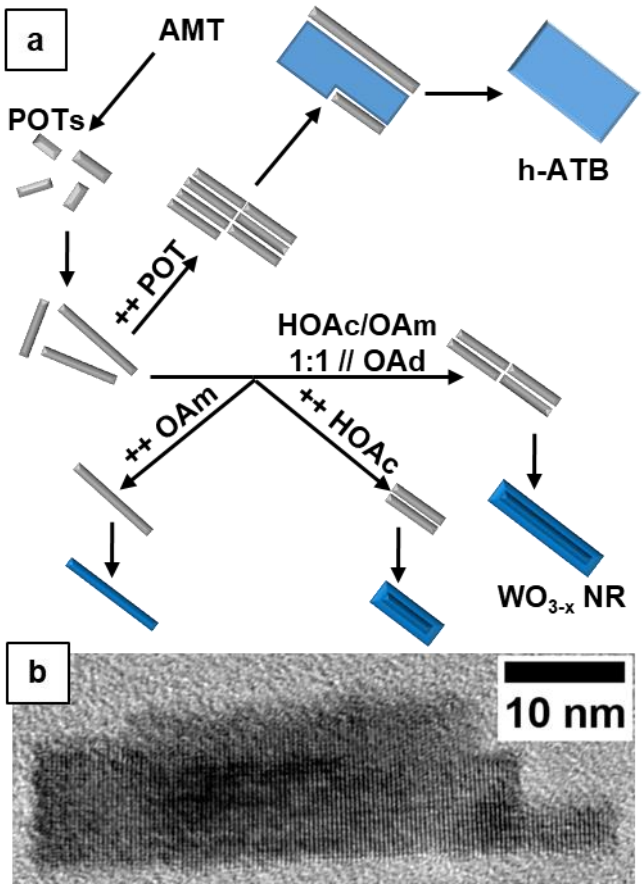

Figure 2.7. a) Proposed reaction mechanism based on the oriented attachment of polyoxotungstates under the influence of polyoxotungstate concentration and surfactant concentration, b) particle from **ATB-2** reaction solution showing evidence for oriented attachment.

Since the presence of OAd leads to the formation of larger nanorods, it seems to be less surface active than to OAm. Additionally, its steric effect (Figure 2.1d) could prevent an oriented attachment to form larger aggregates along the long axis. This leads to decreased h-ATB formation even for higher polyoxotungstate concentrations. For higher heating rates (in combination with lower stirring speeds) the attachment in each direction proceeds faster. These two process variables (as well as higher precursor concentrations) appear to suppress the coordination of OAd, i.e., high heating rates, small stirring rates, and large precursor concentration provide optimal formation conditions for h-ATB.

Evidence for the proposed reaction mechanism is based on particles **ATB-16** and **ATB-17** (Figure S8.1.7), with different HOAc:OAm ratios under optimized bronze conditions. For excess OAm, the bronze particles appear significantly longer (up to ~220*40 nm), whereas length and width become nearly equal for higher HOAc contents (similar as the formation nanorods under standard conditions (**NR-4** and **NR-8**)). Both particles show significant evidence for oriented attachment. Additionally, in **ATB-2** reaction solutions we found bronze crystals built from smaller building blocks as shown in Figure 2.7b, indicating oriented attachment and supporting our proposed reaction mechanism.

To support this hypothesis, Na^+ was tested as prototype cation for the synthesis of hexagonal alkali tungsten bronzes. Figure S8.1.13 shows the synthesis under **ATB-12** conditions for 0.3 equivalents of different sodium compounds per tungsten atom. No preferred formation of hexagonal bronze was observed, only traces of bronze were found for sodium (hydrogen-)carbonate. Higher yields of bronze were obtained for sodium oleate and sodium acetate, but WO_{3-x} nanorods remained the main phase. With sodium acetate in OAd as solvent, enhanced formation of bronze occurred together with the formation of orthorhombic $Na_2W_2O_7$ as byproduct. A possible explanation is that Na^+ cations form stable oleate complexes. These sodium oleates prevent bronze formation *via* oriented attachment in a similar manner as observed for the NH_4^+ /$^-$OAc couple. It has been found that sodium show significantly different behavior than other alkali metals (except for Li^+).[86] Due to its high chemical (Pearson) hardness it can lead to additional reaction pathways, such as the formation of orthorhombic $Na_2W_2O_7$ in our case.[87] Exploring the reactivity of all different alkali metals and their salts for bronze formation is, however, beyond the scope of this manuscript.

2.3.4 Surface Ligands and Composition of h-ATB Nanocrystals from Temperature-Dependent Solid-State MAS ^{1}H-NMR / PXRD Studies

^{1}H-MAS NMR spectroscopy allows the identification of the inorganic (i.e., ^{1}H-containing) species in h-ATB (NH_3, NH_4^+ and H_2O) or surface-bound ligands (HOAc, OAm, H_2O/OH^-) on h-ATB nanoparticles. Together with structural analysis by X-ray diffraction methods, this provides information on the role of ammonium cations in stabilizing this metastable structure and the influence of other small molecules, such as water, that might elude observation by other methods. In terms of applications, such studies are a powerful tool to understand the behavior of a system in different situations.

For this purpose, a sample (**ATB-13c**) was heated stepwise to different temperatures (70 °C, 200 °C, 300 °C, 400 °C, and 500 °C) and kept in air (Figure 2.8a) or under Ar atmosphere (Figure 2.8b) for 5 h at each temperature. The sample annealed at 70 °C showed pairs of overlapping signals at 0 and 2 ppm and between 3 and 9 ppm (maximum at 4.8 ppm, shoulder at 6.7 ppm). The high field signals (0 – 2 ppm) were assigned to the residual surface organics (HOAc, OAm). The remaining signals are a combination of $H_2O/NH_3/NH_4^+$ species and the resonances of protons associated with the olefinic double bonds. This assignment was confirmed by heating experiments and the changes occurring in the corresponding temperature-dependent ^{1}H NMR spectra.

For the sample annealed in air, the signals of the organic components and surface-bound water begin to lose intensity at 200 °C and disappear at 300 °C. At 200 °C, the signal from the ammonium cation (normally at 7.1 ppm) appears high field shifted at 5.3 ppm due to the shielding effect of the crystal structure. At 300 °C, signals appear at 6.7 and 4.6 ppm, while the signal from the ammonium cation at 5.3 ppm has disappeared, presumably due to oxidation of the tungsten by molecular oxygen from air

according to Eq. 2.3. A shoulder at ~5.8 ppm suggests that low levels of ammonium/water may be hidden below the ammonia signal.

$$2\ NH_4^+ + 0.5\ O_2 + 2W^{5+} \rightarrow 2\ NH_3\uparrow + H_2O + 2W^{6+} \quad (2.3)$$

The signals are associated with water (4.6 ppm) and ammonium (6.7 ppm) cations in the channels of hexagonal bronze formed according to Eq. 2.3. There is also a low intensity signal at about 2.5 ppm. This signal was assigned via additional heating experiments to 300 °C with different duration and different aeration after the heating step (Figure S8.1.14).

In the ^{1}H NMR spectrum of a sample measured immediately after heating, this resonance is absent, whereas it appears and increases in intensity with prolonged exposure to air. Therefore, we attribute the resonance at 2.5 ppm to surface-bound water. We observed a negative zeta potential (~ - 35 mV) for **ATB-13c**, indicating the absence of surface OH groups, typically at 1.3 ppm.[71]

Due to hydrogen bonding with these water molecules, the negatively charged WO_{3-x} surface has a strong electron-withdrawing effect. Therefore, the signal of the surface protons at 1.3 ppm is weakly field shifted and appears at 2.5 ppm (as for typical OH^- groups).[88] At 400 °C we observe signals at 6.9, 5.7 and 2.6 ppm. The signal at 2.6 ppm is again assigned to surface water. The signal at 6.9 ppm corresponds to the (attenuated) ammonia signal. The signal at 5.7 ppm is most likely due to water present in the hexagonal channels and residual ammonium cations. A clear assignment is not possible here. At 500 °C, all ^{1}H species have disappeared except for a broad signal at 5.1 ppm, which is probably due to high contents of various aqua species. At 200 °C under Ar atmosphere, a noticeable amount of residual organics remains (which disappears at 300 °C). In addition, there is the signal of an ammonium group at 5.3 ppm. At 300 °C, the ammonium content weakens, but no ammonia signal with increasing intensity is observed, since oxidation of tungsten under Ar is not possible. Only a shoulder at 7.1 ppm indicates small amounts of another (undefined) species.

At 400 °C, there is only one signal stronger electron-withdrawing effects from the tungsten atoms resulting from the free space at 5.7 ppm, which is due to an ammonium cation that is shifted slightly to low field due to the within the hexagonal channels. At 500 °C the ammonium signal at 5.8 ppm is still present, and additional weak signals appear that are compatible with surface OH groups (1.3 ppm) and surface bound water (2.6 ppm). Table 2.3 compiles the ^{1}H-NMR signal assignments for h-ATB together with reference data for h-ATB from the literature,[71] ammonium tungstate and other compounds containing ammonium cations.

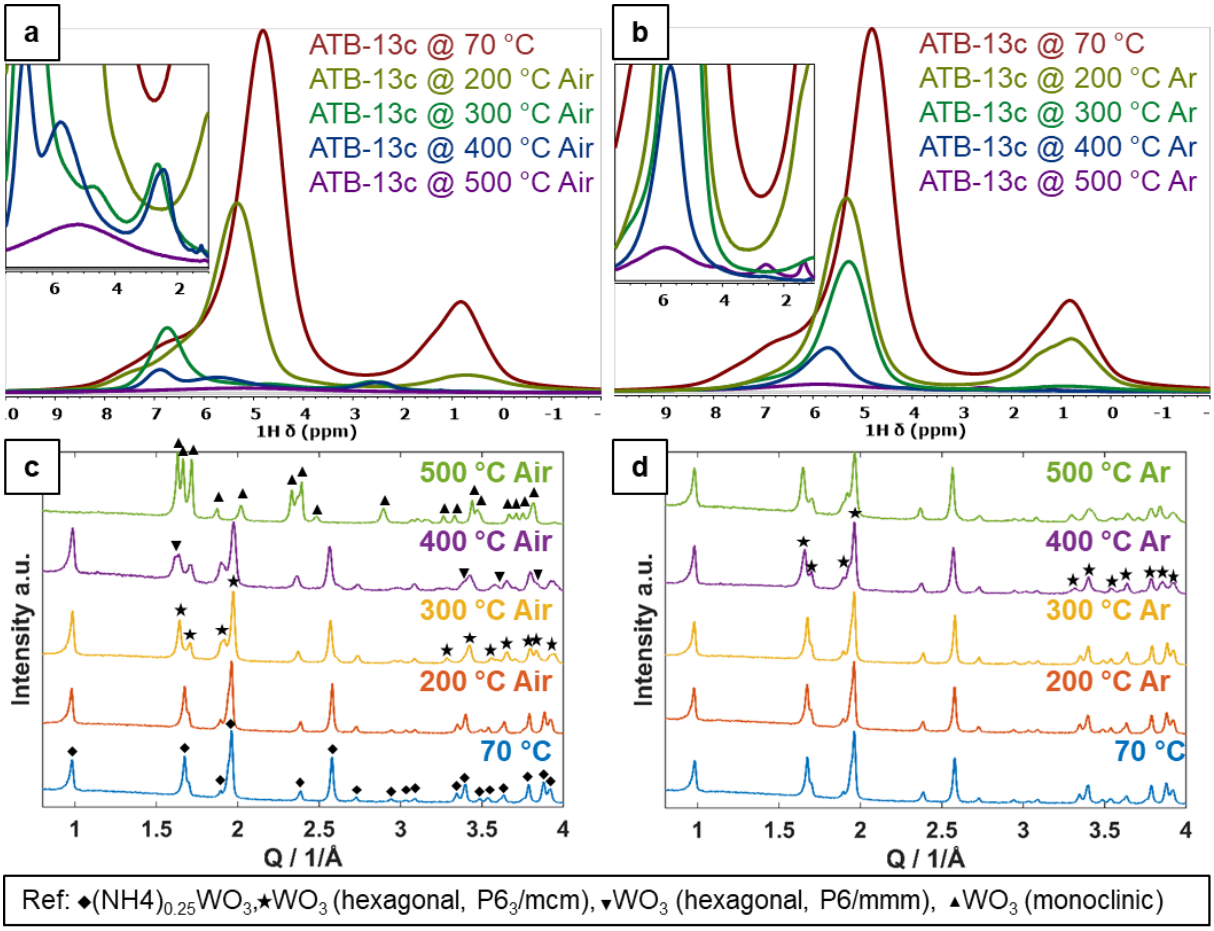

Figure 2.8. a) Solid state ^{1}H-NMR spectra of **ATB-13c** after annealing for 5 h at 70, 200, 300, 400, 500 °C in air. b) Solid state ^{1}H-NMR spectra of **ATB-13c** after annealing for 5 h at 70, 200, 300, 400, 500 °C under Ar. c) PXRD patterns of **ATB-13c** particles heated in air and d) PXRD pattern of **ATB-13c** particles heated under Ar. Marks indicate reflections changing after temperature treatment. Reference patterns of c) and d) are found in Figure S8.1.16 → Figure S8.1.24.

To estimate the amount of ammonium cations incorporated into the hexagonal channels of the h-ATB structure and thus the oxidation state of the tungsten atoms, we successively heated to 200 °C and 300 °C with 5 h equilibration time under argon. At each temperature step we performed a quantitative ^{1}H-NMR experiment. The measurements were performed immediately after the heating step without allowing accumulation of water on the particle surface. At 200 °C the spectrum is dominated by a signal at 5.35 ppm, which has contributions from NH_4^+ (and minor amounts of olefinic protons of residual HOAc/OAm/OAd). The amount of these olefinic protons is < 2 % (based on the integral of the signal at ~1 ppm). Impurities from organic contamination of the labware are possible.[89] The quantity of NH_4^+ at this temperature was determined as 0.13 per WO_3 unit from the total intensity of the deconvoluted integral of the signal at 5.35 ppm (Figure S8.1.15) against an external reference. The resulting composition is $(NH_4)_{0.13}WO_3$, which matches reported bulk compositions for ammonium tungsten bronzes.[71] The associated occupation (0.13) of the *5d* conduction band is compatible with a high charge carrier density of N ~ 6×10^{21} cm^{-3}.[10,17,34]

We note that the decomposition of the ammonium cations to ammonia (present in the hexagonal channels and at the particle surface) starts already at 200 °C. At 300 °C the ammonium content (signal at 3.13 ppm) has decreased to 0.10, i.e., NMR spectra show that the composition of the h-ATB changes with temperature. During heating in air, the color of the samples gradually changed from deep blue (70 -200 °C) over yellowish blue (300-400 °C) to yellow (500 °C), corresponding to a phase transformation of the bronze. The diffractograms at the annealing temperatures (Figure 2.8c) (show a transition from the h-ATB to the hexagonal WO_3 (h-WO_3) structure (200 → 300 °C) in agreement with an oxidation of tungsten centers according to Eq. 2.3. From 300 →400 °C, a partial rearrangement of the hexagonal phase (P63/mcm P6/mmm) was observed. At 500 °C, the transition to the monoclinic WO_3 structure occurs. No color-change was observed for the sample heated in argon (Figure 2.8d), and a transformation to hexagonal WO_3 started at 400 °C. A structural change to the monoclinic WO_3 structure was observed after heating for 5 h at 600 °C (Figure S8.1.25), while the sample color remained blue.

Solid-state ^{1}H NMR studies for WO_{3-x} are not shown because, as expected, mainly decomposition products of organic compounds were found in the spectra. Traces of NH_4^+ could be attributed to surface bound ammonium cations. The powder diffraction pattern showed only one phase transition to monoclinic WO_3 at 500 °C in air.

Table 2.3. Chemical shifts of different ^{1}H signals in ^{1}H- MAS-NMR spectra for h-ATB together with chemical shift of h-ATB and several reference[71] samples.

Substance	chemical shift (NH_4^+) / ppm	chemical shift (NH_3) / ppm	chemical shift (H_2O) / ppm	chemical shift (H_2O/OH, surface) / ppm
h-ATB (this work)	5.3 → 5.7	6.9-6.7	5.7; 4.7	2.6[a]
h-ATB (ref)	5.6-5.2	7.0-6.6	5.8	1.3/0.8
Ammonium paratungstate	7.2	-	5.2	-
NH_4Cl	7.1	-	-	-
NH_4ReO_4	6.2	-	-	-

a. H_2O adsorbed on the negatively charged surfaces of the particles after the heating procedure.

2.3.5 Localized Surface Plasmon Resonances Study of WO_{3-x} and h-ATB

Reduced tungsten oxides are known to exhibit localized surface plasmon resonances. Therefore, the photo-optical properties of WO_{3-x} and h-ATB nanoparticles were investigated. The optical response of anisotropic particles (e.g., nanorods) should lead to two nondegenerate plasmon resonances associated with the longitudinal and transverse modes.[90] The longitudinal mode is generally stronger and lower in

energy. It corresponds to the electron oscillation along the long axis of the nanorod. The higher energy transverse mode is polarized in the perpendicular direction. The absorption spectra of the WO_{3-x} and h-ATB nanorods in Figure 2.9 are consistent with this prediction based on the Gans-theory.[46,91] As the aspect ratio increases, the longitudinal mode shifts to longer wavelengths. In addition to the strong dependence on aspect ratio, the longitudinal mode is also very sensitive to the dielectric function ε_m. This makes plasmonic tungsten oxide and h-ATB nanoparticles interesting substrates for localized surface plasmon resonance sensing.

The UV-Vis-NIR spectra of **NR-1**, **NR-4**, **NR-8** and **ATB-13** in tetrachloroethene (TCE) (Figure 2.9a) show strong NIR absorption in the spectral range from 700 to 3300 nm for all particles. Due to the absorption of tetrachloroethene in this range, the exact position of the absorption band is difficult to determine. Band broadening results from the inhomogeneity of the particles, as can be seen from the histograms of the aspect ratio of selected particles (Figure S8.1.1). For **NR-1**, a broad band with a maximum at ~2750 nm was observed.

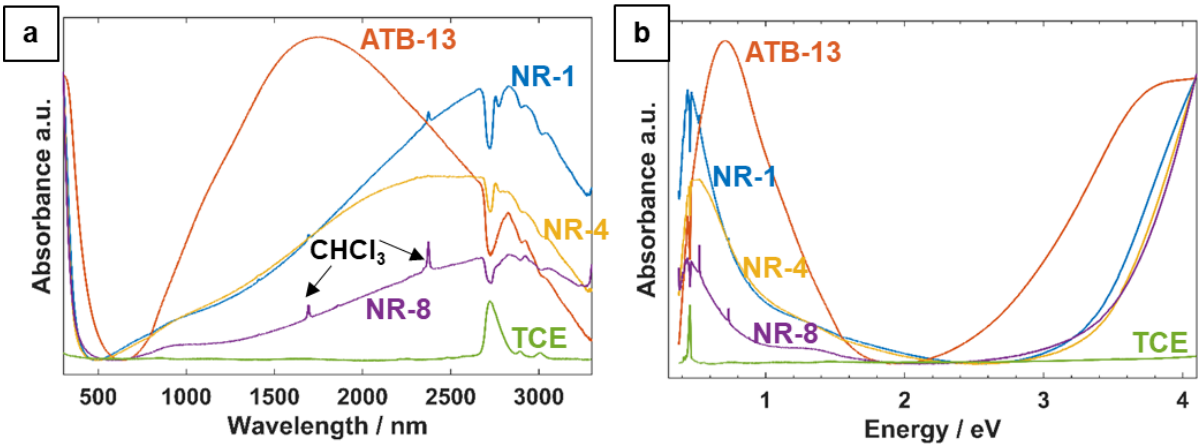

Figure 2.9. a) UV-Vis-NIR spectra of NR-1, NR-4, NR-8 and ATB-13 measured in TCE and b) energy-dependent.

In addition, there is a second maximum at ~950 nm that overlaps with the broader band. **NR-4** particles have a blue-shifted absorption maximum at ~2350 nm compared to **NR-1** particles, while the maximum of particle **NR-8** is red-shifted to ~2850 nm. Both particles showed a second maximum around 950 nm. For the tungsten bronze (**ATB-13**) particles, a broad maximum occurs at ~1750 nm and a second maximum at ~900 nm. The aspect ratio of the particles increases in the order **ATB-13**, **NR-4**, **NR-1**, and **NR-8** (2.4, 4.8, 10.6, and 12.5) (Table 2.2), and the absorption maxima of the particles are red-shifted in exactly this order, although the change for **NR-4** is slightly larger than expected. **NR-4** particles show two maxima in the aspect ratio distribution (~4.0 and 5.5, Figure S8.1.1b) with a relatively broad overall distribution, in agreement with the observed widths of the plasmon bands. Our results are in agreement with results reported by Manthiram et al.[46] based on a synthesis by Yella et al.[47]

Manthiram[46] calculated the energy-dependent absorbance for different aspect ratios (5.5, 11, 22) of $WO_{2.82}$ and estimated that the longitudinal band should be broad and without a maximum for aspect ratios of 11 or higher. The energy-dependent absorption of the particles shown in Figure 2.9b shows that even for the highest achieved aspect ratio of 12.5 (**NR-8**) an absorption maximum occurs at 0.45 eV. For the lowest aspect ratio of 2.4 (**ATB-13**) plasmon excitation results in light absorption in the energy (wavelength) range of 1.9 eV (650 nm) to 0.4 eV (3300 nm) with a maximum at 0.7 eV. **NR-1** and **NR-4** show an absorption at even higher energy than 2 eV with maxima around 0.5 eV. Thus, by choosing the "right" materials and with the proper dimensions, we can tune the absorption of NIR light in a very efficient manner. the entire NIR range and much of the UV-Vis range can be covered. Coincidentally, **ATB-1** (non-purified with a WO_{3-x}/h-ATB ratio of ~1) shows exactly this result (Figure S8.1.26) and is therefore a very promising candidate for efficient NIR-shielding.

2.4 Conclusions

We have elaborated a rapid and highly reproducible synthesis of plasmonic anisotropic tungsten oxide and tungsten bronze nanocrystals in large amounts (grams) by thermal decomposition of commercial ammonium tungstate in the presence of the surfactants oleic acid and oleylamine. The aspect ratio (AR, i.e., length/width) of the resulting tungsten oxide nanorods could be controlled by the surfactant ratio. By increasing the concentration of the starting compound, hexagonal bronze (h-ATB) particles were obtained for a surfactant ratio of 1:1. New insights into the reaction mechanism were obtained by a kinetic analysis of the reaction using electron microscopy and ^{1}H NMR. Burst nucleation led to the formation of hexagonal ammonium bronze (h-ATB) nanocrystals between 250 und 275 °C, while WO_{3-x} nanorods are formed already below 250 °C. The heating rate and stirring speed were found to be critical parameters for the product selection. Due to burst formation, h-ATB was the preferred reaction product at fast heating rates (25 K/min) and slow stirring speeds (~150 rpm), while WO_{3-x} nanorods were formed selectively at slow heating rates (1 K/min) and high stirring speeds (~800 rpm).

While the surfactants oleylamine and oleic acid are known to function as both solvents, surfactants, or reducing agents, we show that the formation of oleyl oleamide from oleic acid and oleylamine is a key factor in controlling product selection. The results of ^{1}H NMR spectroscopy showed that oleyl oleamide (OAd) forms upon heating from the surfactants HOAc and OAm by a condensation reaction that is not catalyzed by the tungsten oxides. We discuss the specific role of OAd. We showed that OAd stabilizes WO_{3-x} nanorods during growth but has no direct effect on the formation of h-ATB nanocrystals. It only binds to WO_{3-x} nanorods due to its steric effect and lower number of surface sites. Since the surfactants HOAc and OAm are typical reagents for the wet chemical preparation of many metal and oxide nanoparticles in a temperature range between 200 °C and 350 °C, the finding that OAd is the active surface reagent instead of HOAc and OAm could also be of importance for many other nanoparticle

syntheses. Oleyl oleamide, the active reagent, could be recovered from the reaction solutions. This significantly improves the yield. ^{1}H NMR spectroscopy showed that the WO_{3-x} nanorods are stabilized by OAm surface ligand, which is formed by decomposition of OAd. Purification of the products followed by ^{1}H NMR control showed a much lower surface complexation for h-ATB nanocrystals.

We propose a mechanism, where polyoxotungstate nuclei formed at temperatures >200 °C serve as prenucleation clusters for both types of particles that grow subsequently *via* oriented attachment. The competition of OAm/OAd and NH_4^+ for surface coordination during growth, the role of HOAc to bind NH_4^+, and finally the concentration of polyoxotungstates during growth are important factors for phase selection.

The combination of X-ray diffraction and solid-state ^{1}H NMR spectroscopic analysis of h-ATB showed an oxidation of the bronze at 300 °C and formation of binary hexagonal (h-WO_3) and monoclinic tungsten oxide (m-WO_3) at higher temperatures. Water was found to cover the negate O^- terminated surfaces after annealing.

UV-Vis-NIR analysis of the products showed the appearance of broad plasmonic bands in the NIR region. The aspect ratio of the WO_{3-x} nanorods and h-ATB nanocrystals results in a pronounced red shift of the absorption maxima. The reaction control of WO_{3-x} allows fine tuning of the NIR absorption of the nanorods. By combining WO_{3-x} nanorods and h-ATB nanocrystals, efficient absorption can be achieved over the entire NIR range between 800 and 3300 nm (~2 - 0.5 eV).

2.5 Experimental section

Materials. All chemicals were used as received without further purification. Oleic acid (90 %, technical grade) was bought from Sigma Aldrich, oleylamine (>50 %, technical grade) and sodium oleate (>97 %) from TCI, ammonium metatungstate hydrate (AMT, >90 % WO_3 basis) from Carl Roth, Na_2CO_3 (99.5 %) from Acros, $NaHCO_3$ from Fisher Scientific and NaAc*3H_2O from Köhler-Koblenz.

Synthesis of Tungsten Oxide Nanoparticles. For a standard synthesis (**NR-1**), 6.36 mL (20 mmol) of oleic acid (HOAc), 6.58 mL (20 mmol) of oleylamine and 352 mg (0.12 mmol) of AMT were put in a 100 mL 3-neck flask equipped with a magnetic stirring bar, temperature controller with heating mantle, plug and reflux condenser connected to a Schlenck-line. The mixture was degassed at 100 °C for 30 min *in vacuo* and then heated under argon to 350 °C with a heating rate of 5 K/min. This temperature was held for 30 min and then cooled down slowly by removing the heating mantle. 15 mL of ethanol were injected at 70 °C to prevent solidification of the solution. The solution was transferred to a 50 mL centrifuge tube. After adding additional 2 ml of $CHCl_3$ and 15 mL of ethanol it was centrifuged at 9000 rpm for 5 min. The upper layer was removed, and the residue was dissolved in 3 mL of chloroform by ultrasonication. The washing procedure was repeated twice. Subsequently, the particles were

dissolved in 3 mL of chloroform and stored for further use. The yield varied between 60-70 % under standard conditions (about 220 mg of particles).

The synthesis of the hexagonal tungsten bronze $(NH_4)_xWO_3$ was carried out under similar conditions by increasing the amount of AMT (up to 1054 mg, 0.36 mmol) and degassing at 75 °C. h-ATB particles were cleaned by dispersing in 5 ml of pure $CHCl_3$ with ultrasonication, centrifugation (9000 rpm for 10 min) and discarding the blue, WO_{3-x}-containing supernatant repeatedly, until it was colorless.

An overview of most relevant synthesis parameters is provided in Table 2.1, a full version in Table S8.1.1.

Synthesis of Oleyl oleamide. Oleyl oleamide was synthesized according to Dalu et al.[81] without the use of additional solvent. 25.4 ml (80 mmol) oleic acid and 26.3 ml (80 mmol) oleylamine were mixed in an 80 ml glass vessel. The vessel was then transferred in a 250 ml Teflon-lined stainless-steel autoclave. The autoclave was sealed and heated to 180 °C for 18 h. The resulting white waxy solid was characterized by ^{1}H- and ^{13}C-NMR spectroscopy and used without further purification. ^{1}H-NMR (400 MHz, $CDCl_3$): δ = 5.51 (s, 1H, N**H**), 5.35 (m, 4H, CH_2-C**H**=C**H**-CH_2), 3.24 (q, 2H, H_2C-**H**$_2$C-N), 2.16 (t, 2H, NOC-C**H**$_2$-CH_2), 2.02 (m, 8H, C**H**$_2$-CH=CH-C**H**$_2$), 1.63 (q, 2H, **H**$_2$C-H_2C-N), 1.49 (q, 2NOC-CH_2-C**H**$_2$), 1.40-1.20 (m, 43H, C**H**$_2$), 0.89 (t, 6H, C**H**$_3$) ^{13}C-NMR (100 MHz, $CDCl_3$): δ = 173.0, 130.0, 129.7, 77.3, 77.0, 76.7, 39.5, 36.9, 32.6, 31.9, 29.9-29.0, 27.2, 26.9, 25.8, 22.7, 14.1. Spectra (Figure S8.1.27) matching closely those reported in literature [65,81] and no traces of oleic acid and oleylamine were found.

2.5.1 Characterization

Transmission Electron Microscopy (TEM). For TEM one drop of a highly diluted solution of particles (~0.2 mg/mL in chloroform) was put onto a carbon-coated copper grid. Images were taken with a FEI Tecnai G2 Spirit microscope equipped with a Gatan US1000 CCD camera at 120 kV. High resolution (HR)-TEM images were measured with a FEI Tecnai F30 operating at 300 kV, equipped with an on axis US4000 CCD 4kx4k camera. For further processing the program ImageJ was used. Histograms are based on 100+ particles measured with a rectangular selection. Data procession was done with Matlab 2018b.

Powder X-Ray Diffraction (PXRD). PXRD studies were carried out on a STOE Standi P using Mo Kα_1 radiation (λ = 0.7093 Å) and a Dectris Mythen 1k detector. The diffractograms were analyzed using Match!3 and plotted with Matlab2018b. All references were taken from the Crystallography Open Database (COD) or International Centre for Diffraction Data (ICDD) PDF database. Rietveld[92] and Pawley[93] refinement were performed with Topas Academic V6. Reflection profiles were generated according to the fundamental parameter approach[94,95] applying a correction for anisotropic crystallite morphologies. Within this model, individual crystallite ($CS_{\underline{h}}$) sizes are computed for each reflection

(*hkl*) according to the quadratic form $CS_{\underline{h}} = {}^{1}/_{\text{norm}} \{ \underline{h}^{T} \times \underline{\underline{C}}_{ij} \times \underline{h} \}$ in which $\underline{h}$ is the reciprocal lattice vector corresponding to (*hkl*) and $\underline{\underline{C}}_{ij} = (a_i)^{½} \times (a_j)^{½}$ is the symmetric second rank tensor of the square roots of the crystallite dimensions in direction *i* and *j* in the basis of the crystal lattice.[96] Structure visualization with VESTA Ver. 3.4.3.

Ultraviolet-Visible-Near Infrared Absorption (UV-Vis-NIR) Spectroscopy. UV-Vis-NIR spectra were taken on a Cary 5G UV-Vis-NIR spectrophotometer. The sample (~ 0.1 mg ml^{-1} in tetrachloroethen (TCE)) was placed in a 1 cm quartz cuvette and measured in the wavelength range from 200 to 3300 nm. Processing and plotting were done with Matlab 2018b. The spectra were normalized at a wavelength of 303 nm.

Nuclear Magnetic Resonance (NMR) spectroscopy. Solution NMR spectra were recorded on a Bruker DRX 400 NMR spectrometer equipped with a commercial Bruker 5 mm 2 channel inversed probe head with z-gradients. All samples were dissolved in a deuterated chloroform before the experiments. The ^{1}H NMR spectra were measured using a 30° flip angle and averaging 32 scans with 2 s recycle delay. The gs (gradient selected) ^{1}H COSY (correlation spectroscopy) spectra were recorded with 1 scan per increment and 1024 increments in the indirect dimension and 2 s repetition time. The ^{13}C spectra were recorded using power gated decoupling with 30° flip pulse and 1064 scans.

Solid state NMR spectra were recorded on a Bruker DSX 400 NMR spectrometer equipped with a 4 mm commercial 3 channel Bruker probe head and 10 kHz magic angle spinning (MAS). The ^{1}H NMR spectra were measured averaging 32 scans and 8 s recycle delay. The spectra were referenced to external adamantine at 1.63 ppm. All NMR spectra were analyzed using MestreNova 10. Intensities of MAS spectra were adjusted according to the receiver gain. Quantitative ^{1}H NMR experiments were performed with samples treated at 200 °C and 300 °C (Ar, 5 h) to calculate the amount of ammonium cations incorporated in the $(NH_4)_xWO_3$ structure. The same rotor was used for recording the spectra of the particles and the reference adamantane. The weight of the rotor was measured empty and filled with each sample; the difference providing the exact sample amount. The integrals of the resp. proton resonances in the reference and the $(NH_4)_xWO_3$ experiments were related to each other allowing estimation of the amounts of the proton species in the particles after deconvolution (where necessary). The spectra were measured with 30° excitation pulse and a recycle delay of 30 s.

Zeta-Potential. Zeta potential was measured Malvern Zetasizer NanoZS with a 633 nm He-Ne-Laser. Samples were measured in milli pore water that was filtered through a 200 µm syringe filter. The particle concentration was about 1 mg/ml.

X-ray photoelectron spectroscopy (XPS). XPS measurements were carried out on an Axis Ultra DLD imaging photoelectron spectrometer. Measurements were carried out using the Hybrid mode with 10 mA and 15 kV at the Al anode. The analysis area was 700 µm * 300 µm (i.e., X-ray spot size). Survey spectra were measured at a pass energy of 80 and elemental spectra at 20 pass energy of the analyzer.

All spectra were charge corrected to a binding energy of 284.8 eV for the C 1s line corresponding to adventitious aliphatic carbon. Measurements were analyzed using the CasaXPS software plotted with Matlab2018b.

2.6 References

1 A. Magneli, *Pure Appl. Chem.*, 1978, **50**, 1261–1271.

2 A. Magnéli, *Acta Crystallogr.*, 1953, **6**, 495–500.

3 R. Pickering and R. Tilley, *J. Solid State Chem.*, 1976, **16**, 247–255.

4 T. Vogt, P. M. Woodward and B. A. Hunter, *J. Solid State Chem.*, 1999, **144**, 209–215.

5 Y. A. Barabanenkov, N. D. Zakharov, I. P. Zibrov, V. P. Filonenko, P. Werner, A. I. Popov and M. D. Valkovskii, *Acta Crystallogr., Sect. B: Struc. Sci.*, 1993, **49**, 169–171.

6 M. Sundberg, N. D. Zakharov, I. P. Zibrov, Y. A. Barabanenkov, V. P. Filonenko and P. Werner, *Acta Crystallogr., Sect. B: Struc. Sci.*, 1993, **49**, 951–958.

7 K. Viswanathan, K. Brandt and E. Salje, *J. Solid State Chem.*, 1981, **36**, 45–51.

8 M. M. Dobson and R. J. D. Tilley, *Acta Crystallogr., Sect. B: Struc. Sci.*, 1988, **44**, 474–480.

9 M. Sundberg, *Acta Crystallogr., Sect. B: Struc. Sci.*, 1976, **32**, 2144–2149.

10 L. Pirker, B. Višić, S. D. Škapin, G. DraŽić, J. Kovač and M. Remškar, *Nanoscale*, 2020, **12**, 15102–15114.

11 C. P. Heinrich, M. Schrade, G. Cerretti, I. Lieberwirth, P. Leidich, A. Schmitz, H. Fjeld, E. Mueller, T. G. Finstad, T. Norby and W. Tremel, *Mater. Horiz.*, 2015, **2**, 519–527.

12 M. J. Sienko and S. M. Morehouse, *Inorg. Chem.*, 1963, **2**, 485–489.

13 M. Green and A. Travlos, *Phil. Mag. B*, 1985, **51**, 501–520.

14 W. Sahle and M. Nygren, *J. Solid State Chem.*, 1983, **48**, 154–160.

15 R. Gehlig, E. Salje, A. F. Carley and M. W. Roberts, *J. Solid State Chem.*, 1983, **49**, 318–324.

16 G. Hägg, *Nature*, 1935, **135**, 874.

17 P. G. Dickens and M. S. Whittingham, *Q. Rev., Chem. Soc.*, 1968, **22**, 30–44.

18 M. Greenblatt, *Acc. Chem. Res.*, 1996, **29**, 219–228.

19 K. L. Ngai and T. L. Reinecke, *J. Phys. F: Met. Phys.*, 1978, **8**, 151–160.

20 K. P. Reis, A. Ramanan and M. S. Whittingham, *J. Solid State Chem.*, 1992, **96**, 31–47.

21 A. Michailovski, F. Krumeich and G. R. Patzke, *Mater. Res. Bull.*, 2004, **39**, 887–899.

22 A. Magnéli, A. I. Virtanen, J. Olsen and N. A. Sörensen, *Acta Chem. Scand.*, 1953, **7**, 315–324.

23 R. K. Stanley, R. C. Morris and W. G. Moulton, *Phys. Rev. B*, 1979, **20**, 1903–1914.

24 J. Besnardiere, B. Ma, A. Torres-Pardo, G. Wallez, H. Kabbour, J. M. González-Calbet, H. J. von Bardeleben, B. Fleury, V. Buissette, C. Sanchez, T. Le Mercier, S. Cassaignon and D. Portehault, *Nat. Commun.*, 2019, **10**, 327.

25 S. K. Deb, *Sol. Energy Mater. Sol. Cells*, 2008, **92**, 245–258.

26 C. Granqvist, *Sol. Energy Mater. Sol. Cells*, 2000, **60**, 201–262.

27 K. L. Ngai and R. Silberglitt, *Phys. Rev. B*, 1976, **13**, 1032–1039.

28 C. J. Raub, A. R. Sweedler, M. A. Jensen, S. Broadston and B. T. Matthias, *Phys. Rev. Lett.*, 1964, **13**, 746–747.

29 H.-J. Lunk, B. Ziemer, M. Salmen and D. Heidemann, *Int. J. Refract. Hard Met.*, 1993, **12**, 17–26.

30 H. Bai, N. Su, W. Li, X. Zhang, Y. Yan, P. Li, S. Ouyang, J. Ye and G. Xi, *J. Mater. Chem. A*, 2013, **1**, 6125–6129.

31 M. Seifollahi Bazarjani, M. Hojamberdiev, K. Morita, G. Zhu, G. Cherkashinin, C. Fasel, T. Herrmann, H. Breitzke, A. Gurlo and R. Riedel, *J. Am. Chem. Soc.*, 2013, **135**, 4467–4475.

32 Y. F. Li, N. Soheilnia, M. Greiner, U. Ulmer, T. Wood, A. A. Jelle, Y. Dong, A. P. Yin Wong, J. Jia and G. A. Ozin, *ACS Appl. Mater. Inter.*, 2019, **11**, 5610–5615.

33 M. A. Lange, Y. Krysiak, J. Hartmann, G. Dewald, G. Cerretti, M. N. Tahir, M. Panthöfer, B. Barton, T. Reich, W. G. Zeier, M. Mondeshki, U. Kolb and W. Tremel, *Adv. Funct. Mater.*, 2020, **30**, 1909051.

34 T. Zheng, W. Sang, Z. He, Q. Wei, B. Chen, H. Li, C. Cao, R. Huang, X. Yan, B. Pan, S. Zhou and J. Zeng, *Nano Lett.*, 2017, **17**, 7968–7973.

35 G. Cui, W. Wang, M. Ma, J. Xie, X. Shi, N. Deng, J. Xin and B. Tang, *Nano Lett.*, 2015, **15**, 7199–7203.

36 G. Kieslich, C. S. Birkel, J. E. Douglas, M. Gaultois, I. Veremchuk, R. Seshadri, G. D. Stucky, Y. Grin and W. Tremel, *J. Mater. Chem. A*, 2013, **1**, 13050–13054.

37 G. Cerretti, M. Schrade, X. Song, B. Balke, H. Lu, T. Weidner, I. Lieberwirth, M. Panthöfer, T. Norby and W. Tremel, *J. Mater. Chem. A*, 2017, **5**, 9768–9774.

38 J. Song, Z.-F. Huang, L. Pan, J.-J. Zou, X. Zhang and L. Wang, *ACS Catal.*, 2015, **5**, 6594–6599.

39 S.-M. Jung, S.-W. Yun, J.-H. Kim, S.-H. You, J. Park, S. Lee, S. H. Chang, S. C. Chae, S. H. Joo, Y. Jung, J. Lee, J. Son, J. Snyder, V. Stamenkovic, N. M. Markovic and Y.-T. Kim, *Nat. Catal.*, 2020, **3**, 639–648.

40 A. Yu, N. Kumagai, Z. Liu and J. Y. Lee, *J. Solid State Electrochem.*, 1998, **2**, 394–400.

41 W. Cheng, Y. Ju, P. Payamyar, D. Primc, J. Rao, C. Willa, D. Koziej and M. Niederberger, *Angew. Chem. Int. Ed.*, 2015, **54**, 340–344.

42 B. J.-W. Liu, J. Zheng, J.-L. Wang, J. Xu, H.-H. Li and S.-H. Yu, *Nano Lett.*, 2013, **13**, 3589–3593.

43 Z. Liu, A. W. A. Murphy, C. Kuppe, D. C. Hooper, V. K. Valev and A. Ilie, *ACS Nano*, 2019, **13**, 3896–3909.

44 A. Rothschild, J. Sloan and R. Tenne, *J. Am. Chem. Soc.*, 2000, **122**, 5169–5179.

45 H. Cheng, M. Klapproth, A. Sagaltchik, S. Li and A. Thomas, *J. Mater. Chem. A*, 2018, **6**, 2249–2256.

46 K. Manthiram and A. P. Alivisatos, *J. Am. Chem. Soc.*, 2012, **134**, 3995–3998.

47 A. Yella, M. N. Tahir, S. Meuer, R. Zentel, R. Berger, M. Panthöfer and W. Tremel, *J. Am. Chem. Soc.*, 2009, **131**, 17566–17575.

48 G. Duan, L. Chen, Z. Jing, P. de Luna, L. Wen, L. Zhang, L. Zhao, J. Xu, Z. Li, Z. Yang and R. Zhou, *Chem. Res. Toxicol.*, 2019, **32**, 1357–1366.

49 C. C. Mardare and A. W. Hassel, *ACS Comb. Sci.*, 2014, **16**, 631–639.

50 M. N. Tahir, B. Oschmann, D. Buchholz, X. Dou, I. Lieberwirth, M. Panthöfer, W. Tremel, R. Zentel and S. Passerini, *Adv. Energy Mater.*, 2016, **6**, 1501489.

51 H. Mehrer, *Diffusion in Solids*, Springer-Verlag Berlin Heidelberg, Berlin, Heidelberg, 2007.

52 K. Lee, W. S. Seo and J. T. Park, *J. Am. Chem. Soc.*, 2003, **125**, 3408–3409.

53 J. Polleux, N. Pinna, M. Antonietti and M. Niederberger, *J. Am. Chem. Soc.*, 2005, **127**, 15595–15601.

54 C. Guo, S. Yin, M. Yan, M. Kobayashi, M. Kakihana and T. Sato, *Inorg. Chem.*, 2012, **51**, 4763–4771.

55 M. Yan, H. Gu, Z. Liu, C. Guo and S. Liu, *RSC Adv.*, 2015, **5**, 967–973.

56 T. Gao and B. P. Jelle, *J. Phys. Chem. C*, 2013, **117**, 13753–13761.

57 C. Guo, S. Yin, L. Huang and T. Sato, *ACS Appl. Mater. Inter.*, 2011, **3**, 2794–2799.

58 T. M. Mattox, A. Bergerud, A. Agrawal and D. J. Milliron, *Chem. Mater.*, 2014, **26**, 1779–1784.

59 E. N. DiMaggio, C. J. Campisano, J. Rowan, G. Dupont-Nivet, A. L. Deino, F. Bibi, M. E. Lewis, A. Souron, D. Garello, L. Werdelin, K. E. Reed and J. R. Arrowsmith, *Science*, 2015, **347**, 1355–1359.

60 N. Pienack and W. Bensch, *Angew. Chem. Int. Ed.*, 2011, **50**, 2014–2034.

61 D. Saha, K. M. Ø. Jensen, C. Tyrsted, E. D. Bøjesen, A. H. Mamakhel, A.-C. Dippel, M. Christensen and B. B. Iversen, *Angew. Chem. Int. Ed.*, 2014, **53**, 3667–3670.

62 C. Tyrsted, N. Lock, K. M. Ø. Jensen, M. Christensen, E. D. Bøjesen, H. Emerich, G. Vaughan, S. J. L. Billinge and B. B. Iversen, *IUCrJ*, 2014, **1**, 165–171.

63 M. Juelsholt, T. Lindahl Christiansen and K. M. Ø. Jensen, *J. Phys. Chem. C*, 2019, **123**, 5110–5119.

64 A. Birkel, F. Reuter, D. Koll, S. Frank, R. Branscheid, M. Panthöfer, E. Rentschler and W. Tremel, *CrystEngComm*, 2011, **13**, 2487–2493.

65 E. Hassanabadi, M. Latifi, A. F. Gualdrón-Reyes, S. Masi, S. J. Yoon, M. Poyatos, B. Julián-López and I. Mora-Seró, *Nanoscale*, 2020, **12**, 14194–14203.

66 M. A. Boles, D. Ling, T. Hyeon and D. V. Talapin, *Nat. Mater.*, 2016, **15**, 141–153.

67 M. Niederberger, G. Garnweitner, F. Krumeich, R. Nesper, H. Cölfen and M. Antonietti, *Chem. Mater.*, 2004, **16**, 1202–1208.

68 R. L. Penn and J. F. Banfield, *Science*, 1998, **281**, 969–971.

69 M. Niederberger and H. Cölfen, *Phys. Chem. Chem. Phys.*, 2006, **8**, 3271–3287.

70 I. M. Szilágyi, J. Madarász, G. Pokol, P. Király, G. Tárkányi, S. Saukko, J. Mizsei, A. L. Tóth, A. Szabó and K. Varga-Josepovits, *Chem. Mater.*, 2008, **20**, 4116–4125.

71 H.-J. Lunk, M. Salmen and D. Heidemann, *Int. J. Refract. Hard Met.*, 1998, **16**, 23–30.

72 H. Sharifi Dehsari, A. Halda Ribeiro, B. Ersöz, W. Tremel, G. Jakob and K. Asadi, *CrystEngComm*, 2017, **19**, 6694–6702.

73 H. Sharifi Dehsari, R. A. Harris, A. H. Ribeiro, W. Tremel and K. Asadi, *Langmuir*, 2018, **34**, 6582–6590.

74 H. Sharifi Dehsari, M. Heidari, A. Halda Ribeiro, W. Tremel, G. Jakob, D. Donadio, R. Potestio and K. Asadi, *Chem. Mater.*, 2017, **29**, 9648–9656.

75 T. D. Schladt, T. Graf and W. Tremel, *Chem. Mater.*, 2009, **21**, 3183–3190.

76 B. Moshofsky and T. Mokari, *Chem. Mater.*, 2013, **25**, 1384–1391.

77 J.-W. Seo, Y.-W. Jun, S. J. Ko and J. Cheon, *J. Phys. Chem. B*, 2005, **109**, 5389–5391.

78 K. Wassermann, M. H. Dickman and M. T. Pope, *Angew. Chem. Int. Ed.*, 1997, **36**, 1445–1448.

79 D. Hunyadi, I. Sajó and I. M. Szilágyi, *J. Therm. Anal. Calorim.*, 2014, **116**, 329–337.

80 A. J. Schultz, H. Horiuchi and H. B. Krause, *Acta Crystallogr C Cryst Struct Commun*, 1986, **42**, 641–644.

81 F. Dalu, M. A. Scorciapino, C. Cara, A. Luridiana, A. Musinu, M. Casu, F. Secci and C. Cannas, *Green Chem.*, 2018, **20**, 375–381.

82 C. Cara, A. Musinu, V. Mameli, A. Ardu, D. Niznansky, J. Bursik, M. A. Scorciapino, G. Manzo and C. Cannas, *Cryst. Growth Des.*, 2015, **15**, 2364–2372.

83 M. B. Mohamed, K. M. AbouZeid, V. Abdelsayed, A. A. Aljarash and M. S. El-Shall, *ACS Nano*, 2010, **4**, 2766–2772.

84 C. D. Baertsch, S. L. Soled and E. Iglesia, *J. Phys. Chem. B*, 2001, **105**, 1320–1330.

85 E. Lassner, *Int. J. Refract. Hard Met.*, 1995, **13**, 35–44.

86 A. Birkel, N. Loges, E. Mugnaioli, R. Branscheid, D. Koll, S. Frank, M. Panthöfer and W. Tremel, *Langmuir*, 2010, **26**, 3590–3595.

87 R. G. Pearson, *Inorg. Chem.*, 1988, **27**, 734–740.

88 H. Nebel, M. Neumann, C. Mayer and M. Epple, *Inorg. Chem.*, 2008, **47**, 7874–7879.

89 E. Schechtel, R. Dören, H. Frerichs, M. Panthöfer, M. Mondeshki and W. Tremel, *Langmuir*, 2019, **35**, 12518–12531.

90 L. M. Liz-Marzán, *Langmuir*, 2006, **22**, 32–41.

91 J. Olson, S. Dominguez-Medina, A. Hoggard, L.-Y. Wang, W.-S. Chang and S. Link, *Chem. Soc. Rev.*, 2015, **44**, 40–57.

92 H. M. Rietveld, *J. Appl. Crystallogr.*, 1969, **2**, 65–71.

93 G. S. Pawley, *J. Appl. Crystallogr.*, 1980, **13**, 630–633.

94 R. W. Cheary and A. Coelho, *J. Appl. Crystallogr.*, 1992, **25**, 109–121.

95 A. A. Coelho, *J. Appl. Crystallogr.*, 2018, **51**, 210–218.

96 D. Gömpel, M. N. Tahir, M. Panthöfer, E. Mugnaioli, R. Brandscheid, U. Kolb and W. Tremel, *J. Mater. Chem. A*, 2014, **2**, 8033–8040.

The following chapter 3 is reproduced from Dalton Transaction, 2021, 50, 14027–14037, DOI: 10.1039/D1DT02243A with permission from the Royal Society of Chemistry.

Authorship Contributions Chapter 3

Conception and design of the study:

[redacted]

Preparation of samples and acquisition of data:

[redacted] – preparation of catalysts

[redacted] – TEM measurements

[redacted] – PXRD measurements

[redacted] – NMR measurements

[redacted] – ζ-potential measurements

[redacted] – BET surface measurements

Analysis and interpretation of data:

[redacted] – PXRD diffraction and refinements

[redacted] – TEM images, ζ-potential

[redacted] – NMR spectroscopy

[redacted] – BET surface analysis

Drafting of the manuscript:

[redacted]

Revising the manuscript critically for important intellectual content:

[redacted]

Preparation of figures:

[redacted]

3. Magneli-Type Tungsten Oxide Nanorods as Catalysts for the Selective Oxidation of Organic Sulfides

3.1 Abstract

Selective oxidation of thioethers is an important reaction to obtain sulfoxides as synthetic intermediates for applications in chemical industry, medicinal chemistry and biology or the destruction of warfare agents. The reduced Magneli-type tungsten oxide WO_{3-x} possesses a unique oxidase-like activity which facilitates the oxidation of thioethers to the corresponding sulfoxides. More than 90 % of the model system methylphenylsulfide could be converted to the sulfoxide with a selectivity of 98 % at room temperature within 30 minutes, whereas oxidation to the corresponding sulfone was on a time scale of days. Concentration of the catalyst had a significant impact on the reaction rate. Reasonable catalytic effects were also observed for the selective oxidation of various organic sulfides with different substituents. The WO_{3-x} nanocatalysts could be recycled at least 5 times without decrease in activity. We propose a metal oxide-catalyzed route based on the clean oxidant hydrogen peroxide. Compared to other molecular or enzyme catalysts the WO_{3-x} system is a more robust redox-nanocatalyst, which is not susceptible to decomposition or denaturation under standard conditions. The unique oxidase-like activity of WO_{3-x} can be used for a wide range of applications in synthetic, environmental or medicinal chemistry.

3.2 Introduction

Organo-sulfur compounds (e.g. cysteine, biotin etc.) are involved in human metabolism. In addition, they form an essential group of plant metabolites (e.g. in the protein fraction) that perform important biological functions. Sulfur compounds are important for food quality and for the production of phyto-pharmaceutics. Plants contain a large variety of other organic sulfur compounds, like thiols (glutathione), sulfolipids and secondary sulfur compounds (alliins, glucosinolates, phytochelatins), which play an important role in physiology and protection against environmental stress and pests or act as strong poisons.[1,2] Therefore, their oxidation is an important reaction, not only for the large-scale synthesis of pharmaceutical compounds,[3] but also biochemically.[4] Other prominent fields are the oxidative desulfurization of fuels[5] or the destruction of chemical warfare agents such as mustard gas.[6] The oxidation can occur in two-steps. The first step leads to sulfoxides, the second oxidation step to sulfones. In the pharmaceutical industry oxidized sulfides are of significant interest. Proton pump inhibitors such as omeprazole and pantoprazole are widely used drugs for acid reflux. An important step in the synthesis is the selective oxidation of a sulfide intermediate to the sulfoxide. As many sulfoxides are chiral compounds, asymmetric oxidation has been a point of interest. By using chiral auxiliars such as (+)-diethyl tartrate[7] and R-(+)-binaphthol,[8] enantioselectivity of the products can be achieved.

A variety of oxidants has been used,[3] aerial oxygen and hydrogen peroxide being the most favorable choices due to their low cost and environmental compability.[9] Elevated temperature, acidic conditions or a catalyst are needed to achieve high conversion rates for the oxidation to sulfoxides and sulfones. High temperatures and acidic conditions can lead to undesired side reactions or decomposition of the reactants. Enhanced selectivity and yields under standard conditions can be achieved with the aid of suitable catalysts.[10,11] Choice and design of efficient catalysts is highly reaction dependent. Substrates and catalyst must be chemically compatible in order to ensure the desired conversion. Most catalysts for sulfide oxidation are molecular coordination compounds like polyoxomolybdates,[12] oxo(salen)chromium complexes,[13] bis(acetylacetonato)oxovanadium(IV) based complexes[14,15] and titanium isopropoxide[7,8] and inorganic compounds like zirconium tetrachloride[16] and sodium tungstate.[9] Biologically, sulfoxidation is catalyzed by chloroperoxidases (CPOs),[17] a class of enzymes that produces natural organochlorides in soils. The first discovered enzyme in this class was CPO from the marine fungus *Caldariomyces fumago*.[18]

Disadvantage of homogeneous or enzymatic catalysts are their poor recyclability and the impurities left in the final product. Heterogeneous catalyst overcome such problems. Among the solid-state compounds nanoparticles have great advantages as catalysts. Their higher surface to volume ratio compared to bulk compounds leads to more catalytically active surface sites.[19] Additionally, their morphology can be tailored synthetically, allowing energetically unfavorable, but highly reactive surfaces to be predominant. Since both oxidation steps for organic sulfides can be catalyzed, selectivity is crucial.

Sulfoxides are the most common targets for sulfide oxidation, and over-oxidation to sulfones must be suppressed. This can be achieved by using stochiometric amounts of the oxidants provided that the formation of sulfoxides in the first reaction step is much faster than formation of sulfones in the second one.

Based on the analogy between the activity of molecular polyoxotungstates,[12] WO_3 and H_2WO_4 as oxidation catalyst,[20] the enhanced activity of Mo-W-O mixed oxide catalysts[21] for partial oxidation of acrolein to acrylic acid[22,23] and the peroxidase-like properties of metal oxide nanoparticles[24–27] or haloperoxidase-like properties of V_2O_5[28] and CeO_2[29] we reasoned that CeO_2 or WO_{3-x} nanoparticles might catalyze the selective oxidation of organic sulfides at ambient conditions in manner similar to metalloenzymes.[24,26,30–32] Tungsten oxides show promising surface coordination properties for different substrates, as they have been investigated as gas-sensors for various application.[33,34] The oxide defect chemistry is crucial for the activity and selectivity of the metal oxide particles.[22,29]

Especially the defect chemistry of stoichiometric WO_3 can be adjusted in the substoichiometric WO_{3-x} shear variants ($2.625 < x < 2.92$, $W_{32}O_{84}$, W_3O_8, $W_{18}O_{49}$, $W_{17}O_{47}$, W_5O_{14}, $W_{20}O_{58}$, and $W_{25}O_{73}$). These so-called Magnéli phases[35,36] and other reduced tungsten oxides show structural and chemical complexity in the solid state coupled with mixed-valence behavior and hopping conductivity for use in thermoelectrics,[37] plasmonics,[38–40] photocatalysis,[41–43] or redox chemistry in electrodes.[44,45] The size of ultra-small Magneli-type WO_{3-x} nanoparticles can be comparable to the diameters of typical polyoxotungstates, a family of well-defined polyanions whose structures in solution are sensitive to chemical environment, pH value, solvent and temperature.[46] We supposed that their structural and redox properties might enable selective oxidation catalysis of organic molecules at ambient conditions similar to natural enzymes[47] or enzyme-mimetic vanadia[48] or ceria nanoparticles.[29,49]

Here we report the selective oxidation of organic sulfides with hydrogen peroxide catalyzed by WO_{3-x} nanorods to sulfoxides at ambient conditions. Based on a kinetic analysis we demonstrate that the reaction is strongly dependent on the solvent and the amount of surface-bound water. The annealing temperature of the particles to remove surfactant and physisorbed water has great impact on the reaction rate. WO_{3-x} nanorods selectively oxidize sulfides to sulfoxides in short reaction times (~30 min) at room temperature, whereas the oxidation to sulfones proceeded on a timescale of days. A screening of different sulfides revealed that the oxidation was significantly faster for aliphatic sulfides, and slower for aromatic or sterically hindered sulfides. Electron withdrawing groups in *p*-position of the aromatic systems lowered the conversion rate while electron donating groups increased it. In contrast, ceria nanoparticles exhibit no product selectivity but were highly efficient catalysts for sulfone production.

3.3 Results and discussion

3.3.1 Evaluation of Reaction Parameters for *in situ* Oxidation of Thioanisole

The oxidation of sulfides consists of two steps, (i) the oxidation to a sulfoxide and (ii) the oxidation to the sulfone. WO_{3-x} nanorods (annealed at 300 °C) catalyze the reaction of thioanisole (metyl phenyl sulfide) to methyl phenyl sulfoxide (MP-sulfoxide) and methyl phenyl sulfone (MP-sulfone) with H_2O_2 (Figure 3.1a). WO_{3-x} nanorods (NRs) were synthesized following ref. [50]. Transmission electron microcopy (TEM) images and an X-ray diffractogram of the WO_{3-x} NRs are shown in Figure 3.2a and b. The structure assignment is based on high resolution transmission electron microscopy (HR-TEM) (inset to Figure 3.2a) and X-ray powder diffraction (PXRD). Since the particle diameter corresponds to only 2-3 unit cells along [010], the X-ray diffractogram contains only two broad reflections that are commonly associated with the phase $WO_{2.72}$ (or $W_{18}O_{49}$).[38,42,44] This makes a clear-cut structure determination difficult, in particular considering partial oxidation during the annealing step. A Pawley refinement[51] of particles annealed at 300 °C (Figure S8.2.1) reveals an increased d-spacing along [010] (from 3.789 to 3.794 Å) compared to non-annealed particles, indicating a partial oxidation of annealed WO_{3-x} nanorods.

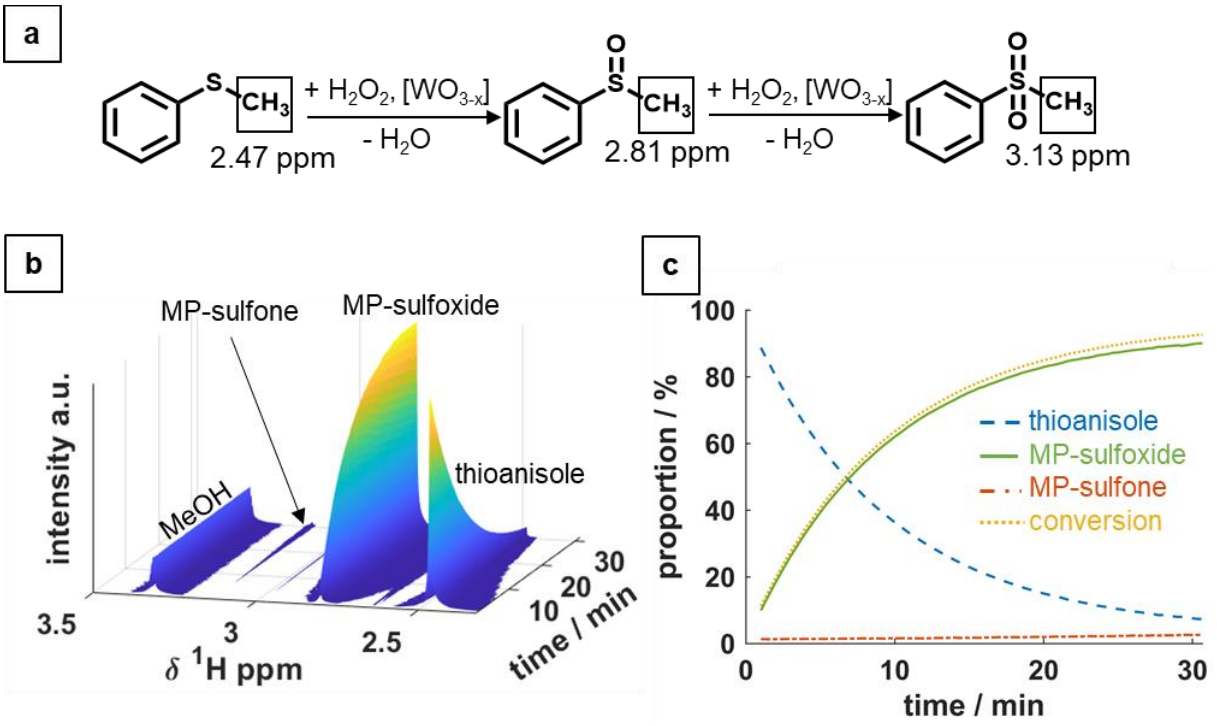

Figure 3.1. a) Oxidation of thioanisole to MP-sulfoxide and MP-sulfon with H_2O_2 catalyzed by WO_{3-x} NRs, b) 3D-plot of an *in situ* kinetic catalysis under standard conditions (30 min, 0.04 mmol of thioanisole, 0.06 mmol of H_2O_2 (60%), 0.85 mg of WO_{3-x} NRs in 0.6 mL of methanol-d_4) and c) change of integrals for the reactant thioanisole (blue) and products MO-sulfoxide (green) and MP-sulfone (red) and conversion rate for thioanisol (dotted line) of the spectra in b).

Since the oxidation front should penetrate into the nanocrystal starting from the surface, a unique composition and formula for the nanorods is not easy to give. Therefore, we use the general formula WO_{3-x}.

Under standard conditions (0.04 mmol thioanisole, 0.06 mmol H_2O_2 (60 %), 0.85 mg WO_{3-x} in 0.6 ml methanol-d_4), a conversion to MP-sulfoxide of 60±9 % was achieved already 10 min after injection of H_2O_2 and an average conversion of 90±4 % after 30 min. The verification of the standard conditions is shown below. Conversion of MP-sulfoxide did not exceed 2±1 % within 30 min, verifying the selectivity of the WO_{3-x} catalyst. Figure 3.1b and c show a kinetic study of the reaction, monitored by recording ^{1}H-NMR spectra every 20 seconds for 30 minutes. The signal of thioanisole (2.47 ppm) decreases, while the signal of MP-sulfoxide (2.81 ppm) evolves simultaneously. The signal intensity of MP-sulfone (3.13 ppm) is very low (<2 %) compared to MP-sulfoxide during 30 min of reaction time. Integration was done only for the aromatic signals to avoid errors due to overlapping CH_3 signals.

The maximum conversion rate dropped already after 5 min for standard conditions. The compositions after 30 min (10 min) were used for all *in situ* experiments as "snapshot" to compare reaction rates.

Table 3.1 compiles the ratios of thioanisole:MP-sulfoxide:MP-sulfone after 10 and 30 min for different reaction variables. Using H_2O_2 in reduced concentration (35 % instead of 60 %) reduced the conversion to MP-sulfoxide after 30 min from 90 to 77 % (60 to 42 % after 10 min). Doubling the concentration of all components and using 60 % H_2O_2 increased the conversion to 94 % already after 10 min. 98 % of the thioanisole were oxidized after 30 min, but only 4 % conversion of the MP-sulfoxide intermediate was oxidized to MP-sulfone. Water impurities in methanol (due to its hygroscopicity) can affect the reactivity of the WO_{3-x} NRs because the thioanisole/H_2O_2 ratio in the reaction solution was kept constant during the experiments.

We conducted a series of experiments to demonstrate that water quenches the reaction significantly. Figure 3.3a shows the effect of additional H_2O and D_2O during the reaction. While 2.34 µL of H_2O or D_2O did not decrease the conversion significantly, higher amounts of of H_2O or D_2O (10 µL) reduced the conversion after 30 min from 92 % to 62 % (for D_2O) and to 64 % (for H_2O). For even higher concentrations of of H_2O or D_2O (50 µL), only 26 % of thioanisole was oxidized for both, D_2O and H_2O. For a reaction solution containing methanol and (H_2O/D_2O) (400:200 µL) in a ratio of 2:1 the conversion converged to 21 %, indicating that the minimum reactivity was reached. Reaction in pure water is not possible due to the low solubility of thioanisole. Water may block catalytic surface sites of the negatively charged WO_{3-x} surface[50], thereby preventing H_2O_2 from activating the surface. In addition, the low solubility of thioanisole in water reduces the local concentration of the reactant as well as mass transfer. The fit curves show an exponential decay of the conversion (Table S8.2.2), in accord the results in ref 52. D_2O appears to lower the reaction rate slightly more (approx. 1-2 %) than H_2O, which might indicate an isotope effect resulting from differences in hydrogen bonding between D_2O and H_2O.[52] Despite the

detrimental effect of water on catalyst activity, hydrogen peroxide is a good oxidant for our model system. It allows high conversion rates and is inexpensive, non-toxic and environmentally friendly.[53–55]

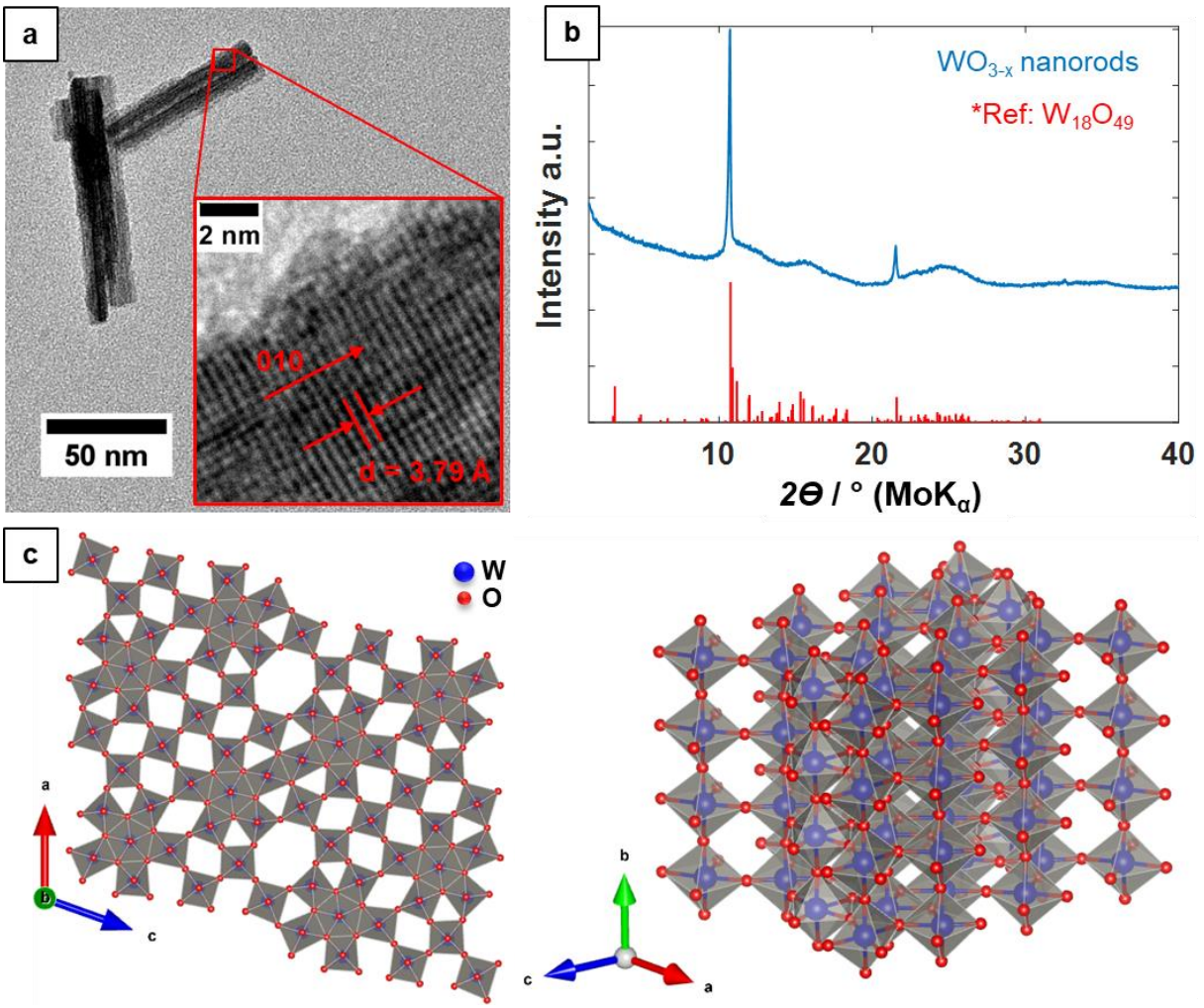

Figure 3.2. a) TEM and HR-TEM image and b) powder X-ray diffractogram of WO_{3-x} NRs annealed at 300 °C with $W_{18}O_{49}$ reference (COD, entry no: 96-152-8167), a Pawley refinement is given in Figure S8.2.1. c) Structure of $W_{18}O_{49}$ projected along [010] and [101]. While the crystal structure of stoichiometric WO_3 contains an infinite 3D network of corner-sharing WO_6 octahedra, dense planar defects are regularly introduced in the parent WO_3 structure with a spacing dictated by the oxide deficiency. This leads to a shear-structure with corner- and edge-sharing octahedra forming pseudo-hexagonal channels in the $W_{18}O_{49}$ structure.

We varied the equivalents of H_2O_2 with respect to thioanisole from 1 to 6 (Table 3.1). The initial conversion after 10 min was highest for 1 equivalent, only 77 % were detected after 30 min. The conversion dropped slightly with increasing H_2O_2 concentration due to higher water content. Still, further oxidation to MP-sulfone did not occur for any H_2O_2 concentration within 30 min > 97.5 % of the product was MP-sulfoxide, based on the MP-sulfoxide:MP-sulfone ratio. We checked the reaction solution for a 3-fold concentration of H_2O_2 after additional 22 h and 13 days (Figure S8.2.7). We found 67 % (22 h) and > 99 % (13 days) of MP-sulfone, with no traces of thioanisole left. This means that the oxidation to sulfone progresses, but only within days. We suggest that the lower conversion of 77 % for

the 1-fold stoichiometric amount of H_2O_2 may be due to a peroxidase-like behavior of WO_{3-x} NRs.[56] The H_2O_2 concentration was ultimately set at 1.5 equivalents to ensure high conversation rates and total conversion to sulfoxide without risking significant overoxidation.

Table 3.1. Composition of the reaction solution after 10 and 30 min during the *in situ* oxidation of thioanisole using WO_{3-x} NRs in 0.6 mL of methanol-d_4 as catalyst and the substrate thioanisole and the oxidant H_2O_2 in variable concentrations.

m(particles) / mg	n(thioanisole) / mmol	n (H_2O_2) / mmol	Ratio sulfide:sulfoxide:sulfone (10 min)	Ratio sulfide:sulfoxide:sulfone (30 min)
0.85	0.04	0.06[a]	39:60:1	8:90:2
0.85	0.04	0.06[b]	58:42:0	22:77:1
1.70	0.04	0.06[a]	3:95:2	3:92:5
1.70	0.08	0.12[a]	6:93:1	2:94:4
2.81	0.13	0.20[a]	3:95:2	2:93:5
0.85	0.04	0.04[a]	34:65:1	32:67:1
0.85	0.04	0.08[a]	37:62:1	6:92:2
0.85	0.04	0.12[a]	45:54:1	10:88:2
0.85	0.04	0.24[a]	55:44:1	18:81:1

a. 60 wt% H_2O_2 in water

b. 35 wt% H_2O_2 in water

Different deuterated solvents were tested as reaction media. Acetonitril-d_3, actetone-d_6 and tetrahydrofurane-d_8 did not show a conversion higher than 1 %. D_2O was not tested, because thioanisole was insoluble and strong quenching was expected. We assume that methanol stabilizes the WO_{3-x} NRs by surface hydrogen bonding.[57] The strength of this bond might be weaker than hydrogen bonding with water/hydrogen peroxide and allows the reaction to proceed.

We checked the effect of different annealing temperatures of WO_{3-x} NRs on the conversion. The results are presented in Figure 3.3b and Table S8.2.3. Maximum conversion of 90 % was achieved after 30 min for an annealing temperature of 300 °C. An annealing temperature of 200 °C decreased the conversion to only 12 %. Based on our temperature-dependent kinetic analysis we assume that temperatures ≥ 250 °C are needed to remove surface-bound water and tensides coordinated at the WO_{3-x} NR surface after synthesis.[50] For annealing temperatures ≥ 350 °C the turnover rate drops from 58 % (350 °C) to 45 % (400 °C) and reaches 3 % (500 °C) after 30 min of reaction time. No significant structural change was observed for temperatures up to 400 ° based on the TEM image and the two reflections of the PXRD

pattern (Figure S8.2.2). A phase transformation to monoclinic WO_3 occurrred at 500 °, indicating that the catalytic reactivity is associated with partially reduced WO_{3-x} NRs.

We performed a set of *ex situ* experiments to demonstrate the stability of the WO_{3-x} NR catalyst and its recyclability after catalysis (Figure 3.4). We could quantitatively oxidize thioanisole (7.3 mmol, 910.5 mg) in 30 min at 25 °C with only 2 wt% (~1 mol%) of WO_{3-x} particles, 1.5 eq of H_2O_2 (35 %) and non-deuterated, non-dried methanol by increasing the WO_{3-x} NR concentration (8.5 mg/mL in methanol) to compensate for water impurities. The reaction was monitored by taking snapshots after 10 and 30 min to ensure compatibility with the *in situ* experiments.

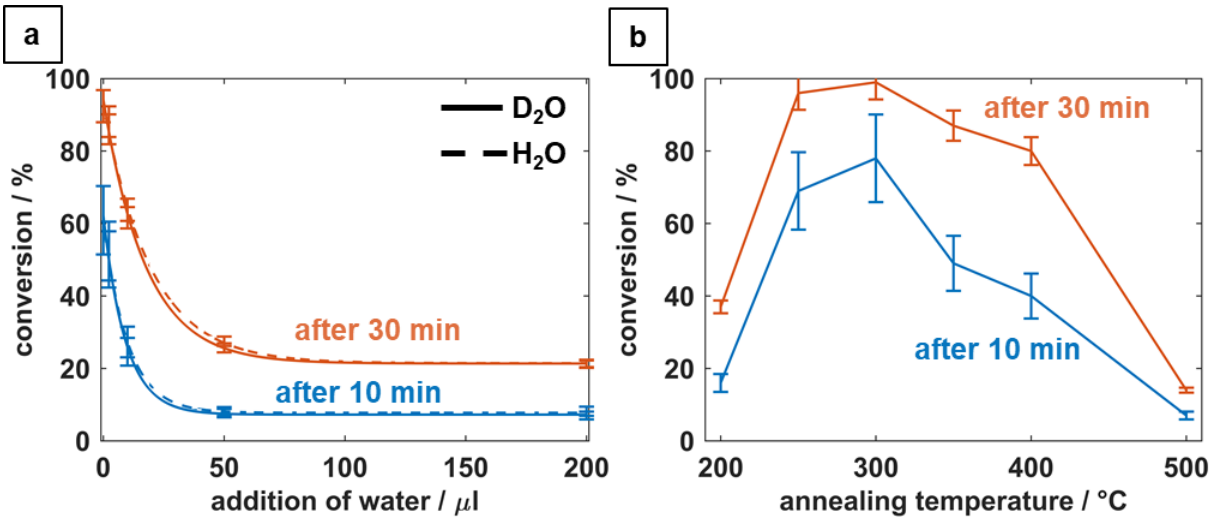

Figure 3.3. a) Effect of H_2O and D_2O on the oxidation of thioanisole with WO_{3-x} NRs (composition and exponential fit data provided in Table S8.2.1 and Table S8.2.2). b) Effect of annealing temperature of WO_{3-x} NRs on the conversion of thioanisole Powder X-ray diffractogram of annealed samples at different temperatures and the compositions of the reaction mixtures are given in Figure S8.2.2 and in Table **S8.2.3**. All experiments performed under standard conditions (0.04 mmol of thioanisole, 0.06 mmol of H_2O_2 (60%), 0.85 mg of WO_{3-x} NRs in methanol-d_4).

Conversion after 30 min remained consistently at 98 % for five cycles. For the last cycle the conversion to MP-sulfoxide was ~98 % already after 10 min. An *in situ* kinetic of the WO_{3-x} NRs collected after the 5th cycle showed a reduced catalytic activity (only 60 % thioanisole oxidized after 30 min). TEM images of the particles after the 6th cycle (Figure S8.2.2c) show that the particles still have a rod-like shape but also with an amorphous rim, possibly due to degradation after repeated exposure to the H_2O_2 oxidant. A PXRD pattern (Figure S8.2.2e) after the 5th cycle showed no evidence of a phase transformation. A slight reflection broadening is compatible with a slightly smaller particle size, i.e., the observed changes in reactivity may be due to surface effects.

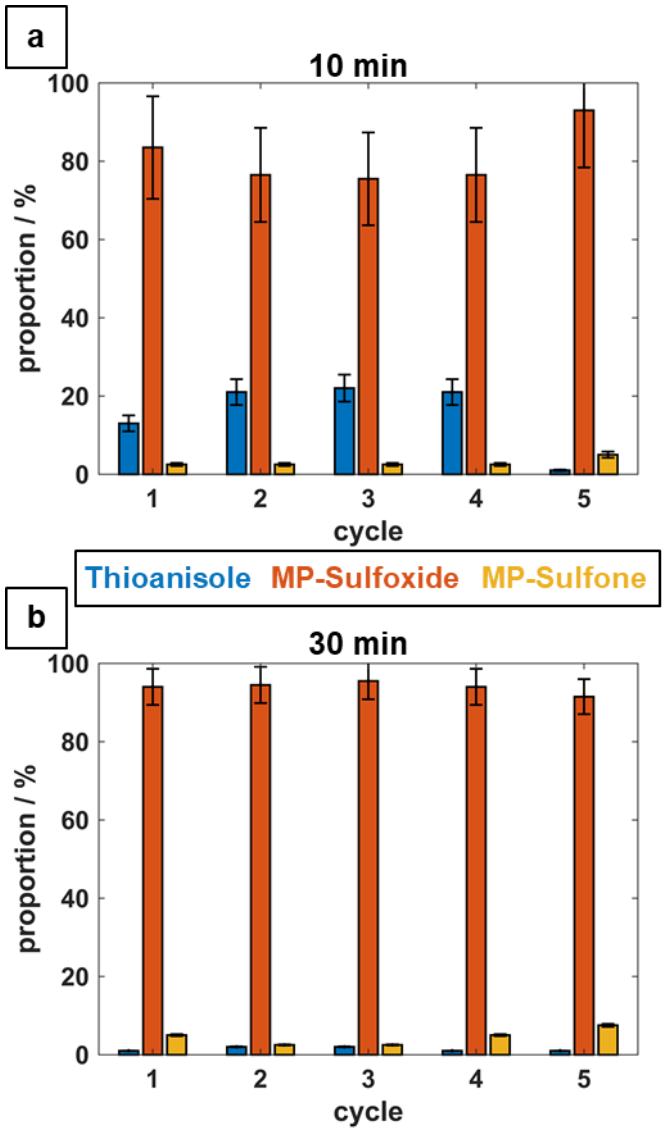

Figure 3.4. Sulfide oxidation capability of recycled WO_{3-x} NRs after a) 10 and b) 30 min.

WO_{3-x} NRs were annealed at 300 °C for 5 h and ground after each cycle. These steps were necessary because water from the aqueous hydrogen peroxide solution and organic residues from catalysis accumulate on the polar surface of the catalyst and reduce its activity. Grinding helped to improve the suspendability of the particles after annealing. After each reaction/purification/grinding step, small losses of WO_{3-x} NRs occurred. WO_{3-x} NRs showed moderate recyclability along with high selectivity, with a total conversion of >500 per W atom. We suppose that higher conversion yields may be possible for higher WO_{3-x} NR concentrations.

3.3.2 Sulfide Screening

We performed a screening of different sulfides to check whether steric and electronic effects have a significant effect on the oxidation reaction. Di-n-propyl sulfide was used as a model compound for purely aliphatic sulfides. The conversion reached 99 % after 30 min (94 % after 10 min). In contrast, the conversion di-t-butyl sulfide was only 73 % after 30 min (48 % after 10 min). We assume that the reaction of aliphatic and sterically less demanding n-propyl-group is significantly faster due to inductive effects. On the other hand, the tert-butyl group sterically hinders the reaction, overcoming the stronger inductive effect of the three separate methyl groups. Diphenyl sulfide with only aromatic substituents showed a significant lower conversion of 35 % after 30 min (14 % and after 10 min) than thioanisole. This indicates that the electron withdrawing effect of the conjugated phenyl-groups and steric hindering lower the reaction rate significantly. The non-conjugated and sterically less demanding dibenzyl sulfide showed a comparable conversion rate to thioanisole with a yield of 92 % after 30 min (59 % after 10 min). To demonstrate the electron withdrawing effect of the aromatic system we conducted a set of experiments using *p*-substituted thioanisole derivatives with +M and -M effect. As expected, the -M group (4-nitrothioanisole) reduced the conversion significantly (35 % after 30 min), whereas the reaction of the +M derivate (4-methoxythioanisole) was faster compared to that of unsubstituted thioanisole (95 % after 30 min, 68 % after 10 min). Surprisingly, 4-aminothioanisole showed a lower conversion than thioanisole (38 % after 30 min) despite the +M substituent. We observed fast precipitation of the WO_{3-x} NRs after injecting the sulfide. This indicates, in accord with the results of our previous study,[50] a passivation of the negatively charged, annealed WO_{3-x} NRs due to binding of the amine substrate on the non-coordinated surface. Finally, dibenzothiophene was tested, showing only marginal oxidation (~ 2 % after 30 min) under standard conditions. We propose that oxidation of dibenzopthiphen is strongly disfavored due to the conjugation of the aromatic system. Nevertheless, we were able to oxidize dibenzothiophene (71 % after 30 min) by using a concentration of 8.5 mg/mL WO_{3-x} NRs under *ex situ* conditions.

No significant formation of sulfones (≥4 %) was found for any of the investigated sulfides. We used MP-sulfoxide as educt under otherwise identical conditions to underline the selectivity of the WO_{3-x} NRs. We overserved a 4 % conversion to MP-sulfone, not significantly higher than for thioanisole (2 % after 30 min). The same applies to dimethyl sulfoxide. A conversion of only 5 % to dimethyl sulfone indicates that even steric and +I effects do not increase the reaction rate of the second oxidation step for WO_{3-x} NRs. As a control, the oxidation of all sulfides (excluding dibenzothiophene) was tested in the absence of the WO_{3-x} catalyst. The conversion was in no case greater than 1 % after 30 min.

Table 3.2. Composition for *in situ* oxidation reaction after 10 and 30 min for different sulfides and sulfoxides under standard conditions (0.85 mg WO_{3-x} catalyst, 0.04 mmol substrate, 0.06 mmol H_2O_2 (60%) in 0.6 ml methanol-d_4).

Substrate	Structure	Ratio sulfide:sulfoxide: sulfone (10 min)	Ratio sulfide:sulfoxide: sulfone (30 min)
Thioanisole	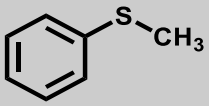	39:60:1	8:90:2
Di-n-propy sulfide	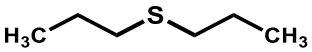	6:93:1	1:95:4
Di-t-butyl sulfide	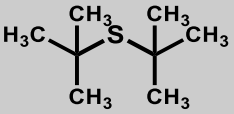	52:48:0	27:73:0
Diphenyl sulfide	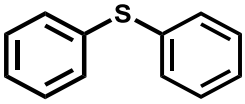	86:14:0	65:35:0
Dibenzyl sulfide	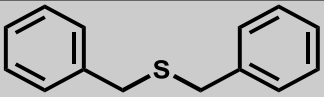	41:58:1	8:91:1
4-Nitrothioanisole	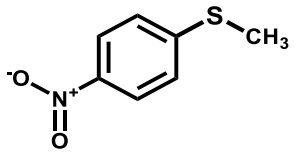	88:12:0	65:35:0
4-Methoxythioanisole	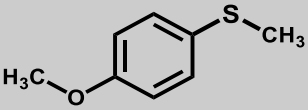	32:68:0	5:93:2
4-Aminothioanisole	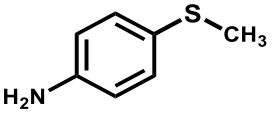	86:14:0	61:39:0
Dibenzothiophene	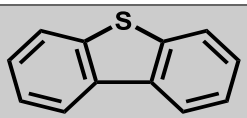	99:1:0 61:39:0[a]	98:2:0 29:71:0[a]
MP-sulfoxide	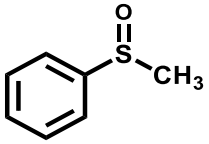	0:98:2	0:96:4
Dimethy sulfoxide	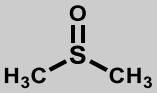	0:97:3	0:95:5

a. *ex situ* kinetic with a particle concentration of 8.5 mg/ml WO_{3-x} NRs instead of 1.42 mg/ml.

3.3.3 Nanoparticle Screening

We performed a series of *ex situ* and *in situ* experiments with different reference compounds to compare WO_{3-x} NRs with other catalyst. Commercially available WO_3, ammonium-metatungstate ($(NH_4)_6H_2W_{12}O_{40}$* H_2O, used as precursor for the synthesis of WO_{3-x} NRs) and sodium tungstate dihydrate were tested as "tungsten oxide" reference compounds. Sodium tungstate was the only reference material that showed a significant conversion, but it showed no selectivity with respect to sulfoxide or sulfone formation. The MP-sulfone content after 30 min was 19 % for the *ex situ* and 9 % for the *in situ* experiment, the MP-sulfoxide content 73 % in both cases. In addition, sodium tungstate dissolved completely in methanol. Despite the recyclability of WO_{3-x} NRs small amounts of free (oligo)tungstate could formed by surface oxidation in the presence of H_2O_2 in large excess.[58] We assume that this effect might be responsible for the slow oxidation to the sulfone, (comparable to the effect of soluble, non-selective Na_2WO_4).

Nanocrystals of the hexagonal ammonium tungsten bronze ($(NH_4)_{\sim 0.2}WO_3$), the second reference material, yielded lower conversion under virtually identical conditions. We assume that the aspect ratio, i.e., the lower surface area of $(NH_4)_{\sim 0.2}WO_3$ particles[50] compared to WO_{3-x} NRs (Table S8.2.3) reduces the conversion rate. The selectivity was comparable to that achieved with WO_{3-x} NRs.

TiO_2 (P25) particles were tested as standard reference material in oxidative catalysis under *ex situ* conditions. TiO_2 (P25) particles showed a slower conversion with much less selectivity for sulfoxide formation than WO_{3-x} NRs. Pure anatase TiO_2 nanocrystals synthesized according to ref. [59,60] showed higher conversion than TiO_2 (P25), but still significantly less than WO_{3-x} with less selectivity (~6 % MP-sulfone after 30 min).

Finally, we investigated ceria nanoparticles (TEM images and PXRD pattern in Figure S8.2.3), synthesized in a deep eutectic solvent with choline cloride.[61] Although the total conversion with CeO_2 nanoparticles was low compared to that obtained for WO_{3-x} NRs (17 % after 30 min), we observed a significantly faster reaction to MP-sulfone than for any other catalyst in this study. We used MP-sulfoxide as starting compound for the oxidation reaction with a CeO_2 nanocatalyst. The conversion to MP-sulfone was higher than the total conversion with thioanisole (28 vs. 15 % after 30 min, with respect to H_2O_2 equivalents). This indicates that for the CeO_2 nanoparticles the reaction rate constant is faster for the second oxidation step where sulfones are formed, whereas the first oxidation step to the sulfoxides is significantly faster for WO_{3-x} NRs. We suppose that the negatively charged surface of the WO_{3-x} NRs (ζ-potential = -39.7 mV) is responsible for an improved binding of the sulfide, whereas the sulfoxide with its negative dipole due to the S=O group is sterically and electronically disfavored. For the positively charged surface of the CeO_2 nanoparticles (ζ-potential = +23.8 mV), the negative portion of the dipole improves a preorganization on the surface, which is responsible for an increased selectivity for sulfoxides.

The BET surface data of WO_{3-x} NRs is significantly lower than CeO_2 and TiO_2 nanoparticles (47.0 m^2/g compared to 133.9 and 151.7 m^2/g respectively, Table S8.2.4). This shows that - even for a lower surface area - the catalytic activity of WO_{3-x} NRs is superior compared to that of other nanocatalysts compiled in Table 3.3.

Table 3.3. Screening of different compounds for their potential in oxidation catalysis for the oxidation of thioanisole.

catalyst	Ratio sulfide:sulfoxide:sulfone (10 min)	Ratio sulfide:sulfoxide:sulfone (30 min)
WO_{3-x} nanorods[a]	39:60:1	8:90:2
WO_{3-x} nanorods[a,c]	0:98:2	0:96:4
WO_{3-x} nanorods[b]	48:51:1	14:84:2
WO_3 reference[b]	98:2:0	97:3:0
$(NH_4)_6H_2W_{12}O_{40}$* H_2O[b]	98:2:0	98:2:0
Na_2WO_4*2 H_2O[a]	54:43:3	18:73:9
Na_2WO_4*2 H_2O[b]	33:57:10	8:73:19
$(NH_4)_{0.2}WO_3$ nanoparticles[a]	81:19:0	53:46:1
$(NH_4)_{0.2}WO_3$ nanoparticles[b]	90:10:0	88:12:0
TiO_2 P25[b]	92:8:0	79:20:1
TiO_2 nanoparticles [b]	82:17:1	55:39:6
CeO_2 nanoparticles [a]	94:5:1	88:9:3
CeO_2 nanoparticles [a,c]	0:87:13	0:72:28
CeO_2 nanoparticles [b]	93:6:1	83:11:6

a. *in situ* experiment

b. *ex situ* experiment

c. MP-sulfoxide as educt

Finally, to classify our results, we compare the WO_{3-x} NRs presented in this work with known sulfide oxidation catalysts operating with H_2O_2 in methanol. Compared to heterogeneous coupled phosphomolybdate with poly(amidiamine) [62] WO_{3-x} NRs show a much faster conversion rate within 30 min rather than in 4 h. MO_3 nanobelts[63] needed elevated temperatures of 70 °C instead of room temperature. WO_3 nanoparticles supported on mesoporous silica (MCM-48) [64] showed comparable selectivity with 50 % H_2O_2, but the reaction time of 4 h is almost one order of magnitude longer than 30 min for WO_{3-x} NRs. (Co^{2+}/Ni^{2+}/Zn^{2+}/Pd^{2+}) Schiff base catslysts[65] had a much lower selectivity without preference for oxidation to sulfoxides. A variety of organic catalysts[66] showed lower conversion rate after much longer reaction time. Triisopropylphenyl amino triphenolate compounds of titanium[67]

had higher turnover rates compared to WO_{3-x} NRs (97 % within 10 min), but recycling was not demonstrated. In general, homogeneous catalysts suffer from increased purification and recycling issues, while heterogeneous WO_{3-x} catalyst can easily be removed and re-used.

3.4 Conclusions

The oxidation of organic sulfides with Magnéli-Type WO_{3-x} NR catalysts was studied for the model system methylphenylsulfide (thioanisole) using H_2O_2 as oxidant at room temperature. Optimized conditions for the selective oxidation to methylphenylsulfoxide were evaluated by monitoring the reaction kinetics using *in situ* ^{1}H-NMR spectroscopy. Oxidation of thioanisole to the corresponding sulfoxide was complete after only 30 min, whereas the oxidation to the sulfone occurred only on a timescale of days. We demonstrate that the reaction is strongly suppressed by excess water, whereas the concentration of the oxidant H_2O_2 is only of minor importance. Water is likely to block negatively charged WO_{3-x} NR surfaces and to compete with H_2O_2 for surface binding. No significant structural or morphological changes occurred when surface-bound water and other residual surface ligands were removed by annealing at 300 °C, but the catalytic activity increased. The concentration of the catalyst had an impact on the reaction, as it lowers the relative water content of the solvent with respect to the nanocatalyst. The reaction proceeds smoothly only in methanol. *Ex situ* experiments showed the recyclability of the WO_{3-x} particles with an overall conversion of >500 with respect to the thioanisole/WO_{3-x} ratio (catalyst loading ~1 mol%) without loss of selectivity. We demonstrate with different aliphatic and aromatic sulfides that the selectivity for sulfoxide formation is universal. Oxidation to sulfones with WO_{3-x} was hindered in any case. Aliphatic sulfides were oxidized faster than their aromatic counterparts, steric hindering lowered the conversion rates. Aromatic systems with electron donating substituents were oxidized faster, electron withdrawing substituents inhibited the oxidization of thioethers to the corresponding sulfoxides. The high selectivity of WO_{3-x} nanorods for the oxidation of thioethers to sulfoxides was demonstrated by using sulfoxides as substrates. Here, conversion to sulfones was negligible.

A screening of other reference catalysts showed significant conversion rates for oxidation reactions only for sodium tungstate dihydrate, but without any selectivity for sulfoxide formation. This behavior is in line with the reported haloperoxidase-like behavior of WO_4^{2-} tungstates in layered double hydroxides.[56] Ceria nanoparticles showed promising selectivity for sulfone oxidation. While the oxidation of sulfides to the corresponding sulfoxides was slow, oxidation of sulfoxide substrates to sulfones was much faster.

Unique features of the selective Magneli-type WO_{3-x} system are that (i) it operates in alcoholic solution and (ii) the oxidation rate is decoupled from the surface acidity. (iii) This allows a high chemoselectivity to be reached for the desired sulfoxide products compared to a high selectivity of CeO_2 for sulfone formation.

Our studies show very promising applications for the mild and selective oxidation of sulfides to sulfoxides and sulfones. Especially for the synthesis of pharmaceutical compounds this selectivity could prove valuable, as it opens a pathway to oxidize only the desired sulfur-group while leaving the rest of the molecule untouched. Further studies could elucidate the effect of surface charge on the substrates as well as the immobilization of the particles for a flow-catalysis, for example in a polymer matrix. Finally, the use of auxiliars for the selective synthesis of chiral sulfoxides may be investigated.

3.5 Experimental section

Materials. All chemicals were used as received without further purification. Thioanisole (≥99 %), methyl phenyl sulfoxide (≥97 %), 4-nitrophenyl methyl sulfide (96 %) and sodium tungstate dihydrate (Na_2WO_4*$2H_2O$, puris) were purchased from Sigma Aldrich, di-n-propyl sulfide (98+ %), diphenyl sulfide (98 %) and dibenzyl sulfide (99 %) from Alfa Aesar, dibenzothiophene (98 %) and H_2O_2 (35 %) from Acros, dimethyl sulfide (DMSO, analytical grade) and H_2O_2 (60 %) from Fisher scientific, 4-methoxyphenyl methyl sulfide from fluorochem, 4-aminophenyl methyl sulfide (97 %) from BLD pharm, di-tert-butyl sulfide (≥98 %) from TCI, Aeroxide titanium oxide (TiO_2 P25) form Degussa, tungsten oxide (WO_3, 99.99 %) from chempur and ammoniummetatungstate ($(NH_4)_6H_2W_{12}O_{40}$* H_2O, 90 % WO_3) from Carl Roth. All deuterated solvents were purchased from Deutero GmbH and had a purity of ≥99.8 %.

Annealing. All nanoparticles were annealed in an air flow of approximetly 90 l/min for 5 h prior to catalytic experiments. An annealing temperature of 300 °C was used unless stated otherwise.

Catalytic Oxidation of Sulfides. For a typical ***in situ*** catalytic measurement 8.5 mg particles were weighted in a 1 ml volumetric flask and dispersed in methanol-d_4. The flask was left in a sonication bath for 1 h and homogenized repeatedly. Afterwards, 100 µl of the freshly homogenized suspension was filled in an NMR-tube with additional 500 µl of methanol-d_4 to target the final particle concentration of 0.85 mg per sample. Upon injection of 0.04 mmol of the sulfide the NMR spectrometer was calibrated towards the sample and an ^{1}H-NMR-spectrum was measured. Afterwards, 0.06 mmol H_2O_2 (60 %) was injected and the measurement sequence (30 min, one spectra every 20 s) started after 1 min. The spectra were evaluated and plotted using Mestrenova 11 and Matlab 2018a, using the aromatic signals for thioanisole to avoid errors for the MP-sulfone due to the methanol signal. To normalize an experimental series (except for different annealing temperatures and for the particle screening), we always performed a control reaction from the same batch of dispersed WO_{3-x} NRs using standard conditions and thioanisole.

A dispersion of WO_{3-x} NRs (1.42 mg/mL) in methanol-d_4 was prepared in a glass flask for ***ex situ*** experiments. The dispersion was left in sonication bath for 1 h with repeated homogenization.

Subsequently, sulfide was added to target a final concentration of 0.67 mol/l. The solution was stirred with a magnetic stirring bar for 15 min to reach room temperature. Afterwards, H_2O_2 was added to reach a concentration of 0.1 mol/L. After 10 and 30 min an aliquot of 400 µL was taken und quenched immediately by injection in 0.2 mL of 1 mol/l KI solution in D_2O. The WO_{3-x} NRs were removed by centrifugation, and the supernatant characterized by ^{1}H-NMR spectroscopy.

For all **recycling** experiments the concentration of particles was kept at 8.5 mg/mL (17 ml, 1 h sonication) in non-deuterated methanol and equilibrated for 30 min at 25 °C (water bath). 861 µL (7.3 mmol) of thioanisole were injected. After equilibrating for 5 min, 938 µL of H_2O_2 (10.9 mmol) were injected. 50 µL aliquots were taken after 0, 10 and 30 min and injected in a solution of 350 µL of methanol-d_4 and 200 µL of D_2O containing 27.3 mg (0.17 mmol) of KI. The WO_{3-x} NRs were again removed by centrifugation, and the supernatant measured by ^{1}H-NMR spectroscopy.

3.5.1 Characterization

Nuclear Magnetic Resonance (NMR) spectroscopy. Solution NMR spectra were recorded on a Bruker DRX 400 NMR spectrometer equipped with a commercial Bruker 5 mm 2 channel inversed probe head with z-gradients. The ^{1}H NMR spectra were measured using a 30° flip angle and averaging 32 scans with 2 s recycle delay. For the *in situ* kinetic experiment, 90 spectra with 4 scans were recorded over a period of 30 min upon injection of H_2O_2 starting after 1 min (3 spectra per min). The wobb was adjusted for each experiment before injection of water to ensure quantitative measurements.

Transmission Electron Microscopy (TEM). For TEM studies one drop of a highly diluted solution of particles (~0.2 mg/mL in chloroform) was put onto a carbon-coated copper grid. Images were taken with a FEI Tecnai G2 Spirit microscope equipped with a Gatan US1000 CCD camera at 120 kV. High resolution (HR)-TEM images were measured with a FEI Tecnai F30 operating at 300 kV, equipped with an on axis US4000 CCD 4kx4k camera. For further processing the program ImageJ was used.

Powder X-Ray Diffraction. (PXRD). PXRD studies were carried out on a STOE Standi P using Mo Kα_1 radiation (λ = 0.7093 Å) and a Dectris Mythen 1k detector. The diffractograms were analyzed using Match!3 and plotted with Matlab2018b. All references were taken from the Crystallography Open Database (COD) or International Centre for Diffraction Data (ICDD) PDF database.

Zeta-Potential. ζ-potentials were measured using a Malvern Zetasizer NanoZS with a 633 nm He-Ne-Laser and folded capillary cells at 25 °. Samples were measured in milli pore water filtered through a 200 µm syringe filter. The particle concentration was about 1 mg/ml.

Specific surface area (BET). Specific surface area measurements were carried out on a 3P Micro 300 gas adsorption instrument using the BET N_2 adsorption method. The samples were heated at 300 °C for 3 h at ambient pressure to remove moisture and surface occupying tensides.

3.6 References

1 R. Bentley, *Chem. Soc. Rev.*, 2005, **34**, 609–624.

2 L. J. de Kok, *Sulphur in plant physiology*, International Fertiliser Society, York, 2002.

3 S. Caron, R. W. Dugger, S. G. Ruggeri, J. A. Ragan and D. H. B. Ripin, *Chem. Rev.*, 2006, **106**, 2943–2989.

4 R. M. Garrett, J. L. Johnson, T. N. Graf, A. Feigenbaum and K. V. Rajagopalan, *Proc. Natl. Acad. Sci. U.S.A.*, 1998, **95**, 6394–6398.

5 J. M. Campos-Martin, M. C. Capel-Sanchez, P. Perez-Presas and J. Fierro, *J. Chem. Technol. Biotechnol.*, 2010, **85**, 879–890.

6 G. W. Wagner and Y.-C. Yang, *Ind. Eng. Chem. Res.*, 2002, **41**, 1925–1928.

7 F. Di Furia, G. Modena and R. Seraglia, *Synthesis*, 1984, **1984**, 325–326.

8 N. Komatsu, Y. Nishibayashi, T. Sugita and S. Uemura, *Tetrahedron Lett.*, 1992, **33**, 5391–5394.

9 R. Noyori, M. Aoki and K. Sato, *Chem. Commun.*, 2003, 1977–1986.

10 R. Schlögl, *Angew. Chem. Int. Ed.*, 2015, **54**, 3465–3520.

11 F. Schüth, *Chemie Unserer Zeit*, 2006, **40**, 92–103.

12 H. An, Y. Hou, S. Chang, J. Zhang and Q. Zhu, *Inorg. Chem. Front.*, 2020, **7**, 169–176.

13 R. Sevvel, S. Rajagopal, C. Srinivasan, N. I. Alhaji and A. Chellamani, *J. Org. Chem.*, 2000, **65**, 3334–3340.

14 G. Licini, V. Conte, A. Coletti, M. Mba and C. Zonta, *Coord. Chem. Rev.*, 2011, **255**, 2345–2357.

15 R. Barret, F. Pautet, P. Bordat, B. Tinland and M. Daudon, *Phosphorus, Sulfur Relat. Elem.*, 1989, **45**, 31–33.

16 K. Bahrami, *Tetrahedron Lett.*, 2006, **47**, 2009–2012.

17 S. Colonna, N. Gaggero, L. Casella, G. Carrea and P. Pasta, *Tetrahedron Asymmetry*, 1992, **3**, 95–106.

18 M. Morrison and G. R. Schonbaum, *Annu. Rev. Biochem.*, 1976, **45**, 861–888.

19 A. M. Molenbroek, S. Helveg, H. Topsøe and B. S. Clausen, *Top. Catal.*, 2009, **52**, 1303–1311.

20 W.-L. Dai, J. Ding, Q. Zhu, R. Gao and X. Yang, in *Catalysis*, Royal Society of Chemistry, Cambridge, 2016, pp. 1–27.

21 R. Kiebach, N. Pienack, W. Bensch, J.-D. Grunwaldt, A. Michailovski, A. Baiker, T. Fox, Y. Zhou and G. R. Patzke, *Chem. Mater.*, 2008, **20**, 3022–3033.

22 R. Schlögl, *Top. Catal.*, 2016, **59**, 1461–1476.

23 P. Kampe, L. Giebeler, D. Samuelis, J. Kunert, A. Drochner, F. Haass, A. H. Adams, J. Ott, S. Endres, G. Schimanke, T. Buhrmester, M. Martin, H. Fuess and H. Vogel, *Phys. Chem. Chem. Phys.*, 2007, **9**, 3577–3589.

24 H. Wei and E. Wang, *Chem. Soc. Rev.*, 2013, **42**, 6060–6093.

25 R. Ragg, F. Natalio, M. N. Tahir, H. Janssen, A. Kashyap, D. Strand, S. Strand and W. Tremel, *ACS Nano*, 2014, **8**, 5182–5189.

26 J. Wu, X. Wang, Q. Wang, Z. Lou, S. Li, Y. Zhu, L. Qin and H. Wei, *Chem. Soc. Rev.*, 2019, **48**, 1004–1076.

27 C. Y. Park, J. M. Seo, H. Jo, J. Park, K. M. Ok and T. J. Park, *Sci. Rep.*, 2017, **7**, 40928.

28 F. Natalio, R. André, A. F. Hartog, B. Stoll, K. P. Jochum, R. Wever and W. Tremel, *Nat. Nanotechnol.*, 2012, **7**, 530–535.

29 K. Herget, P. Hubach, S. Pusch, P. Deglmann, H. Götz, T. E. Gorelik, I. A. Gural'skiy, F. Pfitzner, T. Link, S. Schenk, M. Panthöfer, V. Ksenofontov, U. Kolb, T. Opatz, R. André and W. Tremel, *Adv. Mater.*, 2017, **29**, 1603823 (1-8).

30 R. Ragg, M. N. Tahir and W. Tremel, *Eur. J. Inorg. Chem.*, 2016, **2016**, 1906–1915.

31 C. M. Cordas and J. J. Moura, *Coord. Chem. Rev.*, 2019, **394**, 53–64.

32 T. S. Smith and V. L. Pecoraro, *Inorg. Chem.*, 2002, **41**, 6754–6760.

33 W. Cheng, Y. Ju, P. Payamyar, D. Primc, J. Rao, C. Willa, D. Koziej and M. Niederberger, *Angew. Chem. Int. Ed.*, 2015, **54**, 340–344.

34 M. Righettoni, A. Tricoli and S. E. Pratsinis, *Anal. Chem.*, 2010, **82**, 3581–3587.

35 A. Magnéli, *Nature*, 1950, **165**, 356–357.

36 L. Pirker, B. Višić, S. D. Škapin, G. DraŽić, J. Kovač and M. Remškar, *Nanoscale*, 2020, **12**, 15102–15114.

37 G. Kieslich, G. Cerretti, I. Veremchuk, R. P. Hermann, M. Panthöfer, J. Grin and W. Tremel, *Phys. Status Solidi A*, 2016, **213**, 808–823.

38 A. Yella, M. N. Tahir, S. Meuer, R. Zentel, R. Berger, M. Panthöfer and W. Tremel, *J. Am. Chem. Soc.*, 2009, **131**, 17566–17575.

39 K. Manthiram and A. P. Alivisatos, *J. Am. Chem. Soc.*, 2012, **134**, 3995–3998.

40 S. Cong, Y. Yuan, Z. Chen, J. Hou, M. Yang, Y. Su, Y. Zhang, L. Li, Q. Li, F. Geng and Z. Zhao, *Nat. Commun.*, 2015, **6**, 7800.

41 M. Seifollahi Bazarjani, M. Hojamberdiev, K. Morita, G. Zhu, G. Cherkashinin, C. Fasel, T. Herrmann, H. Breitzke, A. Gurlo and R. Riedel, *J. Am. Chem. Soc.*, 2013, **135**, 4467–4475.

42 H. Bai, N. Su, W. Li, X. Zhang, Y. Yan, P. Li, S. Ouyang, J. Ye and G. Xi, *J. Mater. Chem. A*, 2013, **1**, 6125–6129.

43 T. Zheng, W. Sang, Z. He, Q. Wei, B. Chen, H. Li, C. Cao, R. Huang, X. Yan, B. Pan, S. Zhou and J. Zeng, *Nano Lett.*, 2017, **17**, 7968–7973.

44 Y. Sun, W. Wang, J. Qin, Di Zhao, B. Mao, Y. Xiao and M. Cao, *Electrochim. Acta*, 2016, **187**, 329–339.

45 P. A. Shinde and S. C. Jun, *ChemSusChem*, 2020, **13**, 11–38.

46 M. Juelsholt, T. Lindahl Christiansen and K. M. Ø. Jensen, *J. Phys. Chem. C*, 2019, **123**, 5110–5119.

47 H. L. Holland, *Chem. Rev.*, 1988, **88**, 473–485.

48 R. André, F. Natálio, M. Humanes, J. Leppin, K. Heinze, R. Wever, H.-C. Schröder, W. E. G. Müller and W. Tremel, *Adv. Funct. Mater.*, 2011, **21**, 501–509.

49 K. Korschelt, M. N. Tahir and W. Tremel, *Chem. Eur. J.*, 2018, **24**, 9703–9713.

50 R. Dören, B. Leibauer, M. A. Lange, E. Schechtel, L. Prädel, M. Panthöfer, M. Mondeshki and W. Tremel, *Nanoscale*, 2021, **13**, 8146–8162.

51 G. S. Pawley, *J. Appl. Crystallogr.*, 1980, **13**, 630–633.

52 A. D. Buckingham and L. Fan-Chen, *Int. Rev. Phys. Chem.*, 1981, **1**, 253–269.

53 H. Hosseini-Monfared, C. Näther, H. Winkler and C. Janiak, *Inorg. Chim. Acta*, 2012, **391**, 75–82.

54 M. Azizi, A. Maleki and F. Hakimpoor, *Catal. Commun.*, 2017, **100**, 62–65.

55 A. Bezaatpour, E. Askarizadeh, S. Akbarpour, M. Amiria and B. Babaei, *Mol. Catal.*, 2017, **436**, 199–209.

56 B. Sels, D. de Vos, M. Buntinx, F. Pierard, A. Kirsch-De Mesmaeker and P. Jacobs, *Nature*, 1999, **400**, 855–857.

57 J. Herrera, J. Kwak, J. Hu, Y. Wang, C. Peden, J. Macht and E. Iglesia, *J. Catal.*, 2006, **239**, 200–211.

58 L. D. Pachón and G. Rothenberg, *Appl. Organometal. Chem.*, 2008, **22**, 288–299.

59 C.-T. Dinh, T.-D. Nguyen, F. Kleitz and T.-O. Do, *ACS Nano*, 2009, **3**, 3737–3743.

60 E. Schechtel, R. Dören, H. Frerichs, M. Panthöfer, M. Mondeshki and W. Tremel, *Langmuir*, 2019, **35**, 12518–12531.

61 O. S. Hammond, K. J. Edler, D. T. Bowron and L. Torrente-Murciano, *Nat. Commun.*, 2017, **8**, 14150.

62 Q.-L. Tong, Z.-F. Fan, J.-W. Yang, Q. Li, Y.-X. Chen, M.-S. Cheng and Y. Liu, *Catalysts*, 2019, **9**, 791.

63 M. Jafarpour, M. Ghahramaninezhad and A. Rezaeifard, *RSC Adv.*, 2014, **4**, 1601–1608.

64 D. H. Koo, M. Kim and S. Chang, *Org. Lett.*, 2005, **7**, 5015–5018.

65 S. Menati, H. Amiri Rudbari, B. Askari, M. Riahi Farsani, F. Jalilian and G. Dini, *C. R. Chim.*, 2016, **19**, 347–356.

66 K. A. Stingl and S. B. Tsogoeva, *Tetrahedron Asymmetry*, 2010, **21**, 1055–1074.

67 D. Y. Bae, G. S. Park, N. Ko, K.-S. Son and E. Lee, *Dalton Trans.*, 2019, **48**, 9617–9624.

The following chapter 4 is currently under preparation.

Authorship Contributions Chapter 4

Conception and design of the study:

[redacted]

Preparation of samples and acquisition of data:

[redacted] – preparation of nanocrystals

[redacted] – TEM measurements

[redacted] – PXRD measurements

[redacted] – Mössbauer measurements

Analysis and interpretation of data:

[redacted] – PXRD diffraction analysis and refinements

[redacted] – TEM images

[redacted] – Mössbauer spectroscopy

Drafting of the manuscript:

[redacted]

Revising the manuscript critically for important intellectual content:

[redacted]

Preparation of figures:

[redacted]

4. Exploiting the effect of impurities for the controlled synthesis iron tungsten oxide nanocrystals

4.1 Abstract

Nanomaterials with metal tungstate structures display outstanding functional properties for a variety of applications. Still, the reproducibility of nanocrystals synthesis is a persistent problem, and the key for making uniform nanocrystals remain elusive. In a study exploring the synthesis parameters of iron tungstate, using a seed-mediated approach with oleic acid and oleylamine as surfactants, we serendipitously detected the formation of $FeWO_4$ nanocrystals. We show that oleic acid, depending upon the storage condition, has an iron contamination originating from the container, which ultimately leads to the synthesis of $FeWO_4$ (ferberite) nanocrystals. By starting with pure oleic acid and deliberately adjusting the iron concentration, we can reproducibly drive the reaction to predominantly produce $FeWO_4$ nanocrystals with isotropic and anisotropic morphologies. Furthermore, another iron tungstate nanophase with still unknown structure was synthesized, when using oleyl oleamide as solvent. A similar structure is observed and described for $MgWO_4$ nanocrystals, however detailed structural analysis remains open.

4.2 Introduction

Magnéli phases[1] are a homologous series of stoichiometric line phases of early transition metal suboxides with unusual, but precise compositions like Ti_8O_{15},[2] V_6O_{11}[3], or $W_{18}O_{49}$.[4] The families of tungsten oxide structures with general formulae W_nO_{3n-1} or W_nO_{3n-2} derive from the ReO_3 parent structure.[5] Their oxygen deficiency is compensated by ordered one- or two-dimensional crystallographic shear planes rendering some of the corner-sharing WO_6 octahedra edge-sharing. The electrical and optical properties in bulk W_nO_{3n-2} phases are dominated by partial reduction of the tungsten atoms.

Magneli-type tungsten oxides provide the opportunity to synthesize and study nanocrystals with a variety of diameters, morphologies and size-dependent physical properties. Partially reduced tungsten oxides, in particular $W_{18}O_{49}$ nanocrystals, exhibit high aspect ratios, and therefore show strongly anisotropic physical properties on the nanoscale. In general, tungsten oxides are stable over a wide range of conditions, and their band gaps in the red/infrared range are ideal for the absorption of visible light. This makes them promising candidates for potential applications in photocatalysis,[6,7] photoelectrochemical water splitting,[8,9] in catalysis,[10,11] as anode material in Li-ion batteries,[12,13] for gas sensing,[14,15] or in plasmonics,[16–18] In addition, they are starting material for making WS_2 nanotubes[19] or for antibacterial coatings.[20]

Typical examples of wet-chemical routes for the synthesis of nanoparticles are seeded-growth,[16] the polyol process,[21] or sol-gel routes[22,23] and hydro/solvothermal chemistry.[24] Polyoxoanions (dubbed "molecular metal oxides")[25] which have a good solubility in a variety of solvents, are suitable precursors for the synthesis of metal oxides. Polycondensation from discrete polyoxometalates to solid, amorphous or crystalline, phases is not straightforward.[26] In water-like systems, in particular under solvothermal conditions, water is not an innocent spectator molecule but participates in the reactions by linking metal cations through processes mediated by pH, concentration, and possibly non-innocent counterions. *In situ* methods like X-ray total scattering with pair distribution analysis allow monitoring phase formation starting from clusters in solution *via* amorphous intermediates to the crystalline final product even under hydro/solvothermal conditions.[27–29] Nucleation and crystallization may proceed from clusters[30] *via* amorphous precursors[31] or through the aggregation of clusters or nanoparticles.[32–34]

The colloidal stability of the emerging phases may be improved with the aid of protecting ligands. They can regulate nucleation density and mediate growth processes by acting as capping agents, i.e., adhering to nanoparticle surfaces.[35] These protecting ligands are typically amphiphiles. The hydrophilic head group has nucleophilic properties for complexation of the metal ions, while the hydrophobic tail, containing linear, branched, or aromatic hydrocarbons, is responsible for preventing particle aggregation and dispersing the growing nanoparticles in non-polar solvents.[36] Depending on the solvent, reaction conditions or pH, the head group of some surfactants can be adapted for the respective reaction Still, the purity of the surfactant can affect the outcome of a reaction significantly, because structurally related

impurities can undergo competing reactions during or prior to nanoparticle synthesis.[37] Therefore, contaminated surfactants may lead to unexpected and unpredicted products.[38] Here we report on the effect of a contaminant resulting from surfactant storage, which led unexpectedly to the formation of monoclinic iron tungstate ($FeWO_4$, ferberite, as ternary end member of the wolframite series) nanocrystals and another, to our knowledge, unknown iron tungstate phase.

Structurally, $FeWO_4$ is an ordered derivative of the rutile parent type, the octahedral sites being filled by Fe and W atoms in an alternating fashion.[39] $FeWO_4$ is a antiferromagnetic semiconductor (p-type, E_g = 2.0 eV) with reported Neel-temperatures between 75.9[40] and 54 K.[41] $FeWO_4$ nanocrystals have been prepared from microemulsions,[42] sol-gel chemistry[43] or hydro/solvothermally[44–46], mostly in submicroscale and with no or very limited control on purity or particle aggregation and intergrowth. Our method allows control of size and crystallinity of the synthesized nanocrystals. The electronic and magnetic properties of $FeWO_4$ enable applications as (photo)catalysts[44,47] or electrode material[48] where well-defined, uniform and non-aggregated nanocrystals are highly desired. By exploiting the effects of surfactant impurities, we worked out a reproducible synthesis of $FeWO_4$ nanocrystals.

4.3 Results and discussion

We observed significant differences in the product purity of WO_{3-x} nanorods (**NRs**)[18] caused by the use of oleic acid from manufacturers who supplied the oleic acid (OAc) in glass bottles or in steel canisters (Sigma-Aldrich, technical grade, 90 % both). OAc from steel canisters had a brownish hue after being opened for approx. two years, while oleic acid from glass bottles was clear and colorless (Figure 4.1a, b). When the brownish OAc was used, the average length of WO_{3-x} NRs decreased from 78 nm to 61 nm while the width slightly increased from 8 nm to 12 nm. The TEM images and PXRD patterns of these shorter NRs are shown in Figure 4.2a. Our assumption was, that over time oxidation of the steel with small amounts of water[49] led a subsequent formation of iron containing compounds. To re-enact an iron contamination in pure oleic acid, we synthesized an iron (III) oleate ($Fe(oleate)_3$) complex[50] and mixed it with pure oleic acid (Figure 4.1c). The NRs synthesized with intentionally contaminated OAc (5 % Fe with respect to W) (Figure S8.3.1a) were even smaller than those synthesized with the impure OAc and had a size of ~36 nm*10 nm. However, the diffractograms of the products obtained with commercial and intentionally contaminated OAc showed only two basis reflections of Magneli-type $W_{18}O_{49}$ with rod-like shape ([010] and [020]). The reflection positions are unchanged with respect to those of pure WO_{3-x} NRs as reported in our previous work (ref. [18]), i.e., Fe alters NR growth, but it is not seem to incorporated into the structure at these concentrations, so that no Fe-containing WO_x phase is formed. We only observed a slight increasing in the *d* spacing along [010] of WO_{3-x} NRs changing from 3.789(2) → 3.793(4) → 3.797(4) Å for oleic acid from glass bottle,[18] from steel canister and with 5 mol% $Fe(oleat)_3$ respective, based on Pawley refinements (Figure S8.3.3). As the formation of WO_{3-x} NRs is

favored by the presence of amides (with partial positive charge),[51–53] i.e., $Fe^{2+/3+}$ cations could assemble on negatively charged surfaces of the WO_{3-x} NRs.[11,18] The smaller particle size might therefore be due to ion adsorption and surface passivation during growth, and responsible for the increasing d-spacing. When increasing the ammonium metatungstate (**AMT**) precursor loading from 0.12 to 0.24 mmol we observed only formation of WO_{3-x} NRs when using old or artificially contaminated oleic acid (Figure S8.3.2). Using pure oleic acid under similar conditions led to the formation of significant amount of hexagonal ammonium tungsten bronze.[18] This means that iron cations must block the surface of the NRs during growth and prevent oriented attachment towards bronze NCs.

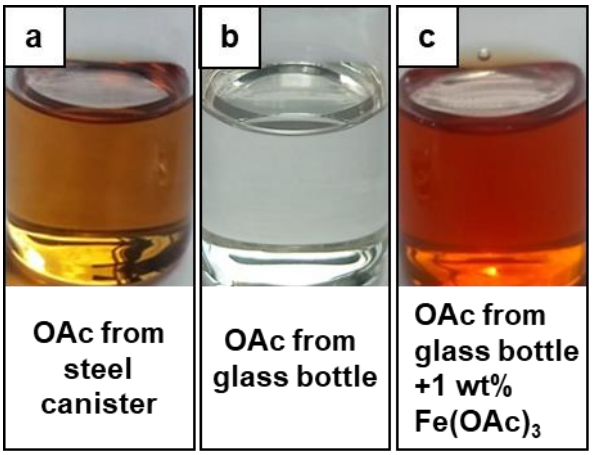

Figure 4.1. Digital photographs of OAc used for particle syntheses. a) OAc from a steel canister, b) OAc from a glass bottle and c) OAc from a glass bottle mixed with ~1 wt% of iron oleate.

When the iron oleate content was gradually increased by 10 and 20 % (with respect to 0.12 mmol AMT precursor), ferberite ($FeWO_4$) was formed as an additional phase (Figure S8.3.1b and Figure 4.2b, respectively). The TEM images show that nanometer-sized nanocrystals (**NCs**) of this phase start to appear in the products next to the WO_{3-x} nanorods. At a Fe:W ratio of 1:1 (1.43:1.43 mmol), $FeWO_4$ was formed as the main product in the form of spherical to elongated, non-aggregated NCs (average diameter 4-5 nm, Figure S8.3.1c). The crystallinity of the $FeWO_4$ NCs significantly improved with a reduced heating rate (**HR**) from 5 to 2.5 K/min (Figure 4.2c), as clearly observable in the respective PXRD patterns of ferberite-type $FeWO_4$ (space group *P2/c*). The NCs showed a cuboidal truncated morphology, with average diameters now between 10 and 14 nm. Additionally, we found hexagonal potassium tungsten bronze as an impurity, likely based on unreacted potassium oleate used for the synthesis of iron oleate. The percentage of this impurity is more present in syntheses employing a HR of 5 K/min (Figure S8.3.1c) compared to 2.5 K/min (Figure 4.2c), as faster HRs favorize hexagonal tungsten bronze formation.[18] Upon annealing in air at 300 and 500 °C (Figure S8.3.4), the presence of hexagonal potassium tungsten bronze in PXRD patterns of samples heated with 2.5 K/min became more clearly visible.

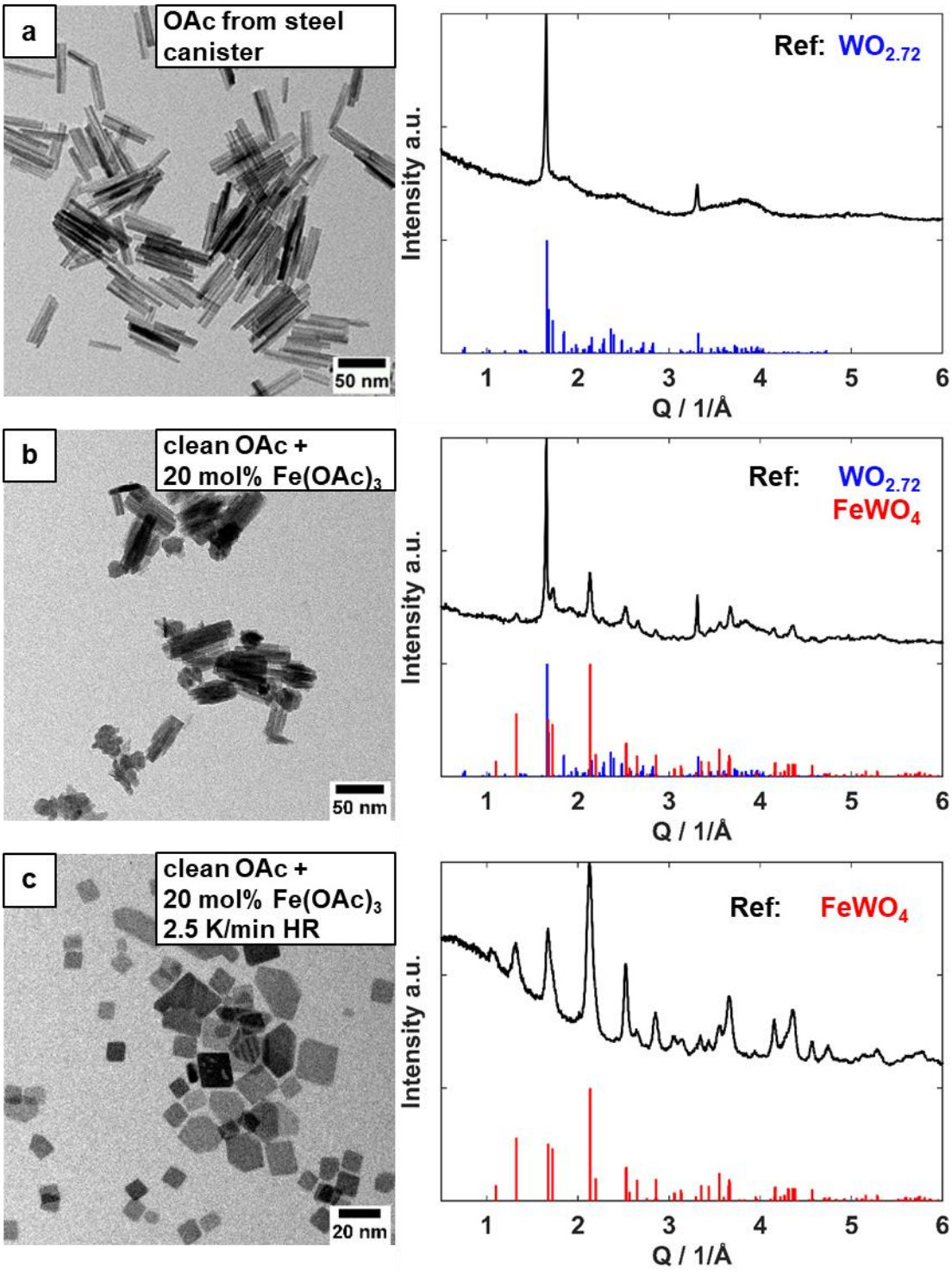

Figure 4.2. TEM images (left) and PXRD patterns (right) of a) WO_{3-x} NRs synthesized with oleic acid from the steel canister, b) addition of 20 mol% iron oleate to the standard synthesis and c) addition of 20 mol% iron oleate to the standard synthesis and a HR of 2.5 K/min. References: $WO_{2.72}$ (space group $P2/m$ (10), COD, Entry No.: 96-152-8167). $FeWO_4$ (Ferberite, space group $P2/c$ (13), COD no. 96-900-8125).

Annealing at 800 °C let to the disappearance of the ferberite phase and the formation of a new phase, while the hexagonal potassium tungsten bronze was still present. As no references were found for this

structure, we attribute the change towards an oxidative decomposition of $FeWO_4$ towards products with an overall composition of Fe_2WO_6 and WO_3 or $Fe_2W_3O_{12}$.

Further optimization of the synthesis parameters included the HR (1 K/min) and variation of the OAc:OAm ratio. The results are shown in Figure S8.3.5. Reducing the HR to 1 K/min further decreased the mean diameter of the NCs (between 9 and 11 nm, Figure S8.3.5a), although the products still contained NCs with diameters up to 25 nm. Anisotropic $FeWO_4$ NCs varying from 15 to 80 nm in length and 8 to 15 nm in width were obtained by increasing the OAc:OAm ratio from 20:20 mmol to 22.5:17.5 mmol (Figure S8.3.5b). At a lower OAc:OAm ratio of 17.5:22.5 mmol, effect was opposite. The NCs became smaller and spherical to slightly elongated with a mean diameter ranging from 3.7 to 4.9 nm (Figure S8.3.5c). The powder diffractogram showed broadening of the reflections, comparable to the ferberite NCs synthesized with 5 K/min HR Figure S8.3.1c.

Thermal decomposition of precursors leads to release of their ionic counterparts. Since 1.43 mmol of $Fe(oleate)_3$ (1:1 Fe to W) is stoichiometrically equivalent to the addition of up to 4.29 mmol anionic oleate, the OAc:OAm ratio is strongly affected. Therefore, iron(III)acetylacetonate ($Fe(acac)_3$) was tested as alternative precursor. Using OAc and OAm in a 1:1 ratio and a HR of 2.5 K/min, we obtained NCs with a diameter of ~20 nm (Figure 4.3a), that are less defined than those synthesized with iron oleate. However, the diffractogram of this product indicated the occurrence of another phase besides Ferberite $FeWO_4$ (spheres in Figure 4.3a). This phase has similarities to hexagonal potassium tungsten bonze, as observed for NCs synthesized with $Fe(oleate)_3$ (Figure S8.3.4).

In our previous study, we found that oleyl oleamide (**OAd**) suppresses the formation of hexagonal ammonium tungsten bronze as a byproduct of the synthesis of WO_{3-x} NRs.[18] Therefore, we tested it as a solvent for the synthesis of $FeWO_4$ NCs to suppress the formation of ferberite type $FeWO_4$ NCs. The powder diffractogram of this product (Figure 4.3b) shows no reflections belonging to a known WO_{3-x} Magneli phase, ferberite, or of any other reported iron tungstate. The strong background signal indicates the presence of a significant amorphous phase. The TEM image (Figure 4.3b) shows strongly agglomerated NCs with an apparent size of ~10 nm. Using $Fe(oleate)_3$ and applying otherwise identical conditions, we obtained the unknown phase again (Figure 4.3c), but PXRD patterns show a better signal to noise ratio and less background contribution. Searching for a reference based on known iron tungstate structures as well as other transition metal tungstates was unsuccessful. Closely matching diffraction patterns were found for two metastable $MgWO_4$ polymorphs (described as triclinic (Figure S8.3.6a, ICDD-ID 00-045-0412)[54] and tetragonal (Figure S8.3.6b, ICDD-ID 00-052-0390)),[55] where only lattice parameters, but no structural description was given. We annealed both samples with unknown $FeWO_4$ structure at 300, 500 and 800 °C for 5 h (synthesized with $Fe(acac)_3$ and $Fe(oleate)_3$, Figure S8.3.7 and Figure S8.3.8, respective). In both cases, the unknown structure remains stable up to a temperature of 500 °C. Samples synthesized with $Fe(acac)_3$ show increasing crystallinity upon annealing while the sample synthesized with $Fe(oleate)_3$ remains unchanged.

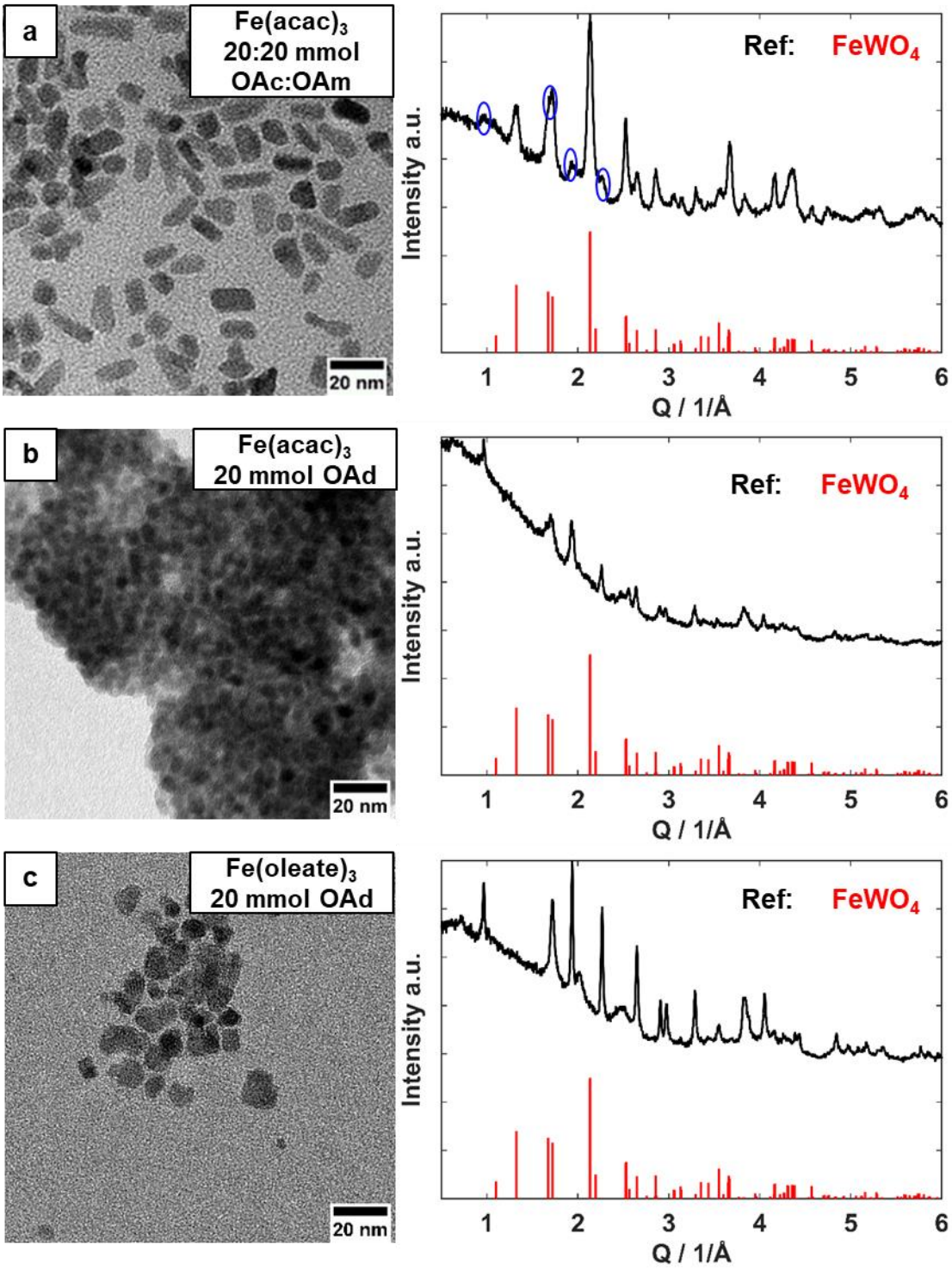

Figure 4.3. TEM images (left) and PXRD patterns (right) of $FeWO_4$ NCs synthesized with HR of 2.5 K/min and a) $Fe(acac)_3$ and 20:20 mmol OAc:OAm, blue markings indicate unknown structure, b) $Fe(acac)_3$ and 20 mmol OAd and c) $Fe(oleate)_3$ and 20 mmol OAd. Reference: $FeWO_4$ (Ferberite, space group $P2/c$ (13), COD no. 96-900-8125), not fitting the PXRD patterns in (b) and (c).

At 800 °C we observe oxidative decomposition and a comparable reflection profile as ferberite $FeWO_4$ NCs annealed at 800 °C (Figure S8.3.4). For unknown iron tungstate NCs synthesized with $Fe(oleate)_3$, we observe no presence of hexagonal potassium tungsten bronze in contrast to ferberite $FeWO_4$. Surprisingly, both undetermined samples showed slightly magnetic behavior. However, we cannot rule out the presence of a magnetic impurity not observed in PXRD, such as magnetite.

Table 4.1. Fit data for the Mössbauer spectra of ferberite $FeWO_4$ NCs (Figure S8.3.5c) and of $FeWO_4$ with unknown structure (Figure 4.3b, c)

Sample	**Fe(II), chemical shift / mm/s**	**Fe(II), quadrupole splitting / mm/s**	**Fe(III), chemical shift / mm/s**	**Fe(III), quadrupole splitting / mm/s**	**Ratio Fe(II): Fe(III) / at%**
$FeWO_4$ Ferberite from ref. [56]	1.11(2)	1.49(3)	-	-	-
$FeWO_4$ Ferberite, this work	1.11(1)	1.59(5)	0.39(1)	0.77(2)	63.4(9):36.6(1)
$FeWO_4$ unknown structure[a]	1.11(1)	1.96(0)	0.39(1)[c]	0.93(2)[c]	64.7(7):24.7(7)[c]: 11.0(1)[d]
$FeWO_4$ unknown structure[a]	1.11(1)	1.96(0)	0.39(1)[d]	ε=0.02(0)[d]	64.7(7):24.7(7)[c]: 11.0(1)[d]
$FeWO_4$ unknown structure[b]	1.07(1)	2.07(7)	0.39(1)	0.00(8)	84.7(9):15.3(6)

a. synthesized with OAd and $Fe(acac)_3$

b. synthesized with OAd and $Fe(oleate)_3$

c. Fe(III) not magnetically ordered

d. Fe(III) with magnetically ordering

Mössbauer spectroscopy was utilized to investigate the oxidation states of both unknown $FeWO_4$ NCs and compare them to "pure" ferberite NCs synthesized with iron oleate (HR of 2.5 K/min). The fit parameters are listed in Table 4.1, the respective spectra shown in Figure S8.3.9. The chemical shift for Fe(II) in ferberite NCs (1.11(2) mm/s) with a quadrupole splitting of 1.49(3) mm/s matches closely the values reported for pure ferberite.[56,57] However, we observe a magnetically disordered Fe(III) signal that is not compatible with $FeWO_4$. It could be related to surface oxidation of the NCs, as well as Fe^{3+} residues from the iron(III)oleate complex used as a precursor.

The chemical shift for Fe(II) in the new $FeWO_4$ phase synthesized with $Fe(acac)_3$ is similar to that of ferberite (1.11(1) mm/s), however the quadrupole splitting is significantly higher (1.96(0) instead of 1.59(5) mm/s for ferberite). This indicates a different bonding constellation of Fe(II) in this structure. For the unknown $FeWO_4$ synthesized with $Fe(oleate)_3$, we observe a chemical shift different from that of ferberite (1.07(1) mm/s) and an even higher quadrupole splitting (2.07(7) mm/s), also indicating a chemical environment that differs significantly form than in ferberite. Both unknown $FeWO_4$ NCs show a Fe(III) signal, similar to ferberite $FeWO_4$. Only for the NCs synthesized with $Fe(acac)_3$ we observed a magnetically ordered Fe(III) environment. Due to the high amorphous content, the Mössbauer spectra showed a relatively low intensity, which can be attributed to a significant energy loss due to elastic recoil.

We attempted to synthesize $MgWO_4$ nanocrystals as reference material. Using magnesium acetylacetonate dihydrate together with AMT as precursors in a ratio 1.43:1.43 mmol Mg:W and the surfactants OAc:OAm in a ratio of 20:20 mmol with a HR of 2.5 K/min. A TEM image and the X-ray powder diffractogram of the resulting products are shown in Figure 4.4a. We obtained nanocrystals with dimensions of ~3*8 nm, whose diffraction pattern matched closely with that of the trigonal/tetragonal structures described in ref. [54,55] and of reported $MgWO_4$ NCs.[58–61]

No structural changes were observed when $MgWO_4$ was annealed up to 500 °C (Figure 4.4b). The structural transformation to monoclinic $MgWO_4$ (huanzalaite), whose structure is closely related to the ferberite structure, was observed after annealing at 800 °C (Figure 4.4 c). Minor amounts (~4 %) of monoclinic WO_3 were formed as byproduct, based on a multiphase Rietveld refinement[62] (Figure S8.3.10).

As no further structural descriptions were found other than the original literature,[54,55] we performed a Pawley refinement[63] of the $MgWO_4$ NCs annealed at 500 °C applying the reported $MgWO_4$ structure using the triclinic model. The fit is presented in Figure 4.5a and is in agreement with the triclinic phase *P*1. For the presumably new phase of $FeWO_4$ we used the same refinement parameters as a good approximation, presented in Figure 4.5b. A more detailed structural solution for both phases is not possible based on the presented powder diffraction data and requires more complicated and in-depth methods such as automated diffraction tomography or beam line diffraction data.

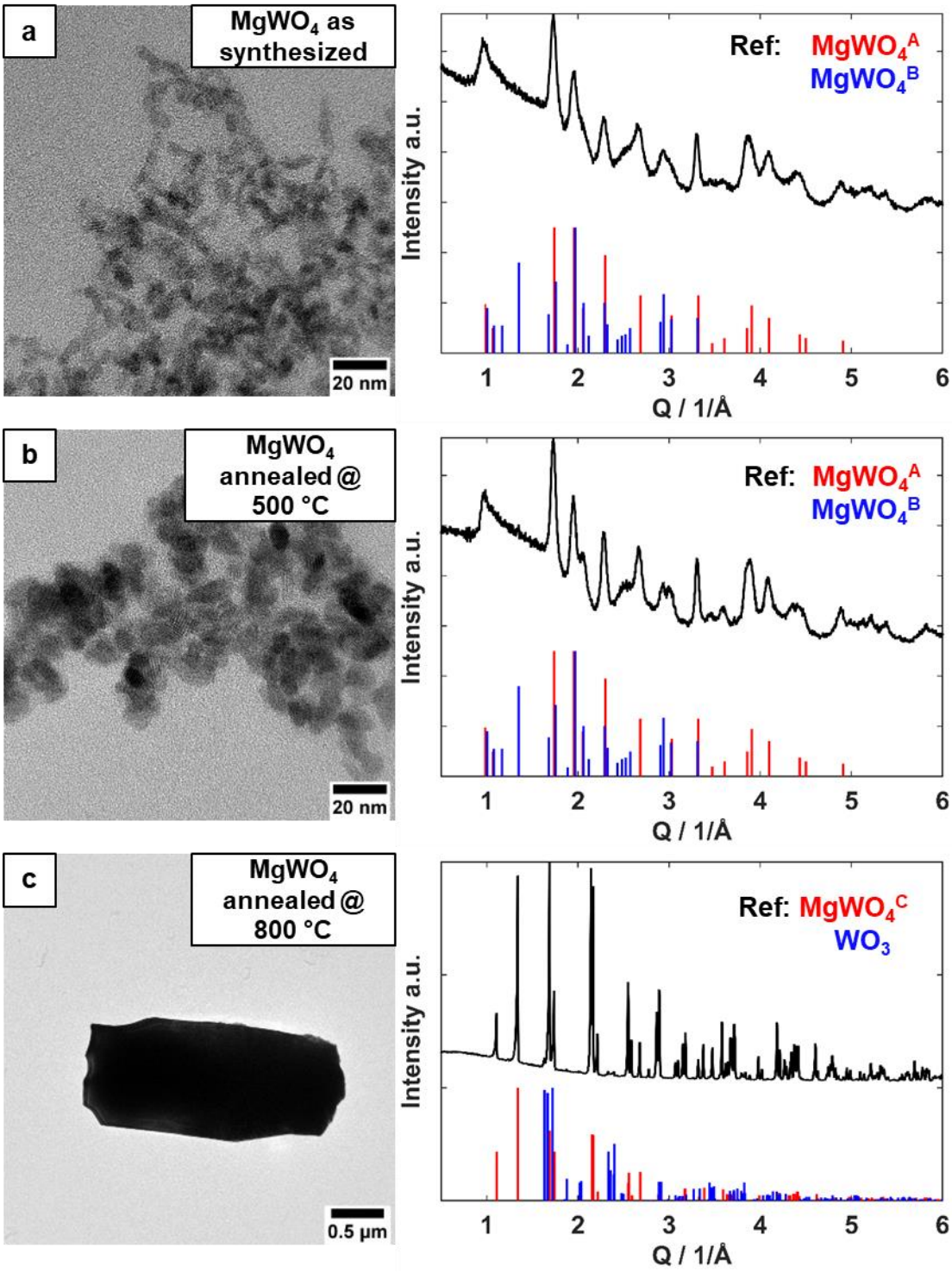

Figure 4.4. TEM images (left) and PXRD patterns (right) of $MgWO_4$ NCs synthesized with $Mg(acac)_2*2H_2O$ and HR of 2.5 K/min. a) as synthesized, b) annealed at 500 °C for 5 h and c) annealed at 800 °C for 5 h. References: $MgWO_4$ (triclinic, PDF, Entry No.: 00-045-0412), $MgWO_4$ (tetragonal, PDF, Entry No.: 00-052-0390), $MgWO_4$ (monoclinic, space group $P2/c$ (13), COD no. 99-501-2719) and WO_3 (monoclinic, space group $P2/n$ (14), COD no. 99-500-3824).

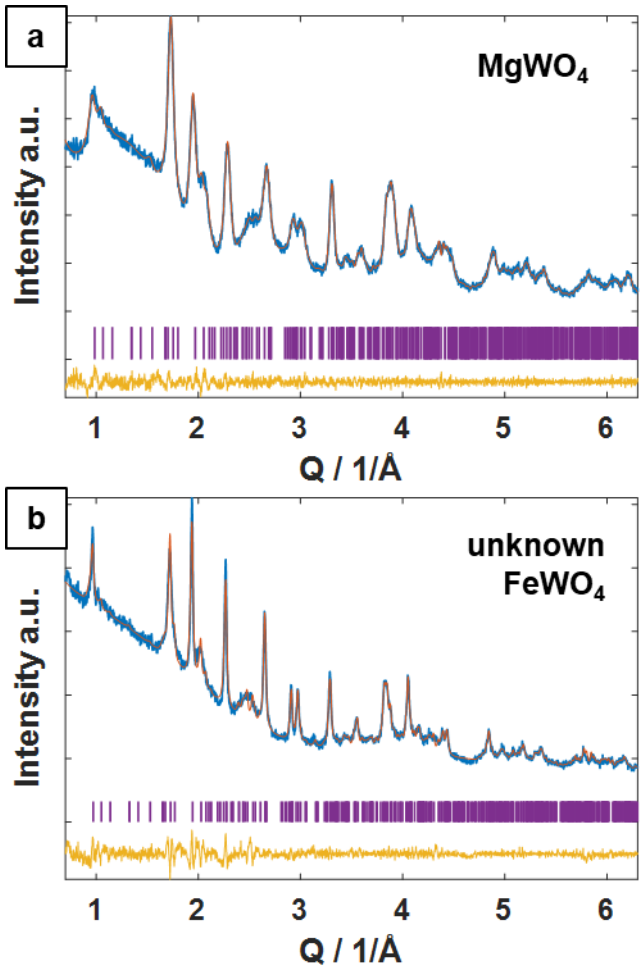

Figure 4.5. Pawley refinements based triclinic (anorthic) space group *P*1 of a) $MgWO_4$ NCs annealed at 500 °C with fit parameters a=5.621(10) Å, b= 6.575(7) Å, c=8.829(11) Å, α=123.0(0) °, β=112.8(1) °, γ=101.7(1) °, rwp=2.41, goodness of fit=0.99, crystallite size=9.6(2) nm and b) unknown $FeWO_4$ synthesized using $Fe(oleate)_3$ with fit parameters a=5.713(3) Å, b=6.661(2) Å, c=8.960(3) Å, α=123.0(0) °, β=113.1(0) °, γ=101.4(0) °, rwp=3.41, goodness of fit =1.43, crystallite size =28.1(7) nm.

4.4 Conclusions

We present that iron impurities form oleic acid stored in a steel canister are significantly influencing the growth of WO_{3-x} NRs (synthesized) in oleic acid and oleylamine solvent mixtures. We were able to artificially reproduce this effect by using iron oleate as an additive. We found ferberite $FeWO_4$ NCs forming as byproduct for higher iron concentration and were able to synthesize ferberite NCs without WO_{3-x} impurities applying a tungsten to iron ratio of 1:1. We determined that slower heating rates increases the crystallinity of the NCs. Upon changing the solvent ratio, we observed significantly increasing particle sizes in case of excess oleic acid and decreasing particle sizes in case of excess oleylamine. When changing the iron precursor to $Fe(acac)_3$, we found evidence of an unknown, not reported structure forming apart from ferberite. Changing the solvents from the oleic acid/oleylamine couple to oleyl oleamide, we found the presumably unknown phase to be the predominant crystalline

product. Using a mixture of oleyl oleamide and iron oleate precursor yielded the same new structure with significantly better resolved powder diffraction patterns. However, we cannot eliminate the possibility of amorphous byproducts. As a potential reference, we found similar metastable $MgWO_4$ reflex profiles described with triclinic or tetragonal models. However, as no structural descriptions are available, we were not able to utilize these models for further describing the new $FeWO_4$ structure. Mössbauer spectroscopy revealed the presence of Fe(II) and Fe(III) in both, ferberite-like and the unknown FeWO4 NCs. The Fe(II) profile of ferberite matches the one presented in literature, whereas the new structure shows an unknown Mössbauer profile.

We were able to synthesize $MgWO_4$ with the same powder diffraction profile as the unknown $FeWO_4$ and similar to structures reported in literature. These crystals were stable up to an annealing temperature of 500 °C and undergo phase transformation towards thermodynamically stable $MgWO_4$ (huanzalait structure, similar to ferberite) at 800 °C. We performed Pawley refinements using the triclinic structural model and obtained well fitted profiles for metastable $MgWO_4$ and new $FeWO_4$ based on the description of triclinic parameters found for $MgWO_4$.

Ongoing research involves more detailed analysis of the unknown structures for both $FeWO_4$ and $MgWO_4$ nanocrystals using electron diffraction methods such as automated electron diffraction tomography. Based on those measurements, a first structural model can be established and used to refine the X-ray powder diffraction data. Additionally, the composition of both unknown structures could be further evaluated using X-ray photoelectron spectroscopy or electron dispersive spectroscopy. Additional purification of the unknown $FeWO_4$ NCs might be another option, e.g. by washing in water to remove soluble amorphous impurities.

4.5 Experimental section

Materials. All chemicals were used as received without further purification. Oleic acid (90 %, technical grade), potassium oleate (technical, 87 % fatty acid) and magnesium acetylacetonate dihydrate (98 %) were bought from Sigma-Aldrich, oleylamine (>50 %, technical grade) was purchased from TCI, ammonium metatungstate hydrate (AMT, >90 % WO_3 basis) was bought from Carl Roth. Iron(III)chloride hexahydrate (98 %) was purchased from abcr, Iron(III)acetylacetonate (>99 %) from Acros.

Synthesis of Iron Oleate. Iron oleate was synthesized using an adopted route according to ref. [50] using potassium oleate instead of sodium oleate.

Synthesis of Oleyl Oleamide. Oleyl oleamide was synthesized according to ref. [18].

Synthesis of Iron/Magnesium Tungstate Nanocrystals. Iron and magnesium tungstate nanocrystals were synthesized utilizing the general experimental procedure described in ref. [18], by addition of varying

amounts of iron oleate, 1.43 mmol $Fe(acac)_3$ or $Mg(acac)_2$ * $2H_2O$. Variations for heating rate and solvents are described in the regarding sections in the results and discussion section.

4.5.1 Characterization

Transmission Electron Microscopy (TEM). For TEM imaging, one drop of a highly diluted solution of nanocrystals (~0.1 mg/mL in chloroform) was put onto a carbon-coated copper grid. Images were acquired using a FEI Tecnai G2 Spirit transmission electron microscope operating at 120 kV, equipped with a Gatan US1000 CCD camera. For further processing the program ImageJ was used. Average sizes are based on 40+ NCs/NRs measured with a rectangular/ellipsoid selection. Data procession was done with Matlab 2018b.

Powder X-Ray Diffraction (PXRD). PXRD patterns were measured on a STOE Standi P using Mo Kα_1 radiation (λ = 0.7093 Å) and a Dectris Mythen 1k detector. The diffractograms were analyzed using the software Match!3 and plotted using Matlab2018b. All references were taken from either the Crystallography Open Database (COD) or the International Centre for Diffraction Data (ICDD) PDF database. Rietveld[62] and Pawley[63] refinements were performed using Topas Academic V6. Reflection profiles were fitted to the fundamental parameter approach[64,65] applying a correction for anisotropic crystallite morphologies as described in ref [66] and [18].

Mössbauer spectroscopy. ^{57}Fe Mössbauer spectra of samples dispersed in paraffine (m.p. 42-44 °C) were recorded with a conventional constant acceleration Mössbauer-spectrometer in transmission geometry with a ^{57}Co source embedded in a Rh-matrix. Isomer shifts are given with respect to α-Fe foil, which was also used for calibration of the spectrometer. Spectra were simulated / fit to experimental data using the Recoil[67] software package.

Recoil − Mössbauer spectral analysis software for Windows, K. Lagarec and D.G. Rancourt, Department of Physics, University of Ottawa, Ottawa, ON, Canada, 1998, version 1.0, pp. 43.

4.6 References

1 A. Magneli, *Pure Appl. Chem.*, 1978, **50**, 1261–1271.

2 Y. Le Page and P. Strobel, *J. Solid State Chem.*, 1982, **43**, 314–319.

3 M. Joos, G. Cerretti, I. Veremchuk, P. Hofmann, H. Frerichs, D. H. Anjum, T. Reich, I. Lieberwirth, M. Panthöfer, W. G. Zeier and W. Tremel, *Inorg. Chem.*, 2018, **57**, 1259–1268.

4 K. Viswanathan, K. Brandt and E. Salje, *J. Solid State Chem.*, 1981, **36**, 45–51.

5 L. Pirker, B. Višić, S. D. Škapin, G. DraŽić, J. Kovač and M. Remškar, *Nanoscale*, 2020, **12**, 15102–15114.

6 M. A. Lange, Y. Krysiak, J. Hartmann, G. Dewald, G. Cerretti, M. N. Tahir, M. Panthöfer, B. Barton, T. Reich, W. G. Zeier, M. Mondeshki, U. Kolb and W. Tremel, *Adv. Funct. Mater.*, 2020, **30**, 1909051.

7 Y. F. Li, N. Soheilnia, M. Greiner, U. Ulmer, T. Wood, A. A. Jelle, Y. Dong, A. P. Yin Wong, J. Jia and G. A. Ozin, *ACS Appl. Mater. Inter.*, 2019, **11**, 5610–5615.

8 T. Zheng, W. Sang, Z. He, Q. Wei, B. Chen, H. Li, C. Cao, R. Huang, X. Yan, B. Pan, S. Zhou and J. Zeng, *Nano Lett.*, 2017, **17**, 7968–7973.

9 G. Cui, W. Wang, M. Ma, J. Xie, X. Shi, N. Deng, J. Xin and B. Tang, *Nano Lett.*, 2015, **15**, 7199–7203.

10 S.-M. Jung, S.-W. Yun, J.-H. Kim, S.-H. You, J. Park, S. Lee, S. H. Chang, S. C. Chae, S. H. Joo, Y. Jung, J. Lee, J. Son, J. Snyder, V. Stamenkovic, N. M. Markovic and Y.-T. Kim, *Nat. Catal.*, 2020, **3**, 639–648.

11 R. Dören, J. Hartmann, B. Leibauer, M. Panthöfer, M. Mondeshki and W. Tremel, *Dalton Trans.*, 2021, **50**, 14027–14037.

12 K. J. Griffith, K. M. Wiaderek, G. Cibin, L. E. Marbella and C. P. Grey, *Nature*, 2018, **559**, 556–563.

13 G. Barim, P. Cottingham, S. Zhou, B. C. Melot and R. L. Brutchey, *ACS Appl. Mater. Inter.*, 2017, **9**, 10813–10819.

14 W. Cheng, Y. Ju, P. Payamyar, D. Primc, J. Rao, C. Willa, D. Koziej and M. Niederberger, *Angew. Chem. Int. Ed.*, 2015, **54**, 340–344.

15 Y. Liang, Y. Yang, C. Zou, K. Xu, X. Luo, T. Luo, J. Li, Q. Yang, P. Shi and C. Yuan, *J. Alloys Compd.*, 2019, **783**, 848–854.

16 A. Yella, M. N. Tahir, S. Meuer, R. Zentel, R. Berger, M. Panthöfer and W. Tremel, *J. Am. Chem. Soc.*, 2009, **131**, 17566–17575.

17 K. Manthiram and A. P. Alivisatos, *J. Am. Chem. Soc.*, 2012, **134**, 3995–3998.

18 R. Dören, B. Leibauer, M. A. Lange, E. Schechtel, L. Prädel, M. Panthöfer, M. Mondeshki and W. Tremel, *Nanoscale*, 2021, **13**, 8146–8162.

19 A. Rothschild, J. Sloan and R. Tenne, *J. Am. Chem. Soc.*, 2000, **122**, 5169–5179.

20 G. Duan, L. Chen, Z. Jing, P. de Luna, L. Wen, L. Zhang, L. Zhao, J. Xu, Z. Li, Z. Yang and R. Zhou, *Chem. Res. Toxicol.*, 2019, **32**, 1357–1366.

21 M. Bourdin, M. Gaudon, F. Weill, M. Duttine, M. Gayot, Y. Messaddeq and T. Cardinal, *Nanomaterials*, 2019, **9**, 1–13.

22 J. Polleux, N. Pinna, M. Antonietti and M. Niederberger, *J. Am. Chem. Soc.*, 2005, **127**, 15595–15601.

23 M. Niederberger, *Acc. Chem. Res.*, 2007, **40**, 793–800.

24 M. S. Whittingham, *Curr. Opin. Solid State Mater. Sci.*, 1996, **1**, 227–232.

25 A. S. Cherevan, S. P. Nandan, I. Roger, R. Liu, C. Streb and D. Eder, *Adv. Sci.*, 2020, **7**, 1903511.

26 M. T. Pope and A. Müller, *Angew. Chem. Int. Ed.*, 1991, **30**, 34–48.

27 M. Juelsholt, T. Lindahl Christiansen and K. M. Ø. Jensen, *J. Phys. Chem. C*, 2019, **123**, 5110–5119.

28 D. Saha, K. M. Ø. Jensen, C. Tyrsted, E. D. Bøjesen, A. H. Mamakhel, A.-C. Dippel, M. Christensen and B. B. Iversen, *Angew. Chem. Int. Ed.*, 2014, **53**, 3667–3670.

29 O. Aalling-Frederiksen, M. Juelsholt, A. S. Anker and K. M. Ø. Jensen, *Nanoscale*, 2021, **13**, 8087–8097.

30 R. E. Ruther, B. M. Baker, J.-H. Son, W. H. Casey and M. Nyman, *Inorg. Chem.*, 2014, **53**, 4234–4242.

31 F. C. Meldrum and H. Cölfen, *Chem. Rev.*, 2008, **108**, 4332–4432.

32 M. Niederberger and H. Cölfen, *Phys. Chem. Chem. Phys.*, 2006, **8**, 3271–3287.

33 R. L. Penn and J. F. Banfield, *Science*, 1998, **281**, 969–971.

34 R. Penn and J. F. Banfield, *Geochim. Cosmochim. Acta*, 1999, **63**, 1549–1557.

35 M. A. Boles, D. Ling, T. Hyeon and D. V. Talapin, *Nat. Mater.*, 2016, **15**, 141–153.

36 T. D. Schladt, K. Schneider, H. Schild and W. Tremel, *Dalton Trans.*, 2011, **40**, 6315–6343.

37 L. M. Liz-Marzán, C. R. Kagan and J. E. Millstone, *ACS Nano*, 2020, **14**, 6359–6361.

38 S. Mülhopt, S. Diabaté, M. Dilger, C. Adelhelm, C. Anderlohr, T. Bergfeldt, J. La Gómez de Torre, Y. Jiang, E. Valsami-Jones, D. Langevin, I. Lynch, E. Mahon, I. Nelissen, J. Piella, V. Puntes, S. Ray, R. Schneider, T. Wilkins, C. Weiss and H.-R. Paur, *Nanomaterials*, 2018, **8**.

39 H. Cid-Dresdner and C. Escobar, *Z. Kristallogr. – Cryst. Mater.*, 1968, **127**, 61–72.

40 H. A. Obermayer, H. Dachs and H. Schröcke, *Solid State Com.*, 1973, **12**, 779–784.

41 M. Almeida, L. S. Cavalcante, C. Morilla-Santos, P. L. Filho, A. Beltrán, J. Andrés, L. Gracia and E. Longo, *Mater. Charact.*, 2012, **73**, 124–129.

42 S. M. Abdelbasir, A. M. Elseman, F. A. Harraz, Y. M. Z. Ahmed, S. M. El-Sheikh and M. M. Rashad, *New J. Chem.*, 2021, **45**, 3150–3159.

43 A. Moorthy, V. R. Bellarmin, B. Kumaran and M. E. R. Saravanan, *Inorg. Nano-Met. Chem.*, 2020, **50**, 1012–1016.

44 B. Jansi Rani, G. Ravi, R. Yuvakkumar, M. Praveenkumar, S. Ravichandran, P. Muthu Mareeswaran and S. I. Hong, *ACS Omega*, 2019, **4**, 5241–5253.

45 Y.-X. Zhou, H.-B. Yao, Q. Zhang, J.-Y. Gong, S.-J. Liu and S.-H. Yu, *Inorg. Chem.*, 2009, **48**, 1082–1090.

46 X. Deng, G. Xie, X. Liu, Y. Wu, L. Qin and Q. Li, *Mater. Res. Express*, 2017, **4**, 75008.

47 R. Bhosale, S. Jain, C. P. Vinod, S. Kumar and S. Ogale, *ACS Appl. Mater. Inter.*, 2019, **11**, 6174–6183.

48 W. Wang, L. Hu, J. Ge, Z. Hu, H. Sun, H. Sun, H. Zhang, H. Zhu and S. Jiao, *Chem. Mater.*, 2014, **26**, 3721–3730.

49 T. Misawa, K. Hashimoto and S. Shimodaira, *Corros. Sci.*, 1974, **14**, 131–149.

50 J. Park, K. An, Y. Hwang, J.-G. Park, H.-J. Noh, J.-Y. Kim, J.-H. Park, N.-M. Hwang and T. Hyeon, *Nat. Mater.*, 2004, **3**, 891–895.

51 R. G. Pearson, *Inorg. Chem.*, 1988, **27**, 734–740.

52 R. G. Pearson, *Acc. Chem. Res.*, 1993, **26**, 250–255.

53 E. Schechtel, R. Dören, H. Frerichs, M. Panthöfer, M. Mondeshki and W. Tremel, *Langmuir*, 2019, **35**, 12518–12531.

54 J. Günter and M. Amberg, *Solid State Ion.*, 1989, **32-33**, 141–146.

55 A. Borshch, Dorokhov YG. and Golub AM., *Ukr. Khem. Zh.*, 1973, 724–726.

56 R. Guillen, J. R. Regnard and J. Amoss, *Phys. Chem. Miner.*, 1982, **8**, 83–86.

57 R. Caruba, A. Baumer, R. Guillén and J.-R. Régnard, *Bull. Minéral.*, 1982, **105**, 246–252.

58 M. Gancheva, A. Naydenov, R. Iordanova, D. Nihtianova and P. Stefanov, *J. Mater. Sci.*, 2015, **50**, 3447–3456.

59 J. Meng, T. Chen, X. Wei, J. Li and Z. Zhang, *RSC Adv.*, 2019, **9**, 2567–2571.

60 S. Wang, H. Gao, C. Chen, Q. Li, C. Li, Y. Wei and L. Fang, *J. Mater. Sci.: Mater. Electron.*, 2019, **30**, 15744–15753.

61 S. Wannapop, T. Thongtem and S. Thongtem, *Appl. Surf. Sci.*, 2012, **258**, 4971–4976.

62 H. M. Rietveld, *J. Appl. Crystallogr.*, 1969, **2**, 65–71.

63 G. S. Pawley, *J. Appl. Crystallogr.*, 1980, **13**, 630–633.

64 R. W. Cheary and A. Coelho, *J. Appl. Crystallogr.*, 1992, **25**, 109–121.

65 A. A. Coelho, *J. Appl. Crystallogr.*, 2018, **51**, 210–218.

66 D. Gömpel, M. N. Tahir, M. Panthöfer, E. Mugnaioli, R. Brandscheid, U. Kolb and W. Tremel, *J. Mater. Chem. A*, 2014, **2**, 8033–8040.

67 K. Lagarec and D. G. Rancourt, *Nucl. Instrum. Methods Phys. Res. B*, 1997, **129**, 266–280.

The following chapter 5 is to be submitted in: Small, 2021.

Authorship Contributions Chapter 5

Conception and design of the study:

[redacted]

Preparation of samples and acquisition of data:

[redacted] – preparation of nanocrystals

[redacted] – biologic evaluations

[redacted] – halooperoxidase assays

[redacted] – leaching assay

[redacted] – TEM measurements

[redacted] – UV-Vis-NIR absorption and reflection spectroscopy

[redacted] – PXRD measurements

[redacted] – XPS measurements

[redacted] – ζ-potential measurements

Analysis and interpretation of data:

[redacted] – PXRD diffraction and refinements

[redacted] – TEM images, XPS spectroscopy, ζ-potential

[redacted] – halooperoxidase data

[redacted] – biological data

[redacted] – UV-Vis-NIR absorption and reflection spectroscopy

Drafting of the manuscript:

[redacted]

Revising the manuscript critically for important intellectual content:

[redacted]

Preparation of figures

[redacted]

5. Cesium tungsten bronze nanocrystals with enzyme-like activity prevent the formation of bacterial biofilms and inhibit fungal colonization

5.1 Abstract

A selective synthesis of hexagonal (h-Cs_xWO_3) and cubic pyrochlore-type (c-Cs_xWO_3) tungsten bronze nanocrystals was devised by tuning the oleic acid (OAc)/oleylamine (OAm) surfactant ratio. OAm excess led to subsequent formation of c-Cs_xWO_3. For higher Cs contents ($0.3 < x < 0.6$) pure c-$Cs_{0.6}WO_3$ nanocrystals were formed. h-Cs_xWO_3, c-Cs_xWO_3 and mixtures of both phases showed strong absorption in the red /infrared spectral range, associated with localized surface plasmons. c-Cs_xWO_3 nanocrystals and Magneli-type WO_{3-x} nanorods are nanoparticle enzyme mimics which prevent the formation of *P. aeruginosa* biofilms by virtue of their haloperoxidase-like activity. WO_{3-x} nanorods and c-$Cs_{0.6}WO_3$ nanocrystals showed a biofilm reduction of 35 %, WO_{3-x} nanorods of 25 %. Reporter assays with the biosensor *A. tumefaciens* A136 showed a quorum quenching activity *via* 3-oxo-C12 lactones. Furthermore, c-$Cs_{0.6}WO_3$ nanocrystals and WO_{3-x} nanorods reduced the growth of the fungus *F. graminearum* by up to 54 %. WO_{3-x} nanorods showed a strong reduction of the mycelium growth, thereby preventing spore formation. The surface plasmon resonance properties of c-Cs_xWO_3/ h-Cs_xWO_3 phase mixtures reduced the growth of the clinically relevant bacteria *S. aureus* and *P. aeruginosa* and of the marine bacterium *P. gallaeciensis* under near-infrared light up to 35 %.

5.2 Introduction

The development of antimicrobial agents is one of the most significant advances in medicine. However, the excessive and sometimes improper use of antibiotics has led to more and more bacteria becoming resistant to antibiotics.[1–4] The increase in antimicrobial resistance (AMR) to important antibiotic groups and the rise in multi-resistant germs are particularly worrying. Single and multidrug-resistant (MDR) microbes are responsible for approximately 700,000 deaths annually worldwide.[4] The World Health Organization (WHO) has designated several drug-resistant pathogenic bacterial strains, e.g., methicillin-resistant *Staphylococcus aureus* (MRSA), that are prevalent in global healthcare. The problem of increasing antibiotic resistance affects human medicine as well as veterinary medicine, agriculture and the environmental sector, and resistant fungal strains, e.g., *Candida auris*, are also becoming increasingly resistant to all available antifungal treatments.[2] Without the development of new antimicrobial agents, WHO predicts that about 10 million people will die annually from previously treatable infections by mid-century.[4]

Although efforts have been made to combat these infections,[5–7] only two new classes of antibiotics, none of which were effective against Gram-negative bacteria, have received international approval in the last 20 years.[1] This has spurred research into the development of alternative antimicrobial nanomaterials. Alternative strategies to inhibit bacterial colonization is to prevent of bacterial adhesion to surfaces. That may be achieved by coating surfaces with antimicrobial agents, which often suffer from serious limitaions.[8] Ag nanoparticles were one of the first nanomaterials to demonstrate high antipathogenic activity.[5,9]

A new and environmentally benign solution is inspired by nature. Bacteria do not live isolated, but in colonies with other bacteria. A fully developed, mature biofilm is very difficult to eradicate and extremely resistant against antimicrobial agents. Therefore, microorganism communities are responsible for the majority of bacterial infections.[10] The bacteria communicate with each other *via* chemical processes and can thus "talk to each other" in the group and jointly develop collective properties such as bioluminescence, virulence, or biofilm formation. They communicate *via* small diffusible molecules in a process known as "quorum sensing" (QS). Gram-negative bacteria communicate *via* acylated homoserine lactones (AHL).[11]

Inactivation of the signaling molecules disrupts microbial communication. This is called quorum quenching (QQ) and can be achieved by inhibiting the production of auto-inducers, their detection by receptors, or their degradation.[12] Some bacterial enzymes can interfere with QS through the degradation or chemical modification of these signaling molecules autoinducers. Chemical modification *via* oxidative halogenation relies on haloperoxidases (**HPO**s), a group of metal-depending or flavoenzymes that use photogenerated H_2O_2 and halides (Cl^-, Br^-, I^-) to form hypohalous acids HOX (X = Cl, Br, I) as short-lived and powerful halogenating and oxidizing agents that halogenate a wide range of

substrates.[13–16] A number of metal complexes,[17] V_2O_5,[18] and CeO_2[19] nanoparticles (NPs) can mimic the catalytic activity of HPOs under ambient conditions.[20] Likewise, WO_4^{2-} tungstate ions intercalated in layered double hydroxides[21] catalyze the formation of hypohalous species and the halogenation of organic substrates *via* W-O_2-peroxo intermediates.[22] Such molecular or nanoparticle enzyme mimics[23,24] have a sustained and long-term activity at ambient conditions and do not suffer from inherent shortcomings such as high cost and poor stability of natural enzymes.

WO_3, the oxide corresponding to WO_4^{2-}, has a band gap of 2.6–2.8 eV, and its redox activity makes WO_3 a reactive photocatalysts.[25] Attempts have been made to use WO_3 as antimicrobial agent for health care applications. Reactive oxygen species (ROS, such as $^{\bullet}O_2^-$, or $^{\bullet}OH$), generated by irradiation WO_3 under ultraviolet (UV) or visible (Vis) light, were proposed for inactivating microorganisms *via* oxidative stress inflicted on the cell membrane[26,27] and for the photodegradation of microorganisms over WO_3 particles[28] or coatings.[29] Light absorption in the visible region was achieved with WO_3*H_2O/Ag/AgBr hybrid particles,[30] and Fe_3O_4/WO_3 immobilized in exfoliated montmorillonite showed antibacterial properties against *E.coli* and *Streptococcus aureus* (*S. aureus*) under NIR laser irradiation.[31]

Tungsten and molybdenum oxide (WO_3 and MoO_3) are among the most acidic transition metal oxides.[25] Thus, surface (Brønsted) acidity under humid conditions has been proposed as an alternative mechanism for the antimicrobial activity,[32] which has been investigated intensively for MoO_3.[33] The local pH drop is the result of a H_3O^+ release concurrent with the formation of MoO_4^{2-} anions. WO_{3-x} has an even higher acidity than MoO_3 and V_2O_5.[34] The presence of tungsten in pseudo-binary $Mo_{1-x}W_xO_3$ is crucial to decrease the solubility of the oxide, meaning that the solubility of WO_3 is significantly lower than for MO_3 under neutral conditions.[35] Its low solubility and mechanical stability make porous hydrophilic WO_3 a durable coating for steel surfaces. Functionalization with perfluoroalkyl-bearing phosphate ligands leads to non-toxic bacteria-repellent surfaces, which are, however, essentially due to the hydrophobic properties of the perfluorinated lubricant.[36]

The screening of a thin film library of molybdenum−tungsten oxides revealed a compositionally dependent antimicrobial activity.[37] This indicates that different acidic[38] and (photo-)electronic[39,40] properties of Magneli-type of tungsten oxides W_nO_{3n-1} or W_nO_{3n-2}[41–43] and tungsten bronzes A_xWO_3 ($0 < x < 1$)[44] may lead to distinct catalytic [45–47] and also different antibacterial properties. We show that, due to their haloperoxidase-like properties, nanocrystalline A_xWO_3 tungsten bronzes (A = K, Rb, Cs) possess antibacterial behavior of against the antibiotic-resistant bacterium *Pseudomonas aeruginosa* (*P. aeruginosa*). Specifically, Magneli-type WO_{3-x} nanorods and cubic pyrochlore cesium tungsten bronze exhibit fungicidal behavior against *Fusarium graminearum* (*F. graminearum*), where WO_{3-x} nanorods strongly suppress mycelial formation of *F. graminearum*. A_xWO_3 nanocrystals (A = Rb, Cs) were prepared by wet chemistry. In addition to the standard hexagonal phase that was obtained in pure form for Cs_xWO_3, a cubic pyrochlore phase was formed for higher Rb and Cs contents. Depending on the

choice of synthetic conditions, hexagonal and/or cubic Cs_xWO_3 nanocrystals with different sizes and morphologies and localized surface plasmon resonance in the range of 800-1500 nm could be prepared.

5.3 Results and discussion

5.3.1 Synthesis of hexagonal and pyrochlore-type alkali metal tungsten bronzes

The synthesis of hexagonal alkali metal tungsten bronze nanocrystals (NCs) was elaborated following ref. [38] starting from 0.3 equivalents of the respective alkali metal carbonate and ammonium metatungstate (AMT) using oleic acid (OAc) and oleylamine (OAm) as surfactants. The alkali metal component added during the reaction resulted in a change in particle morphology and crystal phase compared to "standard" hexagonal ammonium tungsten bronzes (h-$(NH_4)_{0.2}WO_3$, h-ATB).[38] The clearest results were obtained for Cs^+. This indicates that the structure of the hexagonal bronze is stabilized by cations in the channels, since Cs^+ has the largest cation radius in the series NH_4^+, K^+, Rb^+, and Cs^+. Using optimized conditions for the h-ATB synthesis[38] (0.24 mmol AMT, 20:20 mmol OAc:OAm, 25 K/min (75 to 350 °C), 30 min, 250 rpm stirring speed) with 0.43 mmol (0.3 eq with respect to W) of Cs_2CO_3, we obtained a mixture of rectangular and hexagonal disk like nanocrystals with average crystallite size of 20 to 40 nm (Figure S8.4.1b) without WO_{3-x} nanorod (NR) impurities, as observed for h-ATB under similar conditions. The powder X-ray diffraction (PXRD) pattern (Figure S8.4.1a) reveals the formation of the hexagonal cesium-tungsten bronze (**h-$Cs_{0.3}WO_3$**). For an OAc excess (OAc:OAm 22.5:17.5 mmol, Figure S8.4.1a), wo observed no changes of the particles. For an OAm excess (OAc:OAm 17.5:22.5 mmol), the size distribution of the nanocrystals was broader and disk like shapes were less pronounced (Figure S8.4.1c). A mixture of hexagonal and a cubic pyrochlore type cesium tungsten bronze was obtained (~90:10 %; m-$Cs_{0.3}WO_3$). However, the dispersibility in organic solvents (e.g., $CHCl_3$) was significantly better.

Since the synthesis of Cs_xWO_3 is less affected by surface effects than the synthesis of the ammonium tungsten bronzes due of the Pearson hardness of A cations,[48] experiments with different heating rates and stirring speed showed no significant effect on the outcome of the synthesis. A reduction of heating rate led to a decreased crystallite size. Optimum conditions for the synthesis of h-$Cs_{0.3}WO_3$ were 20:20 mmol OAc:OAm and 5 K/min (Figure 5.1a). The crystallites had a size of approx. 20*30 nm and showed rectangular and hexagonal disk like morphologies. Mixed hexagonal/cubic m-$Cs_{0.3}WO_3$ NCs (Figure 5.1b) were synthesized with 17.5:22.5 mmol OAc:OAm and a heating rate of 2.5 K. Here, the NCs had a size of ~20 nm and showed a strong faceting with a partially tetrahedral shape. We performed a Rietveld refinement (Figure S8.4.7) for this sample using the hexagonal (h, $P6_3/mcm$) and cubic (c, $Fd\bar{3}m$) phases and found a composition with the ratio of ~62:38 % h:c. Similar results have been described in the literature without a compelling explanation.[49]

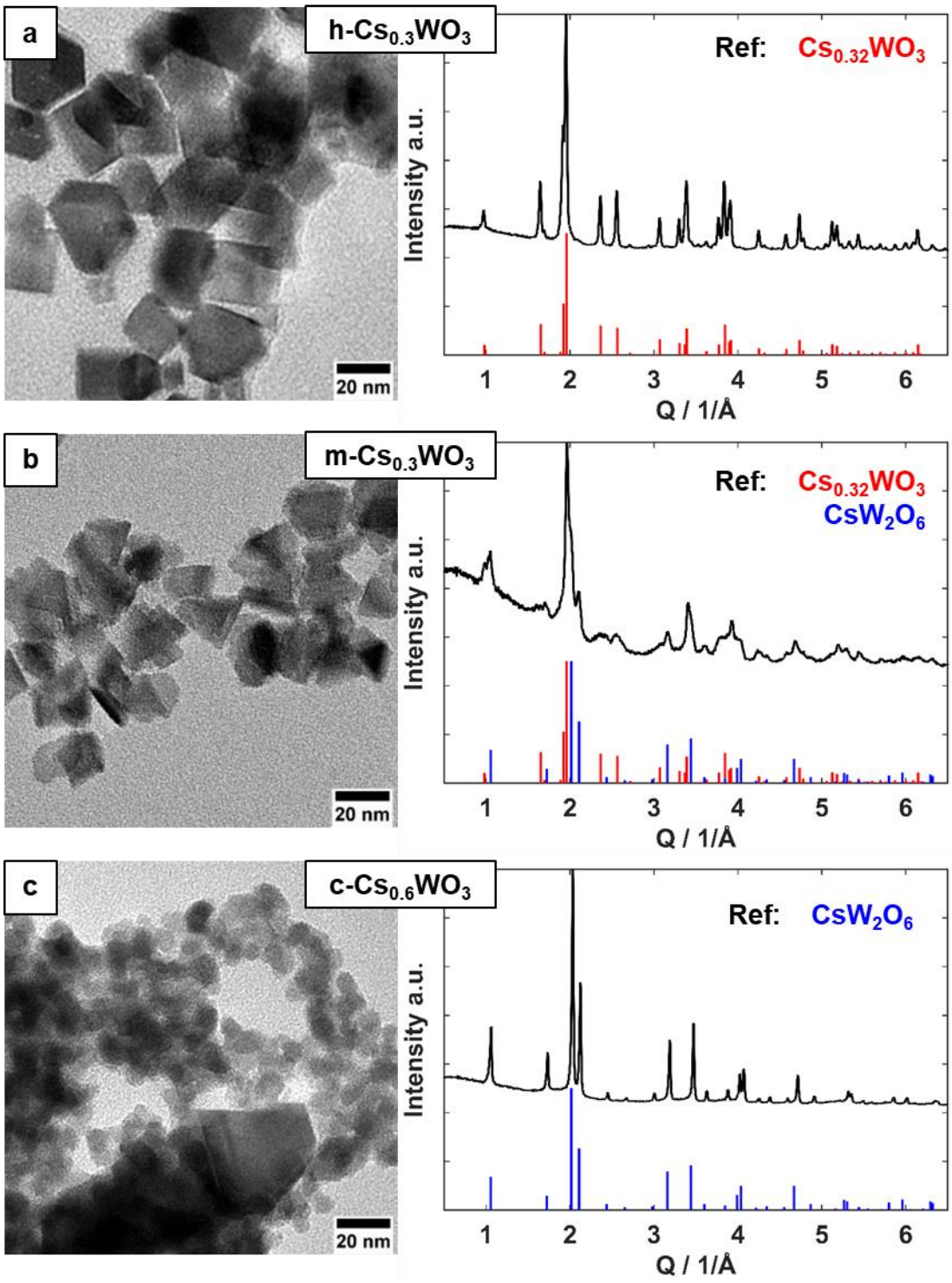

Figure 5.1. a) TEM image and PXRD pattern of hexagonal $Cs_{0.3}WO_3$ NCs synthesized with 20:20 mmol OAc:OAm and heating rate of 5 K/min, b) TEM image and PXRD pattern of mixed cubic/hexagonal $Cs_{0.3}WO_3$ NCs synthesized with 17.5:22.5 mmol OAc:OAm and heating rate of 2.5 K/min and c) TEM image and PXRD pattern of cubic $Cs_{0.6}WO_3$ NCs synthesized with 17.5:22.5 mmol OAc:OAm and heating rate of 5 K/min. PXRD references: $Cs_{0.32}WO_3$ (space group $P6_3/mcm$, ICSD no. 99-501-4972) and $CsW_{1.6}O_3$ (space group $Fd\bar{3}m$, ICSD no. 99-502-4816).

We performed syntheses with higher and lower OAm contents (19:21 and 15:25 mmol OAc:OAm, Figure S8.4.2) and found a ratio of hexagonal:cubic phase (h:c) of 89:11 and 43:57 %, respectively (Figure S8.4.6 and Figure S8.4.8). Crystal growth and phase formation of the pyrochlore-type cubic cesium-tungsten bronze are obviously related to the OAm content for a Cs:W ratio of 0.3:1, but also to the heating rate.

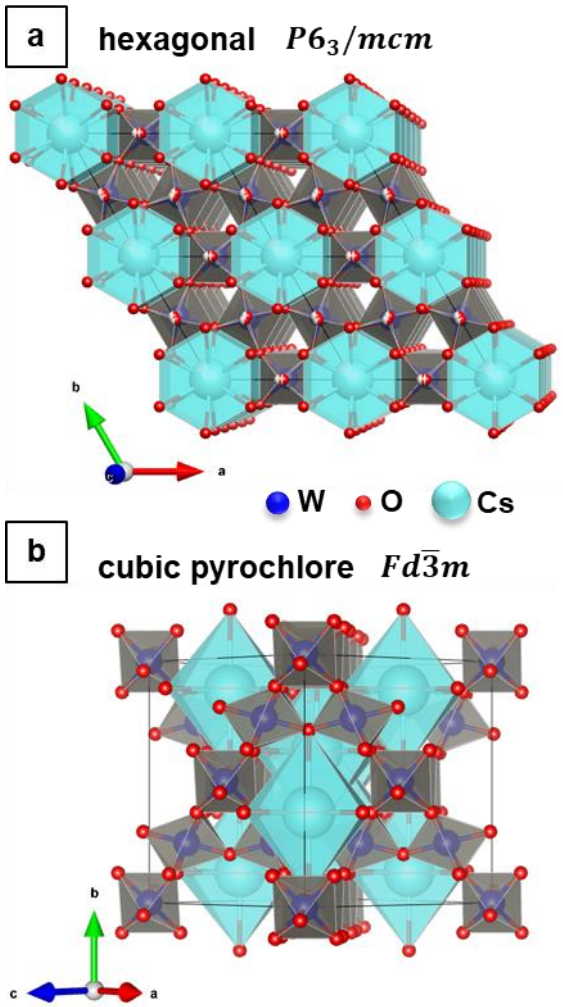

Figure 5.2. Crystal structures of a) hexagonal cesium tungsten bronzes ($P6_3/mcm$) and b) cubic pyrochlore-type tungsten bronze ($Fd\bar{3}m$) in polyhedral representations.

Single-phase pyrochlore type cubic cesium tungsten bronze NCs (c-$Cs_{0.6}WO_3$) were formed with 0.6 eq of Cs^+ for a OAc:OAm ratio of 17.5:22.5 mmol (Figure 5.1c). The nanocrystals were highly agglomerated. The individual nanocrystals had diameters of ~10 nm, and maximum diameters of ~30 nm. For different OAc:OAm ratios (20:20 and 23.5:17.5 mmol, Figure S8.4.3), we observed no significant change of the crystal phase.

Pyrochlore-type tungsten bronzes (WO_3*0.5 H_2O) were detected in an *in-situ* study as intermediates during the formation of h-ATB from AMT in pure OAm. The crystal diameters were smaller than those

of h-ATB.[50] We suggest that Cs^+ cations stabilize the pyrochlore-type cubic intermediate due to their cationic radius, resulting in smaller NCs with pyrochlore structure. The process strongly depends on the Cs:W ratio. We assume that for lower Cs^+ fractions, the surfactant OAm bound to the surface of the intermediates blocks the formation of the hexagonal phase. The formation of cubic tungsten bronzes from AMT and Cs_2CO_3 in OAm has been described before.[51]

Besides the cesium tungsten bronzes, the corresponding rubidium tungsten bronzes were prepared as well. For 0.3 eq of rubidium carbonate and standard conditions for h-ATB formation,[38] we obtained nanocrystals of the hexagonal rubidium-tungsten bronzes (h-$Rb_{0.3}WO_3$) that were smaller than those h-ATB (~50 nm) while they retained their rectangular morphology (Figure S8.4.9). When the heating rate was reduced to 2.5 K/min with an OAc:OAm ratio of 22.5:17.5 mmol, the crystal morphology changed to rectangular and hexagon-like disks. In contrast to cesium tungsten bronzes, we observed no formation of a cubic phase under these conditions. Using 0.6 eq of rubidium under otherwise identical conditions resulted in the formation of a mixed hexagonal and cubic pyrochlore-type rubidium-tungsten bronze (m-$Rb_{0.6}WO_3$). This further underlines the crucial impact of cesium on the stabilization of the cubic pyrochlore structure during the synthesis.

The alkali metal tungsten bronzes (A_xWO_3) are colored metallic solids whose optical properties can be attributed to localized surface plasmon resonances (LSPR) in the visible to near-infrared (Vis-NIR) part of the optical spectrum.[40,49] Figure 5.3a shows the optical spectra (diffuse reflection with $BaSO_4$ background) of the hexagonal and cubic bronzes shown in Figure 5.1, together with the spectra of WO_{3-x} NRs and h-ATB NCs. Figure 5.3b shows the respective spectra of samples after annealing at 300 °C. The diffuse reflectance (DR) mode was chosen due to the lack of solubility of different bronzes after removal of the surface capping agent after annealing. The alkali metal tungsten bronzes, WO_{3-x} NRs and h-ATB NCs show a strong absorption in the visible part of the spectrum. The absorption was lower after annealing at 300 °C. This is most pronounced for c-$Cs_{0.6}WO_3$ NCs. Figure S8.4.10a, c shows the DR spectra of as synthesized h-$Cs_{0.3}WO_3$ and c-$Cs_{0.6}WO_3$ NCs after synthesis and after annealing at 300 and 500 °C. h-$Cs_{0.3}WO_3$ showed a significant decay in absorption after annealing at 500 °C. The plasmon band for c-$Cs_{0.6}WO_3$ NCs is intrinsically lower and weakens after annealing at 300 °C.

The LSPR of tungsten oxide nanocrystals is associated with defects and therefore charge carrier concentration and partial reduction on the particle surface.[40] Therefore, we measured the XPS spectra of h-$Cs_{0.3}WO_3$ and c-$Cs_{0.6}WO_3$ NCs as synthesized and after annealing at 300 and 500 °C. The W 4f core levels are shown in Figure S8.4.12. No reduction of W^{6+} is observed in c-$Cs_{0.6}WO_3$ NCs. Therefore, the Cs^+ content of approx. 0.6 has to be saturated by excess oxygen (0.3 eq), resulting in an overall composition $Cs_{0.6}WO_{3.3}$. The presumed W^{5+} content in h-$Cs_{0.3}WO_3$ NCs is 36 %. As XPS is a surface method with a penetration depth of only ~2 nm,[52] we assume the surface to be slightly more reduced than the bulk. During annealing, the reduction level dropped to 21 % (300 °C) and ~1 % (500 °C), due to oxidation by atmospheric oxygen. As we observe a significant reduction of plasmonic absorption after

oxidation, we assume that the reduced charge carrier concentration due to less reduced W^{6+} is at least partially responsible for the decreasing LSPR.

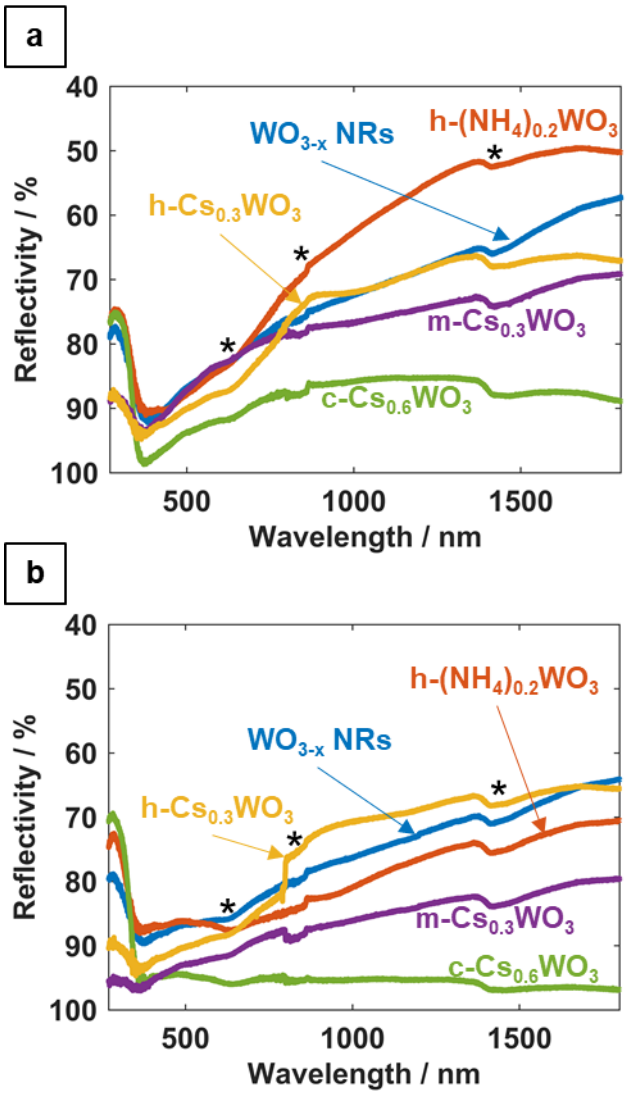

Figure 5.3. Diffuse reflectance spectra of WO_{3-x} NRs, h-ATB, m-$Cs_{0.3}WO_3$, m-$Cs_{0.3}WO_3$ and c-$Cs_{0.6}WO_3$ a) dried at 70 °C and b) annealed at 300 °C for 5 h in air. *Discontinuities are caused by the background of the $BaSO_4$ white standard after the grating change.

5.3.2 Haloperoxidase properties

The HPO activity of WO_{3-x} NRs was evaluated using a standard phenol red assay. In this test, the indicator phenol red (PR) is oxidized to tetrabromophenol blue (TBPB) with four equivalents of H_2O_2 and KBr in water by the catalytic action of tungsten oxides. The reaction kinetics were monitored by UV-Vis spectroscopy as the absorption maximum of phenol red at 434 nm shifts to 590 nm for TBPB upon oxidative bromination. The concentration *c* of TBPB is calculated according to the Lambert-Beer

law (Eq. 5.1) from the absorbance *A*, the molar attenuation coefficient ε of TBPB (72200 1/M*cm) and the path length of the cuvette *l* (1 cm).

$$c = \frac{A}{\varepsilon * l} \tag{5.1}$$

The kinetics was monitored over a 24-hour period. The maximum slope of the kinetics curve was fitted linearly to derive the maximum reaction rate. The results for WO_{3-x} NRs, h-$(NH_4)_{0.2}WO_3$ NCs and cesium tungsten bronzes are shown in Figure 5.4. All samples were annealed at 300 °C or 500 °C in air prior to the activity test to drive of surface ligands and to ensure clean surfaces. Table 5.1 compiles the results of the samples and the reference compounds Na_2WO_4*$2H_2O$ and AMT.

WO_{3-x} NRs annealed at 300 °C and c-$Cs_{0.6}WO_3$ annealed at 500 °C showed the highest activity with turnover rates of up to 0.045 and 0.098 µM/min respectively. h-ATB, h-$Cs_{0.3}WO_3$ and m-$Cs_{0.3}WO_3$ show significantly lower conversion rates. All bronzes except for c-$Cs_{0.6}WO_3$ NCs showed an initialization time of ~7 h before maximum conversion rate was reached. The much shorter initialization time (~20 min) for c-$Cs_{0.6}WO_3$ NCs indicates a higher HPO activity compared to WO_{3-x} NRs. Sodium tungstate was used as water soluble reference with a turnover rate of 0.039 µM/min and an initialization time of ~65 min. Sodium tungstate has been described as catalyst for oxidative halogenation reaction, and showed a reasonable HPO-like activity after ion exchange in double layered hydroxides.[21] The formation of surface tungsten peroxo-complexes is hindered for WO_{3-x} NRs in water.[47] This effect seems significantly less dominant for c-$Cs_{0.6}WO_3$ NCs. The ζ-potential of tungsten oxide nanocrystals did not deviate significantly from the value of -39(5) mV reported for WO_{3-x} and h-ATB.[38,47]

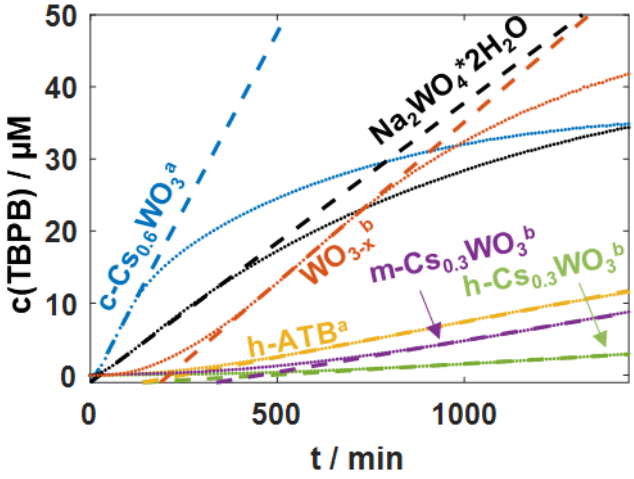

Figure 5.4. Evolution of TBPB concentration over the course of 24 h for WO_{3-x} NRs, h-$Cs_{0.3}WO_3$, m-$Cs_{0.3}WO_3$, c-$Cs_{0.6}WO_3$ and h-ATB NCs, as well as for soluble Na_2WO_4*$2H_2O$ reference.

Table 5.1. Turnover rates, maximum turnovers after 24 h and suitable fitting limits for different tungsten oxide bronzes and reference materials derived from HPO assays. Additional information is supplied in Table S8.4.1.

Sample	Turnover rate / µM*min^{-1}	Turnover 24 h / µM	Lower limit / min	Upper limit / min
c-$Cs_{0.6}WO_3$[a]	0.0978	34.90	50	130
WO_{3-x} NR[b]	0.0448	41.87	500	750
m-$Cs_{0.3}WO_3$[b]	0.0098	11.49	600	1400
h-$Cs_{0.3}WO_3$[b]	0.0030	2.97	800	1400
h-ATB[b]	0.0088	8.80	800	1400
WO_3 Ref	0.0078	7.60	1000	1400
AMT	0.0022	2.01	1000	1400
$Na_2WO_4*2H_2O$	0.0387	34.38	50	130

a: annealed in air at 500 °C (5 h), b: annealed in air at 300 °C (5 h).

5.3.3 Biological properties of tungsten oxide NRs and tungsten bronze NCs

Tungsten oxides inhibit formation of *P. aeruginosa* biofilms

Tungsten oxide bronzes were tested with *Pseudomonas aeruginosa* for their potential to inhibit bacterial biofilm formation and for their ability to interfere with bacterial quorum sensing. *P. aeruginosa*, a Gram-negative, drug-resistant soil bacterium is known for its unity and antibiotic resistance mechanisms. This opportunistic pathogen is known to contaminate drinking water distribution systems and causes a variety of human infections such as cystic fibrosis. *P. aeruginosa* is a potent biofilm producer and therefore widely used as an indicator strain.[53] For biofilm assays, the bacteria were grown in 96-well plates for 72 h in the presence of WO_{3-x} NRs (annealed at 300 °C) and c-$Cs_{0.6}WO_3$ NCs (annealed at 500 °C). $Na_2WO_4*2H_2O$ was used as positive control for soluble tungstates because of its reported HPO property.[21] The absence of any NC/tungstate served as negative control. Both, WO_{3-x} NRs and c-$Cs_{0.6}WO_3$ reduced biofilm formation significantly (Figure 5.5a).

While biofilm reduction with WO_{3-x} NRs was ~25 % c-$Cs_{0.6}WO_3$ NCs reduced biofilm formation by up to 35 %. To ensure that potentially existing antibiotic properties of the tungsten oxide bronze NCs did not compromise the results, biofilm formation was correlated to their respective growth. $Na_2WO_4*2H_2O$ showed less reduction of biofilm formation under similar conditions (10 %). This shows that molecularly dissolved tungstate anions are less active than tungsten oxide bronze NCs. Moreover, there was no significant reduction of bacterial growth, i.e., the toxicity of WO_4^{2-} anions is very low. Since both, WO_{3-x} NRs and c-$Cs_{0.6}WO_3$ NCs, showed high HPO activity, the inhibition of biofilm formation is likely due to the blocking of bacterial communication, i.e., quorum quenching.[12] *P. aeruginosa* biofilm formation, like other virulence factors, is regulated by cell-cell signaling (quorum sensing).[54] Therefore,

WO_{3-x} NRs and c-$Cs_{0.6}WO_3$ NCs can be expected to catalyze the modification of signaling molecules by oxidative halogenation. To gain further insight into quorum quenching activity, we used specific biosensors as readouts. For this purpose, the biosensor *A. tumefaciens* A136 was used. This specific reporter strain can detect external acyl homoserine lactones and produce the enzyme beta-galactosidase, which can be quantitatively measured with 5-bromo-4-chloro-3-indolyl-β-D-galactopyranoside (X-gal).[55] After hydrolytic cleavage by β-galactosidase, colorless X-gal yields galactose and 5-bromo-4-chloro-3-hydroxyindole, which dimerizes spontaneously and is oxidized subsequently to 5,5'-dibromo-4,4'-dichloro-indigo, an intensely blue product which can be determined calorimetrically as a test for the presence of active β-galactosidase. Bacterial communication in *P. aeruginosa* is managed by AHL´s such as 3-oxo-C12.[56] For the X-gal quantification assay, 3-oxo-C12 was added together with H_2O_2 and KBr to the tungsten bronzes to observe a possible modification of the signaling molecules. After 12 hours *A. tumefaciens* A136 and the colorimetric substance X-gal was added to the AHL´s. The effect of the tungsten bronzes on the signaling molecules is shown in Figure 5.5b. The WO_{3-x} NRs decrease the amount of signaling molecules by up to 25 %. Furthermore, the samples including c-$Cs_{0.6}WO_3$ showed a further reduction by up to 35 %. The bottom line is that c-$Cs_{0.6}WO_3$ reduces biofilm formation by interfering with quorum sensing.

The solubility of tungsten oxide bronzes is of critical importance, as they dissolve slowly, especially in basic environment, forming soluble tungstates.[57] Although this effect is significantly less pronounced than for molybdenum oxides,[35] we have examined the stability (or solubility) of Magneli-type tungsten oxide NRs and tungsten bronze NCs in water, specifically in the presence of hydrogen peroxide (Figure S8.4.14). WO_{3-x} NRs show the highest solubility (3 % of tungsten content) in water. The solubility (i.e., leaching) of all other tungsten oxide bronzes was < 1.5 %. This may be due to traces of unreacted AMT or an amorphous tungstate surface layer of tungstate that was not completely removed after synthesis. In the presence of H_2O_2 (concentration 0.1 M, approx. 10-fold with respect to W), the formation of soluble tungstates (i.e., "leaching") in the range of 10 to 15 % was observed for all tungsten bronzes over the course of 7 d. For WO_{3-x} NRs, up to 54 % of the tungsten content went into solution. This shows that the Magnéli-type oxides are more prone to the formation of soluble peroxo species. The higher lattice energy of the tungsten bronze NCs leads to higher stability against oxidation. However, since soluble $Na_2WO_4*2H_2O$ shows lower efficacy in inhibiting biofilm formation than solid WO_{3-x} NRs and c-$Cs_{0.6}WO_3$, NCs over a period of several days, the catalytic effect should be attributed less to the soluble tungstate species and more to the efficacy of WO_{3-x} NRs and c-$Cs_{0.6}WO_3$ NCs. Nevertheless, our work provides new insight for tungsten oxides used in catalysis, since leaching is commonly disregarded. A major advantage over polymers and many insoluble nanomaterials is that due to slow degradation to soluble tungstates and alkali metal cations, no accumulative environmental effects are expected.

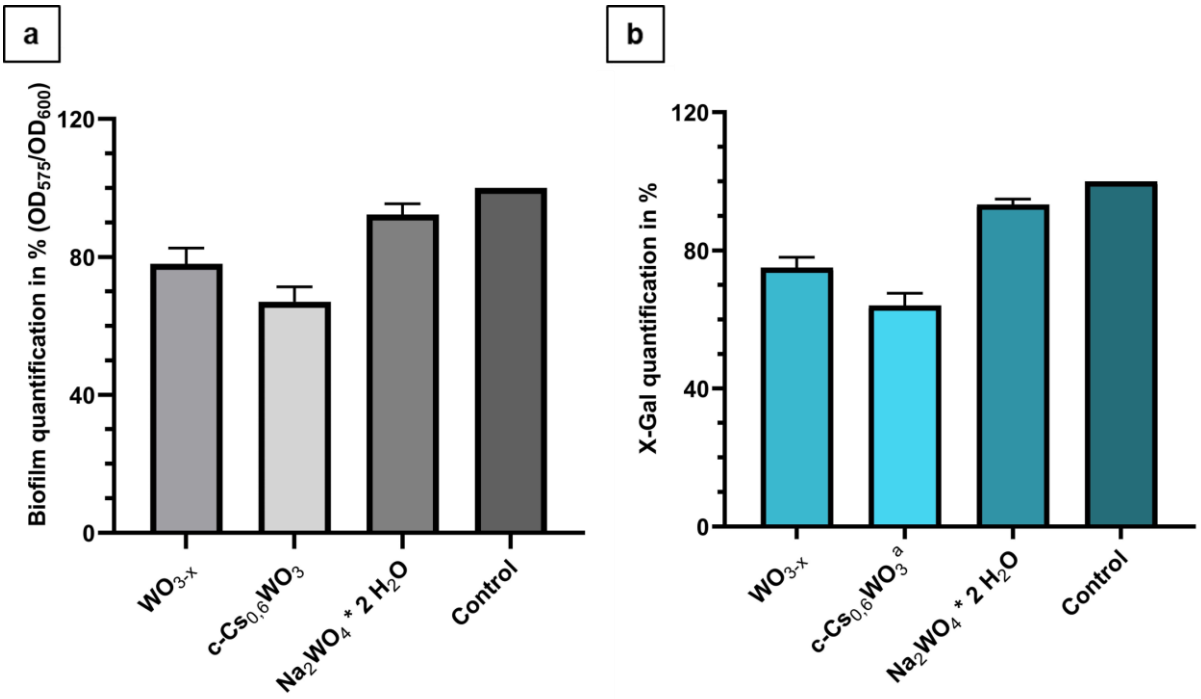

Figure 5.5. Effect of tungsten oxide bronze NCs on bacterial biofilm formation and quorum sensing. a) Crystal violet staining of *P. aeruginosa* grown in LB. The bacteria were cultivated for 72 h at 30 °C in the presence of the tungsten bronzes. After removing the planktonic cells, the attached cells i.e., biofilm were stained. b) X-Gal quantification with the biosensor *A. tumefaciens* A136. The AHL were incubated for 12 h at RT in presence and absence of the tungsten bronzes. The processed AHL were then added to the bacteria, which were cultivated for 8 h at 30 °C in LB medium, which was supplemented with X-Gal.

WO_{3-x} NRs and c-$Cs_{0,6}WO_3$ affect mycelium growth in *F. graminearum*

Because of their HPO activity WO_{3-x} NRs and c-$Cs_{0.6}WO_3$ NCs were examined, together with m-$Cs_{0.3}WO_3$ and h-$(NH_4)_{0.2}WO_3$ NCs for their inhibitory properties of the growth of the fungus *Fusarium graminearum* in the presence of H_2O_2. *F. graminearum* is an ascomycete fungus and the major cause of *Fusarium* head blight in wheat and *Gibberella* ear rot in corn.[58] It can lead to yield losses, grain quality losses and furthermore mycotoxin contamination in cereals, which can affect human health[59] and even lead to death.[60] Antifungal activity is well known for ZnO NPs, but the antimicrobial effect of zinc oxide nanopowders is based on the dissolution of amphoteric Zn^{2+} ions and the subsequent formation of reactive oxygen species (ROS), which damage the lipid cell membrane and lead to the death of the affected cells.[61] Previous studies evaluating the effect of nanoparticles on fungi observed, that nanoparticles can lead to oxidative stress response in fungal cells. It could be observed, that MgO nanoparticles triggered indeed the generation of ROS in *P. nicotianae* and *T. basicola*.[62]

The impact of the NRs and the different NCs on fungal growth is shown in Figure 5.6a, the water-soluble molecular tungstate Na_2WO_4*$2H_2O$ was used as reference.

While m-$Cs_{0.3}WO_3$ NCs did not inhibit fungal growth, Na_2WO_4*$2H_2O$ reduced fungal growth by ~31 % compared to the control, which did not contain any additive. c-$Cs_{0.6}WO_3$ showed the most pronounced inhibiting effect on fungal growth (reduction of ~54 %) while WO_{3-x} reduced the growth about ~46 %. The effect of h-$(NH_4)_{0.2}WO_3$ NCs was comparable with sodium tungstate (28 %). However, for WO_{3-x} NRs we found nearly no evidence for mycelium growth, which means a successful prevention of spore formation and fungal distribution. The effect was less pronounced for h-$(NH_4)_{0.2}WO_3$ and c-$Cs_{0.6}WO_3$ NCs and not observed in the other cases.

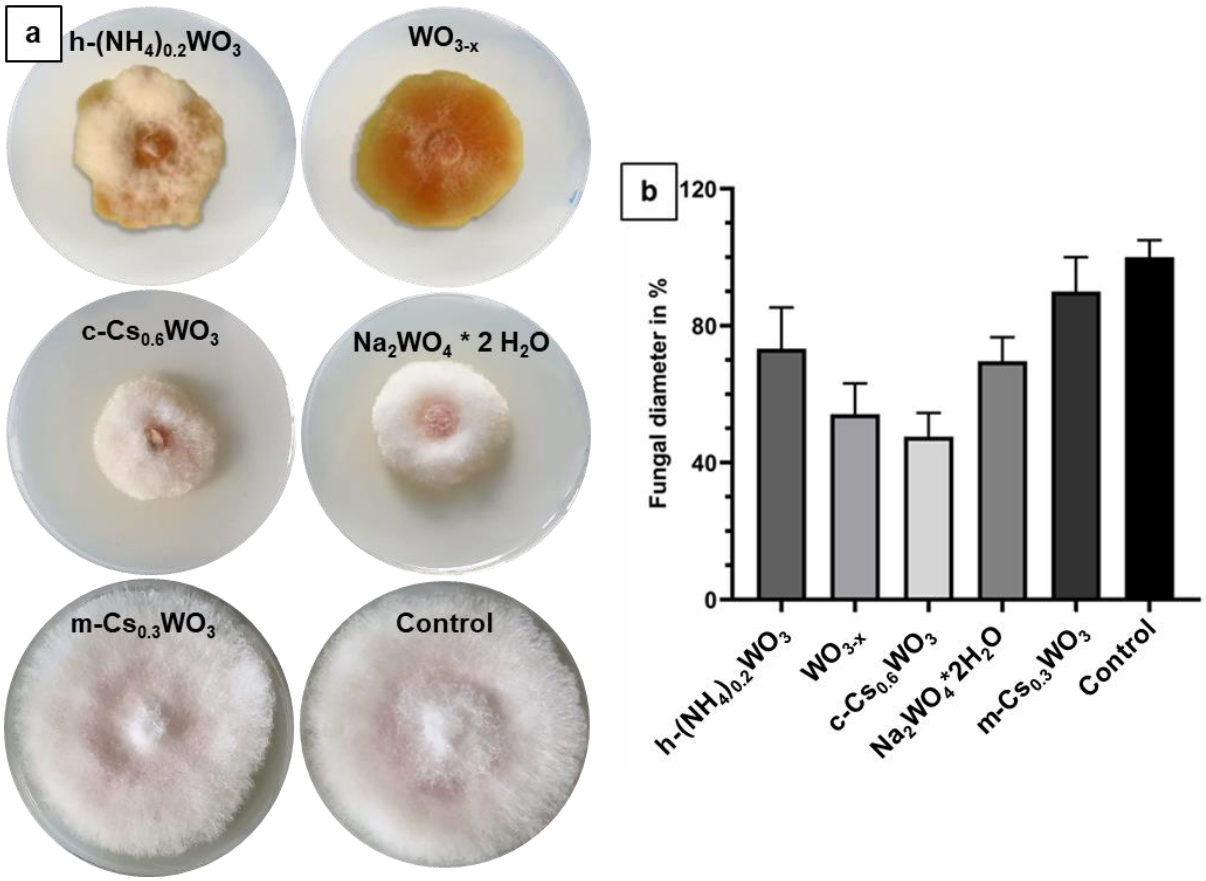

Figure 5.6. Tungsten bronzes inhibit growth of *Fusarium graminearum.* a). The various NCs were added to the liquid HMG medium together with diluted H_2O_2 solution and incubated for 6 h at RT. The agar was then added and *F. graminearum* was placed in the middle of the plate. The results were then pictured after seven days of incubation. b) Effect of tungsten bronzes on the diameter of *F. graminearum*. The measurements were done with ImageJ.

c-$Cs_{0.6}WO_3$ NCs showed a high HOP activity and had the strongest impact on the fungal growth. Therefore, we assume that c-$Cs_{0.6}WO_3$ NCs also interfere with quorum sensing in fungi due to their enzyme-like properties, similar as described above for the growth of bacterial biofilms. As fungal quorum sensing research is still in its infancy, the mode of action of tungsten oxides as quorum quenching compounds remains to be elucidated.[63] Since this retarding effect occurs even in the absence of added bromide ions (e.g., KBr), the antifungal activity could also be due to the peroxidase-like

properties of WO_{3-x}-NRs (or the required bromide ion concentration is provided by the fungus), as tungsten oxide nanomaterials have been shown to exhibit peroxidase-like properties.[64]

Antibacterial activities induced by NIR irradiation

The strong LSPR absorption of the tungsten oxide NRs in the NIR (Figure 5.3) prompted us to evaluate the impact of the LSPR properties on the growth of *Staphylococcus aureus*, *Pseudomonas aeruginosa* and *Phaeobacter gallaeciensis* under IR light (950 nm). *S. aureus* is a Gram-positive, methicillin-resistant (MRSA), opportunistic pathogen that can cause life-threatening infections such as chronic osteomyelitis.[65] *P. gallaeciensis* is a Gram-negative marine bacterium of the clade Roseobacteriaceae, which are known as primary colonizers in a variety of marine biofilms.[66] WO_{3-x} NRs, and m-$Cs_{0.3}WO_3$ NCs were used because they cover different parts of the absorption range in the Vis-NIR region of the optical spectrum. Na_2WO_4*$2H_2O$ was used as reference materials. The effect of the relative NIR exposure on the growth of *S. aureus*, *P. aeruginosa* and *P. gallaeciensis*, corrected by the results without radiation, are shown in Figure 5.7 (absorption spectra shown in Figure 5.3, IR vs no IR in Figure S8.4.15).

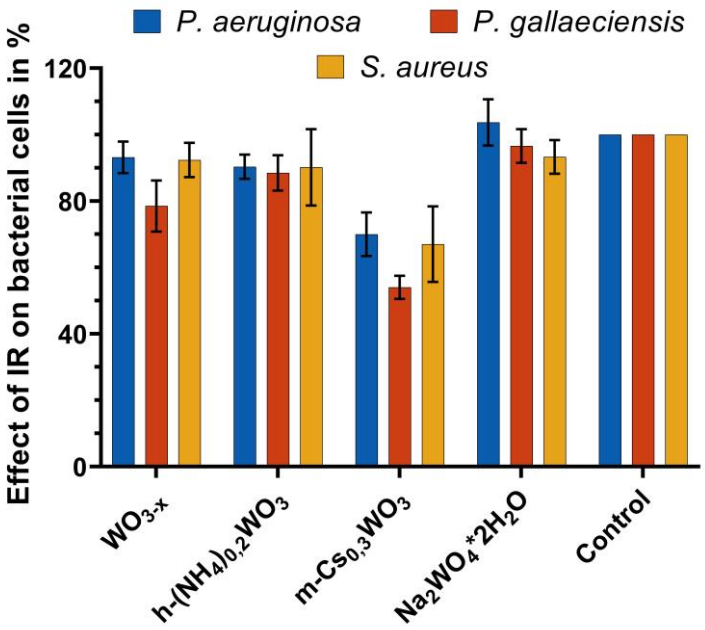

Figure 5.7. Effect of IR light (λ=950 nm) on the growth of *S. aureus*, *P. aeruginosa* and *P. gallaeciensis*. *S. aureus* and *P. aeruginosa* were grown at 30 °C in LB medium, *P. gallaeciensis* was grown at 30 °C in 2216 marine medium. The incubation of the bacteria was done for 72 h in 96-well plates in the absence or presence of tungsten bronzes and 950 nm IR irradiation. OD_{600} was then measured to observe the effect of the tungsten bronzes in combination with IR irradiation in comparison to no irradiation at all.

m-$Cs_{0.3}WO_3$ NCs reduced the growth of all bacteria by 30 to 35 % compared to the control. Water soluble Na_2WO_4*$2H_2O$ showed no difference between NIR exposure and non-exposure. The absorbed

NIR light is converted into thermal energy, which in turn leads to an increase in temperature of the materials.[67,68] Therefore, m-$Cs_{0.3}WO_3$ nanocrystals exhibit (in analogy to gold nanorods[68]) an excellent photothermal energy conversion effect in the NIR region due to their unique LSPR properties,[67] resulting in antifungal activity due to photothermal killing. WO_{3-x} NRs and h-$(NH_4)_{0.2}WO_3$ nanocrystals reduced bacterial growth by ~10 % under NIR light. WO_{3-x} NRs showed a significant antibacterial effect already without irradiation (Figure S8.4.15). As mentioned earlier, the Brønsted acidity may be responsible for this antibacterial effect of WO_{3-x} NRs.[34-36]

5.4 Conclusions

We elaborated a selective synthesis of hexagonal (h-$Cs_{0.3}WO_3$) and cubic pyrochlore-type (c-$Cs_{0.6}WO_3$) tungsten bronze nanocrystals by using the oleic acid (OAc)/oleylamine (OAm) surfactant ratio for phase selection. OAm excess led to preferred formation of the pyrochlore-type cubic cesium tungsten bronze c-Cs_xWO_3 even for Cs:W ratios up to x= 0.3. The resulting phase mixtures containing nanocrystals of the hexagonal and cubic tungsten bronzes h-$Cs_{0.3}WO_3$ and c-$Cs_{0.3}WO_3$ showed strong absorption in the red / infrared spectral range associated with localized surface plasmons. For higher Cs^+ contents of up to x=0.6 we observed only the formation of cubic (pyrochlore-type) c-$Cs_{0.6}WO_3$ nanocrystals. Compared to h-$Cs_{0.3}WO_3$ nanocrystals, c-$Cs_{0.6}WO_3$ nanocrystals were strongly agglomerated, less soluble in organic solvents, and showed a weaker LSPR absorption. c-$Cs_{0.3}WO_3$ and WO_{3-x} NCs showed high haloperoxidase-like activities, demonstrated with the haloperoxidase assay through the catalytic bromination of phenol red to tetrabromophenol blue.

WO_{3-x} NRs and c-$Cs_{0.6}WO_3$ nanocrystals prevent the formation of *P. aeruginosa* biofilms. c-$Cs_{0.6}WO_3$ showed a biofilm reduction of 35 % over a period of three days, while WO_{3-x} NRs showed a reduction of 25%. Control experiments with Na_2WO_4*$2H_2O$ showed only little reduction (10 %), indicating that the presence of soluble tungstates is not the prime reason for the bacteria repelling behavior of WO_{3-x} NRs and c-$Cs_{0.6}WO_3$ NCs. Reporter assays were performed to get a further insight into their quorum quenching activity. WO_{3-x} NRs and c-$Cs_{0.6}WO_3$ modified bacterial signaling molecules, as the biosensor *A. tumefaciens* A136 could detect only 75 % (for WO_{3-x} NRs) and 65 % (for c-$Cs_{0.6}WO_3$) of the initial 3-oxo-C12 lactones compared to the control.

The chemical stability of h-$Cs_{0.3}WO_3$ and c-Cs0.6WO_3 nanocrystals and WO_{3-x} nanorods was studied by determining the W content of the supernatants of nanocrystal dispersions. WO_{3-x} NRs showed W-leaching with time due to its low crystallinity. In contrast, cesium bronze nanocrystals showed a high chemical stability (i.e., very low solubility in water) and low degradation (i.e., no leaching). In the presence of H_2O_2 WO_{3-x} NRs gradually degraded due to the formation of W-peroxido species. However, the quorum quenching activity of both, WO_{3-x} NRs and c-$Cs_{0.6}WO_3$ NCs were higher than the activity of soluble sodium tungstate. Therefore, solubility of the NCs cannot attribute for the antibacterial

activity of the NCs. However, the slow degeneration can prevent long-term accumulation the NCs in organism and therefore reduce toxicological issues.

The antifungal properties of c-$Cs_{0.6}WO_3$ nanocrystals and WO_{3-x} NRs were tested with the fungus *F. graminearum*. Both tungsten bronzes showed antifungal activity and reduced fungal growth up to 54 % within seven days. WO_{3-x} NRs showed a strong reduction of the mycelium growth, thereby preventing spore formation. Finally, the LSPR properties of c-Cs_xWO_3/ h-Cs_xWO_3 phase mixtures reducing the growth of the clinically relevant bacteria *S. aureus* and *P. aeruginosa* and of the marine bacterium *P. gallaeciensis* under NIR light of 950 nm by photothermal energy conversion.

Our findings make tungsten bronzes potential "green" catalysts for antibacterial applications, since no toxically chemicals are released into the environment. Evidence for quorum quenching and therefore a non-biocidal mode of action was provided by the biosensor *A. tumefaciens* A136. Bacterial and fungal biofilms are ubiquitous on domestic, industrial and other surfaces. Conventional biocides (strong oxidants, antibiotics, etc.) are increasingly problematic due to lack of efficacy, non-targeted environmental effects, or development of resistance by microorganisms. Due to their intrinsic catalytic properties and environmental compatibility, engineered tungsten bronzes could find applications for a variety of surface appliances.

5.5 Experimental section

Materials. All chemicals were used as received without further purification. Oleic acid (90 %, technical grade) and sodium tungstate dihydrate (Na_2WO_4*$2H_2O$, >99.0 %) were bought from Sigma Aldrich, oleylamine (>50 %, technical grade) was purchased from TCI, ammonium metatungstate hydrate (AMT, >90 % WO_3 basis) was bought from Carl Roth, cesium carbonate (Cs_2CO_3, 99.5 %) from across and rubidium carbonate (Rb_2CO_3, 99.9 %) was purchased from chempur.

Synthesis of alkali bronze nanocrystals. WO_{3-x} NRs and $(NH)_{0.2}WO_3$ NCs were synthesized according to ref. [38]. For cesium and rubidium tungsten bronzes, the same synthesis was utilized with 0.3 or 0.6 mmol of the respective carbonate. Different variations of the synthesis parameters are discussed in the respective results and discussion section.

Microorganisms and growth conditions. *P. aeruginosa* PA14, *S. aureus* (DSM 11823) and *P. gallaeciensis* (DSM 26640) were obtained from the Deutsche Sammlung für Mikroorganismen und Zellkulturen (DSMZ, Braunschweig, Germany). *A. tumefaciens* A136 was obtained from the lab of Prof. Dr. Kirsten Jung (LMU München, München, Germany) *F. graminearum* was obtained from Prof. Dr. Eckhardt Thines (JGU Mainz, Germany).

P. aeruginosa and *S. aureus* were cultivated aerobically in LB medium [1 % (w/v) NaCl; 1 % (w/v) tryptone; 0.5 % (w/v) yeast extract] at 30 °C. *P. gallaeciensis* was cultivated aerobically in marine broth

2216 (Thermo Fisher, Pittsburgh, USA) at 30 °C. A. tumefaciens A136 was cultivated in LB medium [1 % (w/v) NaCl; 1 % (w/v) tryptone; 0.5 % (w/v) yeast extract] supplemented with 50 µg/ml spectinomycin and 4.5 µg/ml tetracycline to maintain the containing plasmids pCF218 and pCF372.[69] *F. graminearum* was cultivated in HMG medium [0.4 % (w/v) yeast extract; 1 % (w/v) malt extract; 1 % (w/v) glucose; pH = 5.5]. For preparation of agar plates, 1.5 % (w/v) agar was added to the respective medium. Chemicals were purchased from Carl Roth (Karslruhe, Germany).

Biofilm assays. For quantification of bacterial biofilm production, a modified method of already published protocols was used.[70] Briefly, *P. aeruginosa* was cultivated in LB medium over night at 30 °C. Then, the cultures were diluted in the respective medium in the presence or absence of 0,1 mg/ml tungsten oxide bronzes, in a volume of 135 µl per well of a 96-well polystyrene microtiter plate (Sarstedt, Nümbrecht) at a final OD_{600} of 0.5. Additionally, KBr (Roth, Karlsruhe, Germany) and H_2O_2 (Roth, Karlsruhe, Germany) at a final concentration of 32 mM and 0.8 mM respectively were added to the wells. The microtiter plate was then incubated for 72 h under gentle shaking (150 rpm) at 30 °C. Every 24 h H_2O_2 was added at a final concentration of 0.8 mM. Then, the liquid phase of the culture was removed by turning the plate. The planktonic cells were removed by gently submerging the plate two times in a water tub. After drying for 5 min, 135 µl of 1 % (w/v) crystal violet (Merck, Darmstadt) was added to the wells. A well without bacteria served as negative control. After 15 min incubation at room temperature, unbound crystal violet was removed by gently submerging the plate for two times in water. The plate was then air-dried over-night at room temperature. For quantification, 135 µl of 30 % (v/v) acetic acid (Roth, Karlsruhe) was added to solubilize the crystal violet from the biofilm. After 15 min of incubation at room temperature, absorbance was quantified in a plate reader (Tecan, Salzburg) at 575 nm.

Fungal growth assays. To observe antifungal activity of the tungsten bronzes, the various nanocrystals were added to the HMG medium at a final concentration of 0.1 mg/ml. Additionally, 670 µM H_2O_2 was included. After incubation of 6 h at RT, the agar was added, and the plates were poured. Then, *F. graminearum* with a diameter of 1 cm was placed in the middle of the plate and was incubated for seven days at 26 °C. The plates were then photographed, and the diameter was measured using ImageJ 1.53c.

X-gal assay. External 3-oxo-C12 (5 µM) was incubated in presence of 0.1 mg/ml WO_{3-x} NRs. c-$Cs_{0.6}WO_3$ or Na_2WO_4*$2H_2O$ for 12 h at RT. The reaction mixtures were then added to an *A. tumefaciens* A136 culture, which was adjusted to an OD_{600} of 1. After the addition of 250 µg/ml X-gal, the cultures were incubated at 30 °C for 8 h. Afterwards, the cultures were transferred to 1.5 ml tubes and were spin down at 10.000x g for 5 min. The supernatant was then transferred to 96-well plates and the absorbance at 630 nm was measured using a plate reader (Tecan, Switzerland).

Infrared irradiation. For the detection of infrared-initiated antibacterial activity of the tungsten bronzes, *S. aureus*, *P. aeruginosa* and *P. gallaeciensis* were grown over night in their respective medium

at 30 °C. After diluting the bacteria to a final OD_{600} of 0.5 in 96-well plates, the various tungsten bronzes were added at a final concentration of 0.1 mg/ml. Then, the plates were transferred to the microplate reader (Tecan, Switzerland), which monitored the incubation at 30 °C for 72 h. Every 30 minutes the wells were irradiated with 950 nm IR light. To observe the effect of the tungsten bronzes without IR activation, the cultivation was done without 950 nm light beams. After 72 h of cultivation, the OD_{600} was measured to get the final optical density needed for calculations of the IR effect.

5.5.1 Characterization

Transmission electron microscopy (TEM). For TEM one drop of nanocrystal solution (~0.1 mg/mL in chloroform or ethanol) was put onto a carbon-coated copper grid. Images were taken with a FEI Tecnai G2 Spirit microscope equipped with a Gatan US1000 CCD camera at 120 kV. High resolution (HR)-TEM images were measured with a FEI Tecnai F30 operating at 300 kV, equipped with an on axis US4000 CCD 4kx4k camera. For further processing the program ImageJ was used.

Powder X-ray diffraction (PXRD). PXRD studies were carried out on a STOE Standi P using Mo Kα_1 radiation (λ = 0.7093 Å) and a Dectris Mythen 1k detector. The diffractograms were analyzed using Match!3 and plotted with Matlab2018b. All references were taken from the Crystallography Open Database (COD) or International Centre for Diffraction Data (ICDD) PDF database. Rietveld[71] refinements were performed using Topas Academic V6.

Ultraviolet-visible-near infrared absorption (UV-Vis-NIR) spectroscopy. UV-Vis-NIR spectra were taken on a Cary 5G UV-Vis-NIR spectrophotometer operating in a wavelength range from 200 to 1800 nm. Diffuse reflectance measurements were carried out using an Ulbricht spere. Approx. 10 mg of the respective nanocrystals were mixed with ~500 mg $BaSO_4$ and pressed to form a homogeneous surface on a PTFE carrier. The reflectivity was measured within a range of 175 to 2600 nm and a baseline correction was performed using pure $BaSO_4$. Processing and plotting were done with Matlab 2018b.

X-ray photoelectron spectroscopy (XPS). XPS measurements performed on an Axis Ultra DLD imaging photoelectron spectrometer. Measurements were carried out using the Hybrid mode with 10 mA and 15 kV at the Al anode. The analysis area was 700 µm * 300 µm (i.e., X-ray spot size). Survey spectra were measured at a pass energy of 80 and elemental spectra at 20 pass energy of the analyzer. All spectra were charge corrected to a binding energy of 284.8 eV for the C 1s line corresponding to adventitious aliphatic carbon. Measurements were analyzed using the CasaXPS software plotted with Matlab2018b.

Phenol red assay. The haloperoxidase activity was determined by the oxidative bromination of phenol red according to ref.[19]. The time-dependent change in absorbance was followed on a Cary 3500 UV-Vis

spectrometer at a temperature of 25 °C. All nanocrystals were annealed at 300 °C or 500 °C prior to catalytic measurements. The nanocrystals were dispersed in milli pore water and added to a reaction medium with a final concentration of 25 µg/ml nanocrystals, 50 µM phenol red and 25 mM KBr. H_2O_2 with a final concentration of 300 µM was added before the start of the measurement.

Zeta-potential. Zeta potential was measured Malvern Zetasizer NanoZS with a 633 nm He-Ne-Laser. Samples were measured in milli pore water that was filtered through a 200 µm syringe filter. The particle concentration was about 1 mg/ml.

Inductively coupled plasma - mass spectrometry. Type I reagent water (18.2 MΩ*cm) from a Milli-Q system (Merck Millipore, Darmstadt, Germany) and H_2O_2 (30 % (Suprapur), Merck, Darmstadt, Germany) were used for the leaching experiments. Leaching experiments were performed in 15 mL pre-cleaned plastic tubes obtained from Th. Geyer. After weighing in a portion of about 5 mg, the water was added, and the suspension was shaken vigorously. After the corresponding times, the samples were centrifuged at 2500 rpm for 10 min and 1 mL was taken as sample. Subsequently, the missing volume was made up so that an H_2O_2 concentration of 0.1 mol/L was achieved. Then the same procedure as for the water leaching experiments was repeated. For the digestion, approximately 10 mg per sample was weighed into pre-cleaned DigiTUBEs (SCP Science, Quebec, Canada), 10 mL of sodium hydroxide (32 % z.A., Chemsolute, Th. Geyer, Germany) was added, and the suspension was placed on a hot plate at 50 °C for 120 h. After 24 h, 30 mL of type I reagent water was added to the suspension. After this time, the solutions were made up to 50 mL with ultrapure water. At the end the solutions were filled up to 50 mL with ultra-pure water. The leach and digestion samples were diluted from 1:100 to 1:20000 to achieve a concentration between 10 µg/L and 100 µg/L of the elements of interest. The diluted samples were acidified with nitric acid (1.3 % v/v; (65 % z.A. (Chemsolute), Th Geyer, Germany (double sub-boiled)) and stabilized with hydrofluoric acid (0.5 % v/v; 48 % (Ultrapure), Merck, Darmstadt, Germany). For the ICP-MS measurements an Element 2 system (Thermo Fisher Scientific, Bremen, Germany) coupled to an CETAC ASX-520 autosampler (Teledyne CETAC Technologies, Omaha, Nebraska, USA) was used. The system was tuned daily in accordance with the manufacture's guidelines. Mono element standards were used for the external calibration and the internal standard. The Cs (1000 mg/L, Certipur) was purchased from Merck, the tungsten standard (1000 mg/L, Specpure) was purchased from Alfa Aesar.

5.6 References

1 E. Tacconelli, E. Carrara, A. Savoldi, S. Harbarth, M. Mendelson, D. L. Monnet, C. Pulcini, G. Kahlmeter, J. Kluytmans, Y. Carmeli, M. Ouellette, K. Outterson, J. Patel, M. Cavaleri, E. M. Cox, C. R. Houchens, M. L. Grayson, P. Hansen, N. Singh, U. Theuretzbacher, N. Magrini, A. O. Aboderin, S. S. Al-Abri, N. Awang Jalil, N. Benzonana, S. Bhattacharya, A. J. Brink, F. R.

Burkert, O. Cars, G. Cornaglia, O. J. Dyar, A. W. Friedrich, A. C. Gales, S. Gandra, C. G. Giske, D. A. Goff, H. Goossens, T. Gottlieb, M. Guzman Blanco, W. Hryniewicz, D. Kattula, T. Jinks, S. S. Kanj, L. Kerr, M.-P. Kieny, Y. S. Kim, R. S. Kozlov, J. Labarca, R. Laxminarayan, K. Leder, L. Leibovici, G. Levy-Hara, J. Littman, S. Malhotra-Kumar, V. Manchanda, L. Moja, B. Ndoye, A. Pan, D. L. Paterson, M. Paul, H. Qiu, P. Ramon-Pardo, J. Rodríguez-Baño, M. Sanguinetti, S. Sengupta, M. Sharland, M. Si-Mehand, L. L. Silver, W. Song, M. Steinbakk, J. Thomsen, G. E. Thwaites, J. W. M. van der Meer, N. van Kinh, S. Vega, M. V. Villegas, A. Wechsler-Fördös, H. F. L. Wertheim, E. Wesangula, N. Woodford, F. O. Yilmaz and A. Zorzet, *Lancet Infect. Dis.*, 2018, **18**, 318–327.

2 K. Boyce, O. Morrissey, A. Idnurm and I. Macreadie, *Microbiol. Aust.*, 2019, **40**, 87–91.

3 R. Cave, R. Misra, J. Chen, S. Wang and H. V. Mkrtchyan, *Sci. Rep.*, 2019, **9**, 9637.

4 World Health Organization, *Bull. World Health Organ.*, 2016, **94**, 638–639.

5 S. Chernousova and M. Epple, *Angew. Chem. Int. Ed.*, 2013, **52**, 1636–1653.

6 J. Jenkins, J. Mantell, C. Neal, A. Gholinia, P. Verkade, A. H. Nobbs and B. Su, *Nat. Commun.*, 2020, **11**, 1626.

7 L. Tan, J. Li, X. Liu, Z. Cui, X. Yang, K. W. K. Yeung, H. Pan, Y. Zheng, X. Wang and S. Wu, *Small*, 2018, **14**, 1703197.

8 H.-C. Flemming, *Water Res.*, 2020, **173**, 115576.

9 G. Schneider, *Mater. Today: Proc.*, 2017, **4**, S200-S207.

10 T. Bjarnsholt, *APMIS Suppl.*, 2013, 1–51.

11 W.-L. Ng and B. L. Bassler, *Annu. Rev. Genet.*, 2009, **43**, 197–222.

12 C. Grandclément, M. Tannières, S. Moréra, Y. Dessaux and D. Faure, *FEMS Microbiol. Rev.*, 2016, **40**, 86–116.

13 J. N. Carter-Franklin, J. D. Parrish, R. A. Tschirret-Guth, R. D. Little and A. Butler, *J. Am. Chem. Soc.*, 2003, **125**, 3688–3689.

14 H. B. ten Brink, A. Tuynman, H. L. Dekker, W. Hemrika, Y. Izumi, T. Oshiro, H. E. Schoemaker and R. Wever, *Inorg. Chem.*, 1998, **37**, 6780–6784.

15 H. B. ten Brink, H. L. Dekker, H. E. Schoemaker and R. Wever, *J. Inorg. Biochem.*, 2000, **80**, 91–98.

16 V. M. Dembitsky, *Tetrahedron*, 2003, **59**, 4701–4720.

17 M. Mba, M. Pontini, S. Lovat, C. Zonta, G. Bernardinelli, P. E. Kündig and G. Licini, *Inorg. Chem.*, 2008, **47**, 8616–8618.

18 R. André, F. Natálio, M. Humanes, J. Leppin, K. Heinze, R. Wever, H.-C. Schröder, W. E. G. Müller and W. Tremel, *Adv. Funct. Mater.*, 2011, **21**, 501–509.

19 K. Herget, P. Hubach, S. Pusch, P. Deglmann, H. Götz, T. E. Gorelik, I. A. Gural'skiy, F. Pfitzner, T. Link, S. Schenk, M. Panthöfer, V. Ksenofontov, U. Kolb, T. Opatz, R. André and W. Tremel, *Adv. Mater.*, 2017, **29**, 1603823 (1-8).

20 K. Herget, H. Frerichs, F. Pfitzner, M. N. Tahir and W. Tremel, *Adv. Mater.*, 2018, e1707073.

21 B. Sels, D. de Vos, M. Buntinx, F. Pierard, A. Kirsch-De Mesmaeker and P. Jacobs, *Nature*, 1999, **400**, 855–857.

22 B. Sels, P. Levecque, R. Brosius, D. De?Vos, P. Jacobs, D. Gammon and H. Kinfe, *Adv. Synth. Catal.*, 2005, **347**, 93–104.

23 H. Wei and E. Wang, *Chem. Soc. Rev.*, 2013, **42**, 6060–6093.

24 R. Ragg, M. N. Tahir and W. Tremel, *Eur. J. Inorg. Chem.*, 2016, **2016**, 1906–1915.

25 F. Can, X. Courtois and D. Duprez, *Catalysts*, 2021, **11**, 703.

26 G. Duan, L. Chen, Z. Jing, P. de Luna, L. Wen, L. Zhang, L. Zhao, J. Xu, Z. Li, Z. Yang and R. Zhou, *Chem. Res. Toxicol.*, 2019, **32**, 1357–1366.

27 F. Vatansever, W. C. M. A. de Melo, P. Avci, D. Vecchio, M. Sadasivam, A. Gupta, R. Chandran, M. Karimi, N. A. Parizotto, R. Yin, G. P. Tegos and M. R. Hamblin, *FEMS Microbiol. Rev.*, 2013, **37**, 955–989.

28 M. A. Gondal, M. A. Dastageer and A. Khalil, *Catal. Commun.*, 2009, **11**, 214–219.

29 F. Ghasempour, R. Azimirad, A. Amini and O. Akhavan, *Appl. Surf. Sci.*, 2015, **338**, 55–60.

30 P. Wang, B. Huang, X. Qin, X. Zhang, Y. Dai and M.-H. Whangbo, *Inorg. Chem.*, 2009, **48**, 10697–10702.

31 A. I. Mazrad Zihnil, I. In and S. Y. Park, *RSC Adv.*, 2016, **6**, 54486–54494.

32 M. Lackner, S. Maninger and J.-P. Guggenbichler, *Nachr. Chem.*, 2013, **61**, 112–115.

33 C. Zollfrank, K. Gutbrod, P. Wechsler and J. P. Guggenbichler, *Mater. Sci. Eng. C*, 2012, **32**, 47–54.

34 G. Busca, *Phys. Chem. Chem. Phys.*, 1999, **1**, 723–736.

35 Z. Gajarska, K. C. Zelenka, P. Rathner, D. Recktenwald, J. P. Kollender, K. Shahzad, N. Müller, A. W. Hassel and C. C. Mardare, *ACS Appl. Bio Mater.*, 2019, **2**, 1477–1489.

36 A. B. Tesler, P. Kim, S. Kolle, C. Howell, O. Ahanotu and J. Aizenberg, *Nat. Commun.*, 2015, **6**, 8649.

37 C. C. Mardare and A. W. Hassel, *ACS Comb. Sci.*, 2014, **16**, 631–639.

38 R. Dören, B. Leibauer, M. A. Lange, E. Schechtel, L. Prädel, M. Panthöfer, M. Mondeshki and W. Tremel, *Nanoscale*, 2021, **13**, 8146–8162.

39 A. Yella, M. N. Tahir, S. Meuer, R. Zentel, R. Berger, M. Panthöfer and W. Tremel, *J. Am. Chem. Soc.*, 2009, **131**, 17566–17575.

40 K. Manthiram and A. P. Alivisatos, *J. Am. Chem. Soc.*, 2012, **134**, 3995–3998.

41 L. Pirker, B. Višić, S. D. Škapin, G. DraŽić, J. Kovač and M. Remškar, *Nanoscale*, 2020, **12**, 15102–15114.

42 R. Pickering and R. Tilley, *J. Solid State Chem.*, 1976, **16**, 247–255.

43 A. Magnéli, *Acta Crystallogr.*, 1953, **6**, 495–500.

44 P. G. Dickens and M. S. Whittingham, *Q. Rev., Chem. Soc.*, 1968, **22**, 30–44.

45 M. Seifollahi Bazarjani, M. Hojamberdiev, K. Morita, G. Zhu, G. Cherkashinin, C. Fasel, T. Herrmann, H. Breitzke, A. Gurlo and R. Riedel, *J. Am. Chem. Soc.*, 2013, **135**, 4467–4475.

46 Y. F. Li, N. Soheilnia, M. Greiner, U. Ulmer, T. Wood, A. A. Jelle, Y. Dong, A. P. Yin Wong, J. Jia and G. A. Ozin, *ACS Appl. Mater. Inter.*, 2019, **11**, 5610–5615.

47 R. Dören, J. Hartmann, B. Leibauer, M. Panthöfer, M. Mondeshki and W. Tremel, *Dalton Trans.*, 2021, **50**, 14027–14037.

48 R. G. Pearson, *Inorg. Chem.*, 1988, **27**, 734–740.

49 T. M. Mattox, A. Bergerud, A. Agrawal and D. J. Milliron, *Chem. Mater.*, 2014, **26**, 1779–1784.

50 M. Juelsholt, T. Lindahl Christiansen and K. M. Ø. Jensen, *J. Phys. Chem. C*, 2019, **123**, 5110–5119.

51 J. Choi, K. Moon, I. Kang, S. Kim, P. J. Yoo, K. W. Oh and J. Park, *Chem. Eng. J.*, 2015, **281**, 236–242.

52 J. Kawai, H. Adachi, Y. Kitajima, K. Maeda, S. Hayakawa and Y. Gohshi, *Anal. Sci.*, 1997, **13**, 797–801.

53 M. Kostylev, D. Y. Kim, N. E. Smalley, I. Salukhe, E. P. Greenberg and A. A. Dandekar, *Proc. Natl. Acad. Sci. U.S.A.*, 2019, **116**, 7027–7032.

54 P. N. Jimenez, G. Koch, J. A. Thompson, K. B. Xavier, R. H. Cool and W. J. Quax, *Microbiol. Mol. Biol. Rev.*, 2012, **76**, 46–65.

55 K. Tang, Y. Zhang, M. Yu, X. Shi, T. Coenye, P. Bossier and X.-H. Zhang, *Sci. Rep.*, 2013, **3**, 2935.

56 R. S. Smith and B. H. Iglewski, *J. Clin. Invest.*, 2003, **112**, 1460–1465.

57 E. Lassner, *Int. J. Refract. Hard Met.*, 1995, **13**, 35–44.

58 F. A. Pagnussatt, E. M. Del Ponte, J. Garda-Buffon and E. Badiale-Furlong, *Pestic. Biochem. Physiol.*, 2014, **108**, 21–26.

59 R. King, M. Urban and K. E. Hammond-Kosack, *Genome Announc.*, 2017, **5**, 1–2.

60 R. Schoental, *Perspect. Biol. Med.*, 1984, **28**, 117–120.

61 L. He, Y. Liu, A. Mustapha and M. Lin, *Microbiol. Res.*, 2011, **166**, 207–215.

62 J. Chen, L. Wu, M. Lu, S. Lu, Z. Li and W. Ding, *Front. Microbiol.*, 2020, **11**, 365.

63 P. Albuquerque and A. Casadevall, *Med. Mycol.*, 2012, **50**, 337–345.

64 C. Y. Park, J. M. Seo, H. Jo, J. Park, K. M. Ok and T. J. Park, *Sci. Rep.*, 2017, **7**, 40928.

65 T. J. Foster and J. A. Geoghegan, in *Molecular Medical Microbiology*, Elsevier, 2015, pp. 655–674.

66 C. C. C. R. de Carvalho, *Front. Mar. Sci.*, 2018, **5**, 1–11.

67 C. Guo, S. Yin, H. Yu, S. Liu, Q. Dong, T. Goto, Z. Zhang, Y. Li and T. Sato, *Nanoscale*, 2013, **5**, 6469–6478.

68 T. Yang, D. Wang and X. Liu, *Colloids Surf. B*, 2019, **173**, 833–841.

69 J. Zhu, J. W. Beaber, M. I. Moré, C. Fuqua, A. Eberhard and S. C. Winans, *J. Bacteriol.*, 1998, **180**, 5398–5405.

70 K. L. Woo, *J. Vis. Exp.*, 2007, 243.

71 H. M. Rietveld, *J. Appl. Crystallogr.*, 1969, **2**, 65–71.

The following chapter 6 is to be submitted in: Materials Science and Engineering C, 2021.

Authorship Contributions Chapter 6

Conception and design of the study:

[redacted]

Preparation of samples and acquisition of data:

[redacted] – preparation of nanocrystals

[redacted] – biologic evaluations

[redacted] – TEM measurements

[redacted] – PXRD measurements

[redacted] – CLSM measurements

Analysis and interpretation of data:

[redacted] – PXRD diffraction

[redacted] – TEM images

[redacted] – biological data

Drafting of the manuscript:

[redacted]

Revising the manuscript critically for important intellectual content:

[redacted]

Preparation of figures

[redacted]

6. Antimicrobial activity of metal tungstate nanocrystals prevents bacterial biofilm formation

6.1 Abstract

Steel surfaces, widely present in construction, the food industry and the medical sector are frequently exposed to bacterial colonization with severe consequences on consumers' health. Since steel contains a variety of alloying metals such as iron, manganese, cobalt, or tungsten it is important to understand the effects of steel composition on bacterial growth and BF formation. We show that steel promotes bacterial growth and biofilm (**BF**) formation of *Phaeobacter gallaeciensis* by 280 % compared to glass surfaces. This is due to biocorrosion where hydrated metal species such as Fe^{2+} or Mn^{2+} promote bacterial growth even in low concentrations. Confocal laser fluorescence microscopy (**CLFM**) revealed BF formation with a thickness of 30 µm over a 72-hour time frame. Screening of biologically relevant, bivalent cations alloyed in steel revealed that iron and manganese have a strongly promoting effect to BF formation, as they serve as nutrient for bacterial growth. We synthesized $FeWO_4$ and $MnWO_4$ nanocrystals (**NCs**) which inhibit BF formation but show no toxicologic effect towards planktonic cells. The same effect was observed for the nosocomial bacterium *Pseudomonas aeruginosa*. The efficacy is most pronounced for the $MnWO_4$, which showed a decrease of ~40 % in *P. gallaeciensis* and *P. aeruginosa* BF formation. We assume that the incorporation of NCs into the BF matrix ultimately leads to biofilm dispersion.

6.2 Introduction

Metals alloys such as steel are among the most important materials in modern society.[1] Their properties can be tailored to meet specific needs for example in construction, marine environments, food production or biomedicine. Any metal surface in contact with an aqueous or moist environment can suffer from corrosion. Typically, metal corrosion results in soluble metal ions in water, which can be followed by precipitation of metal oxides and hydroxide.[2] Corrosion leads to structural weakening and eventually leads to mechanical failure. Corrosion can even be enhanced with stainless steels, an iron (Fe) alloy with at least 11 wt% chromium (Cr).[3] High corrosion resistance, in combination with good mechanical properties,[1] is the main reason for using stainless steel in more aggressive environments, such as sea water,[4] for food production (e.g. in the meat industry)[5] or in biomedical applications (e.g., orthopedic implants),[6] to achieve biocompatibility and maintain function with time. These aspects are closely related to a high corrosion resistance and physicochemical surface properties that govern protein adsorption and bacteria adhesion.

Bacterial adhesion to stainless steel is a severe challenge for many medical, industrial, or environmental applications. Water systems in industrial sites are prone to biocorrosion as well.[7] Bacteria can oxidize metals, especially iron during metabolic processes.[8,9] The effect of corrosive microbial products on the metal surface can be enhanced when the microorganisms form a biofilm (**BF**), containing exopolymers which impede the diffusion of solutes and have an increased corrosive effect on metal surfaces due to the influence of complexing bioligands (e.g. proteins, lipids, polysaccharides, siderophores and nucleic acids) on the redox potentials of alloyed metals such as iron, copper and manganese.[9–11] These features of located microbial growth are important requirements to enhance biocorrosion and display phenotypic characteristics that differ from those of their planktonic counterparts, like increased tolerance to antibacterial agents.[12] Up to 80 % of all human microbial infections are due to the formation of BF of nonpathogenic microorganisms,[13] which have been shown to be resistant to common disinfection practices.[14]

Smart surface science may inhibit bacterial adhesion and BF development.[15,16] One approach is based on the release of biocidal agents or inhibition of bacterial adhesion.[17] This is done using coatings that release microbiocidal agents such as silver, antibiotics, enzymes, polycations, and antimicrobial peptides into the surrounding aqueous environment.[16] Alternative strategies attempt to prevent film formation with weakly polarizable features that reduce van der Waals forces,[18] superhydrophobic surfaces,[19,20] or create highly hydrated areas via hydrophilic polymers.[21] As these strategies rarely work permanently, it is difficult to combat bacterial attachment by surface patterning or surface chemistry alone.[22]

Therefore, efforts have been made to develop alternative antibacterial compounds and materials.[23–25] Instead of modifying existing antibiotics or synthesizing new antibiotics that could sooner or later cause new resistance, inspiration has come from natural self-defense systems that use enzymes to cause

irreversible damage to bacteria or disrupt BF integrity or disable bacterial communication. BF formation is based on bacterial communication through quorum sensing (**QS**), a cell-to-cell communication process that enables bacteria to synchronize their group behavior during BF formation. One combat strategy focuses on suppression of bacterial communication influencing the relevant signal molecules N-acyl homoserine lactones (**AHL**). AHL directly induces bacterial growth and is therefore a key factor in BF formation.[26,27] Haloperoxidases can catalyze the oxidative bromination of AHL signaling molecules, rendering them useless for QS and thus suppressing BF formation. A number of transition metal complexes,[28,29] V_2O_5,[15,16] and CeO_2[30,31] nanocrystals (**NC**s) can mimic the catalytic activity of haloperoxidase enzymes under ambient conditions.[32] Therefore, these NP enzyme mimics[30,33] display a sustained and long-term activity at ambient conditions to prevent biofouling in moist environments.[23] However, these catalysts need equivalents of hydrogen peroxide and halogenide anions to function, therefore their application is limited. Additionally, the concept can only be applied to bacterial communication of Gram-negative bacteria and existing BF cannot be removed. Finding alternative systems with intrinsic properties to prevent BF growth without need of additives and showing no toxic behavior towards the bacteria, thereby preventing formation of resistances, is highly desired. Biofilm dispersion is a complex field of essential interest, as is represents an non-toxic way that target already existing BFs and is often based on the bacterial nutrient balance.[34,35]

Since iron and manganese, which play a central role in the active sites of different haloperoxidase enzymes,[36–38] and tungsten, which is an active haloperoxidase mimic as WO_4^{2-} anion[28,39] are typical metal components of steel it is important to understand the effects of steel composition on bacterial growth and BF formation. In this work, we compare the growth of the marine bacterium *Phaeobacter gallaeciensis* on building steel S235, laboratory glass, polyethylene (PE), polyethylene terephthalate glycol (PETG), polystyrene (PS) and polycarbonate (PC) surfaces. We show that steel promotes bacterial growth and BF formation compared to glass and polymers. This is due to the well-known biocorrosion, because Fe^{2+} and Mn^2 promote bacterial growth even in very low concentrations. We were able to proof this effect by using the respective salts of the biorelevant steel alloy components. The growth of BF and planktonic cells was homogeneous for all tested metal salts. In contrast, the corresponding $FeWO_4$ and $MnWO_4$ NCs significantly reduced the BF formation while showing a significantly higher amount of planktonic cells. The effect is more pronounced for the $MnWO_4$ than for the $FeWO_4$ NCs and is independent of any additives and synthesis conditions. The inhibition of BF growth for the nosocomial bacterium *Pseudomonas aeruginosa* also demonstrates the clinical relevance. Finally, plausible explanations regarding biofilm dispersion are discussed based on the delicate balance of bacterial BFs towards nutrients and siderophores, which may bind on NC surfaces.

6.3 Results and discussion

6.3.1 Low-carbon steel affects marine bacterial BF formation

Alloy steels are made of iron, carbon and other alloying elements added deliberately such as vanadium, silicon, nickel, manganese, copper, and chromium. Structural steel is a standard construction material made from specific grades of steel and formed in a range of industry-standard cross-sectional shapes. Structural steel grades are produced with specific chemical compositions and mechanical properties. The chemical composition of structural steel is very important and highly regulated because it is a fundamental factor which defines the mechanical properties of the steel. The chemical composition of structural steel S235 is Fe, 94.96%, Al 0.30%, Bi 0.10%, Co 0.30%, Cu 0.40%, Cr 0.30%, Mn 1.65%, Mo 0.08%, Nb 0.06%, Ni 0.30%, Pb 0.40%, Se 0.10%, Si 0.60%, Ti 0.05%, V 0.10%, W 0.30%.[40]

Figure 6.1a compares the bacterial film density *Phaeobacter gallaeciensis* on steel S235 and polymers (PE, PETG, PS, and PC). The bacteria were grown in 24-well plates, including the various placed materials for 72 h and the results normalized towards laboratory glass. The results indicate that adhesion of the Gram-negative marine bacterium *P. gallaeciensis*, which belongs to the clade of Rhodobacteriaceae, a well-known primary colonizer of marine surfaces[41,42] is strongly depending on the material surface. BF adhesion on steel was 280 % higher than on polycarbonate (105 %), which showed a similar BF density than laboratory glass. *P. gallaeciensis* bacteria showed a much higher adhesion density on hydrophilic PC than on the presumably more hydrophobic PE, PETG, and PS surfaces (11, 12 and 14 %).

The 3D structure of the BFs of *P. gallaeciensis* was analyzed by confocal laser scanning microscopy (CLSM, Figure 6.1b-d). For this purpose, the BFs were grown again at 30 °C for 72 h on PC, PE, glass and steel surfaces. After removal of planktonic cells, the remaining attached cells were stained with green fluorescent nucleic acid stain (SYTO 9) and propidium iodide, a live-dead staining method that can detect *all* cells in a given BF. The steel surface was covered with an approximately 30 µm thick BF (Figure 6.1b), confirming the results of the crystal violet assay. The biofilm on glass was significantly less dense and thick (Figure 6.1c, comparable to the PC surface (Figure 6.1e) with a thickness of approx. 10 µm each. For PE, the BF was significantly less dense with a thickness of less than 2 µm (Figure 6.1d).

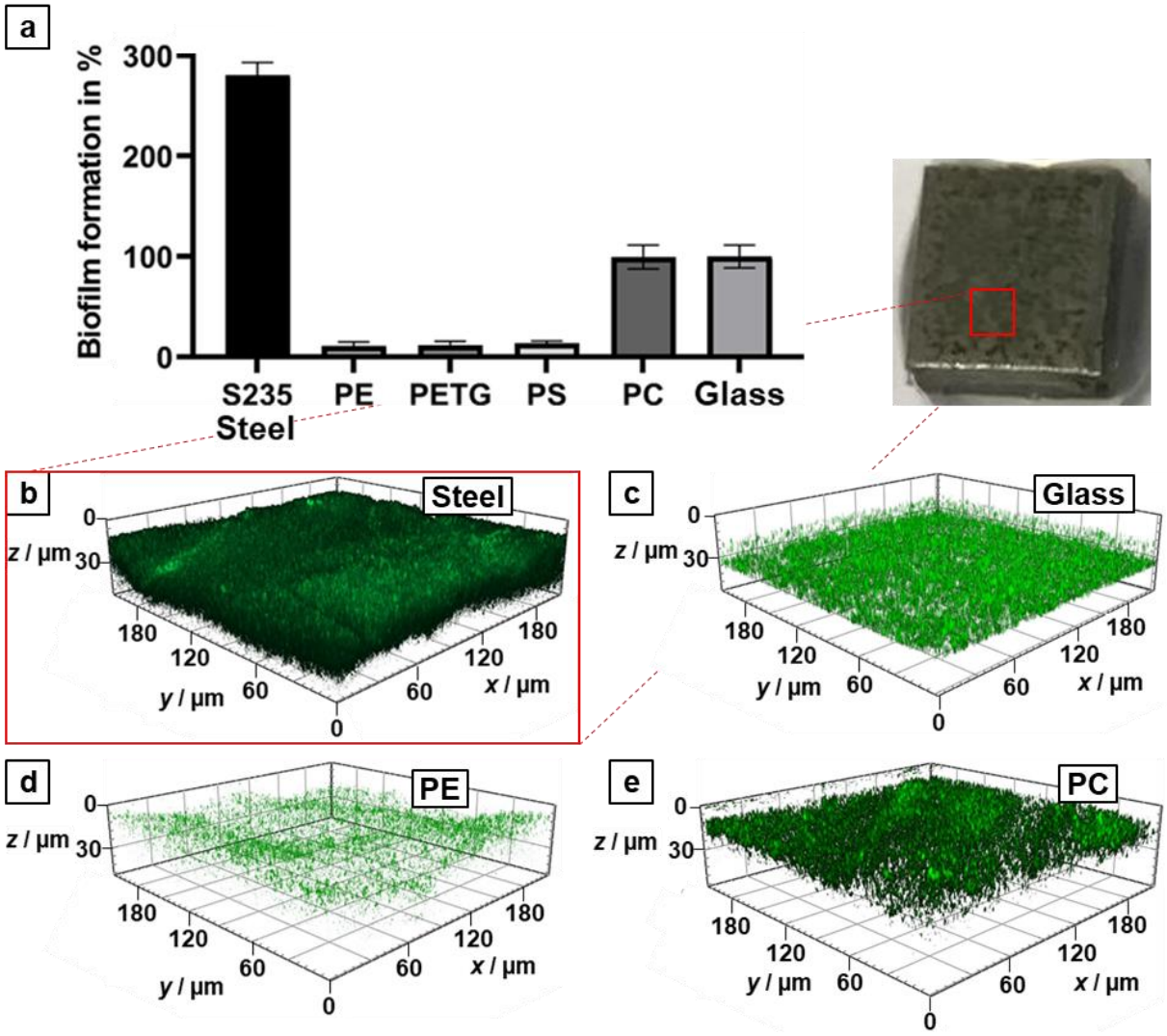

Figure 6.1. a) Comparison of *P. gallaeciensis* BF formation on steel, laboratory glass and different polymer surfaces (polyethylene, PE; polyethylenterephthalat glycol, PETG; polystyrene, PS and polycarbonate, PC), referenced towards the glass surface. (b-e) Confocal laser scanning microscopy images of steel S235 b), glass c), PE d) and PC c) surfaces. The bacteria were cultivated for 72 h at 30 °C in the presence of steel, plastics and glass. The different materials were then rinsed with water to remove the planktonic cells. The remaining attached cells were then stained with crystal violet. For CLSM analysis the attached bacteria were stained with a combined SYTO9/propidium iodide solution. Inset showing the S235 steel surface after cultivation.

6.3.2 Metal ions affect bacterial BF formation

The strongly enhancing effect of S235 steel towards biofilm formation could be explained with biocorrosion of the steel surface by *P. Gallaeciensis*. Therefore, the alloy components of the 3d transition metal series can go into solution as ions. This effect could be enhanced in the presence of atmospheric oxygen due to aerial oxidation. We investigated the growth of *P. gallaeciensis* BF as a function of different metals in in aqueous solution. We focused on the bivalent metals (Fe^{2+}, Mn^{2+}, Co^{2+}, Zn^{2+}, Mg^{2+}, Cu^{2+}) that show biologic relevance[43] and could therefore be responsible for the promoting BF formation effect on steel surfaces.

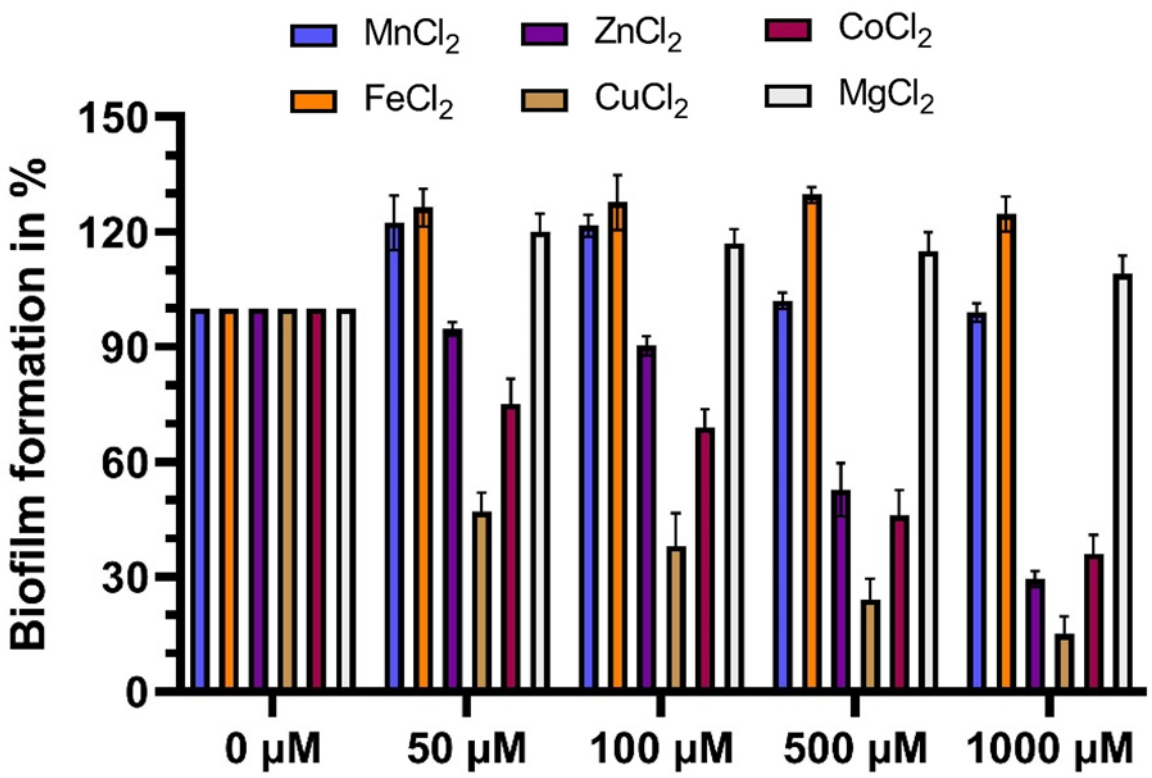

Figure 6.2. Concentration dependent effect of metal cations on bacterial BF formation in *P. gallaeciensis* using solutions of chloride salts of Mn^{2+}, Fe^{2+}, Zn^{2+}, Cu^{2+}, Co^{2+} and Mg^{2+}. Concentrations used were 0, 50, 100, 500 and 1000 µM. For Fe^{2+} oxidation towards Fe^{3+} can be assumed.

P. gallaeciensis BFs were grown in the absence and presence of the solutions of the respective metal cations with various concentrations (0, 50, 100, 500 and 1000 µM) for 72 h at 30 °C in 96-well plates. Figure 6.2 is revealing in several ways. The presence of 50 µmol Cu^{2+} leads to a 40 % decrease in BF formation. This is compatible with the reported antimicrobial effects of copper, its alloys (e.g. brasses, bronzes etc.) based on the toxic effects of Cu^{2+} ions on living cells, algae, spores, fungi, viruses, prokaryotic and eukaryotic organisms even in low concentrations, which are still used for antifouling coatings based on copper compounds and biocide boosters.[44–46] However, the most striking result is that 50 µmol of Mg^{2+}, Mn^{2+}, and Fe^{2+} promote *P. gallaeciensis* BF formation. For Fe^{2+}, which can be oxidized by molecular oxygen towards Fe^{3+}, we observed an increasing of BF formation of 25 %. For Mn^{2+} and Mg^{2+} the BF density is enhanced by 20 % and 15 % respectively. The promoting effect of iron on BF formation has been demonstrated for *P. aeruginosa* due to stimulated exopolysaccharide Ps1 production.[47] A slight increase of BF formation has been reported for Mn^{2+} as well.[48] We observed small decrease of BF formation for Co^{2+} and Zn^{2+}. The negative impact of Zn^{2+} ions on bacterial growth has been described before.[49,50]

We found that Mn^{2+} concentrations up to 100 µM had a positive effect on BF formation (~120 %). Higher concentrations did not show an enhancement of the BF growth compared to the control

experiment (105 % for 1000 µmol). For Fe^{2+}, the effect was constant throughout the series. Already 50 µM of Fe^{2+} increased the BF to 125 % compared to the control. For concentrations up to 1000 µM, no change of the BF formation was observed. However, for Zn^{2+} we observed a concentration dependent reduction of BF formation. While the BF remained stable (>90 %) for concentrations up to 100 µM, we observed a strong reduction to 50 % for a concentration of 500 µM. For a Zn^{2+} concentration of 1000 µM, the BF was reduced to 25 % compared to the control. This indicates a toxic effect of Zn^{2+} on bacterial growth and BF formation of *P. gallaeciensis*. A similar effect was observed for Co^{2+}.

CLSM was performed to visualize the effect of Mn^{2+} and Fe^{2+} on BF formation. BFs were grown for 72 h at 30 °C on microscope slides placed in Petri dishes filled with cultivation medium and dissolved $MnCl_2*4H_2O$ and $FeCl_2*4H_2O$ (50 µM) (Figure S8.5.1b, c). A sample without the metal salt was used as control (Figure S8.5.1a). After staining with SYTO 9 and propidium iodide and removing the planktonic cells the bacterial culture grown in the presence of $MnCl_2$ and $FeCl_2$ showed an enhanced cell attachment. While the BF on the control sample was homogeneously distributed all over the surface (green fluorescence), including several non-colonized (white) spots, the cultures grown in the presence of $MnCl_2$ and $FeCl_2$ showed less non-colonized areas and higher cell attachment to the surface. The resulting fluorescence intensity is based on the total intensity of both dyes.

6.3.3 Synthesis and structural properties of (transition)metal tungstate nanocrystals

The reaction of tungstate (WO_4^{2-}) anions resulting from the oxidation of tungsten during biocorrosion with bivalent metal cations could lead to the formation of metal tungstates.[51] Therefore, MWO_4 NCs (M = Mn^{2+}, Fe^{2+}. Zn^{2+}, Co^{2+}, Mg^{2+}, Sr^{2+} and Ba^{2+}) were synthesized as well-defined reference compounds to compare the effects of divalent main group and transition metals on bacterial growth with that of the metals in their zero-valent oxidation states in steel alloy and of the hydrated metal ions in aqueous solution. NCs were obtained by varying batch sizes, cation salts, heating rate and ratios of solvent and capping agents. An overview of the different NC syntheses relevant for this article is presented in Table S8.5.1. Phase identity was confirmed by powder X-ray diffraction (PXRD), nanocrystal morphologies and sizes of individual nanocrystals were determined using transmission electron microscopy (TEM).

6.3.4 $MnWO_4$ and $FeWO_4$ nanocrystals do not affect bacterial growth but inhibit BF formation in *P. gallaeciensis* and *P. aeruginosa*

Bacterial growth and BF formation of *P. gallaeciensis* was investigated for MWO_4 (M = Mn^{2+} and Fe^{2+}) NCs (Figure 6.3d). $MnWO_4$ and $FeWO_4$ NCs (TEM images in Figure 6.3a, b, PXRD patterns in

Figure S8.5.2) with comparable sizes (< 20 nm) showed a promoting effect on the growth of planktonic cells. This effect was more pronounced for $MnWO_4$ (148 %) than for $FeWO_4$ NCs (127 %) compared to the control (no NCs). However, BF formation was inhibited significantly for $MnWO_4$ (62 %) and moderately for $FeWO_4$ (82 %), although the effect cannot be attributed to haloperoxidase property as no hydrogen peroxide and KBr were used. $(Mn_{1-x}Fe_x)WO_4$ NCs, synthesized with 1:1:2 mixture of Fe:Mn:W (Figure 6.3c) showed an effect between those of pure $MnWO_4$ and $FeWO_4$ (128 % planktonic cells, 72 % BF).

To analyze whether the individual components, 3d metal cations (Mn^{2+} and Fe^{2+}) and the WO_4^{2-} tungstate anions, or a combined intrinsic property of the $MnWO_4$ and $FeWO_4$ NCs are responsible for this inhibiting effect, soluble Na_2WO_4 was tested, which showed only a moderate and equal reduction of planktonic cells growth and BF formation (86 % each). Together with the control for hydrated Mn^{2+} cations this shows that the inhibiting effect of $MnWO_4$ on BF formation effect cannot be attributed to dissolved Mn^{2+} cations but must be an intrinsic property of $MnWO_4$ and $FeWO_4$.

To support this hypothesis, we expanded the studies to nosocomial pathogens. Here the effect of $MnWO_4$ and $FeWO_4$ NCs on *P. aeruginosa* growth was tested (Figure 6.3e). We observed inhibition of BF formation similar to *P. gallaeciensis*. $MnWO_4$ NCs showed a strong reduction in BF formation while enhancing planktonic cell growth (61 and 150 % respective). The effect was again less pronounced with $FeWO_4$ (82 % BF and 109 % planktonic cells).

To rule out the possibility that the preparation parameters affect the biological properties of the metal tungstate NCs, different solvent ratios were tested for $FeWO_4$ synthesis (excess of oleic acid, excess of oleylamine, (Figure S8.5.3). No significant effects were detectable within experimental error, although the NCs had quite different diameters (~30*15 nm vs ~5 nm) depending on the preparation conditions (Figure S8.5.4, Table S8.5.1). The effect of different manganese precursors (manganese oleate, manganese acetate and manganese acetylacetonate, all >20 nm, Figure S8.5.5) was investigated for $MnWO_4$. No significant change of biological activity was found either (Figure S8.5.6). This indicates that the biological activity is independent of the size of the NCs and rather related to the intrinsic properties of $MnWO_4$ and $FeWO_4$. In contrast, no significant effect on bacterial proliferation and BF formation was observed for $CoWO_4$, $MgWO_4$, $SrWO_4$ and $BaWO_4$ for both, *P. gallaeciensis* and *P. aeruginosa* (Figure S8.5.7 and Figure S8.5.8). For $ZnWO_4$ NCs we found indications for antimicrobial behavior (Supporting information, Figure S8.5.9 and Figure S8.5.10).

As the reduction of BF formation and the enhancement of bacterial growth are equally opposite for all $FeWO_4$ and $MnWO_4$ NCs, we suppose that the increasing number of planktonic cells is due to a weakening of the BF matrix. Comparable effects may be expected for haloperoxidase mimicking NCs due to the bromination of AHLs, although BF formation is quenched from the beginning. This only works in the presence of H_2O_2/KBr, which was not added and used in our experiments. Therefore,

neither any haloperoxidase activity nor the effect of the hydrated metal cations can explain the suppression of BF formation specifically for $MnWO_4$ and $FeWO_4$ NCs. One possible explanation is the incorporation of NCs in the BF matrix during its formation. Subsequently, the NCs cause the BF to dissolve after it is formed. The disruption of BF after formation is a rather complex process that can occur for a variety of reasons and is known as biofilm dispersion.[34]

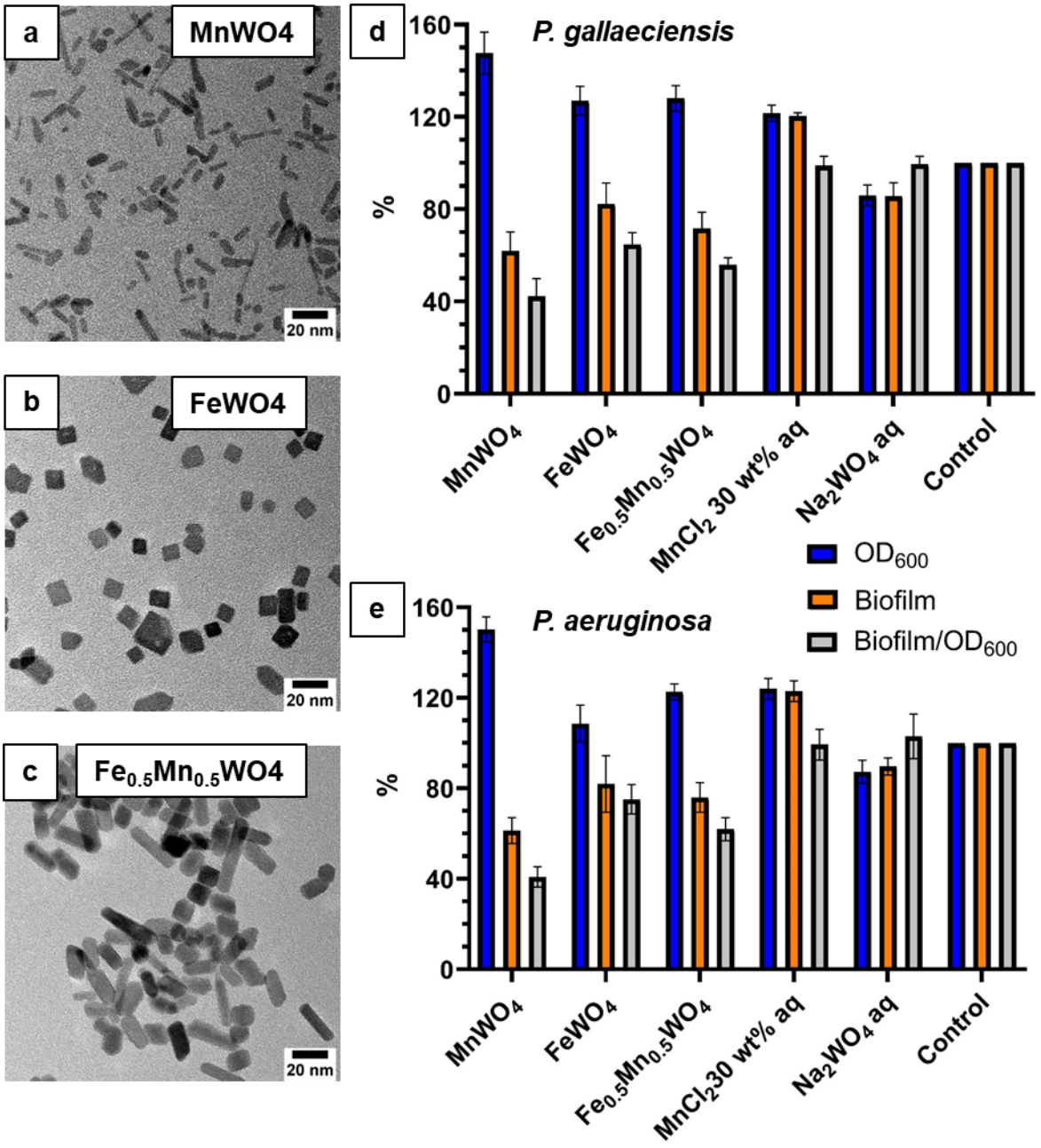

Figure 6.3. TEM images of a) $MnWO_4$, b) $FeWO_4$ and c) $(Fe_{0.5}Mn_{0.5})WO_3$ nanocrystals. BF formation and bacterial growth for d) *P. gallaeciensis* and e) *P. aeruginosa* as a function of nanocrystal composition ($MnWO_4$, $FeWO_4$ and $(Fe_{0.5}Mn_{0.5})WO_3$, 0.1 mg/ml each) and $MnCl_2$ (30 wt%, 150 µM) $Na_2WO_4*2H_2O$ (0.1 mg/ml, 303 µM) as water soluble reference compounds.

It is known that *P. aeruginosa* produces siderophores called pyoverdine for scavenging iron as important nutrient.[52] Therefore, bacteria can attach to the metal tungstate surfaces within the biofilm and attempt to degrade the NCs for iron acquisition. Alternatively, pyoverdine may bind on the NC surfaces via catechol, carboxylic acid and primary amine groups.[53–57] It has been shown that iron uptake in *P. aeruginosa* is directly related to biofilm formation process.[58] Binding pyoverdine on the surface of NCs could therefore disrupt the iron balance and induce biofilm disintegration. On the other hand, free iron can lead to a biofilm degradation in response by *P. aeruginosa*.[59] Furthermore, it was observed, that manganese, which can be scavenged by bacteria as well,[60] can induce the swarming ability in *Bacillus cereus* (*B. cereus*).[61] In *P. aeruginosa*, the complex swarming motility is strictly required for biofilm dispersion.[62] Bioinformatic analysis of *P. gallaeciensis* revealed specific ABC-like transporters (transport system superfamily that is one of the largest and possibly one of the oldest gene families) for iron and manganese.[63] It can therefore be assumed, that $MnWO_4$ and $FeWO_4$ induced biofilm degradation may be due to three different types of effects. (i) By degrading the NCs incorporated in the matrix the biofilm may become porous and brittle, thereby triggering the disintegration process. (ii) Accumulation of free iron or manganese in the matrix can lead to controlled biofilm degradation. (iii) Siderophores relevant for biofilm formation and virulence may bind to $MnWO_4$ and $FeWO_4$ NC surfaces, rendering them useless for bacterial nutrient balance and resulting in biofilm dispersion.

6.4 Conclusions

We showed that structural steel surfaces have a strongly promoting effect on the growth and BF formation of the marine bacterium *P. gallaeciensis*, whereas bacterial growth on hydrophobic polymer surfaces was slow due to their wetting properties, and more hydrophilic polymer surfaces showed a moderate bacterial growth. Structural steel contains a large variety of alloying metals, the most prominent representatives besides Fe being Mn, Co, Ni, Cu and W. The effect of the divalent metal ions Mn^{2+}, Fe^{2+}, Co^{2+}, Zn^{2+}, Cu^{2+} and Mg^{2+} as well as tungsten (as the water stable tungstate WO_4^{2-} anion) on BF formation was analyzed. Hydrated Mn^{2+} and Fe^{2+} ions in aqueous solution had a promoting effect on BF formation, while the ratio between BF and planktonic cells remained constant. $MnWO_4$ and $FeWO_4$ had a significant inhibiting effect on the BF of *P. gallaeciensis* and *P. aeruginosa* while the amount of platonic cells was significantly enhanced. The inhibiting effect was independent of the preparation of the $MnWO_4$ and $FeWO_4$ nanocrystals and is seems due specifically to the intrinsic properties $MnWO_4$ and $FeWO_4$, because $CoWO_4$, $MgWO_4$, $SrWO_4$ and $BaWO_4$ showed no effect on BF formation and $ZnWO_4$ showed antibacterial behavior but had no impact on BF formation. We assume that $MnWO_4$ and $FeWO_4$ NCs are incorporated in the biofilm matrix, colonized, and potentially degraded by the bacteria. Previous studies have shown the importance of hydrated Fe^{2+} and Mn^{2+} cations for biofilm disintegration and swarming behavior of various microorganisms. Alternatively,

siderophores could bind onto the $MnWO_4$ and $FeWO_4$ NC surfaces and disrupt the nutrient balance, resulting in bacterial biofilm dispersion. Therefore, $MnWO_4$ and $FeWO_4$ NCs are potent candidates for use in antibiofilm applications.

6.5 Experimental section

Materials. All chemicals were used as received without further purification. Oleic acid (90 %, technical grade), potassium oleate (technical grade, 87 % fatty acid), manganese (II) acetylacetonate, manganese chloride (97 %) and sodium tungstate dihydrate (99 %) were bought from Sigma-Aldrich, oleylamine (>50 %, technical grade) was purchased from TCI, ammonium metatungstate hydrate (AMT, >90 % WO_3 basis) was bought from Carl Roth. Iron (III)chloride hexahydrate (98 %), manganese (II) acetate tetrahydrate (99 %) and zinc acetylacetonate hydrate were purchased from abcr. Iron (III)acetylacetonate (>99 %) was bought from Acros, cobalt (II) carbonate (99 %) and zinc carbonate (basic, 97 %) form Alfa Aesar and Magnesium acetate tetrahydrate from Riedel-de Haën.

Synthesis of Oleate Precursors. Iron oleate was synthesized according to ref.[64] using potassium oleate instead of sodium oleate. A synthesis published for zinc oleate according to ref.[65], using potassium oleate instead of sodium oleate was used for the synthesis of manganese(II) oleate, using manganese(II) chloride.

Synthesis of (Transition-)Metal Tungstate Nanocrystals. The synthesis of metal tungstate NCs was performed according to our previously published synthesis route[66] with small variations. In general, 0.12 mmol ammonium metatungstate hydrate and 1.43 mmol of metal salt were dispersed in a combination of total 40 mmol oleic acid and oleylamine. Upon degassing at 100 °C, the solution was heated to 350 °C using a defined ramp. Details regarding the used metal salts, oleic acid to oleylamine ratio and heating rates are found in Table S8.5.1. After cooling down, the suspension was mixed with ethanol and centrifuged for 2 min at 9000 rpm. After two additional cleaning steps with dispersing in chloroform and precipitation in ethanol the NCs were dried at 70 °C for 18 h. All NCs were annealed at 300 °C for 5 h in air to remove residual organics before being used in biotests. Additionally, the NCs were washed to remove biologic contaminations and unreacted educts.

Microorganisms and growth conditions. *P. aeruginosa* PA14 and *P. gallaeciensis* (DSM 26640) were obtained from the 'Deutsche Sammlung für Mikroorganismen und Zellkulturen' (DSMZ, Braunschweig, Germany). *F. graminearum* was obtained of the lab of Prof. Dr. Eckhardt Thines (JGU Mainz, Germany). *P. aeruginosa* was cultivated aerobically in LB medium [1 % (w/v) NaCl; 1 % (w/v) tryptone; 0.5 % (w/v) yeast extract] at 30 °C. *P. gallaeciensis* was cultivated aerobically in marine broth 2216 (Thermo Fisher, Pittsburgh, USA) at 30 °C. *F. graminearum* was cultivated in HMG medium

[0.4 % (w/v) yeast extract; 1 % (w/v) malt extract; 1 % (w/v) glucose; pH = 5,5]. For preparation of agar plates, 1.5 % (w/v) agar was added to the respective medium.

6.5.1 Characterization

Transmission Electron Microscopy (TEM). For TEM imaging, one droplet (~20 µl) of a diluted solution of NCs (~0.1 mg/mL in chloroform or ethanol) was put onto a carbon-coated copper grid. Images were acquired with a FEI Tecnai G2 Spirit microscope equipped with a Gatan US1000 CCD camera at 120 kV. For further processing the program ImageJ was used.

Powder X-Ray Diffraction (PXRD). PXRD studies were carried out on a STOE Standi P using Mo Kα_1 radiation (λ = 0.7093 Å) and a Dectris Mythen 1k detector. The diffractograms were analyzed using Match!3 and plotted with Matlab2018b. All references were taken from the Crystallography Open Database (COD) or International Centre for Diffraction Data (ICDD) PDF database.

Surface colonization assay. Different materials (Glass, S235 structural steel, PETG, PE, PC and PS) were cut to a size of 1 cm^2, disinfected and placed in 24 well plates (Sarstedt, Nürnbrecht). *P. gallaeciensis* was then cultivated in 2216 medium over night at 30 °C. The cultures were then diluted in 2216, in a volume of 1 ml per Well (Sarstedt, Nürnbrecht) at a final OD_{600} of 0.5 and added to the several materials. The 24-well plates were then incubated for 72 h at 30 °C. Then, the materials were taken out of the wells, rinsed with water to get rid of the planktonic bacteria and stained with 1 % (w/v) crystal violet for 30 min. The materials were then washed twice to get rid of the unbound crystal violet. After drying overnight, the samples were treated with 30 % (v/v) acetic acid (Carl Roth, Karlsruhe) to solubilize the crystal violet solution and then quantified at 575 nm in a plate reader (Tecan, Salzburg).

Metal salt-dependent biofilm formation. *P. gallaeciensis* was cultivated in 2216 medium over night at 30 °C. The cultures were then diluted in 2216, in a volume of 1 ml per metal salt at a final OD_{600} of 0.5. $FeCl_2$, $MnCl_2$, $ZnCl_2$, $MgCl_2$, $CuCl_2$ and $CoCl_2$ (Carl Roth, Karlsruhe) were then prepared in different salt end concentrations (50 µM, 100 µM, 500 µM, 1000 µM) and added to the bacteria inside 96 well plates (Sarstedt, Nürnbrecht). The 96 well plate was then incubated for 72 h at 30 °C. Then, the microtiter plate was rinsed with water to remove the planktonic cells. After drying for 20 min, 135 µl of 1 % (w/v) crystal violet (Merck, Darmstadt) was added to the wells. After 30 min, the crystal violet was removed, and the plate was washed two times with water to remove the unbound crystal violet. After drying overnight, 135 µl of 30 % (v/v) acetic acid was added. Then, the absorbance was quantified in a plate reader (Tecan, Salzburg) at 575 nm.

Metal tungstate-dependent biofilm formation. For quantification of bacterial biofilm production, a modified method of previously published protocols was used.[67] Briefly, *P. gallaeciensis* and *P. aeruginosa* were incubated overnight aerobically in 2216 and LB medium, respectively. The cultures

were then diluted in their respective medium in a volume of 135 µl per well of a 96-well microtiter plate (Sarstedt, Nürnbrecht) at a final OD_{600} of 0.5. Additionally, metal tungstates were added to the wells at a final concentration of 0.1 mg/ml. Wells without metal tungstates and addition of their respective metal salts served as control. The plates were then incubated for 72 h at 30 °C. Then, the microtiter plates were measured in a plate reader (Tecan, Salzburg) at 600 nm to quantify the amount of the planktonic cells. After the measurement, the plates were rinsed with water to remove the planktonic cells. After letting the plates dry for 20 min, 135 µl of 1 % (w/v) crystal violet (Merck, Darmstadt) were added to the wells. After 30 min incubation at room temperature, unbound crystal violet was removed by gently submerging the plates two times in water. The plate was then air-dried overnight at room temperature. For quantification, 135 µl of 30 % (v/v) acetic acid (Carl Roth, Karlsruhe) was added to each well. The absorbance was then quantified in a plate reader (Tecan, Salzburg) at 575 nm.

Confocal laser scanning microscopy. *P. gallaeciensis* was cultivated in 2216 medium over night at 30 °C. The cultures were then diluted in 2216, in a volume of 10 ml per petri dish (Sarstedt, Nürnbrecht) for metal salt-dependent biofilm formation and 1 ml per well of a 24-well plate (Sarstedt, Nürnbrecht) for the surface colonization assay, at a final OD_{600} of 0.5. Additionally, $MnCl_2*4H_2O$ (Roth, Karlsruhe, Germany) or $FeCl_2*4H_2O$ (Roth, Karlsruhe, Germany) at a final concentration of 5 µM respectively were added to the dishes for the metal salt-dependent biofilm assay. The microscope slides were then added to the petri dishes. The petri dishes were then incubated for 72 h at 30 °C. For the surface colonization assay, different materials (Glass, S235 structural steel, PE, and PC) were cut to a size of 1 cm^2. The materials were then added to the bacteria in 24- well plates and incubated for 72 h at 30 °C. Then, the microscope slides and the materials were rinsed with water to remove the planktonic cells. Afterwards, the slides were placed in 10 ml of a combined SYTO 9 and propidium iodide solution (Thermo Fisher, Pittsburgh, USA) and incubated for 30 minutes at 30 °C. The materials were placed in 1 ml SYTO 9/ propidium iodide solution in 24-well plates. Then, the slides and materials were rinsed again with water and mounted on the microscope application. BF samples were examined on an Axio Imager 2 (Carl Zeiss, Jena, Germany). The fluorophore SYTO9 was visualized with an excitation of 470 nm while propidium iodide was visualized with an excitation of 558 nm. The images were then proceed using the ZEN 3.3 blue software.

6.6 References

1 N. R. Baddoo, *J. Constr. Steel Res.*, 2008, **64**, 1199–1206.

2 T. Misawa, K. Hashimoto and S. Shimodaira, *Corros. Sci.*, 1974, **14**, 131–149.

3 R. O. Adams, *J. Vac. Sci. Technol.*, 1983, **1**, 12–18.

4 S. J. Yuan, S. O. Pehkonen, Y. P. Ting, E. T. Kang and K. G. Neoh, *Ind. Eng. Chem. Res.*, 2008, **47**, 3008–3020.

5 H. Wang, L. Cai, Y. Li, X. Xu and G. Zhou, *Food Control*, 2018, **91**, 397–403.

6 R. Malhotra, B. Dhawan, B. Garg, V. Shankar and T. C. Nag, *Indian J. Orthop.*, 2019, **53**, 148–153.

7 S. E. Coetser and T. E. Cloete, *Crit. Rev. Microbiol.*, 2005, **31**, 213–232.

8 N. Kip and J. A. van Veen, *ISME J.*, 2015, **9**, 542–551.

9 D. Enning and J. Garrelfs, *Appl. Environ. Microbiol.*, 2014, **80**, 1226–1236.

10 S. Shafeeq, S. Pannanusorn, Y. Elsharabasy, B. Ramírez-Zavala, J. Morschhäuser and U. Römling, *FEMS Yeast Res.*, 2019, **19**, 1–13.

11 W. Dou, D. Xu and T. Gu, *Microb. Biotechnol.*, 2021, **14**, 803–805.

12 H.-C. Flemming and J. Wingender, *Nat. Rev. Microbiol.*, 2010, **8**, 623–633.

13 V. Vishwakarma, *J. Basic Microbiol.*, 2020, **60**, 198–206.

14 A. Bridier, R. Briandet, V. Thomas and F. Dubois-Brissonnet, *Biofouling*, 2011, **27**, 1017–1032.

15 S. H. Yoon, N. Rungraeng, W. Song and S. Jun, *J. Food Eng.*, 2014, **131**, 135–141.

16 I. Banerjee, R. C. Pangule and R. S. Kane, *Adv. Mater.*, 2011, **23**, 690–718.

17 A. K. Epstein, A. I. Hochbaum, P. Kim and J. Aizenberg, *Nanotechnology*, 2011, **22**, 494007.

18 K. Autumn, M. Sitti, Y. A. Liang, A. M. Peattie, W. R. Hansen, S. Sponberg, T. W. Kenny, R. Fearing, J. N. Israelachvili and R. J. Full, *Proc. Natl. Acad. Sci. U.S.A.*, 2002, **99**, 12252–12256.

19 A. B. Tesler, P. Kim, S. Kolle, C. Howell, O. Ahanotu and J. Aizenberg, *Nat. Commun.*, 2015, **6**, 8649.

20 F. Hizal, N. Rungraeng, J. Lee, S. Jun, H. J. Busscher, H. C. van der Mei and C.-H. Choi, *ACS Appl. Mater. Inter.*, 2017, **9**, 12118–12129.

21 G. Gao, D. Lange, K. Hilpert, J. Kindrachuk, Y. Zou, J. T. J. Cheng, M. Kazemzadeh-Narbat, K. Yu, R. Wang, S. K. Straus, D. E. Brooks, B. H. Chew, R. E. W. Hancock and J. N. Kizhakkedathu, *Biomaterials*, 2011, **32**, 3899–3909.

22 A. K. Epstein, T.-S. Wong, R. A. Belisle, E. M. Boggs and J. Aizenberg, *Proc. Natl. Acad. Sci. U.S.A.*, 2012, **109**, 13182–13187.

23 K. Herget, H. Frerichs, F. Pfitzner, M. N. Tahir and W. Tremel, *Adv. Mater.*, 2018, e1707073.

24 B. Albada and N. Metzler-Nolte, *Acc. Chem. Res.*, 2017, **50**, 2510–2518.

25 M. Wegener, M. J. Hansen, A. J. M. Driessen, W. Szymanski and B. L. Feringa, *J. Am. Chem. Soc.*, 2017, **139**, 17979–17986.

26 W.-L. Ng and B. L. Bassler, *Annu. Rev. Genet.*, 2009, **43**, 197–222.

27 R. S. Smith and B. H. Iglewski, *J. Clin. Invest.*, 2003, **112**, 1460–1465.

28 B. Sels, D. de Vos, M. Buntinx, F. Pierard, A. Kirsch-De Mesmaeker and P. Jacobs, *Nature*, 1999, **400**, 855–857.

29 V. Conte and B. Floris, *Dalton Trans.*, 2011, **40**, 1419–1436.

30 K. Herget, P. Hubach, S. Pusch, P. Deglmann, H. Götz, T. E. Gorelik, I. A. Gural'skiy, F. Pfitzner, T. Link, S. Schenk, M. Panthöfer, V. Ksenofontov, U. Kolb, T. Opatz, R. André and W. Tremel, *Adv. Mater.*, 2017, **29**, 1603823 (1-8).

31 H. Frerichs, E. Pütz, F. Pfitzner, T. Reich, A. Gazanis, M. Panthöfer, J. Hartmann, O. Jegel, R. Heermann and W. Tremel, *Nanoscale*, 2020, **12**, 21344–21358.

32 J. Wu, X. Wang, Q. Wang, Z. Lou, S. Li, Y. Zhu, L. Qin and H. Wei, *Chem. Soc. Rev.*, 2019, **48**, 1004–1076.

33 H. Wei and E. Wang, *Chem. Soc. Rev.*, 2013, **42**, 6060–6093.

34 K. P. Rumbaugh and K. Sauer, *Nat. Rev. Microbiol.*, 2020, **18**, 571–586.

35 K. Sauer, M. C. Cullen, A. H. Rickard, L. A. H. Zeef, D. G. Davies and P. Gilbert, *J. Bacteriol.*, 2004, **186**, 7312–7326.

36 A. Timmins and S. P. de Visser, *Catalysts*, 2018, **8**, 314.

37 D. Sheng and M. H. Gold, *Arch. Biochem. Biophys.*, 1997, **345**, 126–134.

38 A. Butler, *Curr. Opin. Chem. Biol.*, 1998, **2**, 279–285.

39 V. M. Martínez, G. de Cremer, M. B. J. Roeffaers, M. Sliwa, M. Baruah, D. E. de Vos, J. Hofkens and B. F. Sels, *J. Am. Chem. Soc.*, 2008, **130**, 13192–13193.

40 R. Gomeringer, R. Kilgus, V. Menges, S. Oesterle, T. Rapp, C. Scholer, A. Stenzel, A. Stephan and F. Wieneke, *Tabellenbuch Metall. Mit Formelsammlung*, Europa-Lehrmittel, Haan-Gruiten, 48th edn., 2019.

41 M. R. Seyedsayamdost, R. J. Case, R. Kolter and J. Clardy, *Nat. Chem.*, 2011, **3**, 331–335.

42 C. C. C. R. de Carvalho, *Front. Mar. Sci.*, 2018, **5**, 1–11.

43 L. A. Finney and T. V. O'Halloran, *Science*, 2003, **300**, 931–936.

44 R. B. Thurman, C. P. Gerba and G. Bitton, *Crit. Rev. Environ. Sci. Technol.*, 1989, **18**, 295–315.

45 S. W. J. Gould, M. D. Fielder, A. F. Kelly, M. Morgan, J. Kenny and D. P. Naughton, *Ann. Microbiol.*, 2009, **59**, 151–156.

46 C.-L. Chen, J. S. Maki, D. Rittschof and S. L.-M. Teo, *Int. Biodeterior. Biodegradation*, 2013, **83**, 71–76.

47 S. Yu, Q. Wei, T. Zhao, Y. Guo and L. Z. Ma, *Appl. Environ. Microbiol.*, 2016, **82**, 6403–6413.

48 G. Zhou, L.-J. Li, Q.-S. Shi, Y.-S. Ouyang, Y.-B. Chen and W.-F. Hu, *Can. J. Microbiol.*, 2014, **60**, 5–14.

49 D. H. Nies, *Appl. Microbiol. Biotechnol.*, 1999, **51**, 730–750.

50 M. Mergeay, D. Nies, H. G. Schlegel, J. Gerits, P. Charles and F. van Gijsegem, *J. Bacteriol.*, 1985, **162**, 328–334.

51 J. Silva, E. N. Codaro, R. Z. Nakazato and L. Hein, *Appl. Surf. Sci.*, 2005, **252**, 1117–1122.

52 A. Bonneau, B. Roche and I. J. Schalk, *Sci. Rep.*, 2020, **10**, 120.

53 E. Schechtel, R. Dören, H. Frerichs, M. Panthöfer, M. Mondeshki and W. Tremel, *Langmuir*, 2019, **35**, 12518–12531.

54 K. V. Korpany, D. D. Majewski, C. T. Chiu, S. N. Cross and A. S. Blum, *Langmuir*, 2017, **33**, 3000–3013.

55 T. D. Schladt, K. Schneider, H. Schild and W. Tremel, *Dalton Trans.*, 2011, **40**, 6315–6343.

56 P. Daniel, S. I. Shylin, H. Lu, M. N. Tahir, M. Panthöfer, T. Weidner, A. Möller, V. Ksenofontov and W. Tremel, *J. Mater. Chem. C*, 2018, **6**, 326–333.

57 W. Kaim and B. Schwederski, *Bioanorganische Chemie. Zur Funktion chemischer Elemente in Lebensprozessen*, Teubner, Wiesbaden, 4th edn., 2005.

58 E. Banin, M. L. Vasil and E. P. Greenberg, *Proc. Natl. Acad. Sci. U.S.A.*, 2005, **102**, 11076–11081.

59 B. B. Lanter, K. Sauer and D. G. Davies, *mBio*, 2014, **5**, e01206-14.

60 J. P. Cowen, G. J. Massoth and E. T. Baker, *Nature*, 1986, **322**, 169–171.

61 M. S. Hussain, M. Kwon and D.-H. Oh, *PLoS One*, 2018, **13**, e0200958.

62 Y.-M. Cai, A. Hutchin, J. Craddock, M. A. Walsh, J. S. Webb and I. Tews, *Sci. Rep.*, 2020, **10**, 6232.

63 O. Frank, S. Pradella, M. Rohde, C. Scheuner, H.-P. Klenk, M. Göker and J. Petersen, *Stand. Genomic Sci.*, 2014, **9**, 914–932.

64 J. Park, K. An, Y. Hwang, J.-G. Park, H.-J. Noh, J.-Y. Kim, J.-H. Park, N.-M. Hwang and T. Hyeon, *Nat. Mater.*, 2004, **3**, 891–895.

65 W. S. Chiu, P. S. Khiew, D. Isa, M. Cloke, S. Radiman, R. Abd-Shukor, M. H. Abdullah and N. M. Huang, *Chem. Eng. J.*, 2008, **142**, 337–343.

66 R. Dören, B. Leibauer, M. A. Lange, E. Schechtel, L. Prädel, M. Panthöfer, M. Mondeshki and W. Tremel, *Nanoscale*, 2021, **13**, 8146–8162.

67 G. A. O'Toole, *J. Vis. Exp.*, 2011, 1–3.

7. Conclusions

The goal of this work was to establish new syntheses for tungsten oxide nanocrystals that can easily be reproduced and adapted for other nanocrystal syntheses. For this purpose, a fundamental understanding of the underlying processes had to be established and the influence of different parameters were to be evaluated. It was found that, next to the solvent ratio of oleic acid and oleylamine, the heating rate and the precursor concentration is a crucial factor for the selectivity of either WO_{3-x} nanorods or hexagonal ammonium tungsten bronze nanocrystals from ammonium metatungstate. Both types of nanomaterials grow from the same nucleation species via oriented attachment. By identifying the condensation product of oleic acid and oleylamine, namely oleyl oleamide, as surface active and phase selective species, production of gram-scale batches of nanocrystals is possible.

The tungsten oxide-based nanocrystals can show a partial reduction from W^{6+}, resulting in a strong absorption of near-infrared light by the nanocrystals, associated with localized surface plasmon resonance. As all nanocrystals display anisotropic growth, a splitting of the plasmonic band in a transversal and a longitudinal band can be observed. The maximum of the bands increases with greater aspect ratio of the nanocrystals.

In this work, WO_{3-x} nanorods were found as active catalysts for the selective oxidation of organic sulfides towards sulfoxides using aqueous hydrogen peroxide within short reaction times. The catalysis was performed in methanolic solution, and the turnover was observed by an in-situ NMR method. Excess of water reduced the reactivity, as water blocks the negatively charged tungsten oxide surfaces and is in concurrence with hydrogen peroxide. Moreover, one advantage of those nanorods is the negligible overoxidation towards sulfones within the timescale of hours. Within days however, the oxidation towards sulfones was quantitative. Annealing of the nanocrystals was needed to remove surfactants and water from the surface before they could be used in catalysis. A temperature of 300 °C was determined as optimum. Additionally, the catalyst could be successfully recycled five times without loss of activity. A variety of sulfides were tested, and aliphatic sulfides exert the fastest reaction, while aromatics slow the reaction. Electron withdrawing groups lower the reaction speed additionally, while electron donating substituents improve the reaction speed compared to non-substituted aromatics. The hexagonal ammonium tungsten bronze nanocrystals show significantly less activity, but a similar selectivity towards sulfoxides. Ceria nanocrystals, tested under similar conditions, display less overall activity, but a significantly faster reaction of sulfoxides to sulfones than sulfides to sulfoxides.

During the synthesis evaluation of WO_{3-x} nanorods, inconsistencies were observed when using an older batch of oleic acid stored in a steel canister. These nanocrystals were smaller, and no

traces of hexagonal ammonium tungsten bronze were detected. As this oleic acid showed a reddish-brown color, iron was suspected to be leaching from the steel canister into the oleic acid. To simulate this effect, as synthesized iron-oleate was used as an additive to pure oleic acid. Syntheses with high iron concentration led to formation of iron tungstate nanocrystals with ferberite structure. By using a different iron precursor, iron acetylacetonate, an iron tungstate structure unknown to literature can be observed next to ferberite. It is possible to synthesize this structure near pure by using oleyl oleamide as solvent as well as iron acetylacetonate or iron oleate precursors. By comparison with known structures, two reported magnesium tungstate phases with tetragonal and trigonal structure were the only ones showing similarities, although detailed structural descriptions were missing. Hence, this magnesium tungstate phase was synthesized as reference and its structure was applied as a basis for the determination of a structural model of the new iron tungstate phase. Ongoing research involves the structural identification of both magnesium and iron tungstate structures by automated electron diffraction tomography and high-resolution transmission electron microscopy. The main goal is to present a detailed structural description of both systems for the first time.

Moreover, hexagonal cesium tungsten bronze nanocrystals were synthesized by the addition of 0.3 equivalents cesium carbonate to tungsten bronze synthesis. These crystals partially show a hexagonal disk structure, in contrast purely rectangular ammonium tungsten bronze. It was possible to produce smaller nanocrystals with tetrahedral shape by increasing the oleylamine content, without observing WO_{3-x} nanorods as a side product. However, significant impurity of pyrochlore-type cubic cesium tungsten bronze was observed when using a high oleylamine to oleic acid ratio. Increasing the Cs content to 0.6 per W yields pure cubic cesium tungsten bronze. It was found that, besides WO_{3-x} nanorods, the pure cubic cesium tungsten bronze shows reasonable catalytic activity for oxidative bromination in a phenol red assay, indicating a haloperoxidase enzyme mimetic activity. Based on those results, the biofilm inhibiting properties of the WO_{3-x} nanorods, as well as for cubic cesium tungsten bronze, against *Pseudomonas aeruginosa*, a prominent bacterium responsible for nosocomial infections, were investigated. Furthermore, a peroxidase-like activity can be observed against the fungus *Fusarium graminearum*. Here, both nanocrystals showed similar inhibition in the fungal growth. However, especially for WO_{3-x} NRs, a significant reduction of mycelium growth is observed, which results in successfully suppressing the fungal distribution via spores. Additionally, the anti-micro-bacterial properties of different plasmonic tungsten oxide nanomaterials were investigated. It was found that especially the mixed hexagonal/cubic cesium tungsten bronzes show strong absorption in the visible to near-infrared spectra of light. By using irradiation of 950 nm, the growth of different nosocomial (*P. aeruginosa*, *S. aureus*) and marine bacteria (*P. gallaeciensis*) can be reduced by 30 to 35 % with respect to the not-irradiated sample. This effect is attributed to hyperthermia based on the absorption of NIR light by the nanocrystals.

In a final project, the biofilm formation on steel surfaces was investigated. On steel surfaces, the biofilm formation of the marine bacterium *P. gallaeciensis* was increased by nearly 300 %, compared to glass or polymeric surfaces. As the most prominent components of steel are iron and manganese, their separate influence towards the biofilm formation was investigated and both exhibited a significant promoting influence for growth and biofilm formation of several bacteria. In this context, different tungstate materials were investigated towards their respective influence. In accordance with the results for their salt, the manganese tungstate nanocrystals show a significantly higher growth of planktonic cells of *P. gallaeciensis* than the control experiment without nanocrystals. However, the biofilm formation is significantly reduced. The same effect can be observed for iron tungstate nanocrystals, but with slightly smaller impact. For nosocomial relevant *P. aeruginosa* the same opposing effects are observed, indicating a genal influence towards Gram-negative bacteria. A potential explanation for the effect is the nurturing effect of iron and manganese towards such bacteria. By mimicking the presence of nutrient with their surface, the nanocrystals could induce biofilm dispersion by absorbing relevant siderophores to their surfaces.

In summary, a great variety of tungsten oxide-based nanocrystals could be synthesized by tuning reaction parameters of a general heat up synthesis using oleic acid and oleylamine as solvents. The resulting nanocrystals show promising properties as organic catalysts and antibiotic agents. Further investigation has to be applied to find the underlying mechanisms of the crystallite formation, which can then be used to tailor the nanocrystal-properties for certain applications. Additionally, the identity of several NCs has to be further evaluated to gain knowledge of their structure. This work demonstrates that many and even inconspicuous parameters can lead to unexpected results, which proves that an open eye and critical analysis of results and even unwanted impurities can lead to positive results. Those on the other hand can lead to new perspectives and can open pathways for new research topics.

8. Appendix

8.1 Supporting Information for Chapter 2

The following chapter 8.1 is reproduced from Nanoscale, 2021, 13, 8146-8162, DOI: 10.1039/d0nr09055g with permission from the Royal Society of Chemistry.

8.1.1 Author Contributions

Conception and design of the study:

[redacted]

Preparation of samples and acquisition of data:

[redacted] – preparation of samples

[redacted] – TEM measurements

[redacted] – PXRD measurements

[redacted] – NMR measurements

[redacted] – UV-Vis-NIR measurements

[redacted] – XPS measurements

[redacted] – ζ-potential measurements

Analysis and interpretation of data:

[redacted] – PXRD diffraction and refinements

[redacted] – TEM images

[redacted] – NMR spectroscopy

[redacted] – UV-Vis-NIR spectroscopy, ζ-potential

[redacted] – XPS spectroscopy

Drafting of the supporting information:

[redacted]

Revising the supporting information critically for important intellectual content:

[redacted]

Preparation of figures:

[redacted]

Table S8.1.1. Overview of synthesis for nanorods (**NR-X**), HATB (**ATB-X**), synthesis with ODE (**ODE-X**) and oleyl oleamide (**Amid-X**) with reaction conditions and estimated ratio of WO_{3-x} and HATB. (c) indicates cleaned particles.

Particle Label	**HOAc:OAm:ODE / mmol**	**n(AMT) / mmol**	**Heating Rate / K/min**	**Stirring speed / rpm**	**% HATB (compared to WO_{3-x})**
NR-1	20:20:0	0.12	5	500	<2
NR-2	22.5:17.5:0	0.12	5	500	<2
NR-3	25:15:0	0.12	5	500	<2
NR-4	30:10:0	0.12	5	500	<2
NR-5	40:0:0	0.12	5	500	<2
NR-6	17.5:22.5:0	0.12	5	500	<2
NR-7	15:25:0	0.12	5	500	<2
NR-8	10:30:0	0.12	5	500	<2
NR-9	0:40:0	0.12	5	500	<2
NR-10	20:20:0	0.12	2.5	500	<2
NR-11	20:20:0	0.12	10	500	<5
NR-12[a]	20:20:0	0.12	5	500	<2
NR-13[b]	20:20:0	0.12	5	500	<2
NR-14	20:20:0	0.36	2,5	1000	50:50
NR-15	20:20:0	0.24	1	800	<4
NR-16	40:40:0	0.48	1	800	<10
ODE-1	10:10:20	0.12	5	500	<10
ODE-2	5:5:30	0.12	5	500	<5
ODE-3	2.5:2.5:35	0.12	5	500	<2
ODE-4	0:0:40	0.12	5	500	n.d.
ATB-1	20:20:0	0.24	5	500	40-80
ATB-2(c)	20:20:0	0.36	5	500	80-90(>90)
ATB-3	22.5:17.5:0	0.24	5	500	<2
ATB-4	25:15:0	0.24	5	500	<2
ATB-5	17.5:22.5:0	0.24	5	500	<5
ATB-6	15:25:0	0.24	5	500	<2
ATB-7	20:20:0	0.24	10	500	70-90
ATB-8	20:20:0	0.24	2.5	500	<10

ATB-9	20:20:0	0.24	10	0	>90
ATB-10	20:20:0	0.24	10	200	>85
ATB-11	20:20:0	0.24	10	1000	<20
ATB-12(c)	20:20:0	0.24	25	150	>95 (>98)
ATB-13(c)	40:40:0	0.48	25	150	>95 (>98)
ATB-14	20:20:0	0.12	25	150	>70
ATB-15(c)	20:20:0	0.36	25	150	>95 (>98)
ATB-16	15:25:0	0.24	25	150	40-60
ATB-17	25:15:0	0.24	25	150	>90
Amide-1	20 mmol amide[c]	0.12	5	500	<2
Amide-2	20 mmol amide[c]	0.36	5	500	<5
Amide-3	20 mmol amide[c]	0.24	25	150	>90
Amide-4	11 g amide[d]	0.12	5	500	<2
Amide-5	10 g amide[d] + 4.5 mmol OAm	0.12	5	500	<2
Amide-6	10 g amide[d] + 4.5 mmol OAm	0.24	25	150	>95

a. 15 min at 350 °C, b. 60 min at 350 °C, c. oleyl oleamide (OAd) synthesized hydrothermally without purification d. Reaction solution of NR-1 containing a ratio of ~87:13 OAd:HOAc (approximately 4.9 mmol HOAc for 11 g).

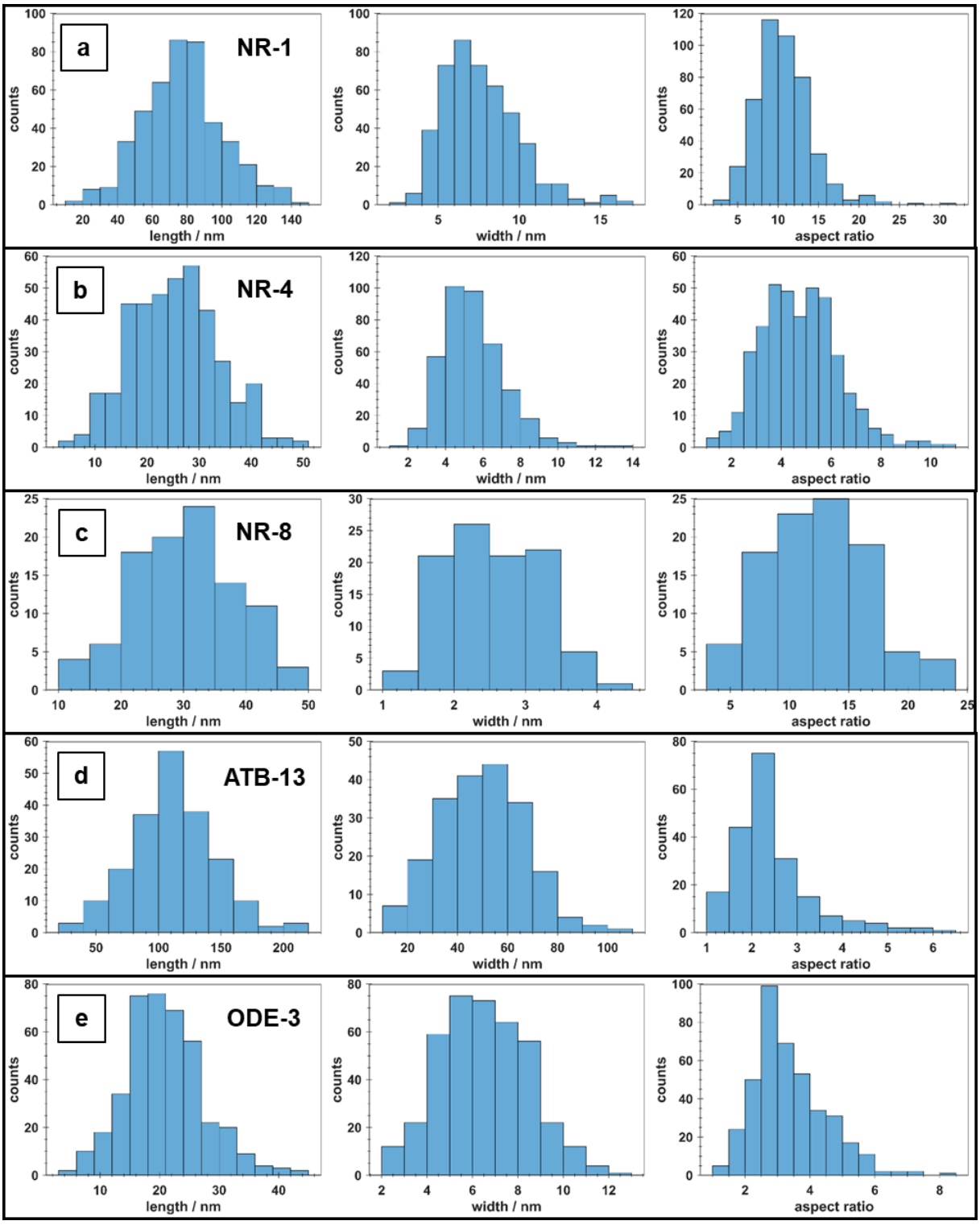

Figure S8.1.1. Length (left), width (mid) and AR (right) histograms for a) **NR-1**, b) **NR-4**, c) **NR-8**, d) **ATB-13** and e) **ODE-3** particles. Corresponding average values are given in Table 2.2.

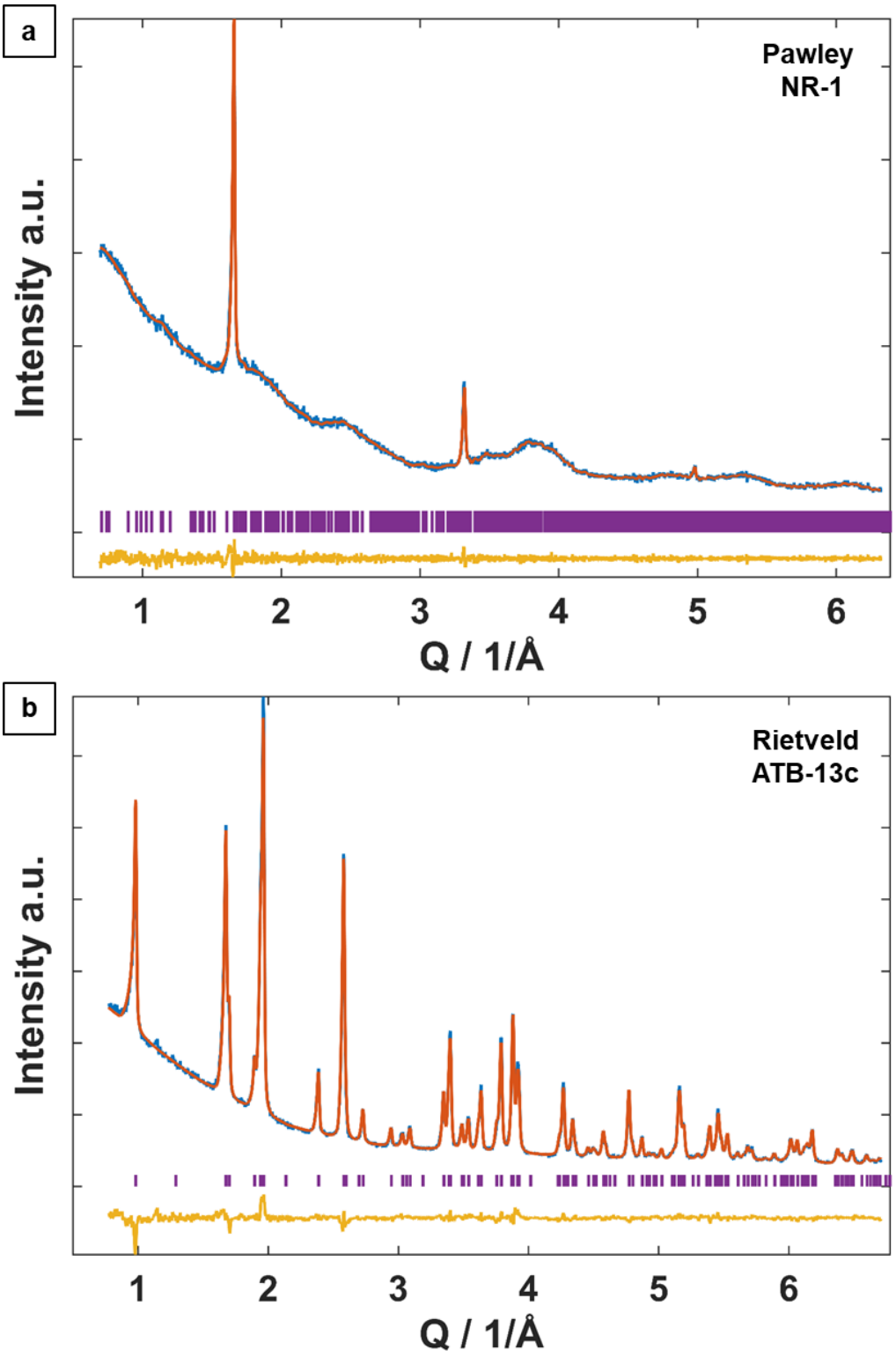

Figure S8.1.2. a) Pawley Refinement of **NR-1** (WO_{3-x} nanorods) using space group P2/m, angles α=β=90 °, γ=115.21 ° and an anisotropic shape description for the crystallite size and b) Rietveld refinement of **ATB-13c** (h-ATB) based on $K_{0.26}WO_3$ with space group $P6_3$ and angles α=β=90 °, γ=120 °, preferred orientation along [020]. NH_4^+ content was fixed at 0.2 per tungsten. Potential impurities due to WO_{3-x} cannot be ruled out. Lattice parameters are compiled in Table S3.

Table S8.1.2. Refinement data for different pure samples from Rietveld and Pawley refinements.

sample	a / Å	b / Å	c / Å	cryst. Size	r_wp (gof)
NR-1[a]	18.51	3.79	14.25	6.8*84.7*9.6[c]	2.35 (1.05)
NR-4[a]	18.31	3.79	14.06	3.8*39.1*5.0[c]	2.30 (1.08)
NR-8[a]	18.20	3.80	14.00	2.5*27.6*2.2[c]	2.46 (1.11)
Amide-1[a]	18.32	3.78	14.05	5.3*71.5*6.5[c]	2.93 (1.02)
Amide-2[a]	18.32	3.79	14.03	6.0*82.8*7.9[c]	2.92 (1.02)
ATB-12c[b]	7.39	= a	7.51	49.8	3.78 (1.19)
ATB-13c[b]	7.39	= a	7.50	60.3	3.42 (1.05)
ATB-15c[b]	7.39	= a	7.50	50.5	4.94 (1.22)

a. Pawley refinement of nanorods with α=β=90 °, γ=115.21

b. Rietveld refinement of h-ATB with α=β=90 °, γ=120 °

c. anisotropic crystallite size calculated by a quadratic form for a*b*c.

Table S8.1.3. Assignment of Miller-Indices from HATB/$WO_{2.72}$ references towards phase mixture of sample **ATB-1** ($WO_{2.72}$: COD, Entry No.: 96-152-8167, $(NH_4)_{0.25}WO_3$: ICDD, PDF Entry No.: 01-073-1084, $(NH_4)_{0.33}WO_3$: ICDD, PDF Entry No.: 00-042-0452)

Q / 1/Å (Intensity a.u.) Sample ATB-1	**hkl (Ref $WO_{2.72}$)**	**hkl (Intensity a.u.) (Ref $(NH_4)_{0.25}WO_3$)**	**hkl (Intensity a.u.) (Ref $(NH_4)_{0.33}WO_3$)**
0.98 (714.3)	-	100	100
1.67 (1000)	010	002	002
1.89 (417.9)	-	111	111
1.95 (712.9)	-	200	102/200
2.38 (303.8)	-	112	112
2.57 (500.5)	-	202	202
3.32 (278.8)	020	004	004
3.39 (281.1)	-	302/202	220
3.61 (216.6)	-	213	-
3.78 (306.6)	-	222	222
3.87 (316.3)	-	204	204
3.91 (264.8)	-	312	400
4.26 (203.2)	-	402	402
4.32 (162.3)	-	313	313
4.56 (153.5)	-	411	411
4.76 (202.7)	-	224	412?
4.86 (154.0)	-	314	-
5.15 (194.8)	-	413/404	-
5.18 (168.4)	-	331/502	-
5.37 (161.9	-	206/332/225	-
5.44 (183.7)	-	422	-

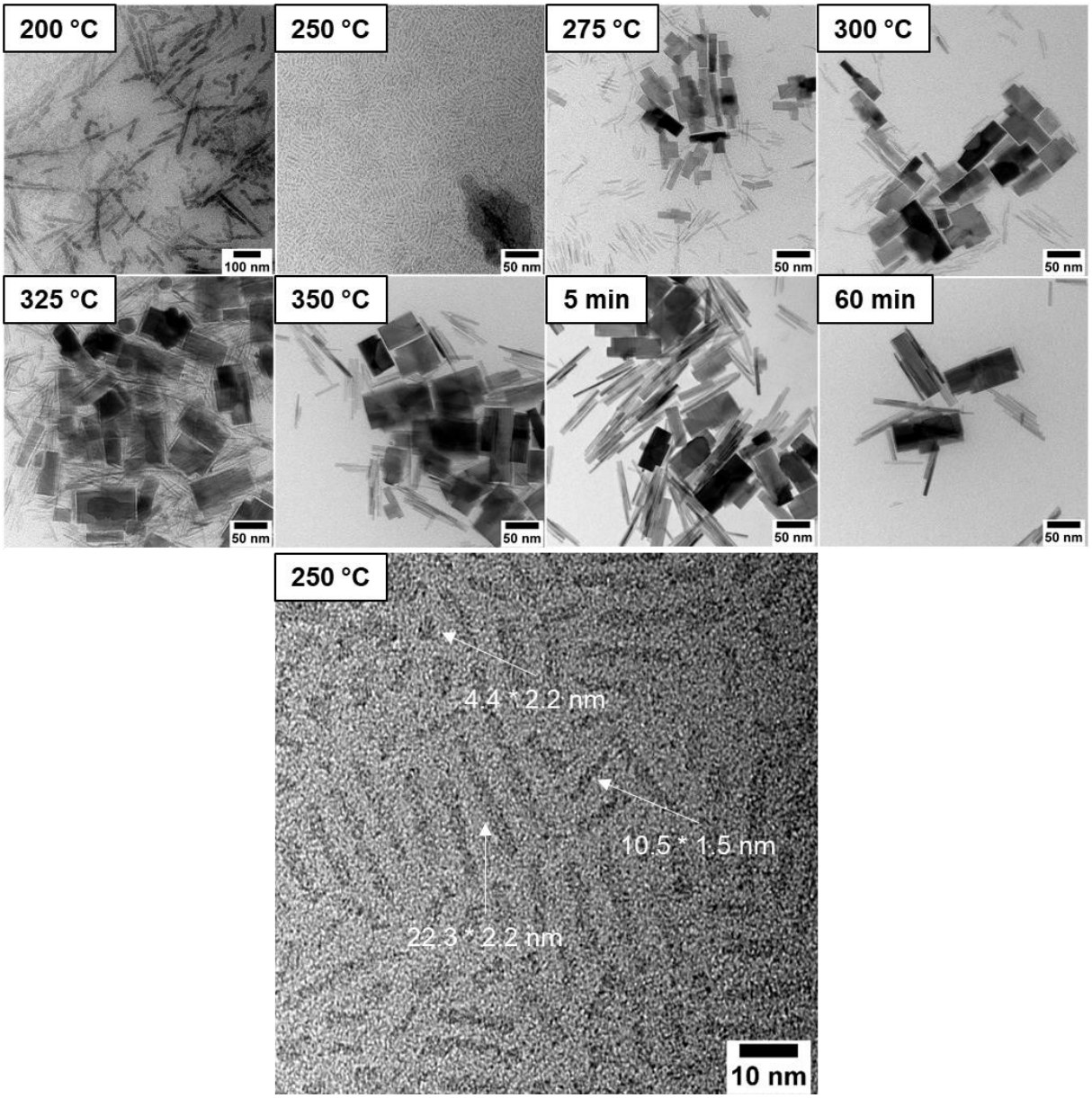

Figure S8.1.3. TEM images of the reaction solution for **ATB-1** at different temperature steps as well as at different points of time of the final temperature of 350 °C. HR-TEM image of rods found at 250 °C with size of selected particles.

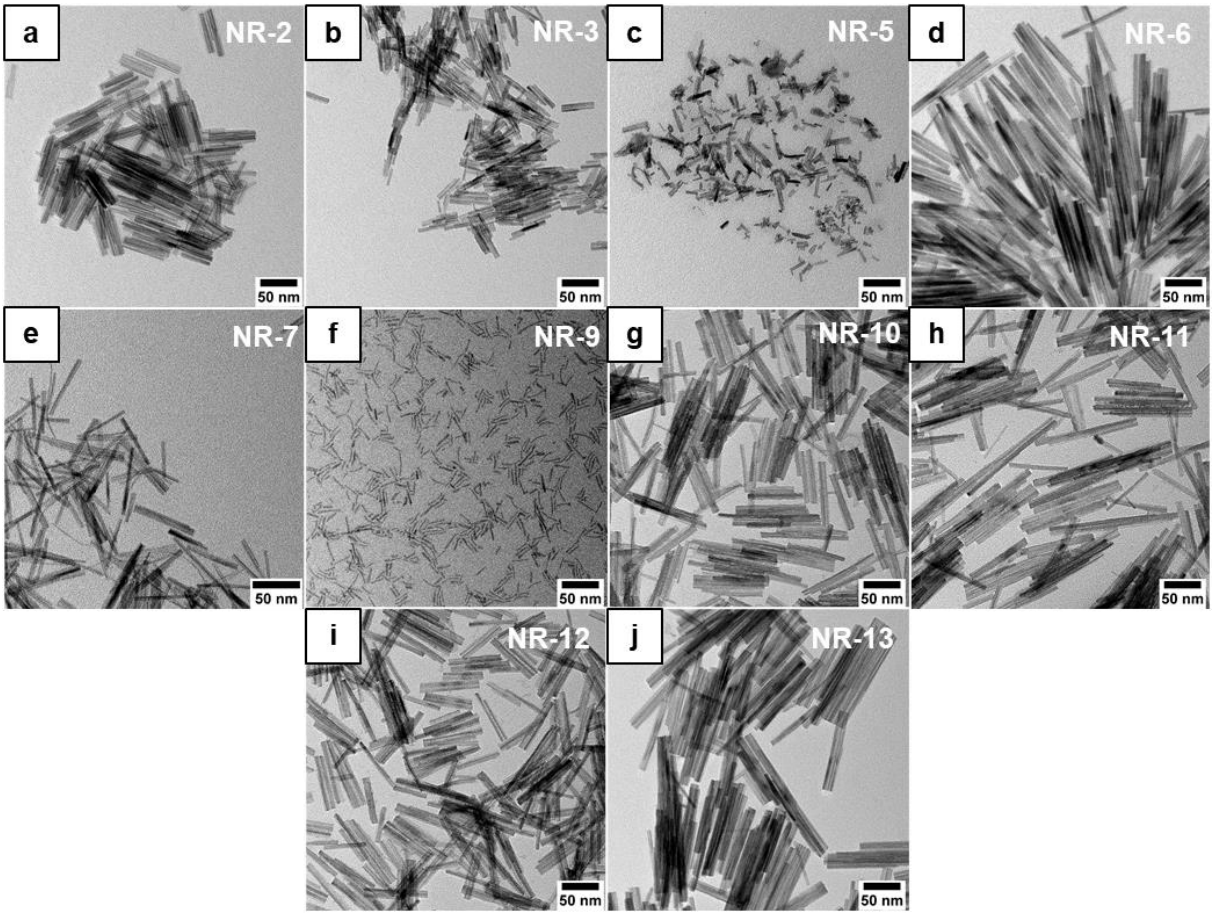

Figure S8.1.4. TEM images of WO_{3-x} nanorods based on the standard synthesis (**NR-1**) with different HOAc:OAm ratios a) 22.5:17.5 mmol (**NR-2**), b) 25:15 mmol (**NR-3**), c) 40:0 mmol (**NR-5**), d) 17.5:22.5 mmol (**NR-6**), e) 15:25 mmol (**NR-7**) and f) 0:40 mmol (**NR-9**) as well as 20:20 mmol HOAc:OAm with heating rate of g) 2.5 K/min (**NR-10**), h) 10 K/min (**NR-11**), i) 15 min at 350 °C (**NR-12**) and j) 60 min at 350 °C (**NR-13**).

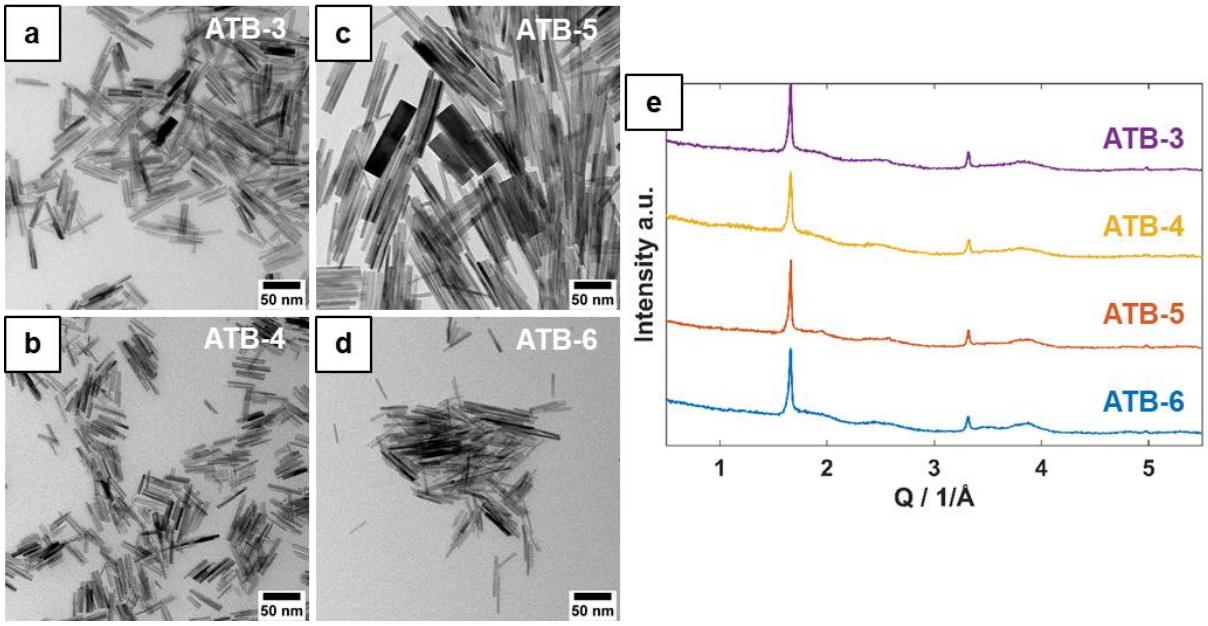

Figure S8.1.5. TEM images of particles with according to **ATB-1** standard synthesis (Table S8.1.1) with different HOAc/OAm ratios. a) 22.5:17.5 mmol (**ATB-3**), b) 25:15 mmol (**ATB-4**), c) 17.5:22.5 mmol (**ATB-5**), d) 15:25 mmol (**ATB-6**) and e) the corresponding PXRD-patterns of (a-d)

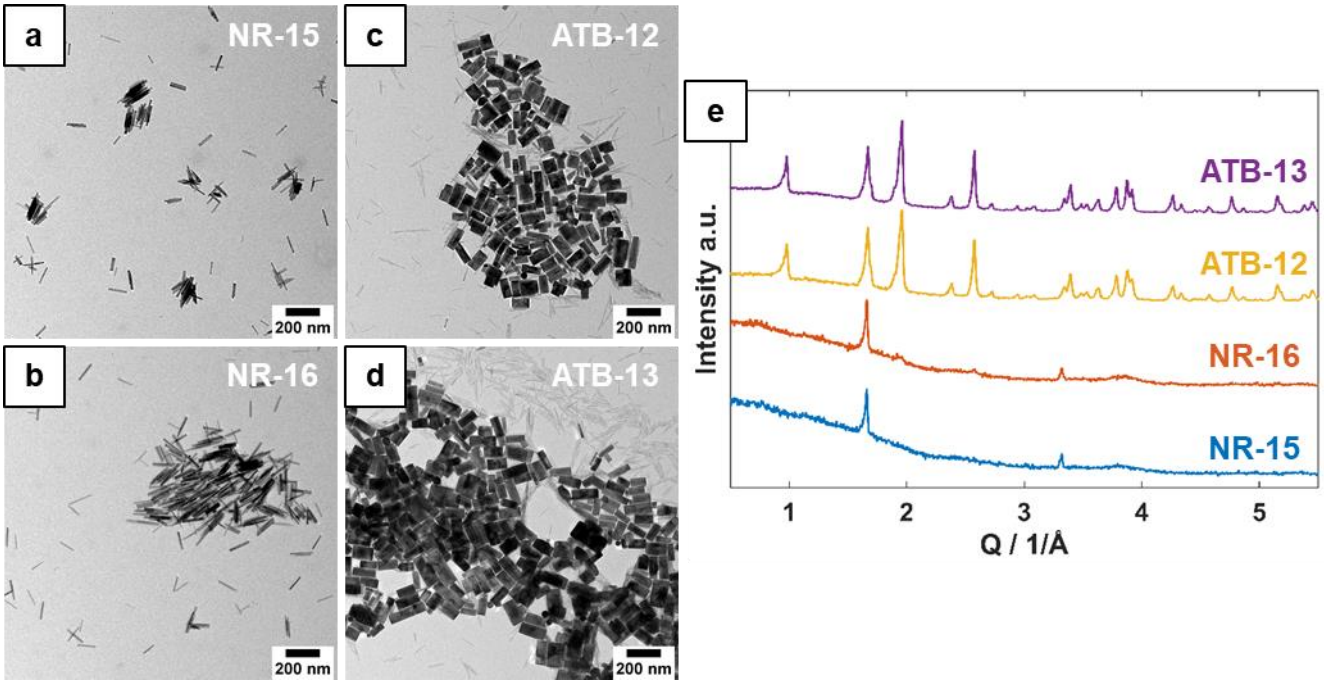

Figure S8.1.6. TEM images of upscaled synthesis a) **NR-15**, b) **NR-16**, c) **ATB-12**, d) **ATB-13** and e) corresponding PXRD patterns.

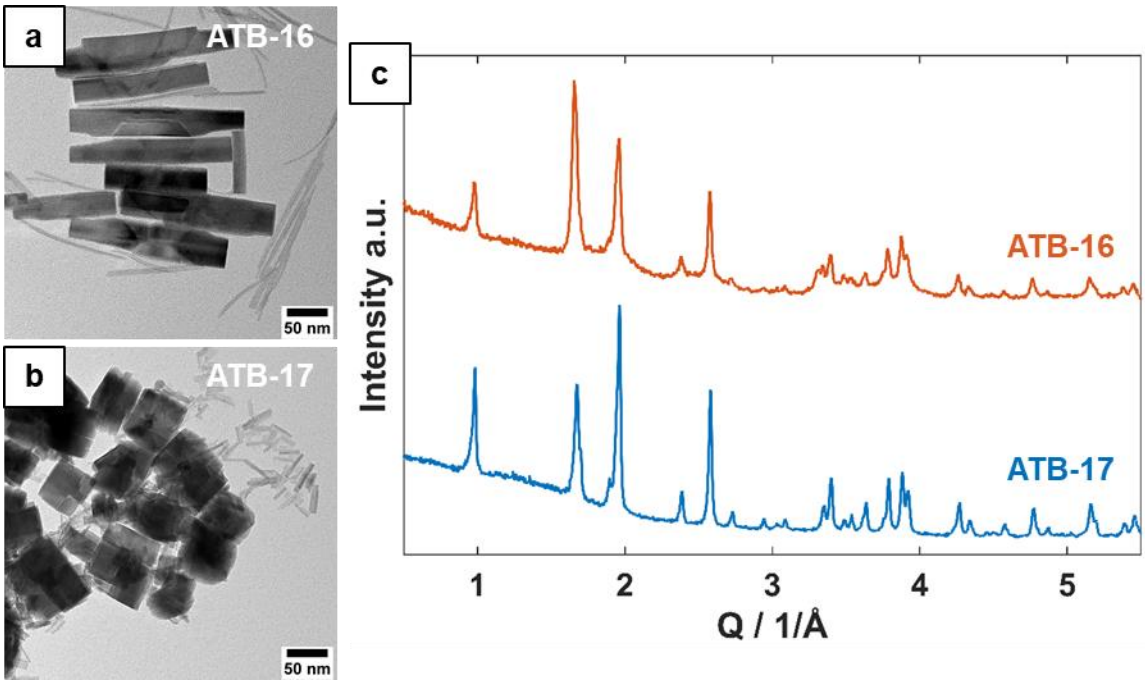

Figure S8.1.7. TEM images of particles with according to optimized bronze synthesis (**ATB-12)** with different HOAc/OAm ratios a) 15:25 mmol (**ATB-16**), b) 25:15 mmol (**ATB-17**) and c) the corresponding PXRD-patterns of a) and b).

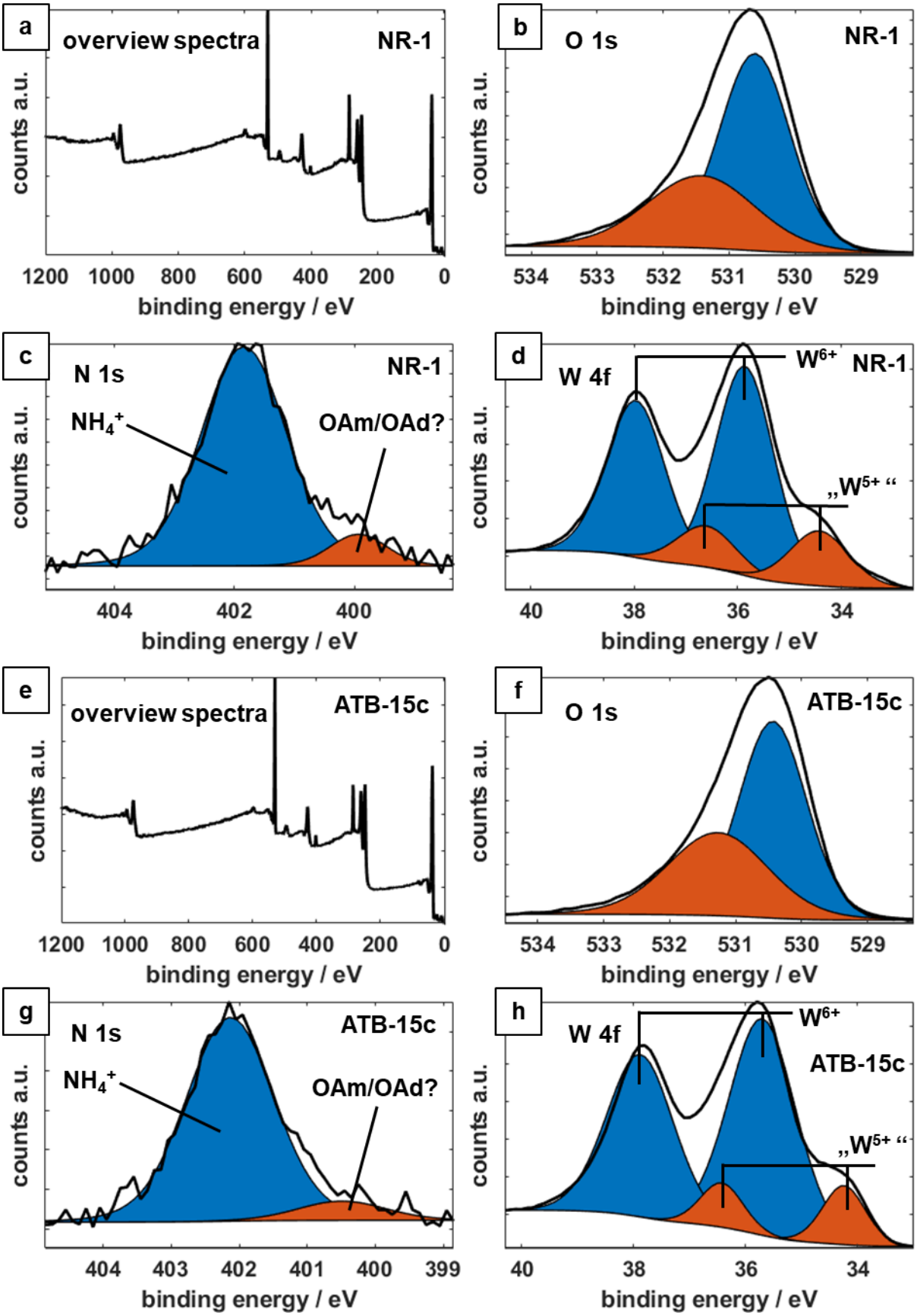

Figure S8.1.8. XPS Spectra of (a-d) WO_{3-x} (**NR-1**) particles (e-f) and h-ATB (**ATB-15c**) particles, showing overview spectra, O 1s, N 1s and W 4f core level.

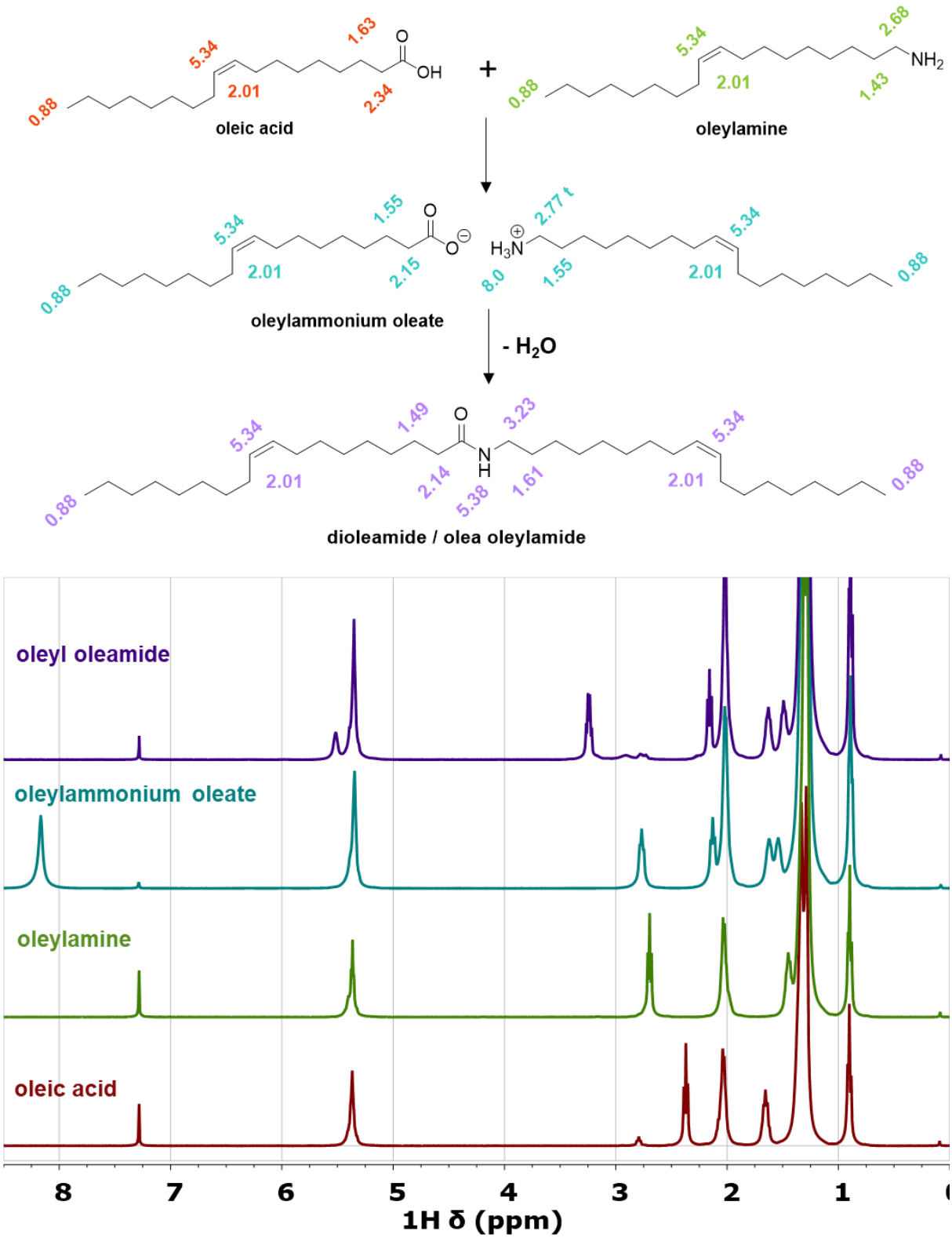

Figure S8.1.9. Reaction of oleic acid and oleylamine to oleylammoniumoleat and condensation towards oleyl oleamide with respective ^{1}H-NMR spectra measured in $CDCl_3$.

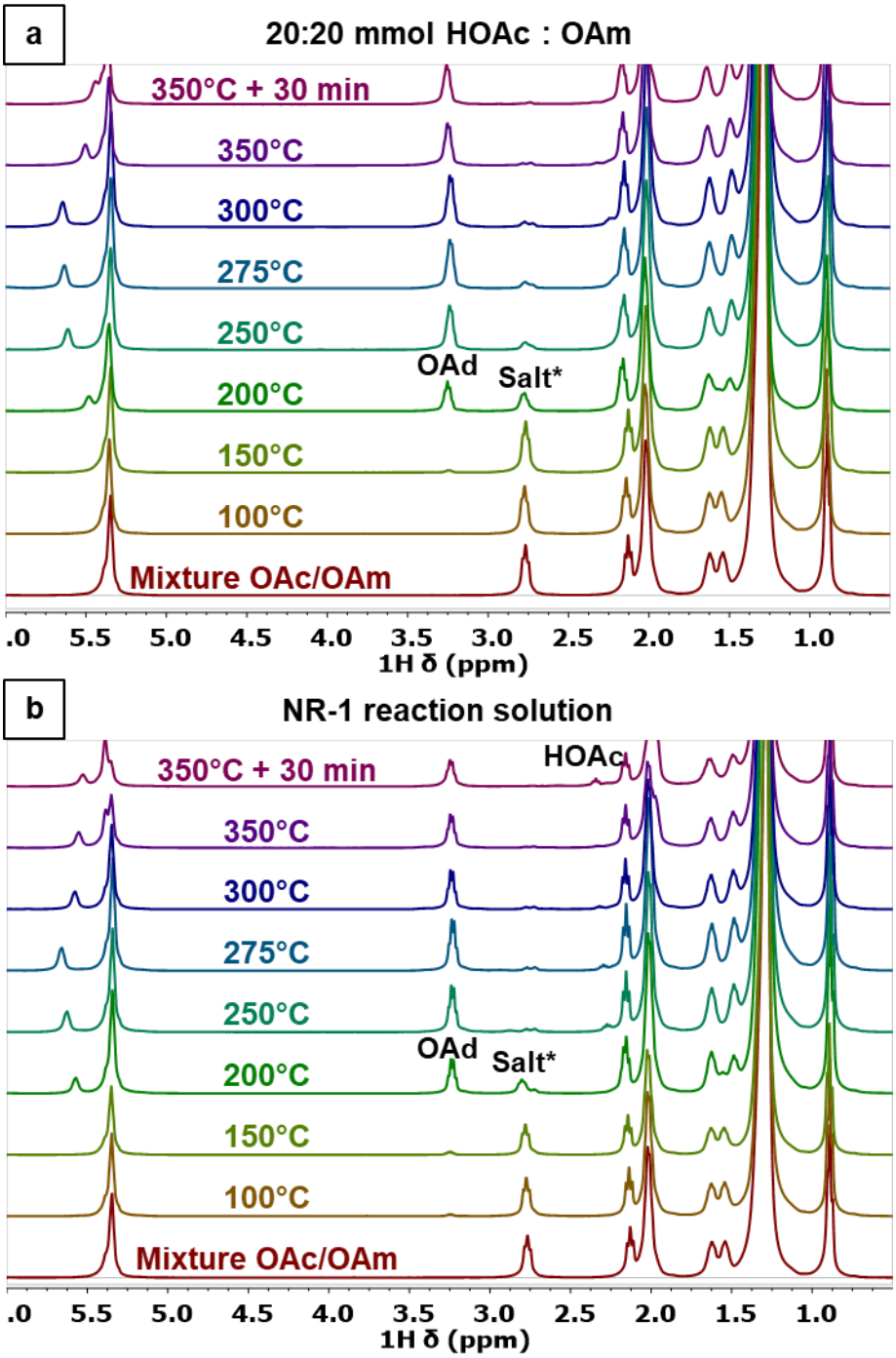

Figure S8.1.10. ^{1}H-NMR kinetics of a reaction solution according to **NR-1** at different temperatures a) without and b) with AMT. In both cases the immediate formation of oleylammoniumoleate (salt*) from HOAc and OAm is observed, as well as the progressing formation of oleyl oleamide (OAd). For (b) we observe free HOAc at the end of the reaction although all HOAc/OAm was bound as OAd before, indicating cleavage of the amide by WO_{3-x} NRs.

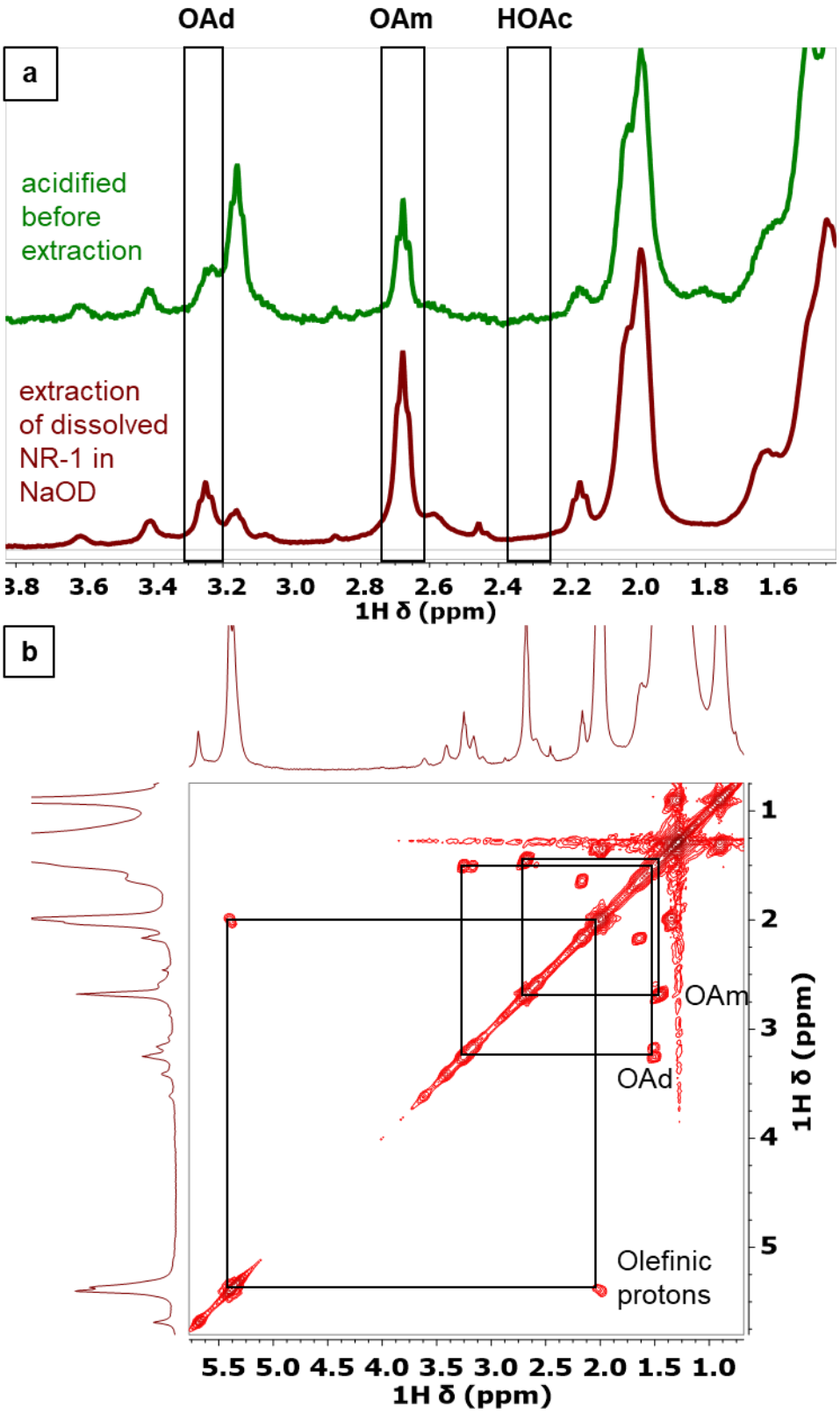

Figure S8.1.11. a) ^{1}H-NMR spectra of **NR-1** particles dissolved in 6.7 M NaOD and extracted with 0.5 ml $CDCL_3$ (maroon) after acidification of the NaOD solution with DCl and then again extracted with 0.5 ml $CDCl_3$ (green) and b) COSY spectra of basic extraction. All spectra show peaks of OAd and OAm, as well as small amounts of undefined byproducts, but no traces of HOAc.

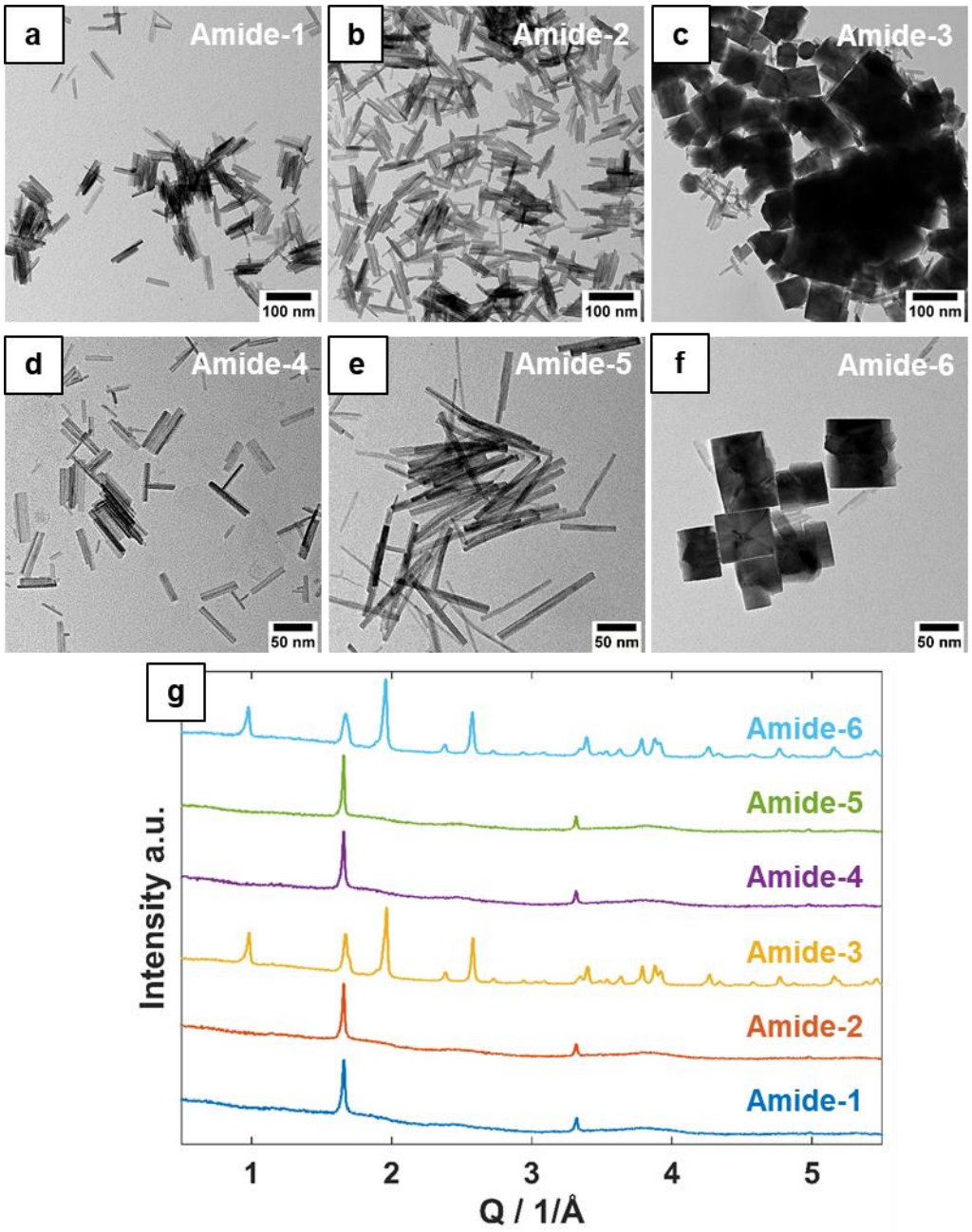

Figure S8.1.12. Particles synthesized with oleyl oleamide instead of the HOAc/OAm couple, a) using **NR-1** conditions (**Amide-1**), b) with threefold (0.36 mmol) AMT **(Amide-2)**, c) using **ATB-12** conditions (**Amide-3**) and synthesis reusing **NR-1** reaction solution d) under **NR-1** conditions (**Amide-4**), e) with addition of OAm under **NR-1** conditions (**Amide-5**), f) with addition of OAm under **ATB-12** conditions (**Amide-6)** and g) PXRD patterns of the particles shown in (a-f).

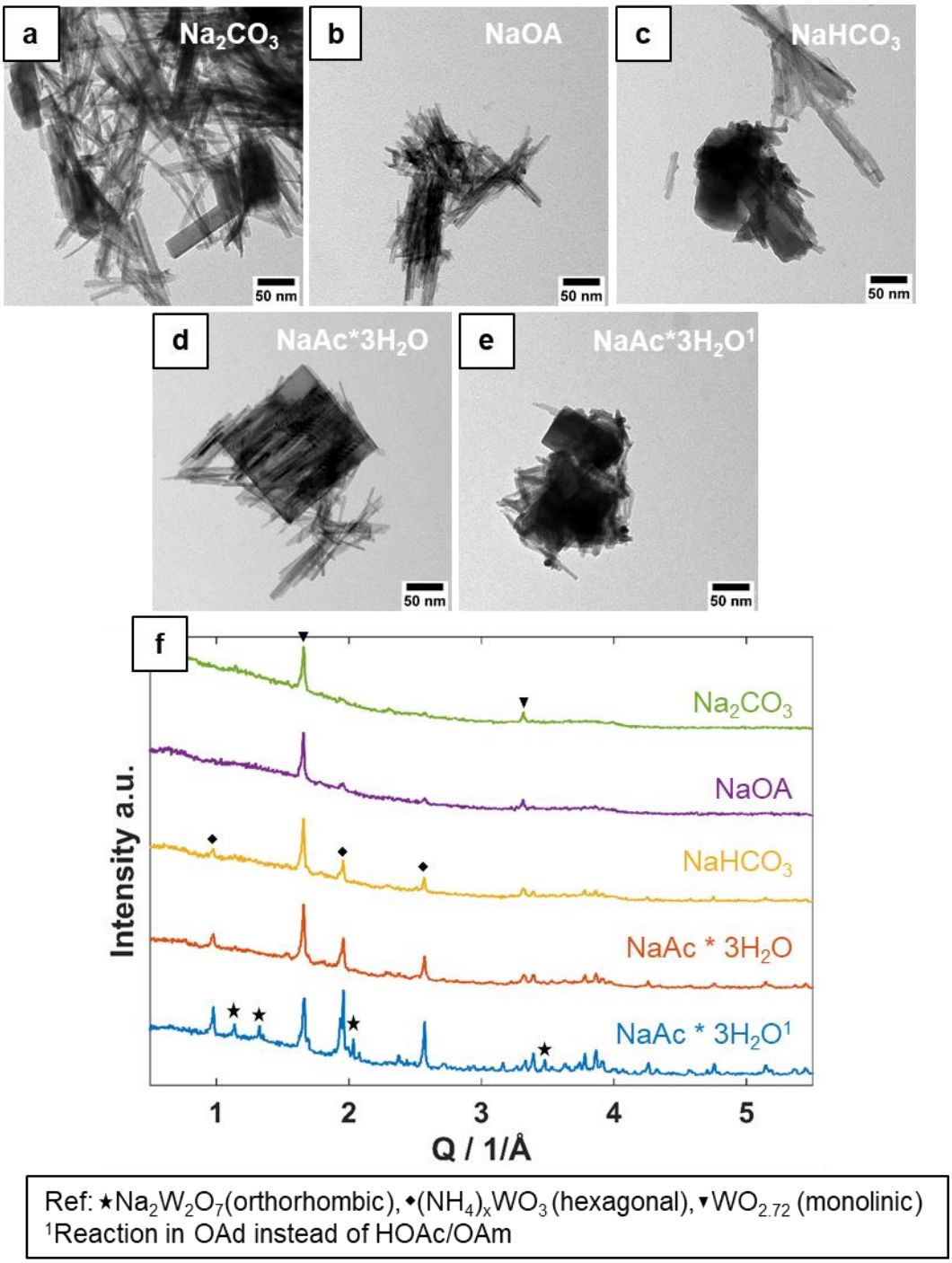

Figure S8.1.13. TEM images of particles with according to optimized bronze synthesis (**ATB-12)** with addition of different sodium salts (0.3:1 Na:W) a) disodium carbonate, b) sodium oleate, c) sodium hydrogen carbonate, d), sodium acetate trihydrate, e) sodium acetate trihydrate in OAd f) the corresponding PXRD-patterns of (a-e).

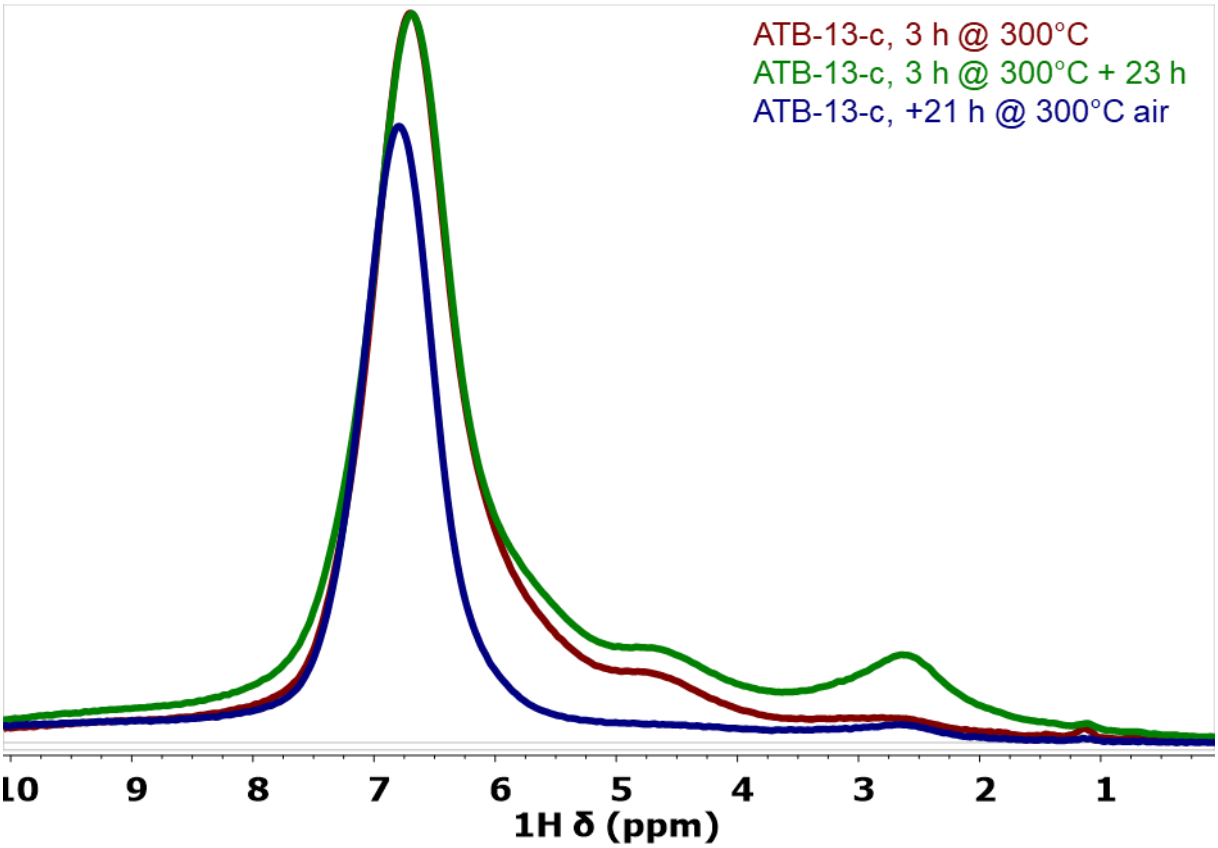

Figure S8.1.14. MAS ^{1}H-NMR spectra of **ATB 13-c** particles after 3 h at 300 °C in air, (directly measured, maroon), after 23 h in air and after additional annealing at 300 °C (air) for 21 h.

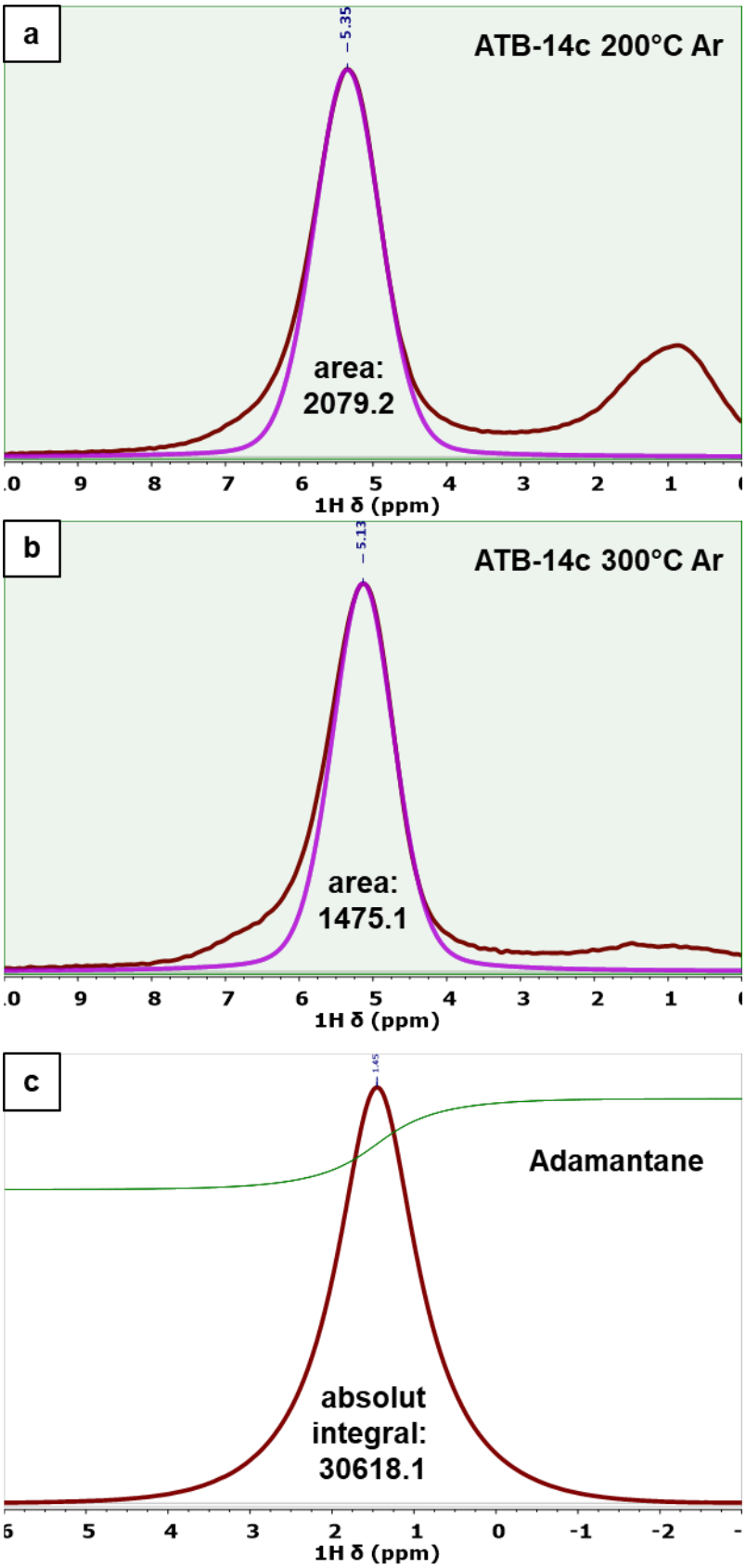

Figure S8.1.15. Deconvolution of NH_4^+ signal of a) ATB-14c for 5 h at 200 °C and b) ATB-14c for 5 h at 300 °C and c) ^{1}H-NMR spectra of adamantane. Samples measured with the same receiver gain, rotor and referenced towards external adamantane standard. Sample weights were taken into account.

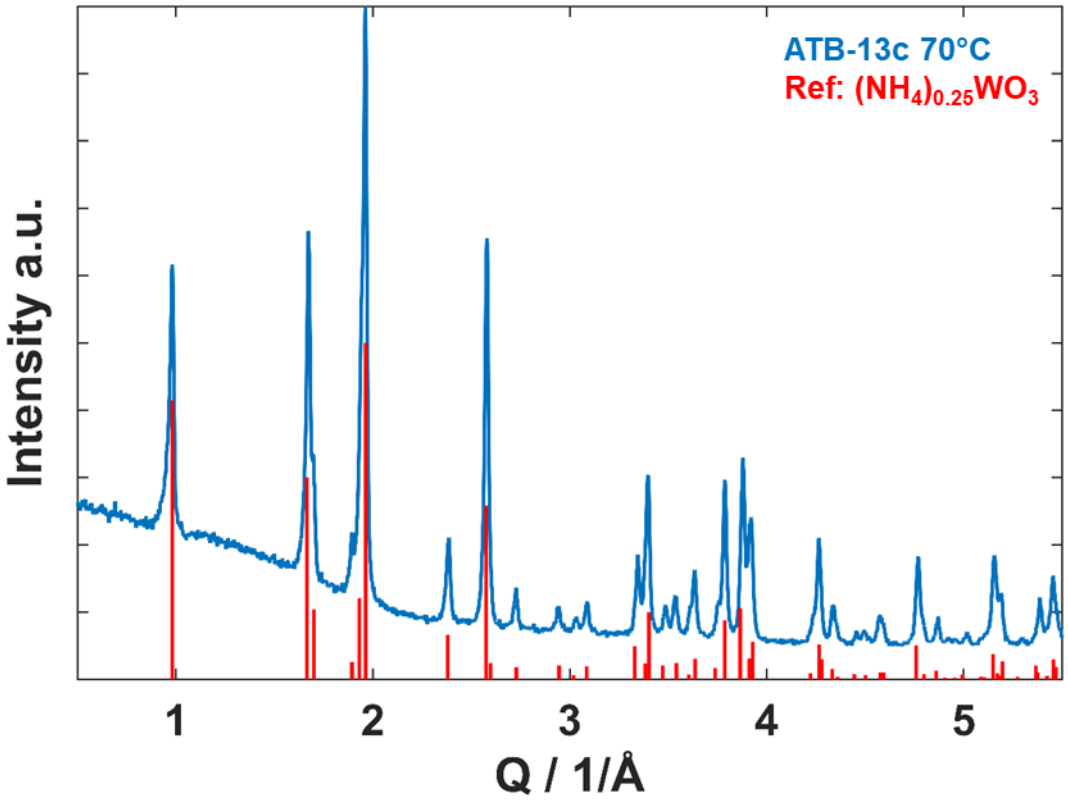

Figure S8.1.16. PXRD pattern of **ATB-13c** 70 °C with $(NH_4)_{0.25}WO_3$ Reference ($P6_3/mcm$, ICDD, PDF Entry No.: 01-073-1084).

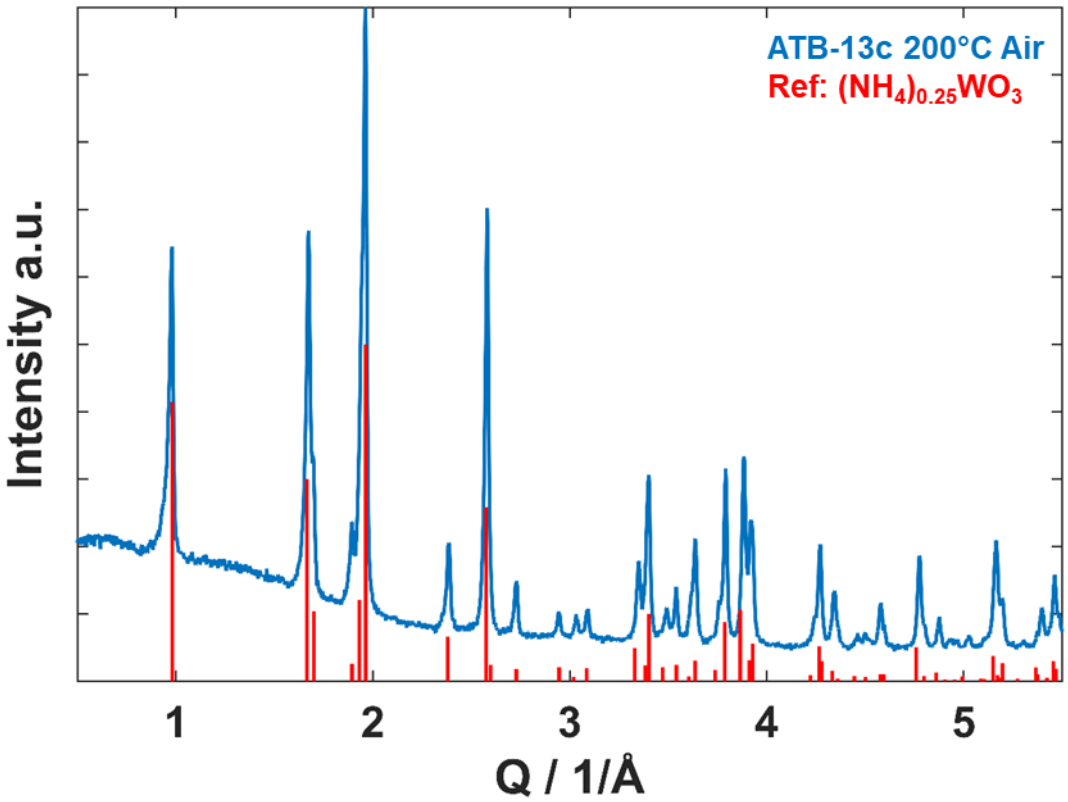

Figure S8.1.17. PXRD pattern of **ATB-13c** 200 °C (Air) with $(NH_4)_{0.25}WO_3$ reference ($P6_3/mcm$, ICDD, PDF Entry No.: 01-073-1084).

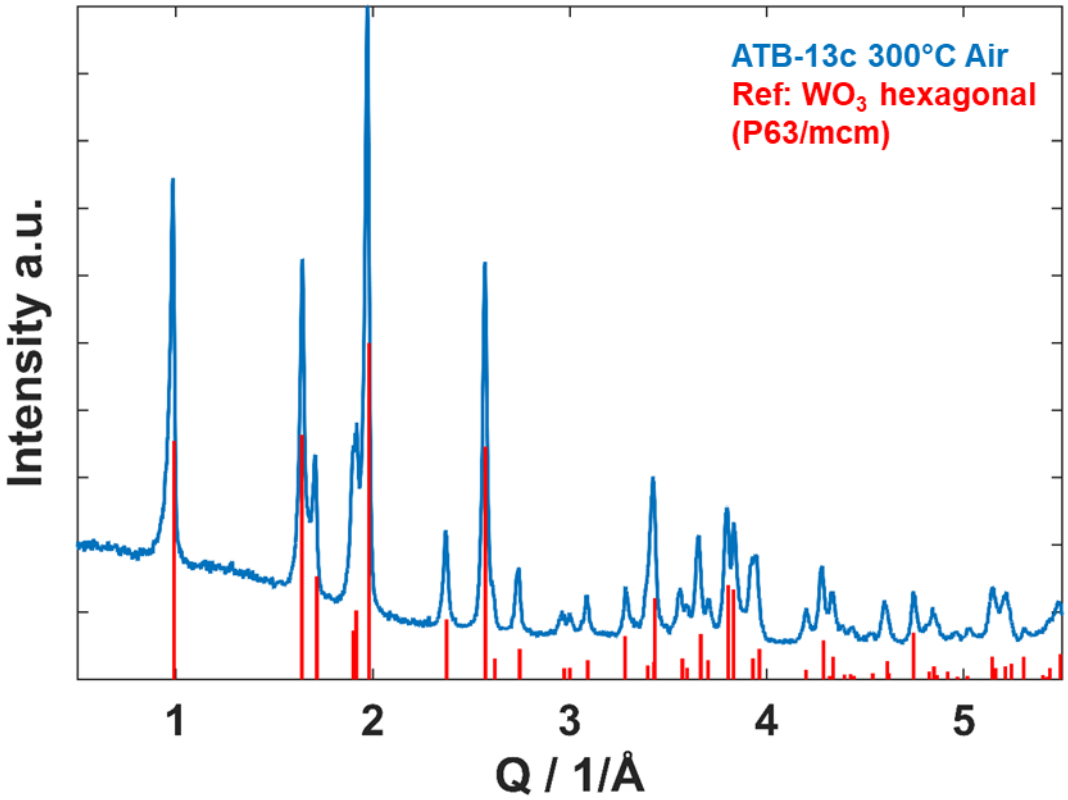

Figure S8.1.18. PXRD pattern of **ATB-13c** 300 °C (Air) with hexagonal WO_3 reference ($P6_3/mcm$, ICSD, Entry No.: 99-503-1860).

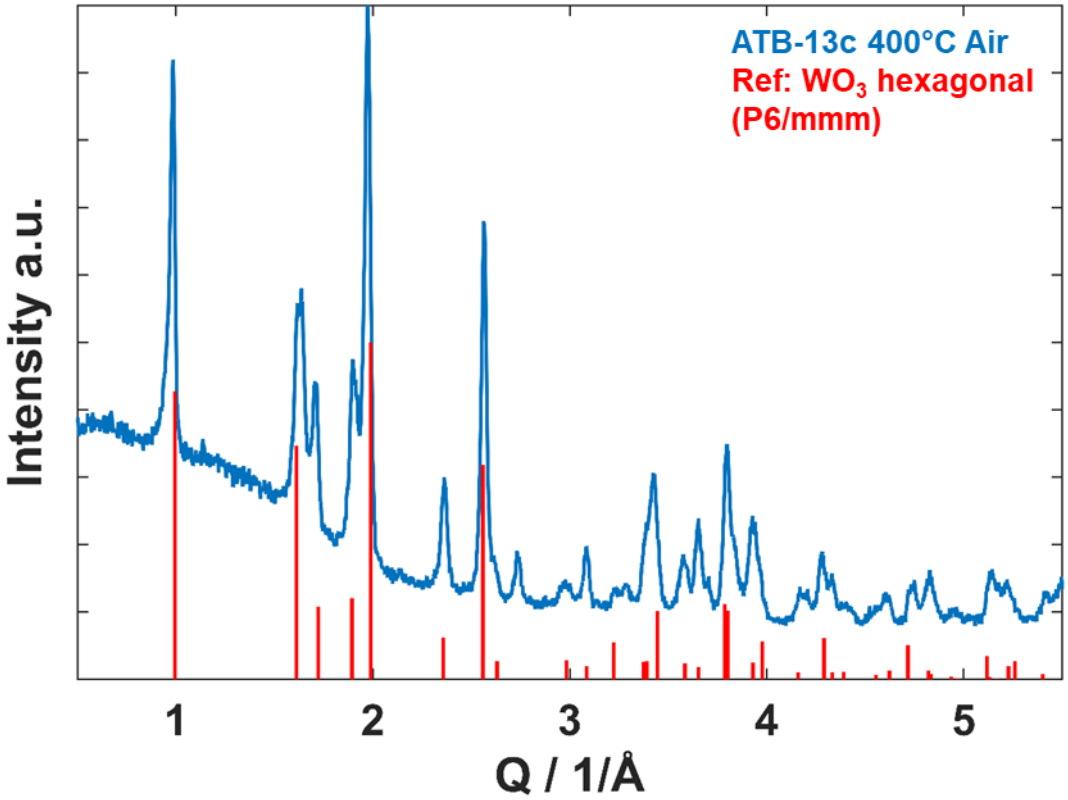

Figure S8.1.19. PXRD pattern of **ATB-13c** 400 °C (Air) with hexagonal WO_3 reference (P6/mmm, ICSD, Entry No.: 99-501-1286).

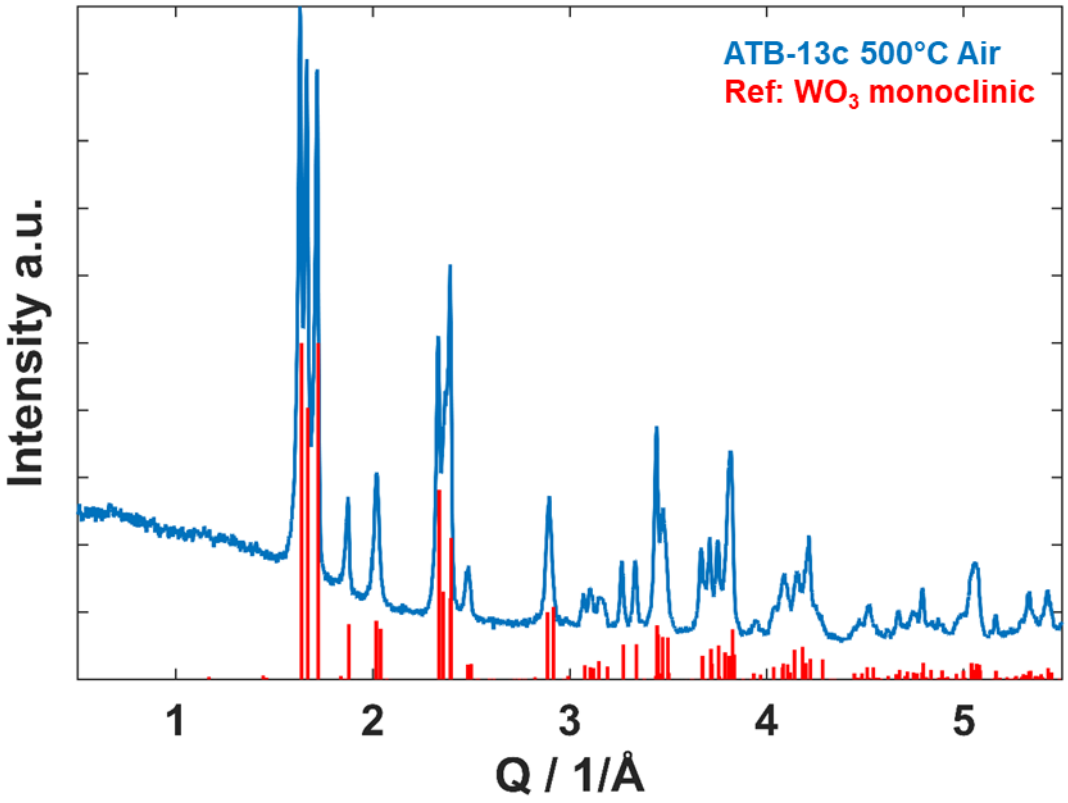

Figure S8.1.20. PXRD pattern of **ATB-13c** 500 °C (Air) with monoclinic WO_3 reference ($P2_1/n$, COD, Entry No.: 96-152-8916.

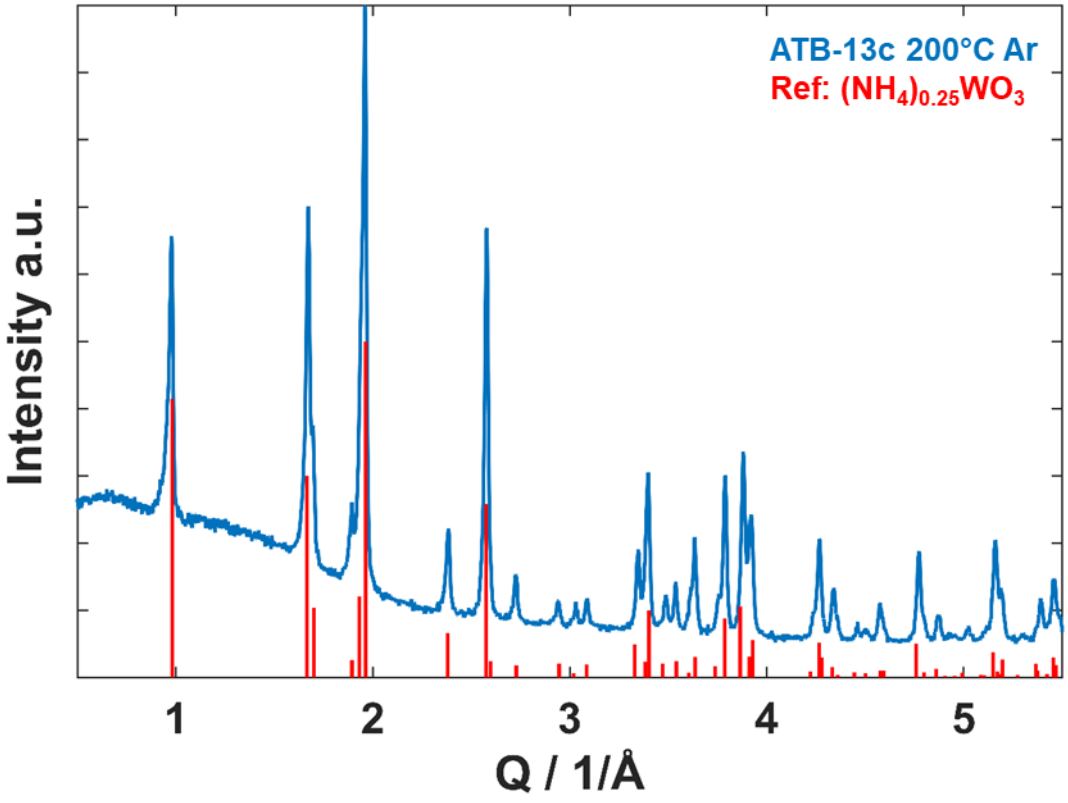

Figure S8.1.21. PXRD pattern of **ATB-13c** 200 °C (Ar) with $(NH_4)_{0.25}WO_3$ reference ($P6_3/mcm$, ICDD, PDF Entry No.: 01-073-1084).

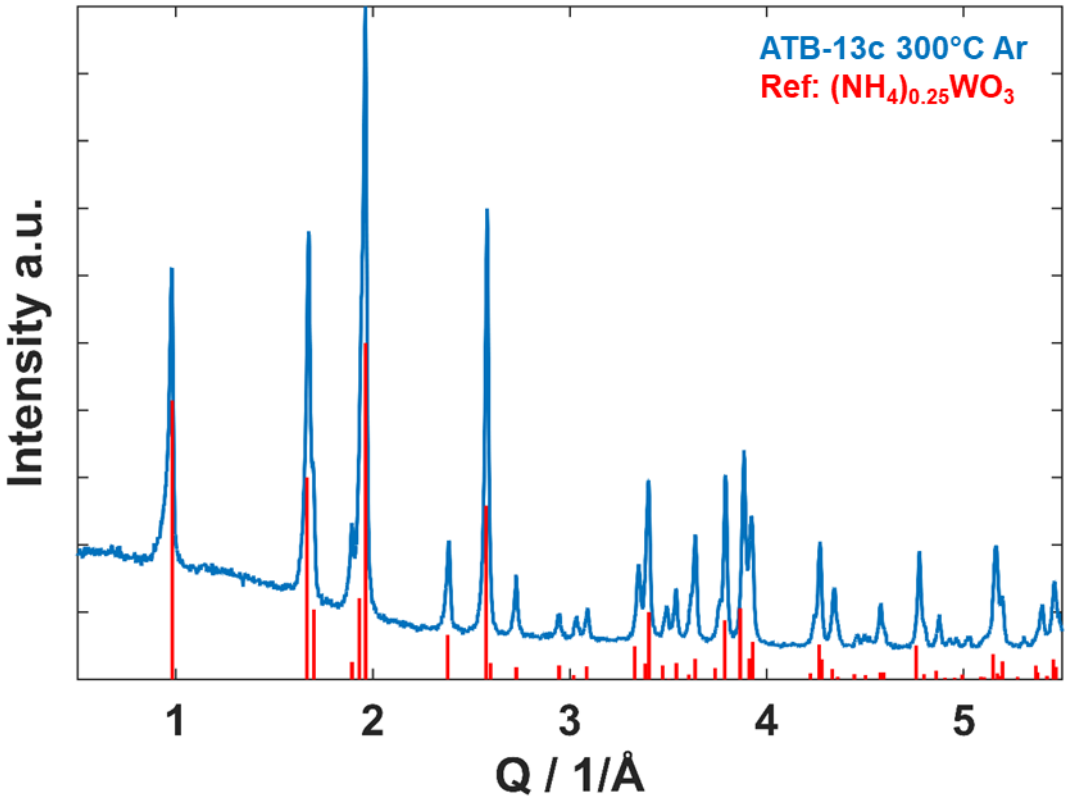

Figure S8.1.22. PXRD pattern of **ATB-13c** 300 °C (Ar) with $(NH_4)_{0.25}WO_3$ reference ($P6_3/mcm$, ICDD, PDF Entry No.: 01-073-1084).

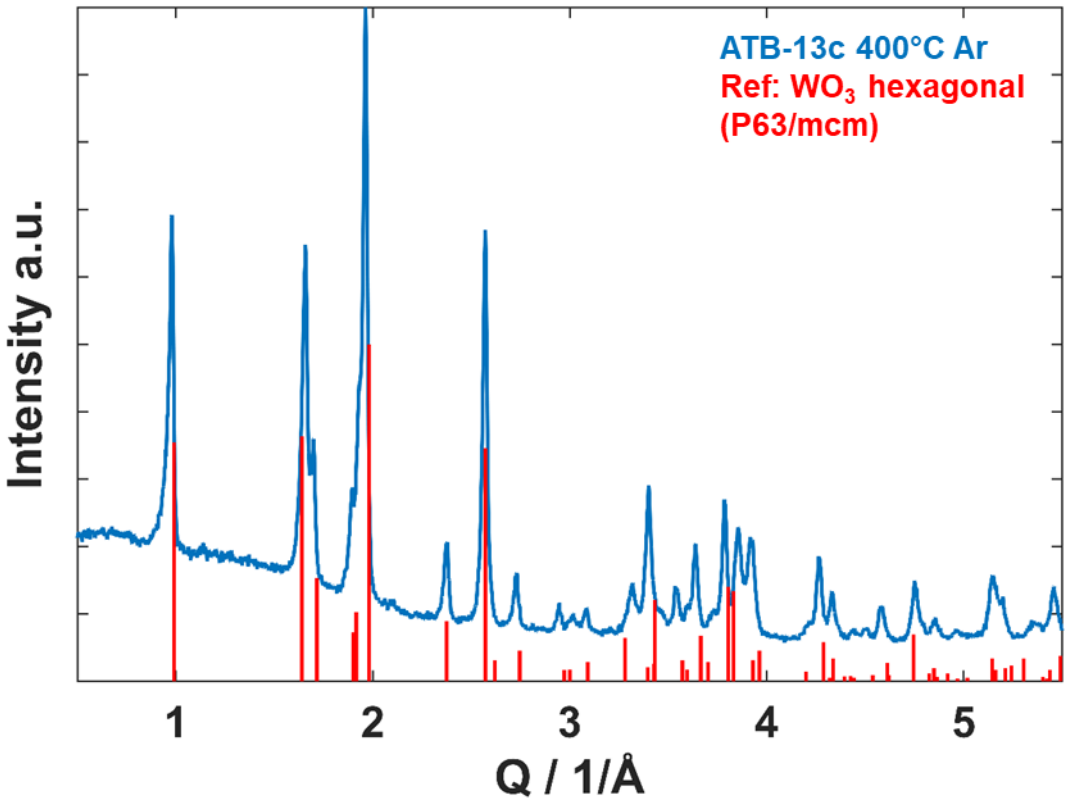

Figure S8.1.23. PXRD pattern of **ATB-13c** 400 °C (Ar) with hexagonal WO_3 reference ($P6_3/mcm$, ICSD, Entry No.: 99-503-1860).

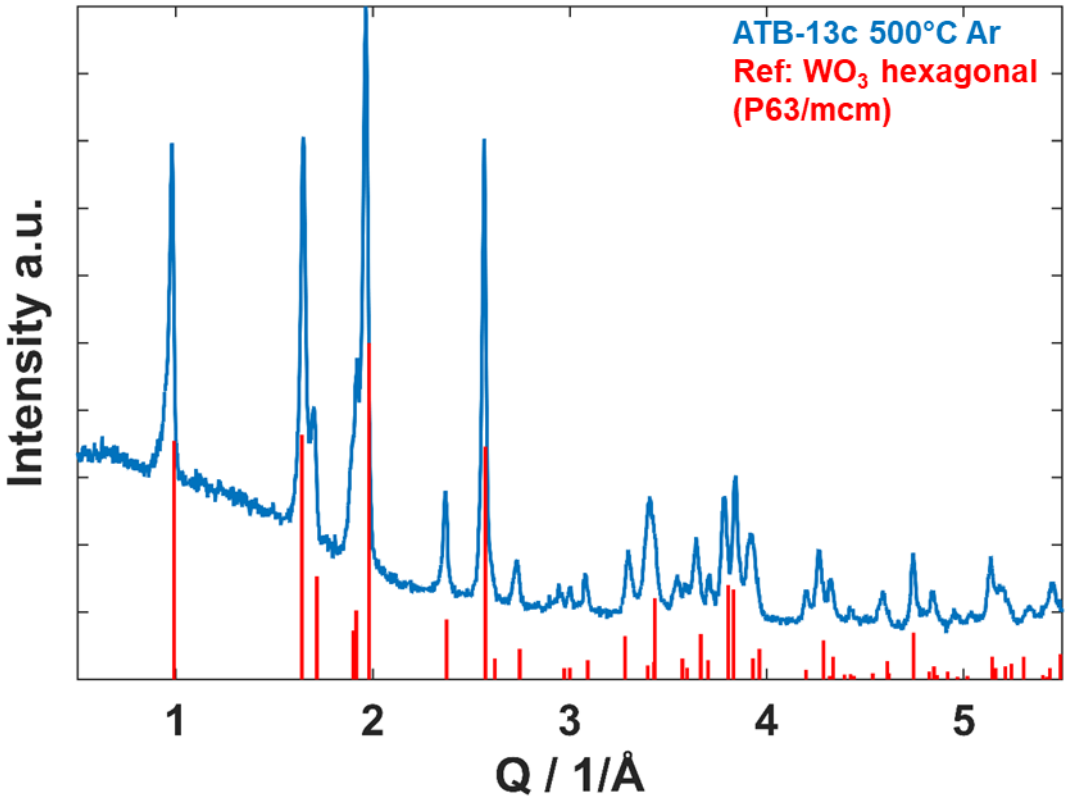

Figure S8.1.24. PXRD pattern of **ATB-13c** 500 °C (Ar) with hexagonal WO_3 reference ($P6_3/mcm$, ICSD, Entry No.: 99-503-1860).

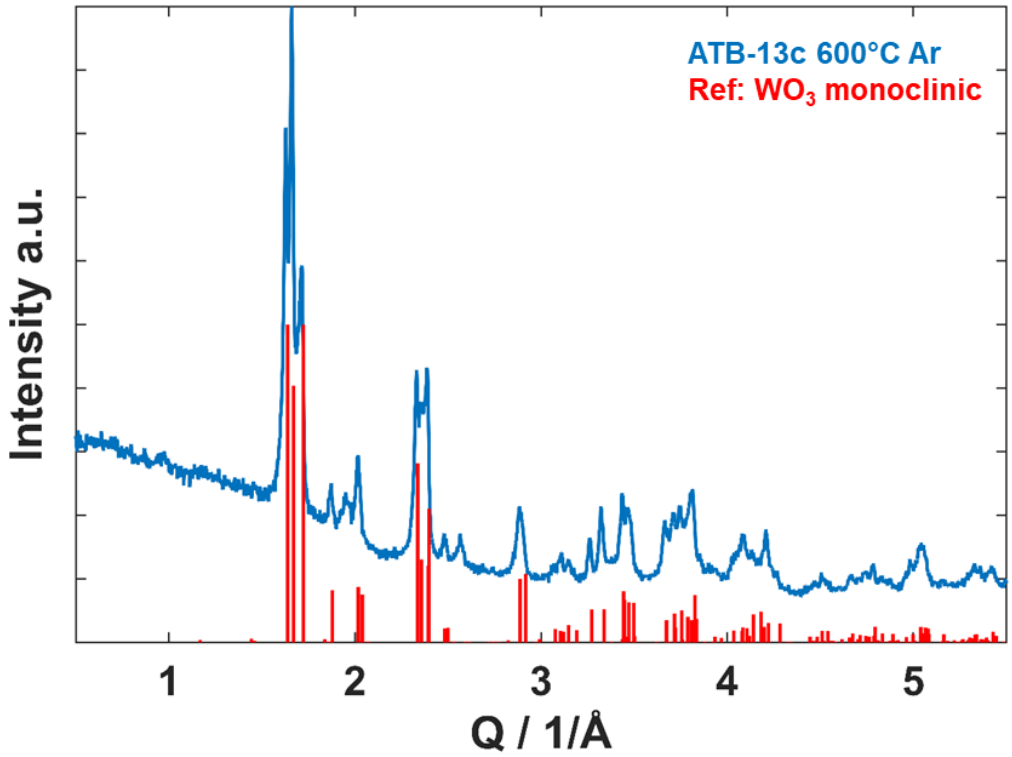

Figure S8.1.25. PXRD pattern of **ATB-13c** 600 °C (Ar) with monoclinic WO_3 reference ($P2_1/n$, COD, Entry No.: 96-152-8916).

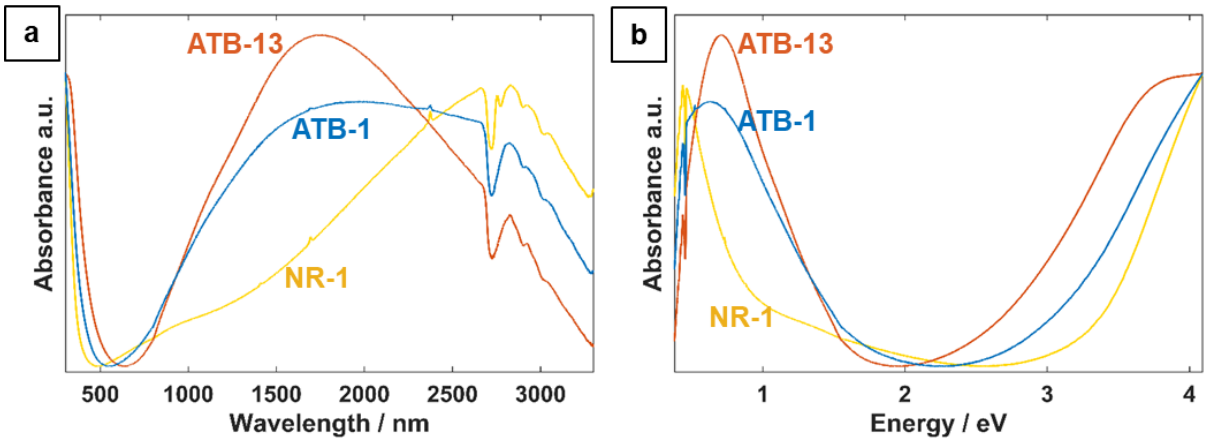

Figure S8.1.26. a) UV-Vis-NIR spectra of **NR-1**, **ATB-1** and **ATB-13** measured in TCE and b) Energy dependent absorption of the respective particles.

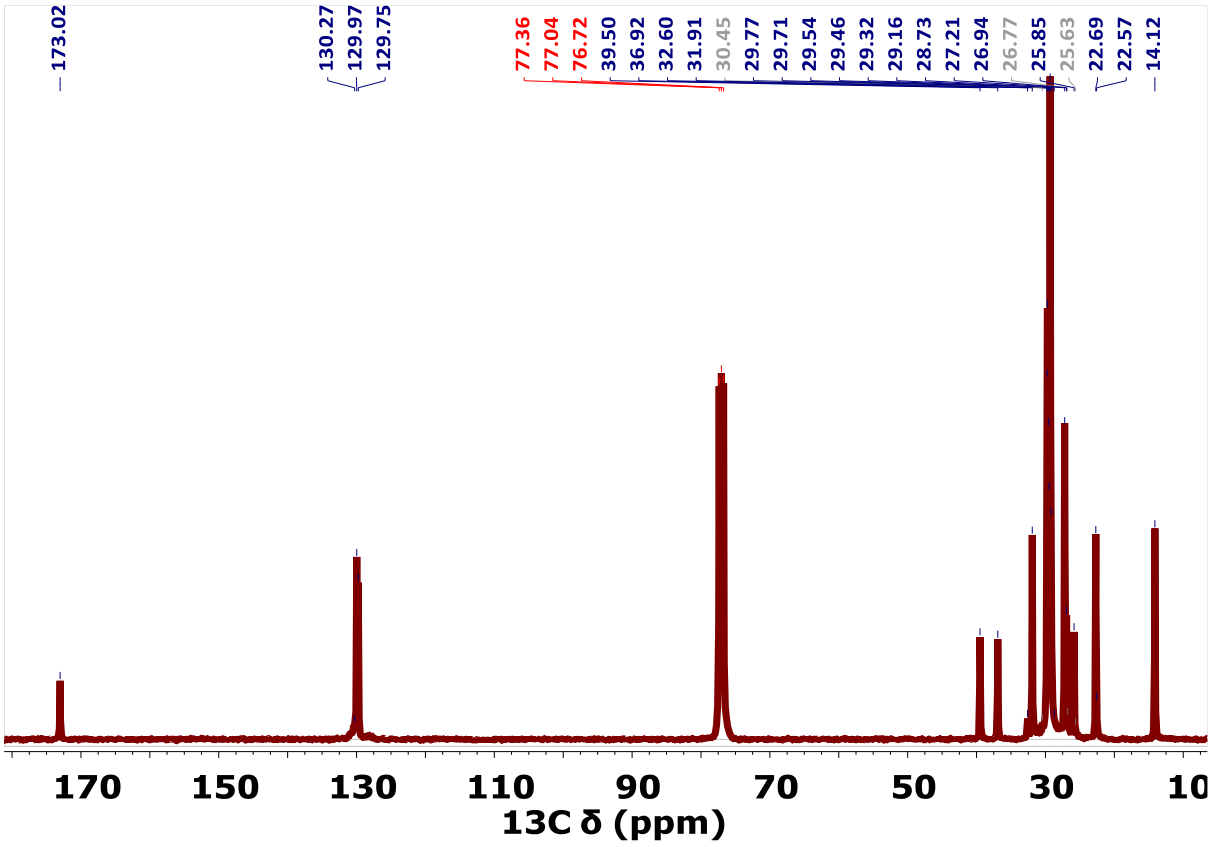

Figure S8.1.27. ^{13}C-NMR spectra of oleyl oleamide.

8.1.2 Effect of Surfactant Concentration

The effect of surfactant concentration was studied with octadec-1-en (ODE) as a high-boiling non surface-active solvent that allowed diluting the HOAc/OAm surfactant concentration by partially replacing the total amount of HOAc and OAm (40 mmol under standard conditions, **NR-1**) with ODE. TEM images (Figure S8.1.28a-d) show significantly smaller particle sizes for 20, 30 and 35 mmol of ODE (**ODE-1**, **ODE-2** and **ODE-3**). For lower ODE concentrations (**ODE-1** and **ODE-2**) a formation of trace amounts of HATB was observed (XRD, Figure S8.1.28e). For **ODE-3**, the mean length of the particles was reduced to approx. 20 nm and no HATB formation was observed. In the absence of HOAc/OAm surfactants (ODE only, 40 mmol, **ODE-4**), no WO_{3-x} was formed based on a PXRD analysis, anyhow the background is similar to all PXRD patterns of WO_{3-x} nanoparticle in this work. The surfactants HOAc and OAm have, even in small amounts, a pronounced effect on the growth of the HATB nanoparticles and WO_{3-x} NRs. This means, that in contrast to ODE, oleyl oleamide (OAd) must clearly act as surfactant, even without free surface-active groups as COOH or NH_2, as it yields WO_{3-x} NRs under comparable conditions (**Amide-1**). The maximum of **ODE-1** → **ODE-3** NIR absorption (Figure S8.1.28f) shifts systematically with particle size (i. e. aspect ratio), as expected for plasmonic nanoparticles. As **ODE-4** shows a plasmonic band as well, we expect small, x-ray amorphous particles to be within the sample.

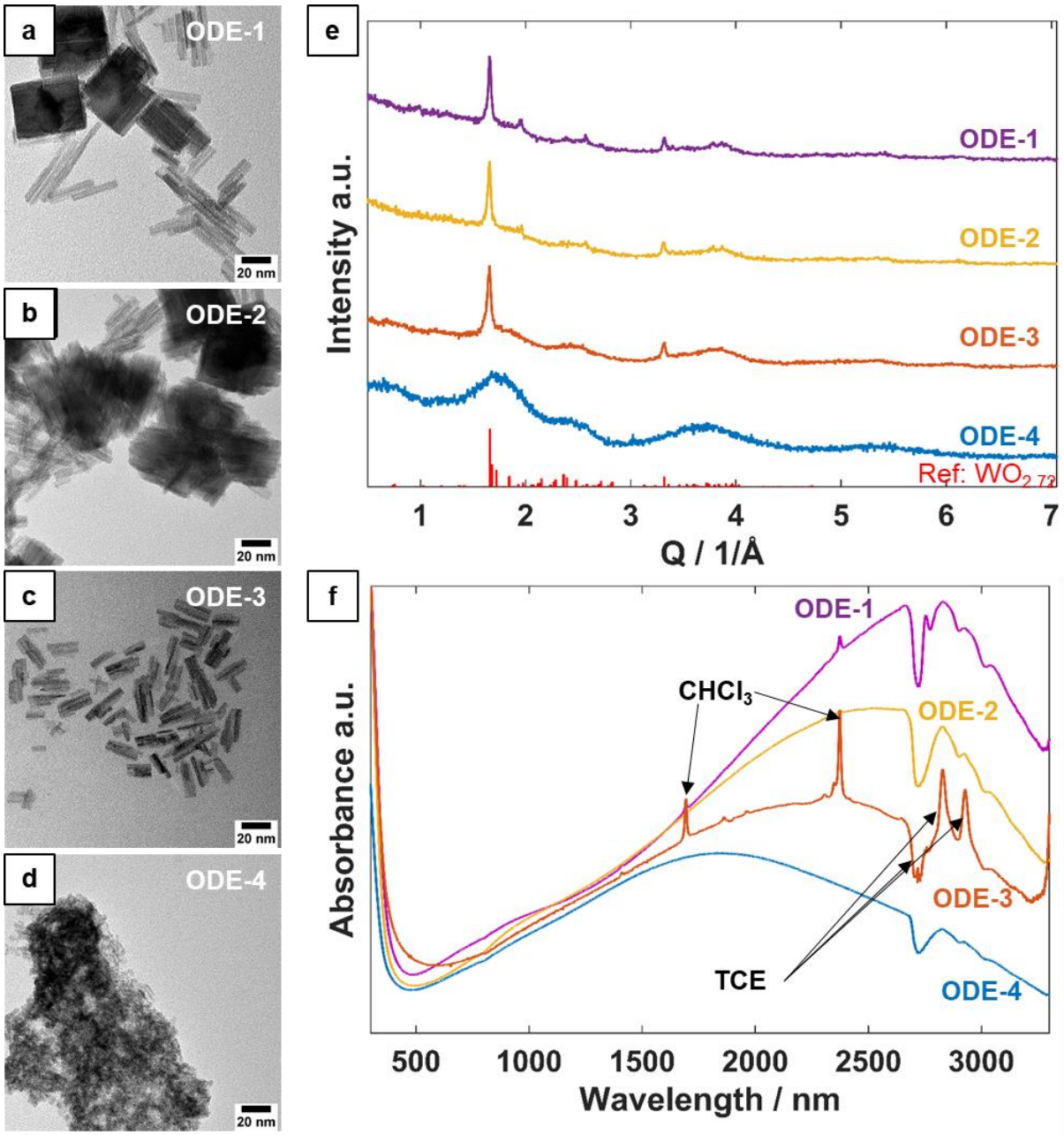

Figure S8.1.28. Effect of replacing HOAc/OAm (ratio still 1:1) with different amounts of ODE. a) 20 mmol ODE, 10 mmol HOAc, 10 mmol OAm (**ODE-1**), b) 30 mmol ODE, 5 mmol HOAc, 5 mmol OAm (**ODE-2**), c) 35 mmol ODE, 2.5 mmol HOAc, 2.5 mmol OAm (**ODE-3**), d) 40 mmol ODE, no HOAc/OAm (**ODE-4**), e) PXRD patterns and f) UV-Vis-NIR spectra of the shown particles (a-d).

8.2 Supporting Information for Chapter 3

The following chapter 8.2 is reproduced from Dalton Transaction, 2021, 50, 14027–14037, DOI: 10.1039/D1DT02243A with permission from the Royal Society of Chemistry.

8.2.1 Author Contributions

Conception and design of the study:

[redacted]

Preparation of samples and acquisition of data:

[redacted] – preparation of catalysts

[redacted] – TEM measurements

[redacted] – PXRD measurements

[redacted] – NMR measurements

[redacted] – ζ-potential measurements

[redacted] – BET surface measurements

Analysis and interpretation of data:

[redacted] – PXRD diffraction and refinements

[redacted] – TEM images, ζ-potential

[redacted] – NMR spectroscopy

[redacted] – BET surface analysis

Drafting of the supporting information:

[redacted]

Revising the supporting information critically for important intellectual content:

[redacted]

Preparation of figures:

[redacted]

Materials. All chemicals were used as received without further purification. Choline chloride (≥98 %) and cerium(III) nitrate hexahydrate (99.5 %, REacton) was purchased from Alfa Aesar, urea (99.5 %, analytical grade) was bought from Acros organics.

Tungsten oxide nanoparticle synthesis. **W**O_{3-x} nanorods (conditions **NR-1**) and ammonium tungsten bronze ($(NH_4)_{\sim 0.2}WO_3$) nanoparticles (conditions **ATB-15c**) were synthesized according to our previous publication.[1]

CeO_2 nanoparticle synthesis. CeO_2 nanoparticles were synthesized based on a synthesis of Hammond et. al.[2] Choline chloride and urea were mixed in molar ratio of 2:1 and heated to 80 °C for 14 h to gain the deep eutectic solvent reline. The reline was dried at 70 °C under reduced pressure for 6 h. $Ce(NO_3)_3{\cdot}6H_2O$ (750 mg; 1.7 mmol) was dissolved in reline (40 mL), transferred into a stainless steel autoclave (total volume: 50 mL) and heated to 100 °C for 10 h. The highly viscous gel-like reaction mixture was poured into Milli-Q-water (140 mL). The purple product was separated from the suspension by centrifugation (6000-9000 rpm, 10 min), washed three times with Milli-Q-water and three times with ethanol and dried at 80 °C for 14 h. The nanoparticles were calcined at 300 °C for 5 h bevor being used in catalytic experiments.

TiO_2 nanoparticles. Anatase TiO_2 nanoparticles were synthesized according our previous study,[3] based on a synthesis published by Dinh et. al.[4]

General Considerations. We attribute slight variations for the different standard *in situ* reactions mainly to residual moisture in the different methanol-d_4 batches, water adsorbed to the particles from air, as well as small weighing/pipetting errors.

Table S8.2.1. Product composition with additional water to standard *in situ* experiment (0.85 mg WO_{3-x} nanorods, 0.04 mmol thioanisole, 0.06 mmol H_2O_2 (60 %) in 0.6 ml methanol-d_4).

Addition of water / µl	Ratio sulfide:sulfoxide:sulfone (10 min)	Ratio sulfide:sulfoxide:sulfone (30 min)
0	39:60:1	8:91:2
2.34[a]	50:50:0	14:85:1
2.34[b]	48:52:0	12:87:1
10[a]	73:26:1	36:62:2
10[b]	75:25:0	39:61:0
50[a,c]	92:8:0	72:28:0
50[b,c]	92:8:0	74:26:0
200[a,c]	92:7:1	79:21:0
200[b,c]	93:7:0	79:21:0

a. addition of H_2O. b. addition of D_2O. c. total volume fixed to 600 µl.

$$\boldsymbol{r = a * e^{-b*V} + c}$$

r = conversion / %

V= added volume of H_2O / D_2O

Table S8.2.2. Fit parameters for water curves according to the equation above.

Curve	a	b	c
D_2O 10 min	55.059	0.108	7.256
H_2O 10 min	53.252	0.100	7.775
D_2O 30 min	72.944	0.057	21.365
H_2O 30 min	71.523	0.051	21.457

Table S8.2.3. Product composition after annealing at different temperatures for standard *in situ* experiment (0.85 mg WO_{3-x} nanorods, 0.04 mmol thioanisole, 0.06 mmol H_2O_2 (60 %) in 0.6 ml methanol-d_4).

Annealing temperature / °C	**Crystallographic phase**	**Ratio sulfide:sulfoxide:sulfone (10 min)**	**Ratio sulfide:sulfoxide:sulfone (30 min)**
70[a]	WO_{3-x}	96:4:0	90:10:0
200	WO_{3-x}	92:8:0	88:12:0
250	WO_{3-x}	51:49:0	17:82:1
300	WO_{3-x}	39:60:1	8:90:2
350	WO_{3-x}	70:30:0	41:58:0
400	WO_{3-x}	77:23:0	55:45:0
500	WO_3 (monoclinic)	97:3:0	97:3:0

a. Particles additionally dried @ 40 °C under reduced preasure (~$1*10^{-2}$ mbar), 1.7 mg particles in 0.6 ml methanol-d_4, 0.2 mmol thioanisole, 0.3 mmol H_2O_2 (60 %).

Table S8.2.4. BET surface area and ζ – potential of nanoparticles used for sulfide oxidation.

catalyst	**Specific surface area / m^2g^{-1}**	**ζ – potential / mV**
WO_{3-x} nanorods	47.0	-39.7
$(NH_4)_{0.2}WO_3$ nanoparticles	22.8	-36.8
WO_3 reference (monoclinic)	2.7	-39.3
CeO_2 nanoparticles	133.9	23.8
TiO_2 nanoparticles	151.7	-9.1
TiO_2 P25	49.7	17.7

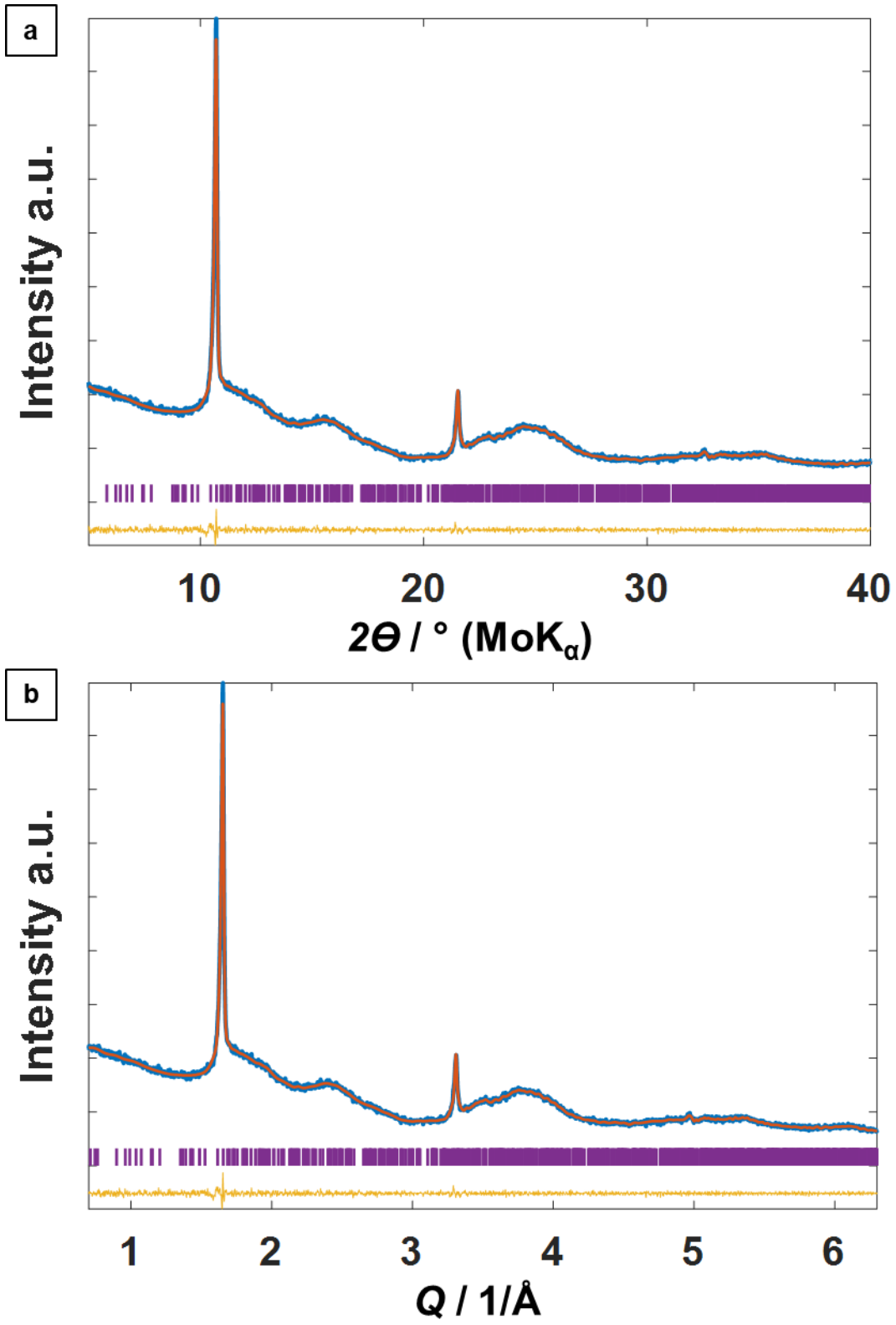

Figure S8.2.1. Pawley refinements of WO_{3-x} NRs annealed at 300°C using space group *P2/m* and a quadratic form to compensate the anisotropy.[1] Refined parameters are: R_{wp}: 2.23, GOF: 1.08, crystal size (a*b*c): 4.1*72.6*4.3 nm. Lattice parameters: *a*=18.196 Å, *b*=3.794 Å and *c*= 14.000 Å.

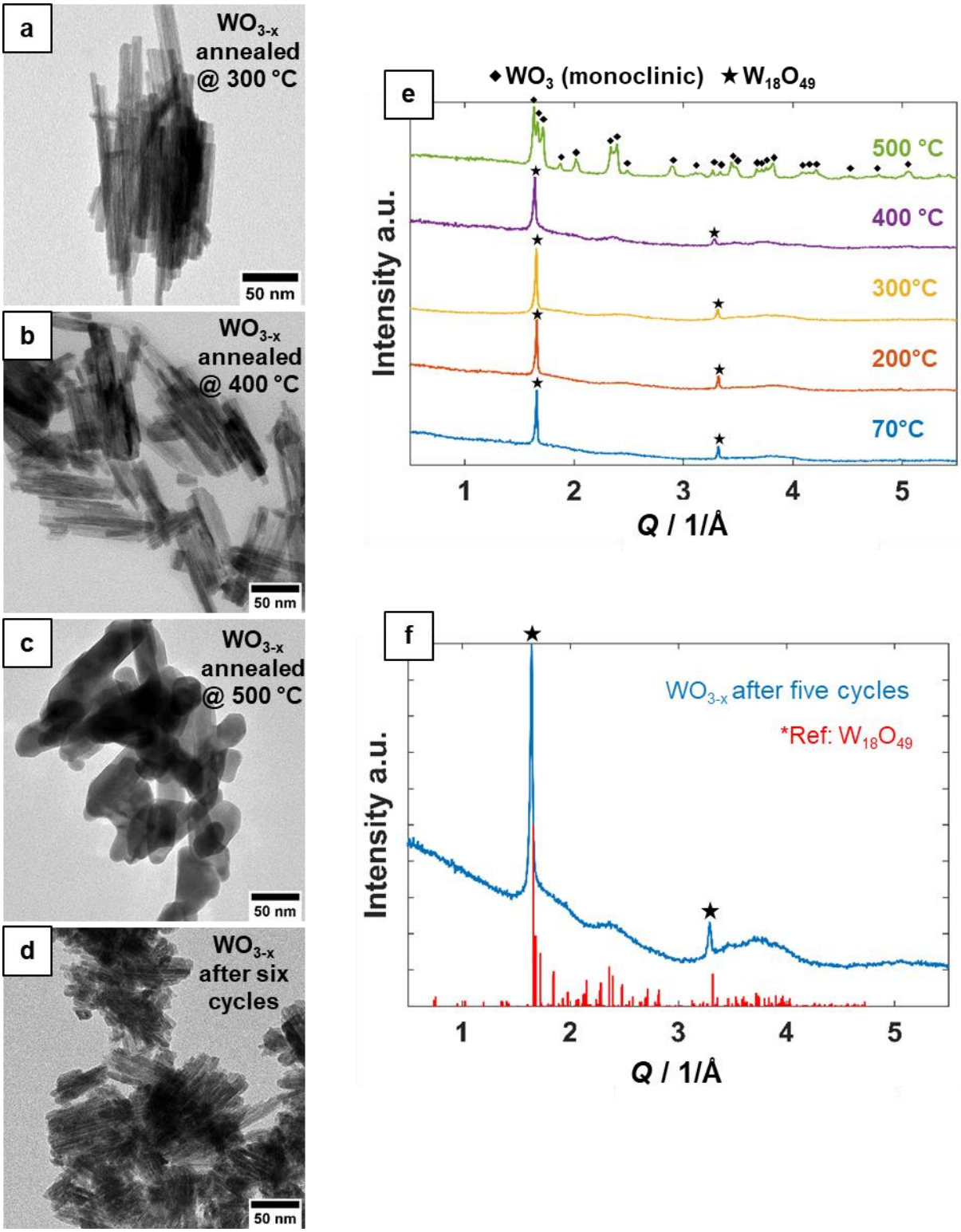

Figure S8.2.2. TEM images of WO_{3-x} nanorods annealed at a) 300 °C, b) 400 °C, c) 500 °C and d) after six reaction cycles. e) P-XRD patterns of annealed WO_{3-x} nanorods up to 500 °C and f) after five reaction cycles. References: $W_{18}O_{49}$ ($WO_{2.72}$, COD, Entry No.: 96-152-8167), WO_3 (monoclinic, COD, Entry No.: 96-152-8916).

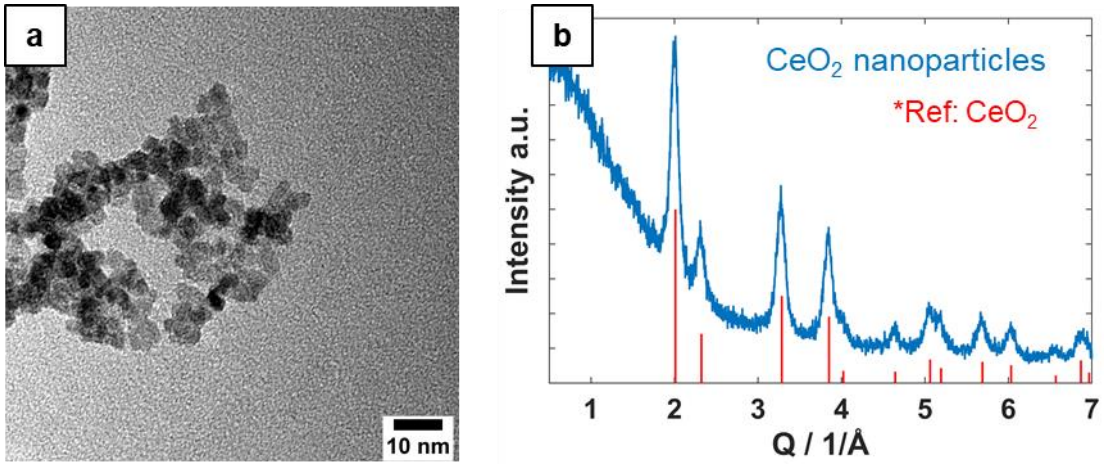

Figure S8.2.3. a) TEM image and b) P-XRD pattern of CeO_2 nanoparticles. Reference: Cerianite (CeO_2), COD, Entry No.: 96-900-9009).

8.2.2 ^{1}H-NMR characterization

Thioanisole (methyl phenyl sulfide)

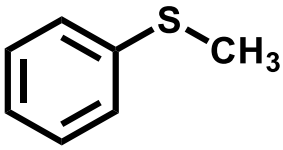

^{1}H-NMR (400 MHz, d_4-MeOD) δ (ppm): 7.29-7.26 (m, 4H), 7.15-7.12 (m,1H) 2.48 (s, 3H).

Published elsewhere[5]: **^{1}H-NMR** (400 MHz, $CDCl_3$) δ (ppm): 7.32-7.20 (m, 4H), 7.17-7.07 (m, 1H), 2.47 (s, 3H).

Methyl phenyl sulfoxide

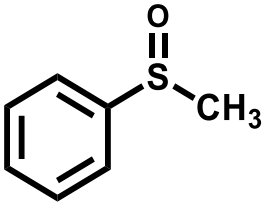

^{1}H-NMR (400 MHz, d_4-MeOD) δ (ppm): 7.74-7.61 (m, 5H), 2.81 (s, 3H).

Published elsewhere[6]: **^{1}H-NMR** (400 MHz, $CDCl_3$) δ (ppm): 7.62-7.60 (m, 2H), 7.51-7.44 (m,3H), 2.68 (s, 3H).

Methyl phenyl sulfone

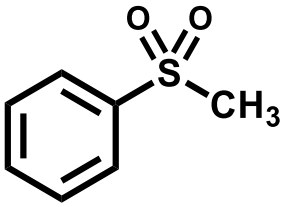

^{1}H-NMR (400 MHz, d_4-MeOD) δ (ppm): 7.99-7.95 (m, 2H), ~7.66-7.54 (m, 3H)[a], 3.13 (s, 3H).

Published elsewhere[6]: **^{1}H-NMR** (400 MHz, $CDCl_3$) δ (ppm): 7.92 (d, *J* = 7.5 Hz, 2H), 7.66-7.54 (m,3H), 3.04 (s, 3H).

a. Signals of the aromatic protons partially overlapping with those of MP-sulfoxide. MP-sulfone content calculated as 2.5 times the integral of the signal at 7.99-7.95 ppm. The MP-sulfoxide contend was calculated as the integral of the signal at 7.62-7.44 ppm minus the 1.5 times the integral of the signal at 7.99-7.95 ppm.

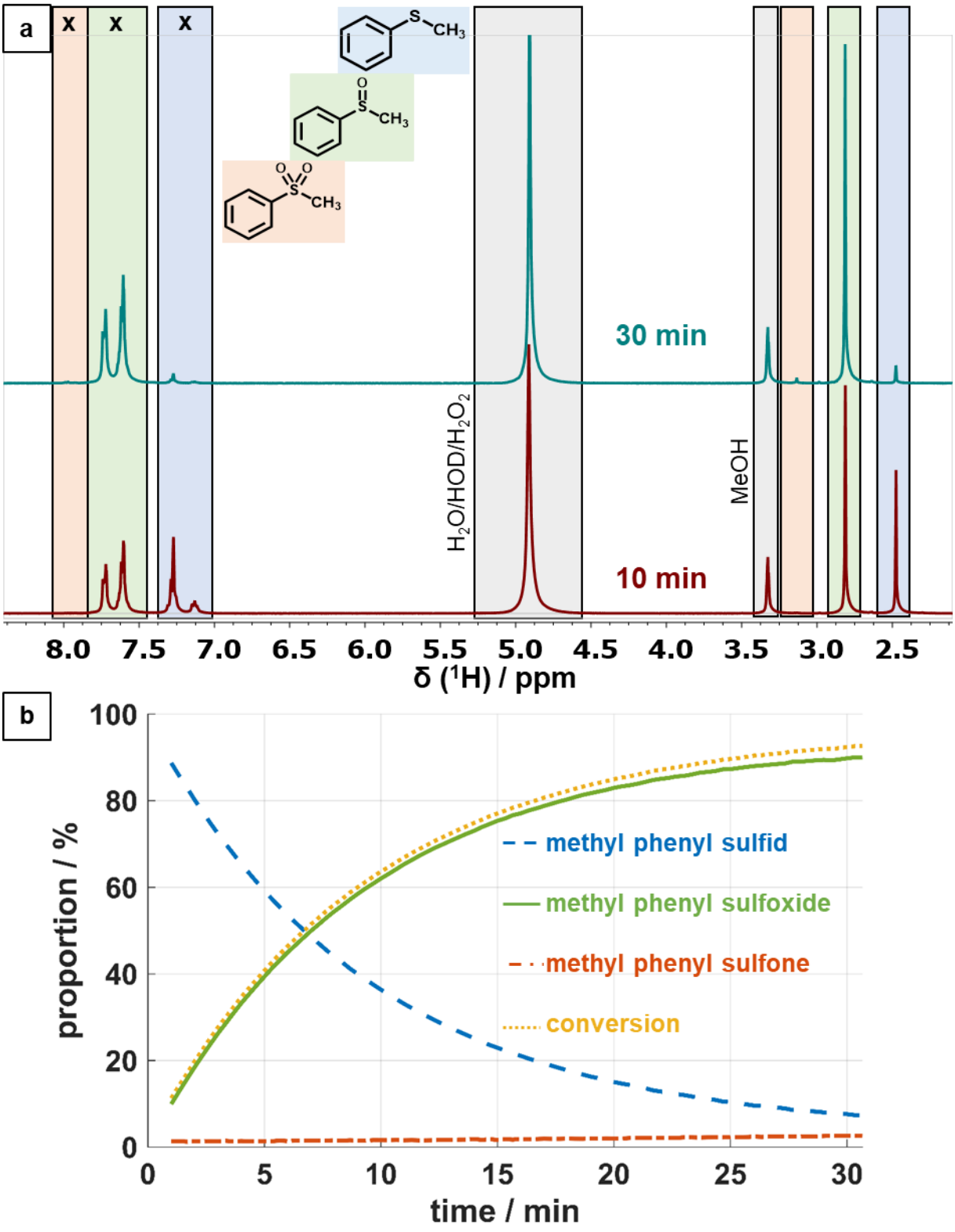

Figure S8.2.4. a) ^{1}H-NMR spectra of a standard catalysis (0.04 mmol thioanisole, 0.06 mmol H_2O_2 (60 %), 0.85 mg WO_{3-x} nanorods in 0.6 mL of methanol-d4) after 10 and 30 min, x marking the peaks used for integration. b) Time dependent composition during the catalysis based on ^{1}H-NMR data.

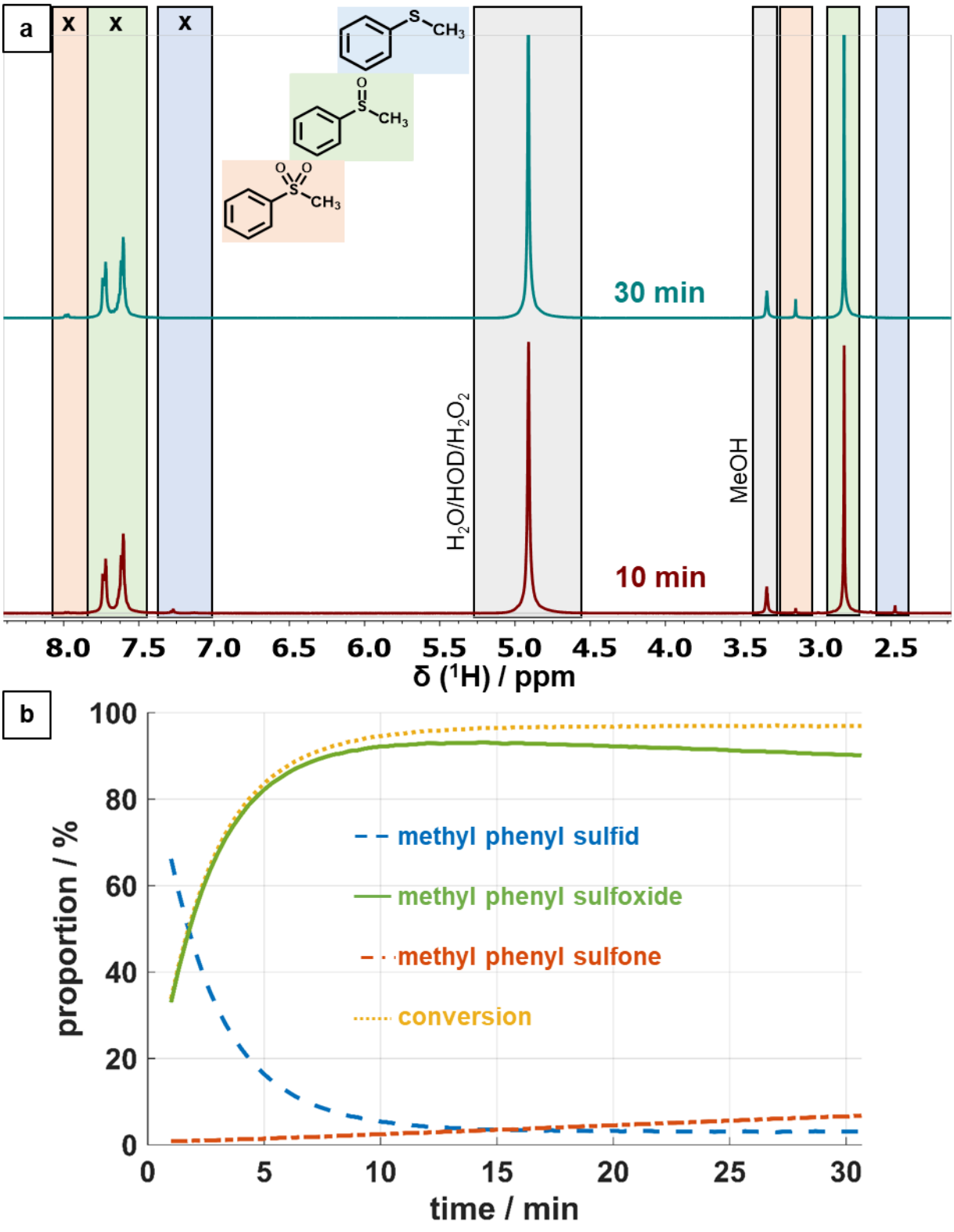

Figure S8.2.5. a) ^{1}H-NMR spectra of a catalysis with double amounts (0.08 mmol thioanisole, 0.12 mmol H_2O_2 (60 %), 1.7 mg WO_{3-x} nanorods in 0.6 mL of methanol-d_4) after 10 and 30 min, **x** marking the peaks used for integration. b) Time dependent composition during the catalysis based on ^{1}H-NMR data.

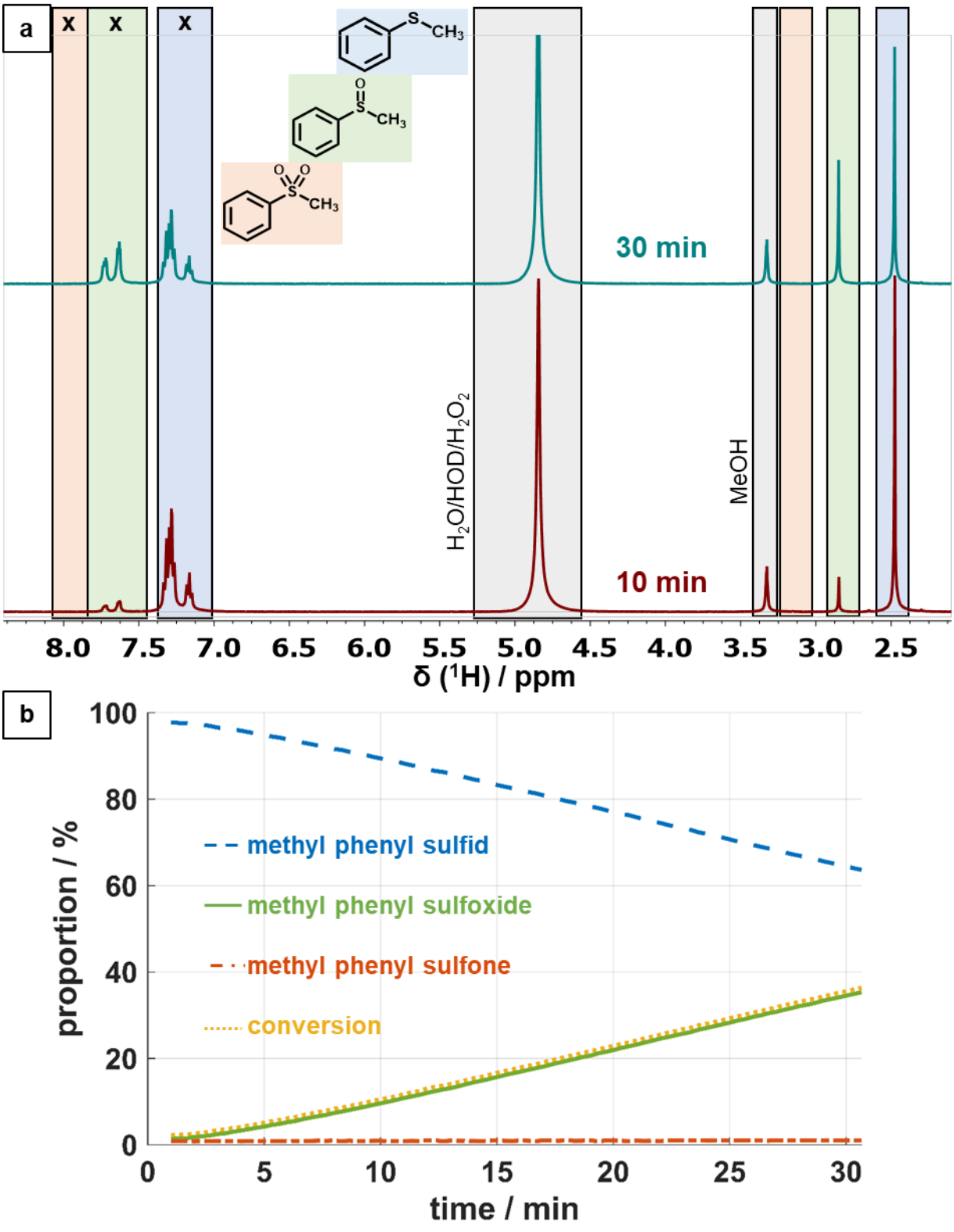

Figure S8.2.6. a) ^{1}H-NMR spectra of a catalysis with water influence (0.04 mmol thioanisole, 0.06 mmol H_2O_2 (60 %), 0.85 mg WO_{3-x} nanorods in 0.4 mL of methanol-d_4 and 0.2 ml D_2O) after 10 and 30 min, **x** marking the peaks used for integration. b) Time-dependent composition during the catalysis based on ^{1}H-NMR data.

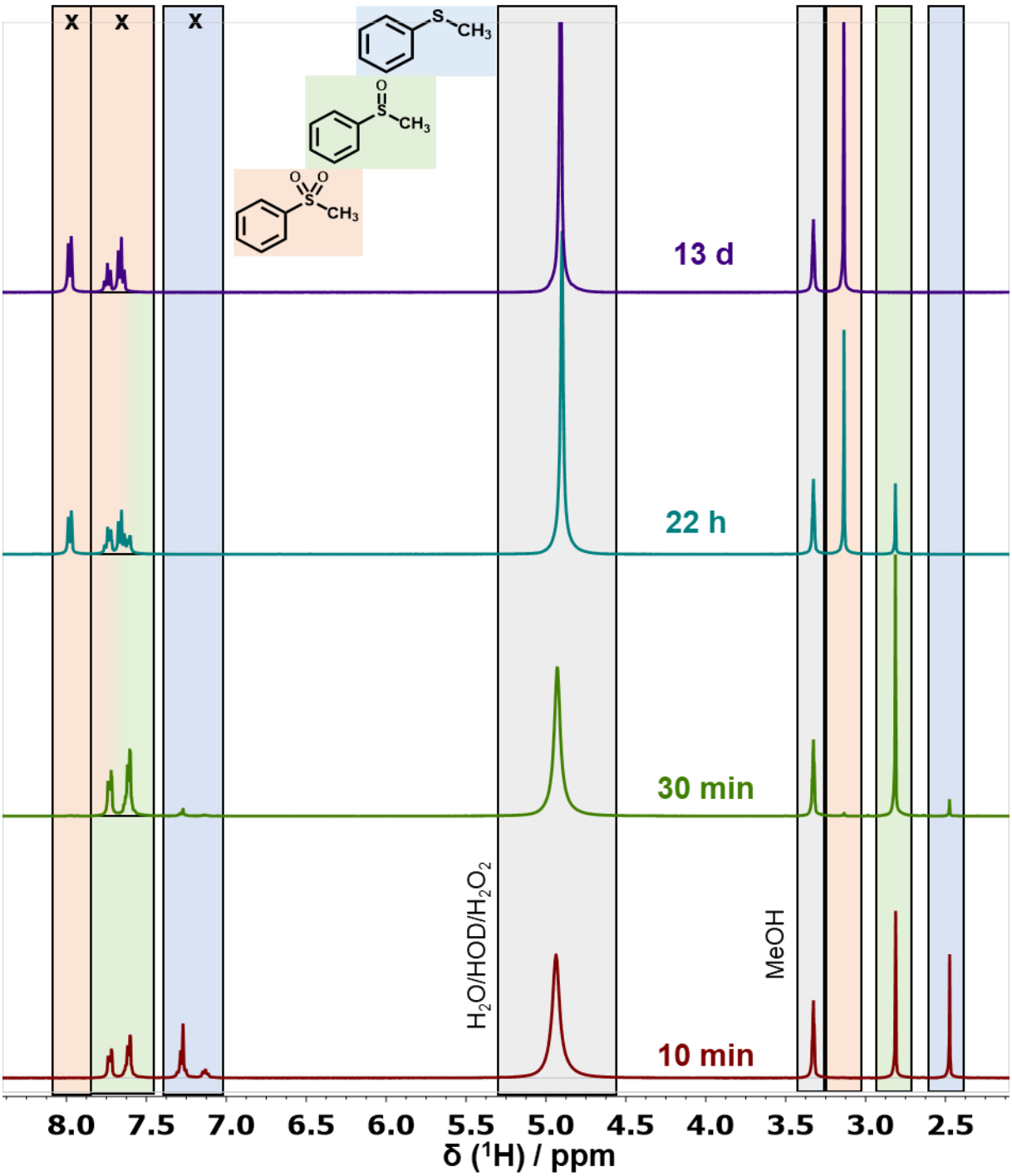

Figure S8.2.7. ^{1}H-NMR spectra of a standard catalysis (0.04 mmol thioanisole, 0.12 mmol H_2O_2 (60 %), 0.85 mg WO_{3-x} nanorods in 0.6 mL of methanol-d_4) after 10 min, 30 min, 22h and 13 d, **x** marking the peaks used for integration.

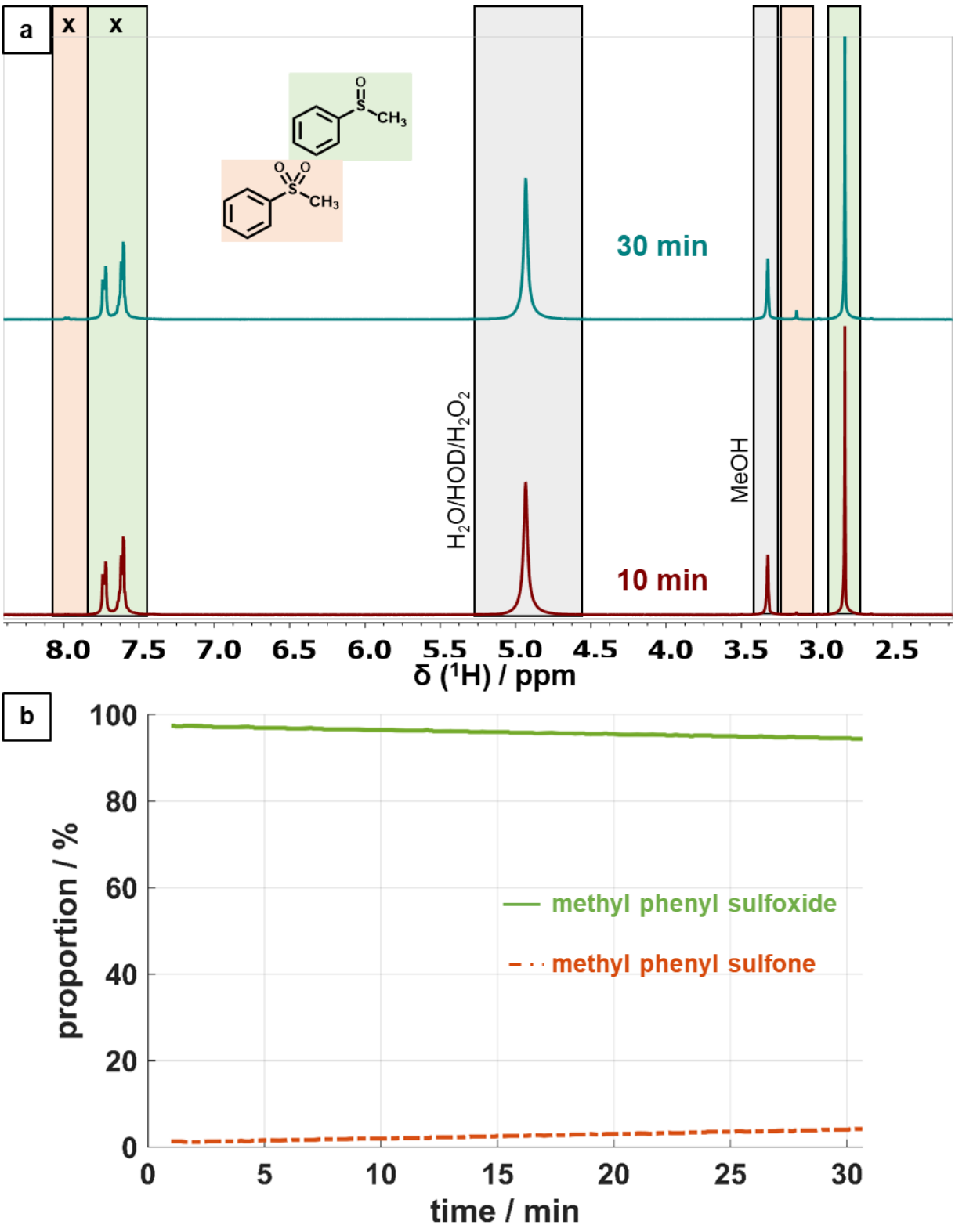

Figure S8.2.8. a) ^{1}H-NMR spectra of an oxidation catalysis using sulfoxides (0.04 mmol MP-sulfone, 0.06 mmol H_2O_2 (60 %), 0.85 mg WO_{3-x} nanorods in 0.6 mL of methanol-d_4) after 10 and 30 min, **x** marking the peaks used for integration. b) Time-dependent composition during the catalysis based on ^{1}H-NMR data.

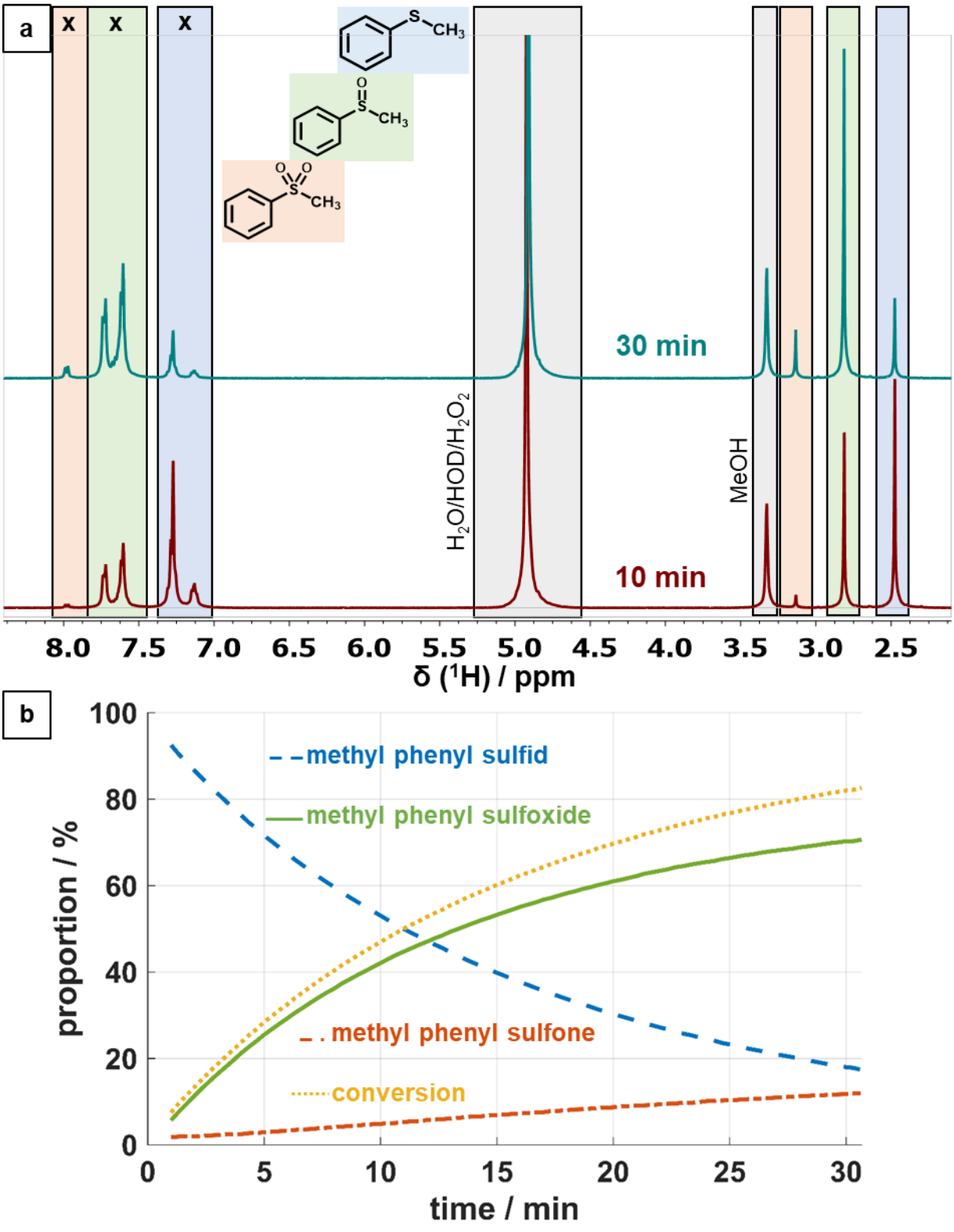

Figure S8.2.9. a) ^{1}H-NMR spectra of a standard oxidation catalysis (0.04 mmol thioanisole, 0.06 mmol H_2O_2 (60 %), 0.85 mg Na_2WO_4 * $2H_2O$ in 0.6 mL of methanol-d_4) after 10 and 30 min, **x** marking the peaks used for integration. b) Time-dependent composition during the catalysis based on ^{1}H-NMR data.

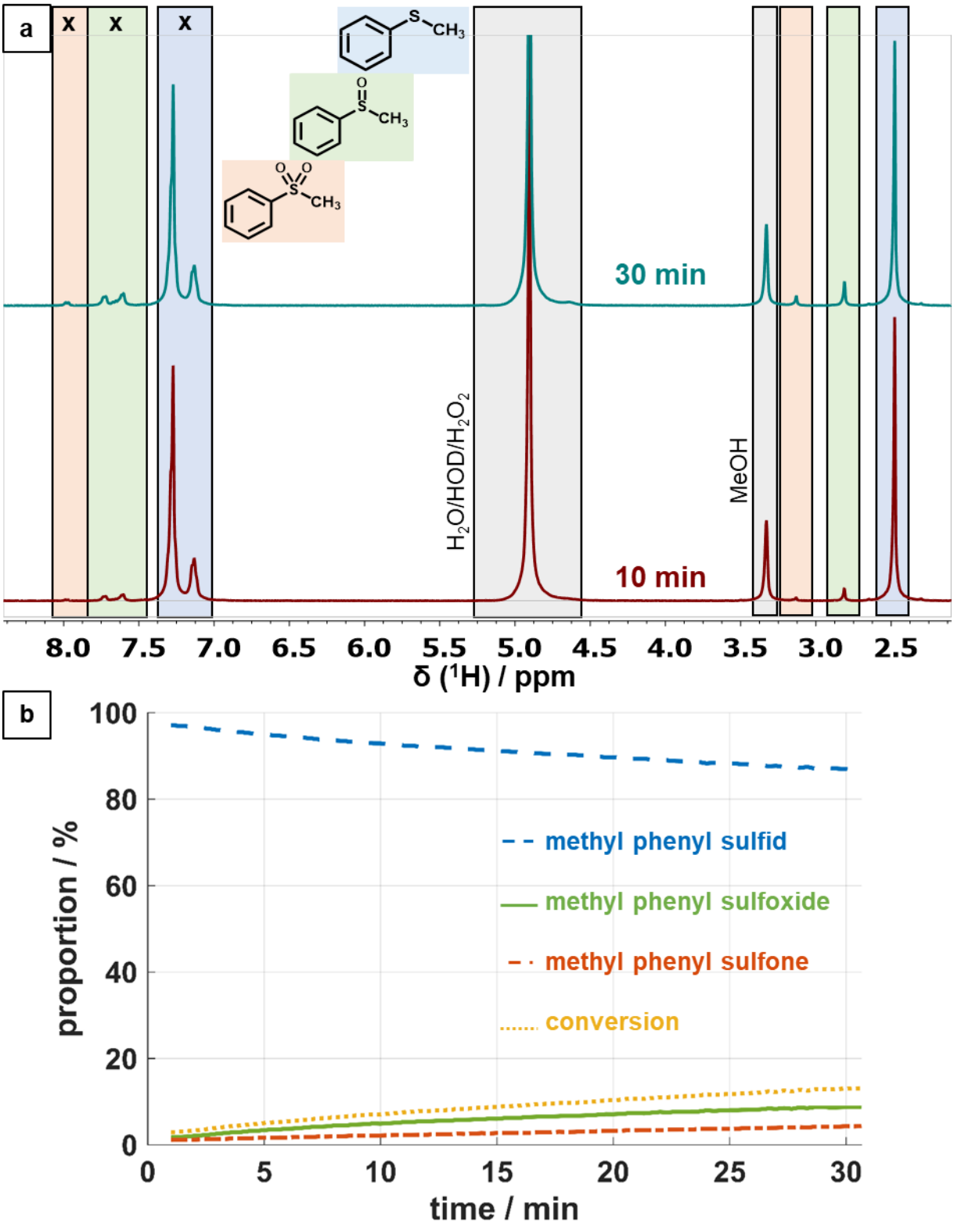

Figure S8.2.10. a) ^{1}H-NMR spectra of a standard catalysis (0.04 mmol thioanisole, 0.06 mmol H_2O_2 (60 %), 0.85 mg CeO_2 nanoparticles in 0.6 mL of methanol-d_4) after 10 and 30 min, **x** marking the peaks used for integration. b) Time-dependent composition during the catalysis based on ^{1}H-NMR data.

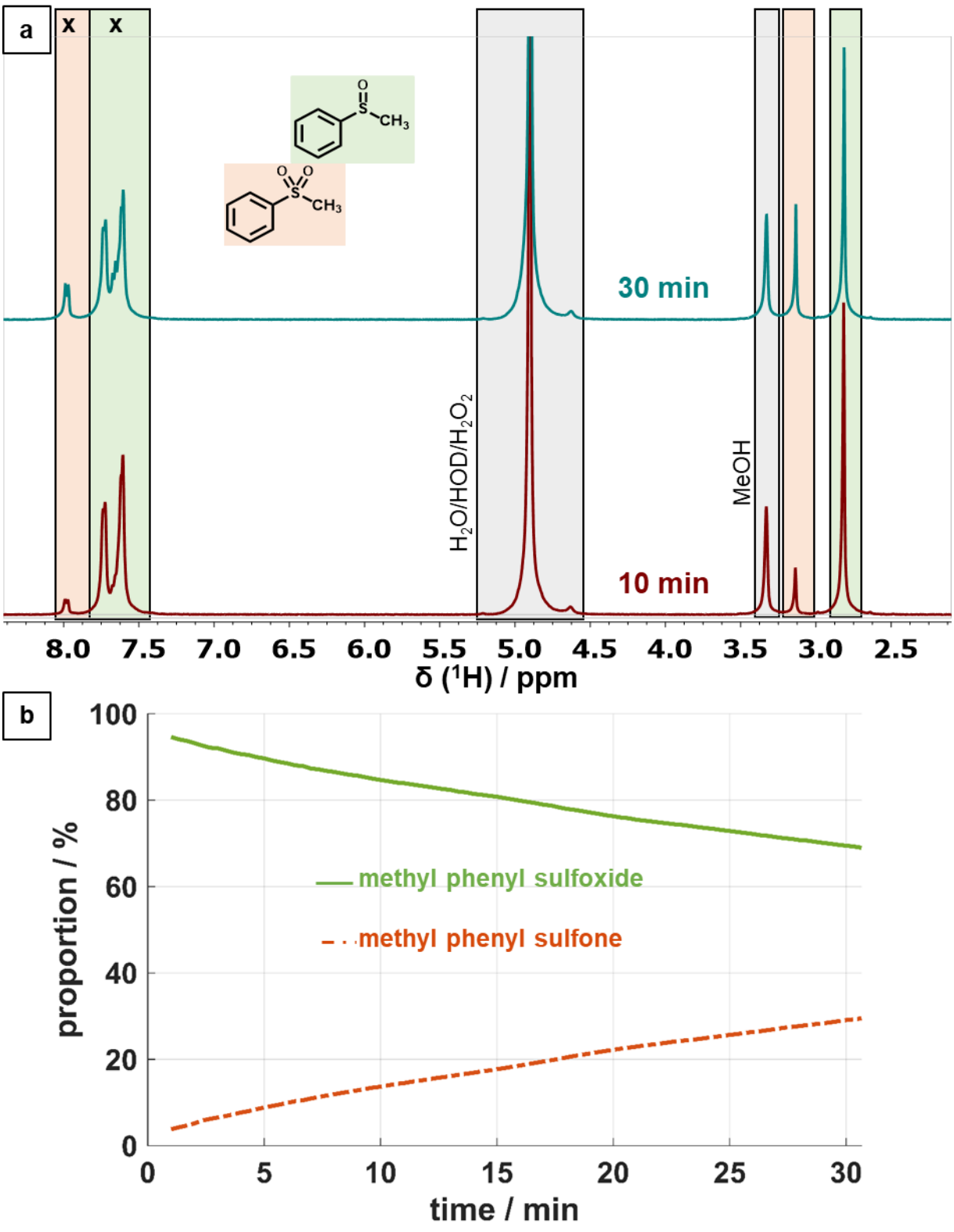

Figure S8.2.11. a) ^{1}H-NMR spectra of a catalysis using sulfoxide (0.04 mmol MP-sulfoxide, 0.06 mmol H_2O_2 (60 %), 0.85 mg CeO_2 nanoparticles in 0.6 mL of methanol-d_4) after 10 and 30 min, **x** marking the peaks used for integration. b) Time-dependent composition during the catalysis based on ^{1}H-NMR data.

Di-n-propyl sulfide

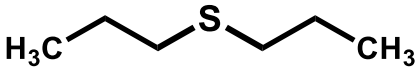

^{1}H-NMR (400 MHz, d_4-MeOD) δ (ppm): 2.49 (t, *J* = 7.2 Hz, 4H), 1.66-1.56 (m, 4H), 1.00 (t, *J* = 7.4 Hz, 6H).

Published elsewhere[7]: **^{1}H-NMR** (400 MHz, $CDCl_3$) δ (ppm): 2.47 (t, *J* = 7.4 Hz, 4H), 1.59 (sext, *J* = 7.4 Hz, 4H), 0.97 (t, *J* = 7.4 Hz, 6H).

Di-n-propyl sulfoxide

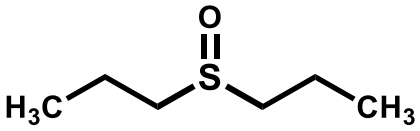

^{1}H-NMR (400 MHz, d_4-MeOD) δ (ppm): 2.83-2.72 (m, 4H), 1.87-1.77 (m, 4H), 1.12 (t, *J* = 7.4 Hz, 6H).

Published elsewhere[6]: **^{1}H-NMR** (400 MHz, $CDCl_3$) δ (ppm): 2.72-2.53 (m, 4H), 1.83-1.73 (m,4H), 1.05 (t, *J* = 7.4 Hz, 6H).

Di-n-propyl sulfone

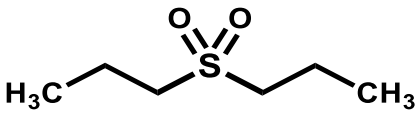

^{1}H-NMR (400 MHz, d_4-MeOD) δ (ppm): 3.07-3.03 (m, 4H), ~1.88-1.75 (m, 4H)[a], ~1.12 (t, *J* = 7.4 Hz, 6H)[a].

Published elsewhere[6]: **^{1}H-NMR** (400 MHz, $CDCl_3$) δ (ppm): 2.90-2.86 (m, 4H), 1.86-1.76 (m,4H), 1.02 (t, *J* = 7.4 Hz, 6H).

a. Signals of the protons partially overlapping with those of di-n-propyl sulfoxide.

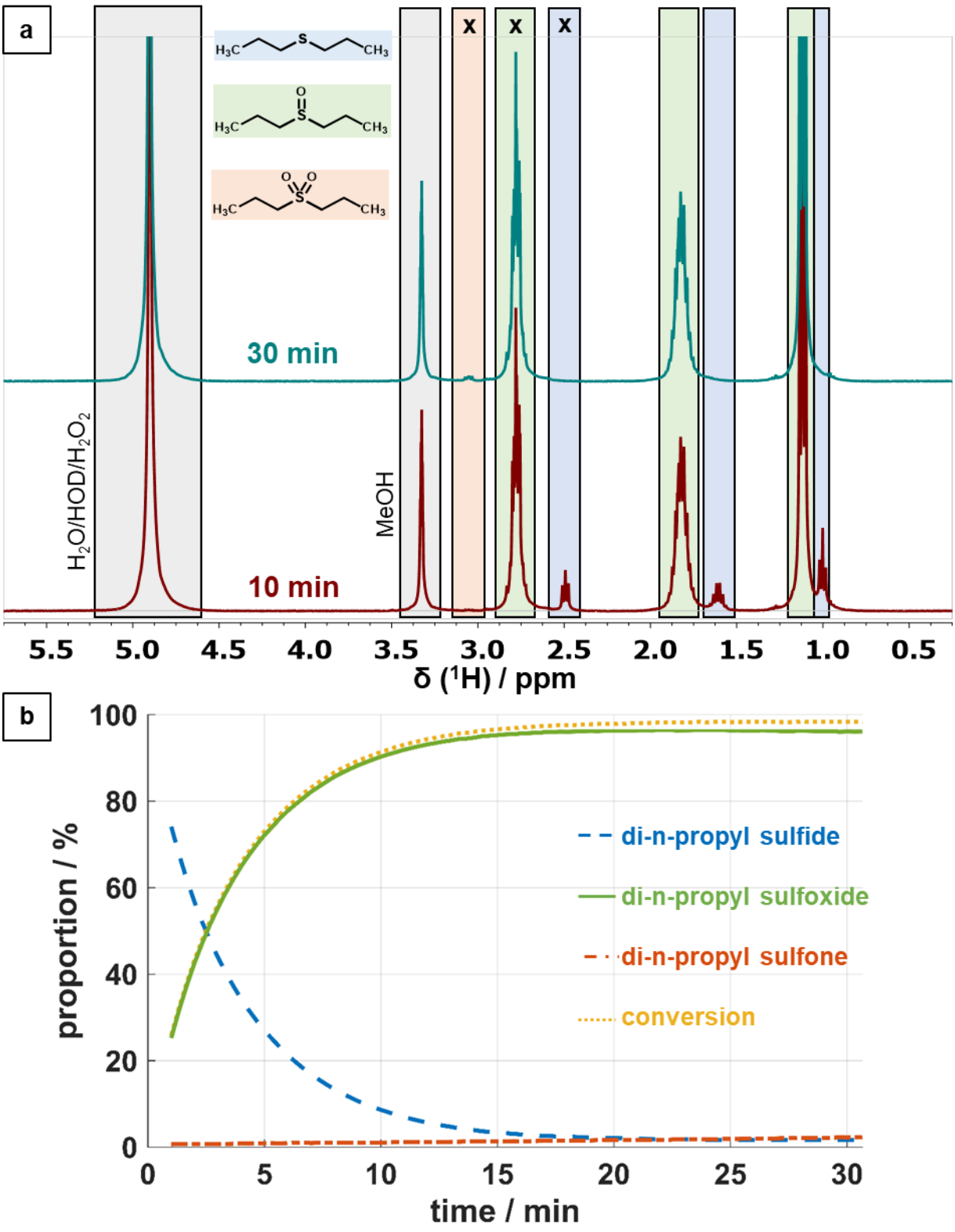

Figure S8.2.12. a) ^{1}H-NMR spectra of a standard catalysis (0.04 mmol di-n-propyl sulfide, 0.06 mmol H_2O_2 (60 %), 0.85 mg WO_{3-x} nanorods in 0.6 mL of methanol-d_4) after 10 and 30 min, **x** marking the peaks used for integration. b) Time-dependent composition during the catalysis based on ^{1}H-NMR data.

Di-tert-butyl sulfide

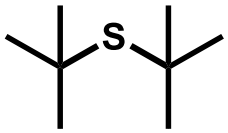

^{1}H-NMR (400 MHz, d_4-MeOD) δ (ppm): 1.42 (s, 18H).

Published elsewhere[8]: **^{1}H-NMR** (400 MHz, $CDCl_3$) δ (ppm): 1.42 (s, 18H).

Di-tert-butyl sulfoxide

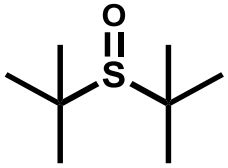

^{1}H-NMR (400 MHz, d_4-MeOD) δ (ppm): 1.37 (s, 18H).

Published elsewhere[9]: **^{1}H-NMR** (400 MHz, $CDCl_3$) δ (ppm): 1.12 (s, 18H).

Di-tert-butyl sulfone

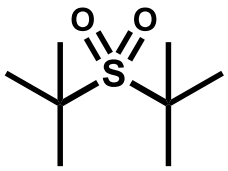

Not observed.

Published elsewhere[9]: **^{1}H-NMR** (400 MHz, $CDCl_3$) δ (ppm): 1.31 (s, 18H).

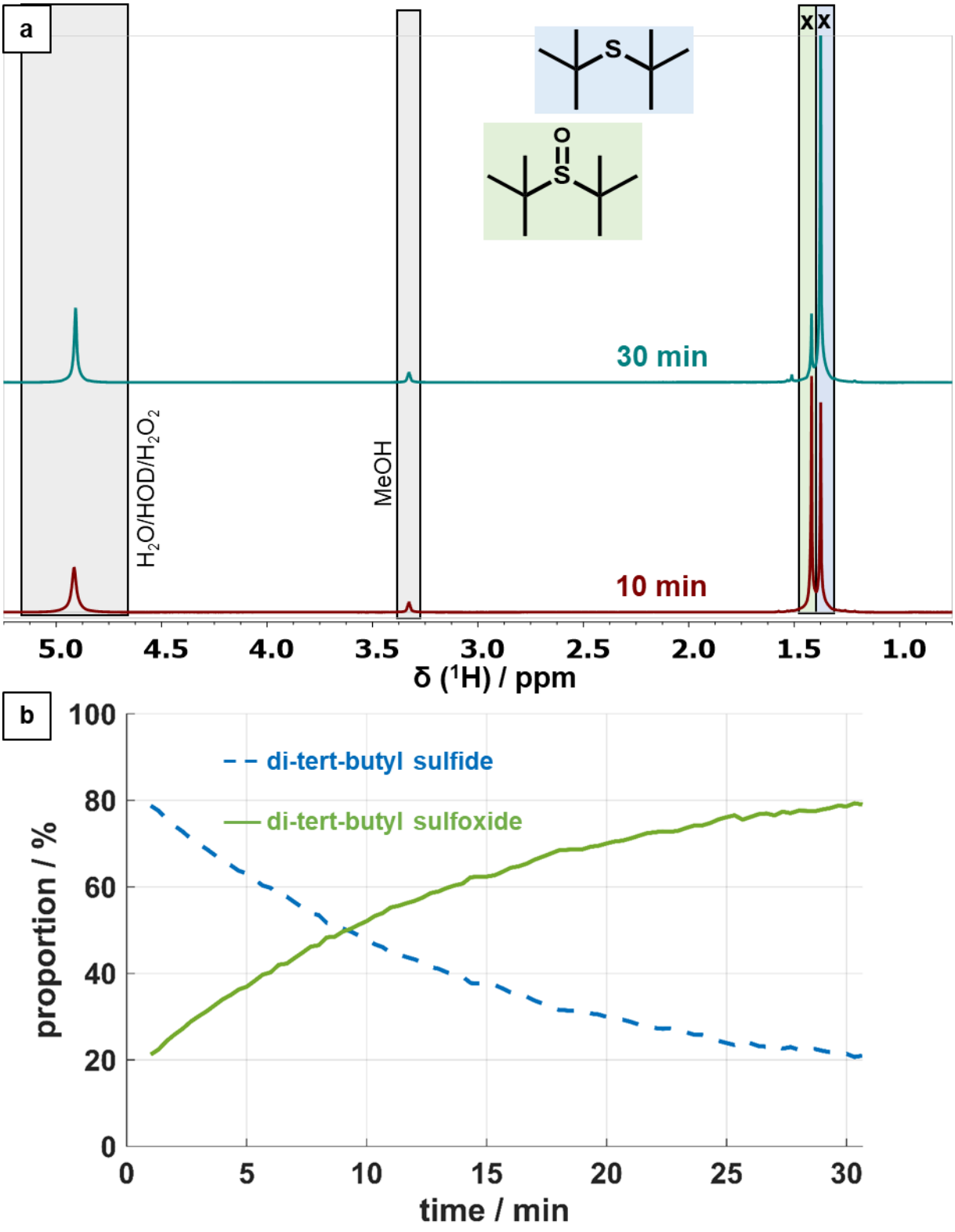

Figure S8.2.13. a) ^{1}H-NMR spectra of a standard catalysis (0.04 mmol di-tert-butyl sulfide, 0.06 mmol H_2O_2 (60 %), 0.85 mg WO_{3-x} nanorods in 0.6 mL of methanol-d_4) after 10 and 30 min, **x** marking the peaks used for integration. b) Time-dependent composition during the catalysis based on ^{1}H-NMR data.

Diphenyl sulfide

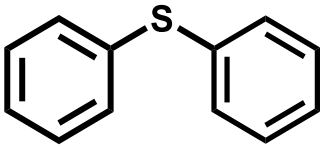

^{1}H-NMR (400 MHz, d_4-MeOD) δ (ppm): 7.33-7.24 (m, 10H).

Published elsewhere[5]: **^{1}H-NMR** (400 MHz, $CDCl_3$) δ (ppm): 7.39 (d, *J* = 7.4 Hz, 4H), 7.34 (dd, *J* = 9.9, 4.8 Hz, 4H), 7.28 (dd, *J* = 7.6, 5.1 Hz, 2H).

Diphenyl sulfoxide

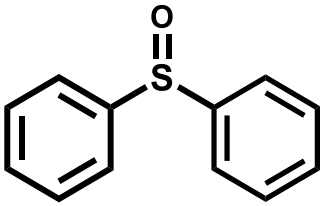

^{1}H-NMR (400 MHz, d_4-MeOD) δ (ppm): 7.72-7.69 (m, 4H), 7.55-7.53 (m, 6H).

Published elsewhere[6]: **^{1}H-NMR** (400 MHz, $CDCl_3$) δ (ppm): 7.66-7.64 (m, 4H), 7.49-7.42 (m, 6H).

Diphenyl sulfone

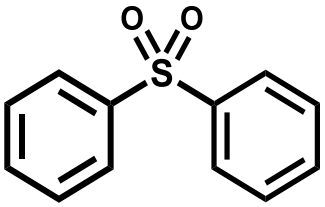

Not observed.

Published elsewhere[6]: **^{1}H-NMR** (400 MHz, $CDCl_3$) δ (ppm): 7.96-7.94 (m, 4H), 7.59-7.49 (m, 6H).

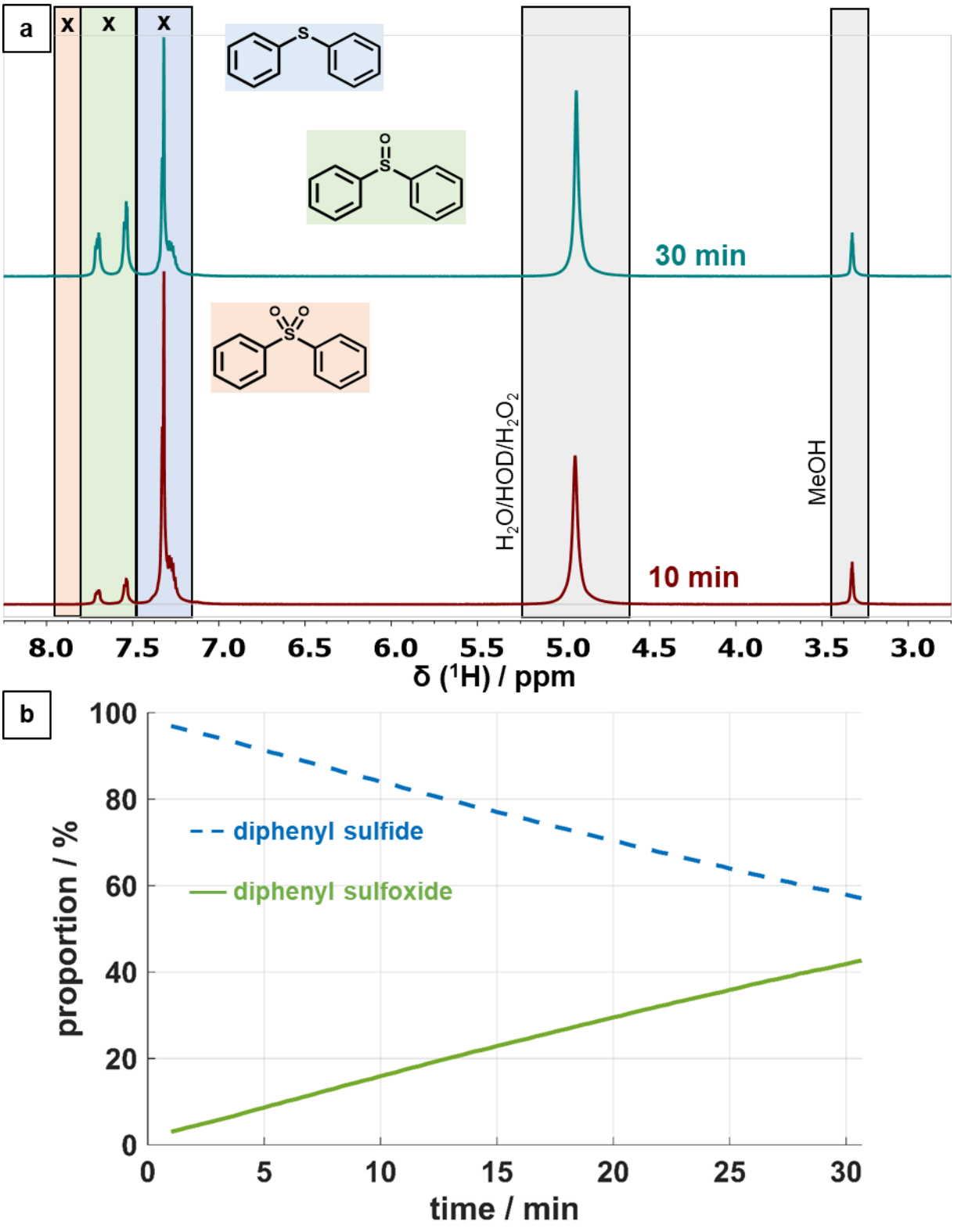

Figure S8.2.14. a) ^{1}H-NMR spectra of a standard catalysis (0.04 mmol diphenyl sulfide, 0.06 mmol H_2O_2 (60 %), 0.85 mg WO_{3-x} nanorods in 0.6 mL of methanol-d_4) after 10 and 30 min, **x** marking the peaks used for integration. b) Time-dependent composition during the catalysis based on ^{1}H-NMR data.

Dibenzyl sulfide

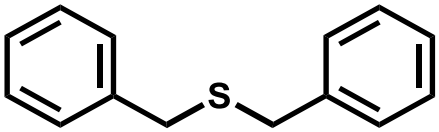

^{1}H-NMR (400 MHz, d_4-MeOD) δ (ppm): 7.31-7.23 (m, 10H), 3.61 (s, 4H).

Published elsewhere[10]: **^{1}H-NMR** (400 MHz, $CDCl_3$) δ (ppm): 7.26-7.14 (m, 10H), 3.55 (s, 4H).

Dibenzyl sulfoxide

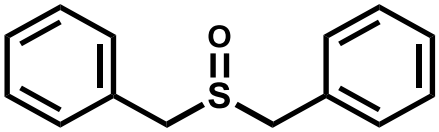

^{1}H-NMR (400 MHz, d_4-MeOD) δ (ppm): 7.41-7.36 (m, 10H), 4.20 (d, *J* = 13.0, 2H), 3.98 (d, *J* = 13.0, 2H).

Published elsewhere[6]: **^{1}H-NMR** (400 MHz, $CDCl_3$) δ (ppm): 7.38-7.24 (m, 10H), 3.91 (d, *J* = 12.0, 2H), 3.86 (d, *J* = 12.0, 2H).

Dibenzyl sulfone

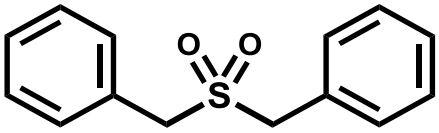

^{1}H-NMR (400 MHz, d_4-MeOD) δ (ppm): 7.60-7.55 (m, 10H), 4.38 (s, 4H).

Published elsewhere[11]: **^{1}H-NMR** (400 MHz, $CDCl_3$) δ (ppm): 7.40-7.46 (m, 10H), 4.16 (s, 4H).

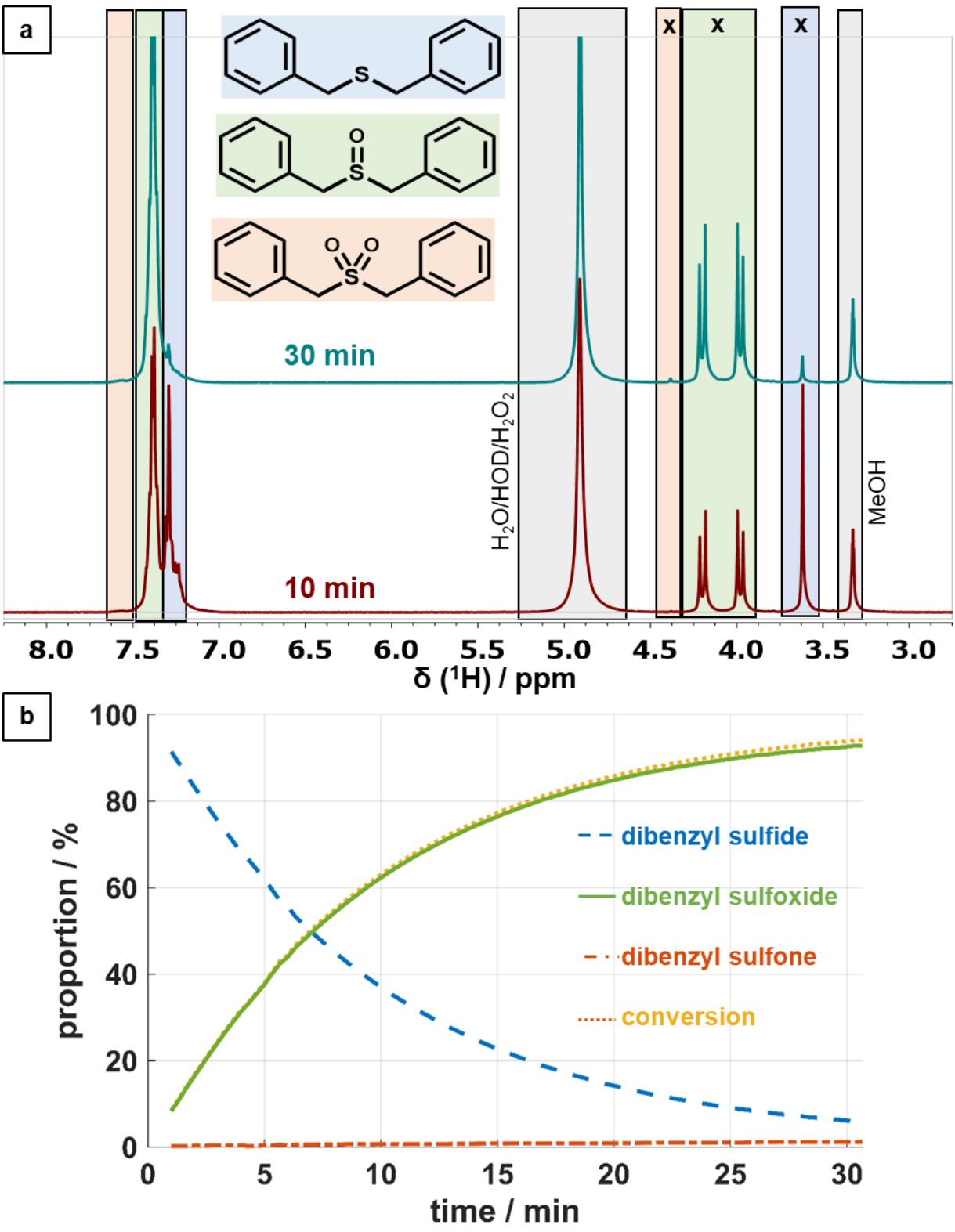

Figure S8.2.15. a) ^{1}H-NMR spectra of a standard catalysis (0.04 mmol dibenzyl sulfide, 0.06 mmol H_2O_2 (60 %), 0.85 mg WO_{3-x} nanorods in 0.6 mL of methanol-d_4) after 10 and 30 min, **x** marking the peaks used for integration. b) Time-dependent composition during the catalysis based on ^{1}H-NMR data.

4-Nitrothioanisole (4-nitrophenyl methyl sulfide)

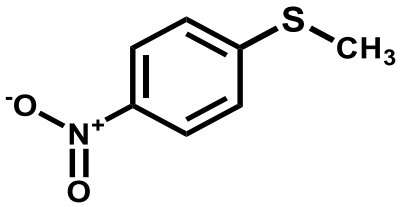

^{1}H-NMR (400 MHz, d_4-MeOD) δ (ppm): 8.16 (d, *J* = 9.0 Hz, 2H), 7.42 (d, *J* = 9.0 Hz, 2H), 2.59 (s, 3H).

Published elsewhere[12]: **^{1}H-NMR** (400 MHz, $CDCl_3$) δ (ppm): 8.24-8.04 (m, 2H), 7.34-7.14 (m, 2H), 2.54 (s, 3H).

4-Nitrophenyl methyl sulfoxide

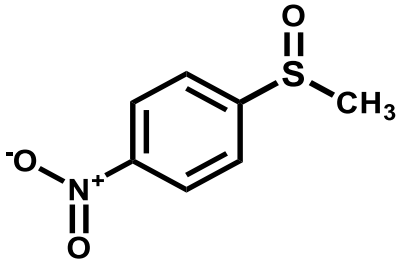

^{1}H-NMR (400 MHz, d_4-MeOD) δ (ppm): 8.45 (d, *J* = 8.9 Hz, 2H), 7.96 (d, *J* = 8.9 Hz, 2H), 2.89 (s, 3H).

Published elsewhere[13]: **^{1}H-NMR** (300 MHz, $CDCl_3$) δ (ppm): 8.36 (d, *J* = 8.7 Hz, 2H), 7.82 (d, *J* = 8.7 Hz, 2H), 2.78 (s, 3H).

4-Nitrophenyl methyl sulfone

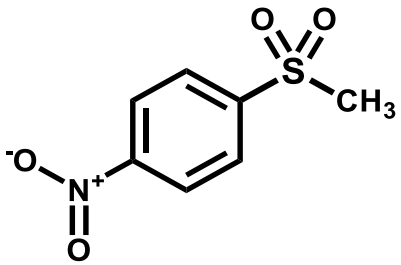

Not observed.

Published elsewhere[13]: **^{1}H-NMR** (300 MHz, $CDCl_3$) δ (ppm): 8.43 (d, *J* = 8.8 Hz, 2H), 8.16 (d, *J* = 8.8 Hz, 2H), 3.12 (s, 3H).

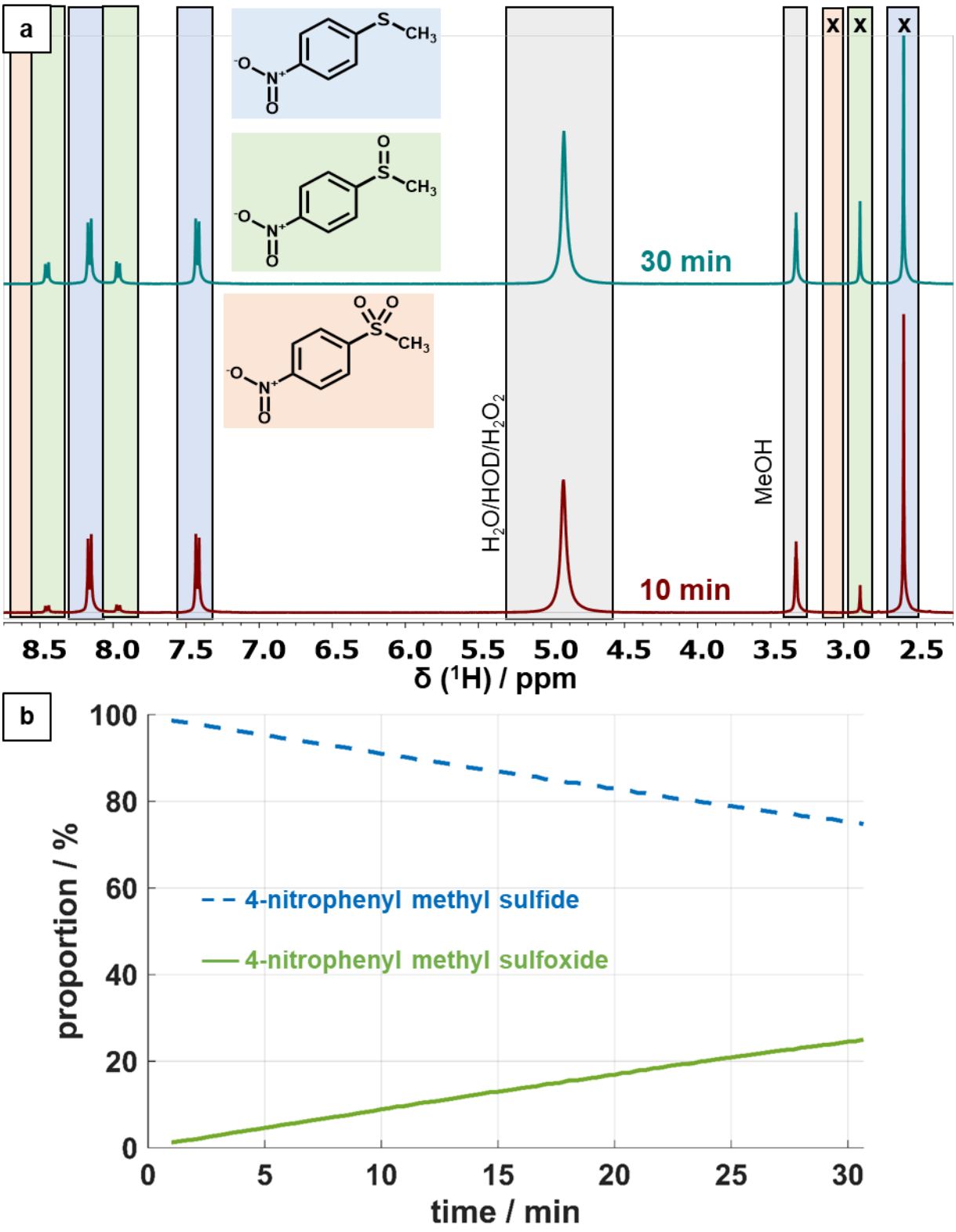

Figure S8.2.16. a) ^{1}H-NMR spectra of a standard catalysis (0.04 mmol 4-nitrophenyl methyl sulfide, 0.06 mmol H_2O_2 (60 %), 0.85 mg WO_{3-x} nanorods in 0.6 mL of methanol-d_4) after 10 and 30 min, **x** marking the peaks used for integration. b) Time-dependent composition during the catalysis based on ^{1}H-NMR data.

4-Methoxythioanisole (4-methoxyphenyl methyl sulfide)

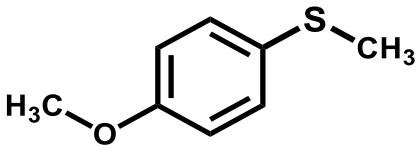

^{1}H-NMR (400 MHz, d_4-MeOD) δ (ppm): 7.27 (d, *J* = 8.8 Hz, 2H), 6.88 (d, *J* = 8.8 Hz,2H), 3.78 (s, 3H), 2,42 (s, 3H).

Published elsewhere[5]: **^{1}H-NMR** (400 MHz, $CDCl_3$) δ (ppm): 7.23 (d, *J* = 8.6 Hz, 2H), 6.81 (d, *J* = 8.6 Hz,2H), 3.75 (s, 3H), 2,40 (s, 3H).

4-Methoxyphenyl methyl sulfoxide

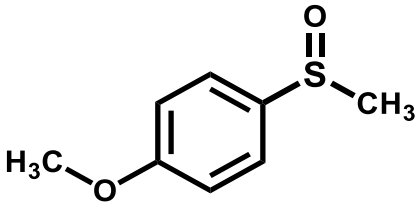

^{1}H-NMR (400 MHz, d_4-MeOD) δ (ppm): 7.68 (d, *J* = 8.7 Hz, 2H), 7.15 (d, *J* = 8.7 Hz, 2H), 3.88 (s, 3H), 2,79 (s, 3H).

Published elsewhere[13]: **^{1}H-NMR** (300 MHz, $CDCl_3$) δ (ppm): 7.53-7.58 (m, 2H), 7.01-6.96 (m, 2H), 3.81 (s, 3H), 2,65 (s, 3H).

4-Methoxyphenyl methyl sulfone

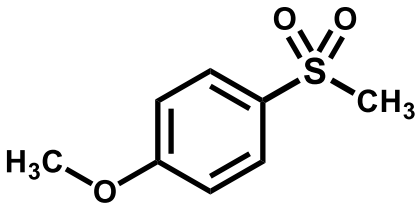

^{1}H-NMR (400 MHz, d_4-MeOD) δ (ppm): 7.89 (d, *J* = 8.4 Hz, 2H), [a](2H), [a](3H), 3.01 (s, 3H).

Published elsewhere[13]: **^{1}H-NMR** (300 MHz, $CDCl_3$) δ (ppm): 7.87 (d, *J* = 8.8 Hz, 2H), 7.02 (d, *J* = 8.8 Hz, 2H), 3.89 (s, 3H), 3.03 (s, 3H).

a. Signal intensity partially too low for assignment.

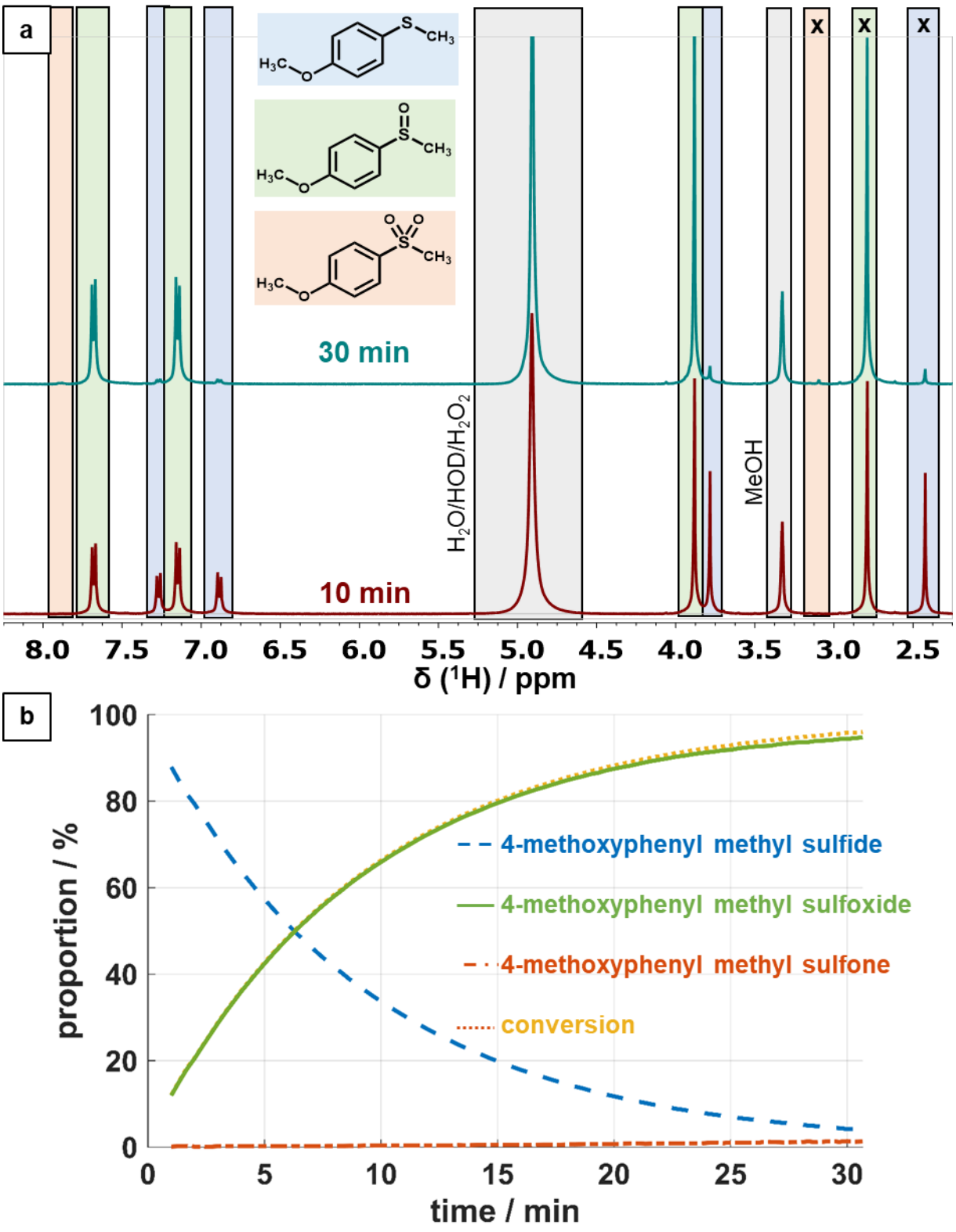

Figure S8.2.17. a) ^{1}H-NMR spectra of a standard catalysis (0.04 mmol 4-methoxyphenyl methyl sulfide, 0.06 mmol H_2O_2 (60 %), 0.85 mg WO_{3-x} nanorods in 0.6 mL of methanol-d_4) after 10 and 30 min, **x** marking the peaks used for integration. b) Time-dependent composition during the catalysis based on ^{1}H-NMR data.

4-Aminothioanisole (4-aminophenyl methyl sulfide)

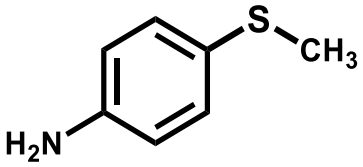

^{1}H-NMR (400 MHz, d_4-MeOD) δ (ppm): 7.14 (d, *J* = 8.6 Hz, 2H), 6.68 (d, *J* = 8.6 Hz, 2H), 2.37 (s, 3H).

Published elsewhere[12]: **^{1}H-NMR** (400 MHz, $CDCl_3$) δ (ppm): 7.21-7.11 (m, 2H), 6.65-6.60 (m, 2H), 3.38 (s, 2H), 2.41 (s, 3H).

4-Aminophenyl methyl sulfoxide

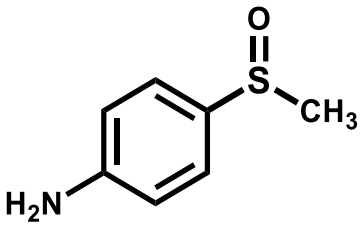

^{1}H-NMR (400 MHz, d_4-MeOD) δ (ppm): 7.46 (d, *J* = 8.7 Hz, 2H), 6.80 (d, *J* = 8.7 Hz, 2H), 2.76 (s, 3H).

Published elsewhere[14]: **^{1}H-NMR** (400 MHz, $CDCl_3$) δ (ppm): 7.45 (d, *J* = 8.8 Hz, 2H), 6.76 (d, *J* = 8.8 Hz, 2H), 3.79 (s, 2H), 2.69 (s, 3H).

4-Aminophenyl methyl sulfone

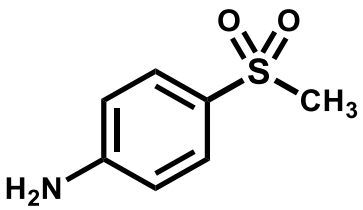

Not observed.

Published elsewhere[15]: **^{1}H-NMR** (400 MHz, $CDCl_3$) δ (ppm): 7.66 (d, *J* = 8.5 Hz, 2H), 6.69 (d, *J* = 8.5 Hz, 2H), 4.26 (s, 2H), 2.99 (s, 3H).

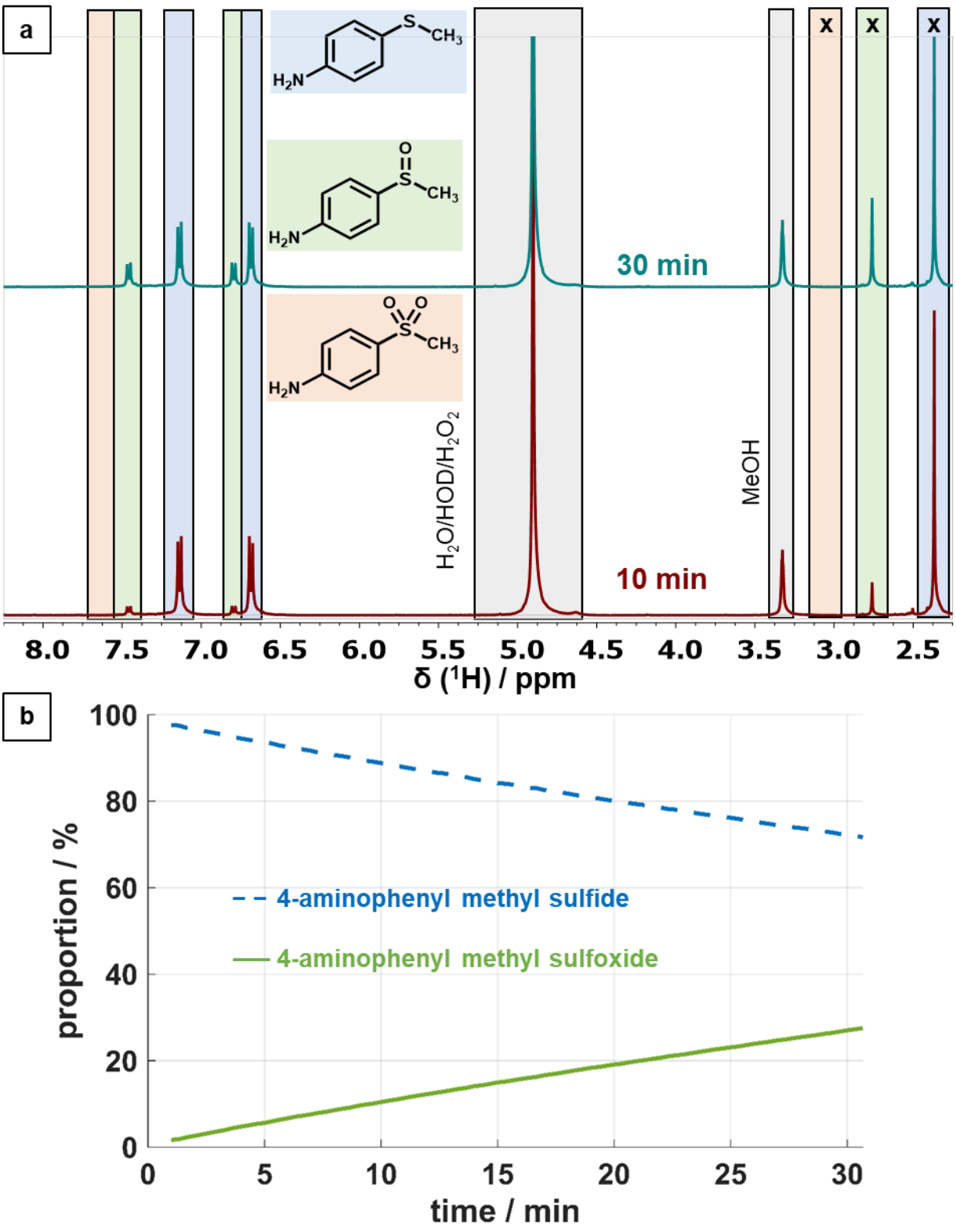

Figure S8.2.18. a) ^{1}H-NMR spectra of a standard catalysis (0.04 mmol 4-aminophenyl methyl sulfide, 0.06 mmol H_2O_2 (60 %), 0.85 mg WO_{3-x} nanorods in 0.6 mL of methanol-d_4) after 10 and 30 min, **x** marking the peaks used for integration. b) Time-dependent composition during the catalysis based on ^{1}H-NMR data.

Dimethyl sulfoxide (DMSO)

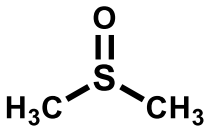

^{1}H-NMR (400 MHz, d_4-MeOD) δ (ppm): 2.68 (s, 3H).

Published elsewhere[16]: **^{1}H-NMR** (400 MHz, $CDCl_3$) δ (ppm): 2.50 (s, 6H).

Dimethyl sulfone

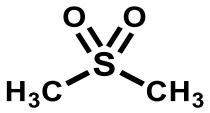

^{1}H-NMR (400 MHz, d_4-MeOD) δ (ppm): 3.03 (s, 3H).

Published elsewhere[16]: **^{1}H-NMR** (400 MHz, $CDCl_3$) δ (ppm): 2.97 (s, 6H).

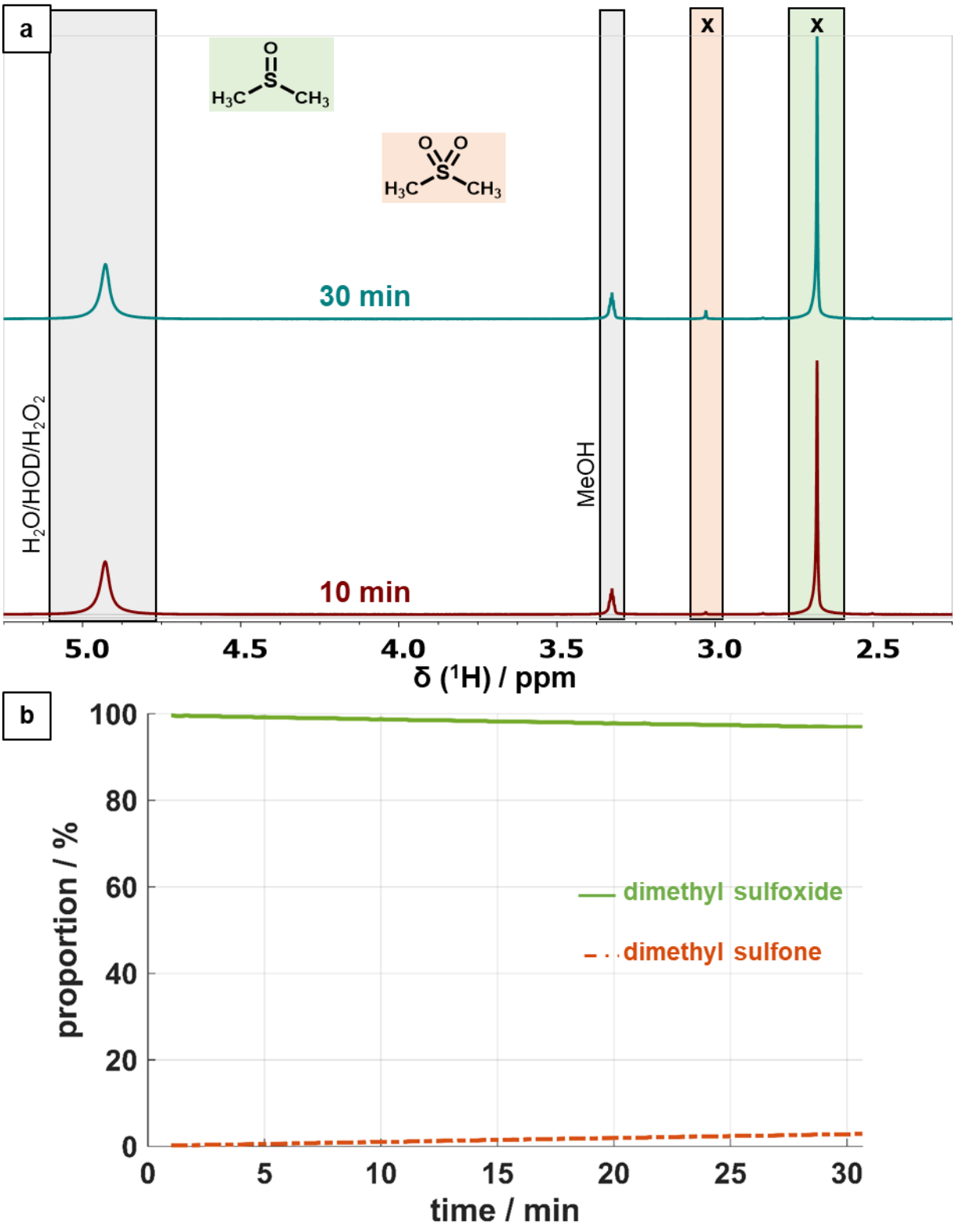

Figure S8.2.19. a) ^{1}H-NMR spectra of a catalysis using sulfoxides (0.04 mmol DMSO, 0.06 mmol H_2O_2 (60 %), 0.85 mg WO_{3-x} nanorods in 0.6 mL of methanol-d_4) after 10 and 30 min, **x** marking the peaks used for integration. b) Time-dependent composition during the catalysis based on ^{1}H-NMR data.

Dibenzothiophene (DBT)

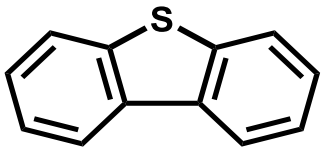

^{1}H-NMR (400 MHz, d_4-MeOD) δ (ppm): 8.27-8.24 (m, 2H), 7.91-7.89 (m, 2H), 7.51-7.49 (m, 4H).

Published elsewhere[17]: **^{1}H-NMR** (400 MHz, $CDCl_3$) δ (ppm): 8.21-8.13 (m, 2H), 7.91-7.82 (m, 2H), 7.51-42 (m, 4H).

Dibenzothiophene sulfoxide

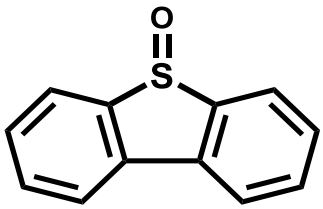

^{1}H-NMR (400 MHz, d_4-MeOD) δ (ppm): 8.05 (dd, *J* = 7.7, 4.3 Hz, 4H), 7.75 (t, *J* = 7.6 Hz, 2H), 7.63 (t, *J* = 7.7 Hz, 2H).

Published elsewhere[16]: **^{1}H-NMR** (400 MHz, $CDCl_3$) δ (ppm): 7.99 (d, *J* = 7.6 Hz, 2H), 7.82 (d. *J* = 7.7 Hz, 2H), 7.61 (t, *J* = 7.5 Hz, 2H), 7.51 (t, *J* = 7.5 Hz, 2H).

Dibenzothiophene sulfone

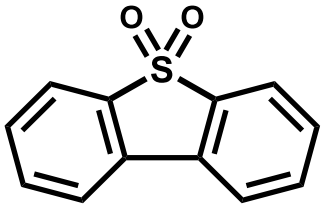

^{1}H-NMR (400 MHz, d_4-MeOD) δ (ppm): 8.08-8.03 (m, 4H), 7.80 (t, *J* = 8.8 Hz, 2H), 7.66 (t, *J* = 8.4 Hz, 2H).

Published elsewhere[16]: **^{1}H-NMR** (400 MHz, $CDCl_3$) δ (ppm): 7.83-7.78 (m, 4H), 7.66-7.62 (m, 2H), 7.55-7.51 (m, 2H).

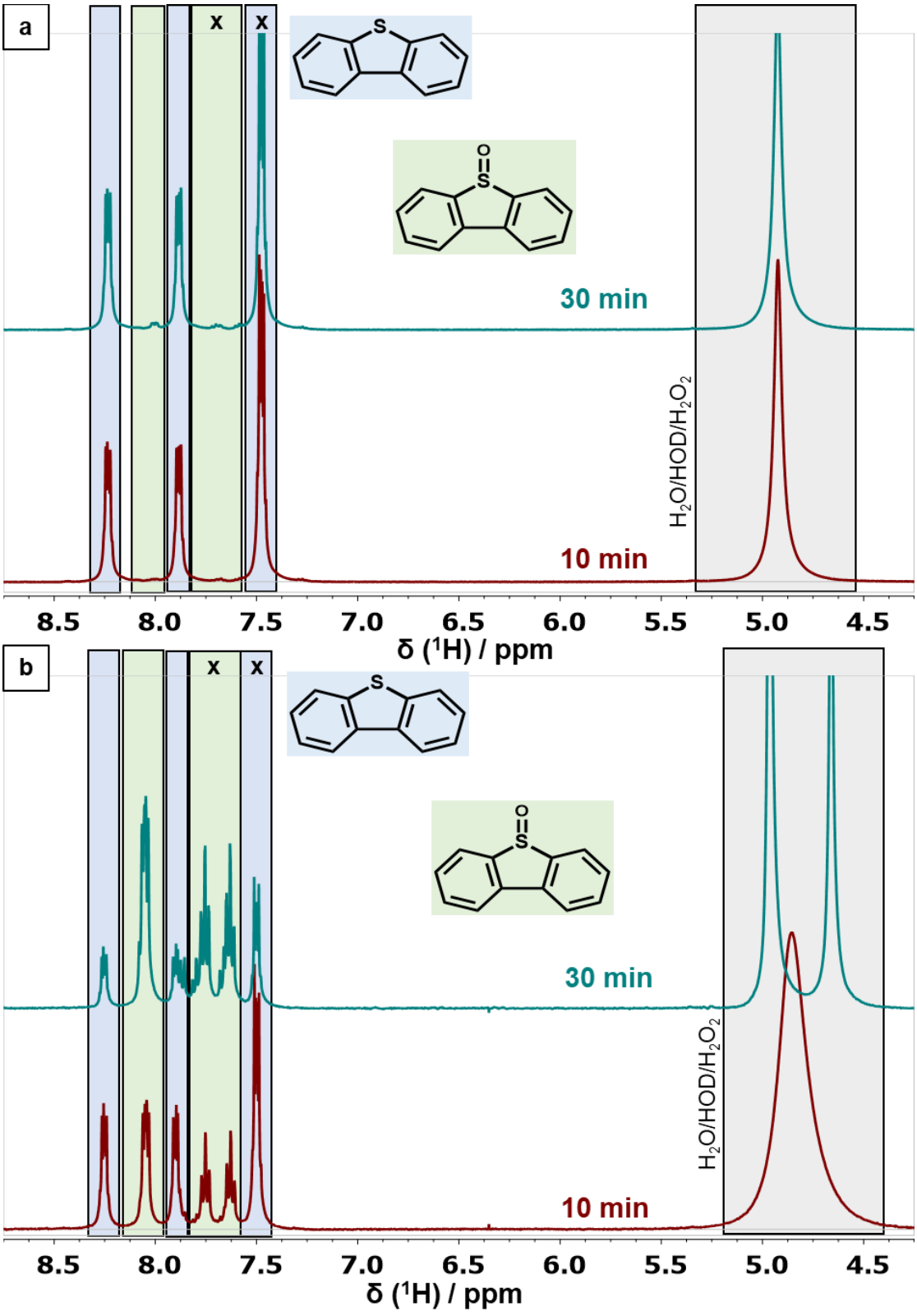

Figure S8.2.20. a) ^{1}H-NMR spectra of a standard catalysis (0.04 mmol dibenzothiophen, 0.06 mmol H_2O_2 (60 %), 0.85 mg WO_{3-x} nanorods in 0.6 mL of methanol-d_4) after 10 and 30 min. b) ^{1}H-NMR spectra of an *ex situ* catalysis (0.04 mmol dibenzothiophen, 0.06 mmol H_2O_2 (60 %), 8.5 mg WO_{3-x} nanorods in 1 mL of methanol-d_4) after 10 and 30 min. **x** marking the peaks used for integration.

8.2.3 References

1 R. Dören, B. Leibauer, M. A. Lange, E. Schechtel, L. Prädel, M. Panthöfer, M. Mondeshki and W. Tremel, *Nanoscale*, 2021, **13**, 8146–8162.

2 O. S. Hammond, K. J. Edler, D. T. Bowron and L. Torrente-Murciano, *Nat. Commun.*, 2017, **8**, 14150.

3 E. Schechtel, R. Dören, H. Frerichs, M. Panthöfer, M. Mondeshki and W. Tremel, *Langmuir*, 2019, **35**, 12518–12531.

4 C.-T. Dinh, T.-D. Nguyen, F. Kleitz and T.-O. Do, *ACS Nano*, 2009, **3**, 3737–3743.

5 R. Ma, A.-H. Liu, C.-B. Huang, X.-D. Li and L.-N. He, *Green Chem.*, 2013, **15**, 1274–1279.

6 B. Yu, C.-X. Guo, C.-L. Zhong, Z.-F. Diao and L.-N. He, *Tetrahedron Lett.*, 2014, **55**, 1818–1821.

7 E. P. Levanova, V. S. Nikonova, V. A. Grabel'nykh, N. V. Russavskaya, A. I. Albanov, I. B. Rozentsveig and N. A. Korchevin, *Russ. J. Gen. Chem.*, 2018, **88**, 383–388.

8 Spectral Database for Organic Compounds (SDBS), https://sdbs.db.aist.go.jp/sdbs/cgi-bin/direct_frame_top.cgi, (accessed 29 June 2021).

9 Y. Li, S. A.-E.-A. Rizvi, D. Hu, D. Sun, A. Gao, Y. Zhou, J. Li and X. Jiang, *Angew. Chem. Int. Ed.*, 2019, **58**, 13499–13506.

10 E. Voutyritsa, M. Garreau, M. G. Kokotou, I. Triandafillidi, J. Waser and C. G. Kokotos, *Chem. Eur. J.*, 2020, **26**, 14453–14460.

11 B. Zhang, S. Li, S. Yue, M. Cokoja, M.-D. Zhou, S.-L. Zang and F. E. Kühn, *J. Organomet. Chem.*, 2013, **744**, 108–112.

12 L. Blank, M. Fagnoni, S. Protti and M. Rueping, *Synthesis*, 2019, **51**, 1243–1252.

13 C. Yang, Q. Jin, H. Zhang, J. Liao, J. Zhu, B. Yu and J. Deng, *Green Chem.*, 2009, **11**, 1401–1405.

14 Y. Monguchi, T. Ida, T. Maejima, T. Yanase, Y. Sawama, Y. Sasai, S. Kondo and H. Sajiki, *Adv. Synth. Catal.*, 2014, **356**, 313–318.

15 D. Han, S. Li, S. Xia, M. Su and J. Jin, *Chem. Eur. J.*, 2020, **26**, 12349–12354.

16 B. Yu, A.-H. Liu, L.-N. He, B. Li, Z.-F. Diao and Y.-N. Li, *Green Chem.*, 2012, **14**, 957–962.

17 B. Higginson, J. Sanjosé-Orduna, Y. Gu and R. Martin, *Synlett*, 2021, **32**, 1633–1636.

8.3 Supporting Information for Chapter 4

8.3.1 Author Contributions

Conception and design of the study:

[redacted]

Preparation of samples and acquisition of data:

[redacted] – preparation of nanocrystals

[redacted] – TEM measurements

[redacted] – PXRD measurements

[redacted] – Mössbauer measurements

Analysis and interpretation of data:

[redacted] – PXRD diffraction analysis and refinements

[redacted] – TEM images

[redacted] – Mössbauer spectroscopy

Drafting of the supporting information:

[redacted]

Revising the supporting information critically for important intellectual content:

[redacted]

Preparation of figures:

[redacted]

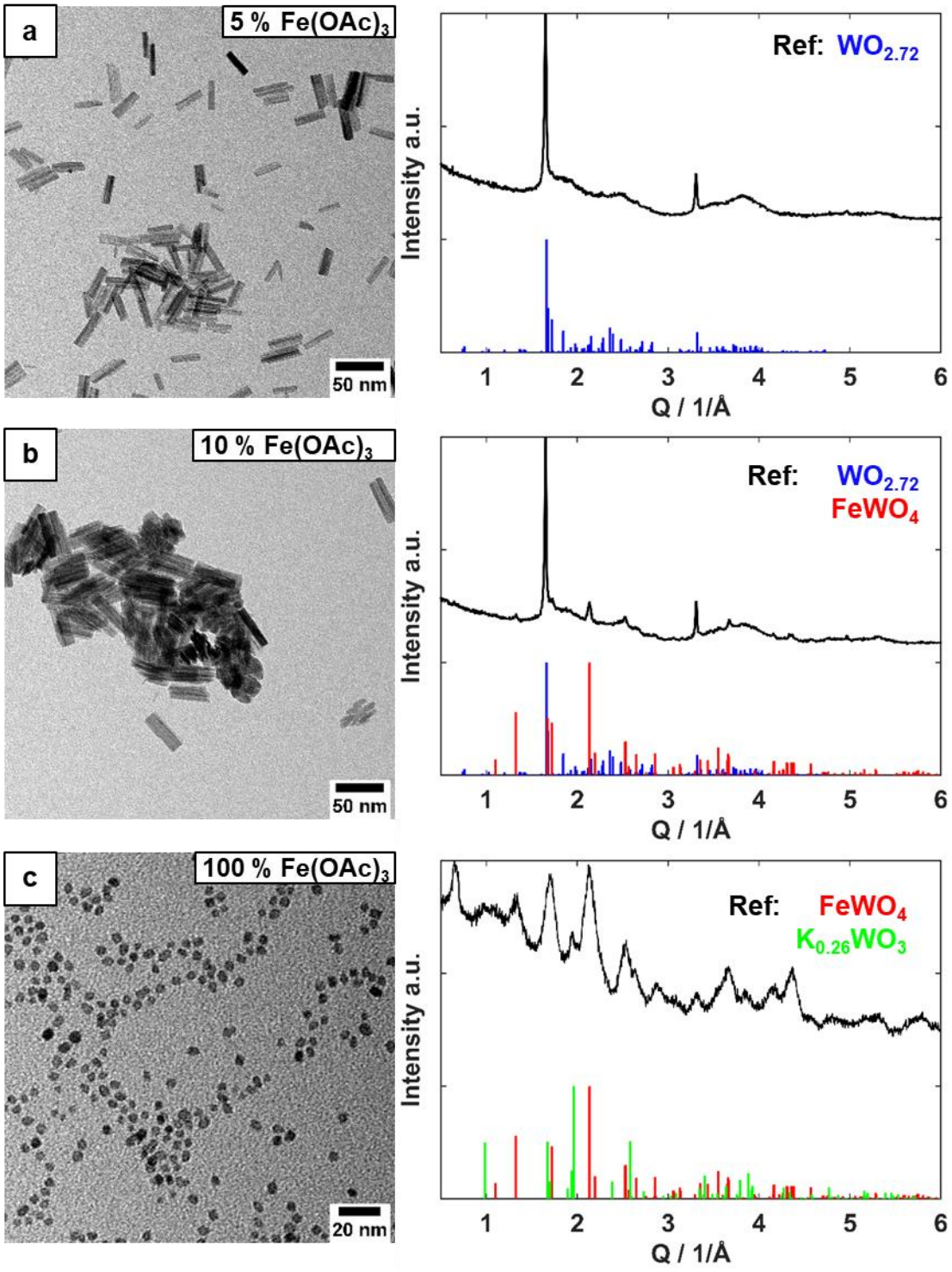

Figure S8.3.1. TEM images (left) and PXRD patterns (right) of a) WO_{3-x} NRs synthesized with oleic acid from the steel can, b) addition of 20 mol% iron oleate to the standard synthesis and c) addition of 20 mol% iron oleate to the standard synthesis and a HR of 2.5 K/min. References: $WO_{2.72}$ (space group $P2/m$ (10), COD, Entry No.: 96-152-8167). $FeWO_4$ (Ferberite, space group $P2/c$ (13), COD no. 96-900-8125) and $K_{0.26}WO_3$ (hexagonal, space group $P6_3$ (173), ICSD no. 99-501-7632).

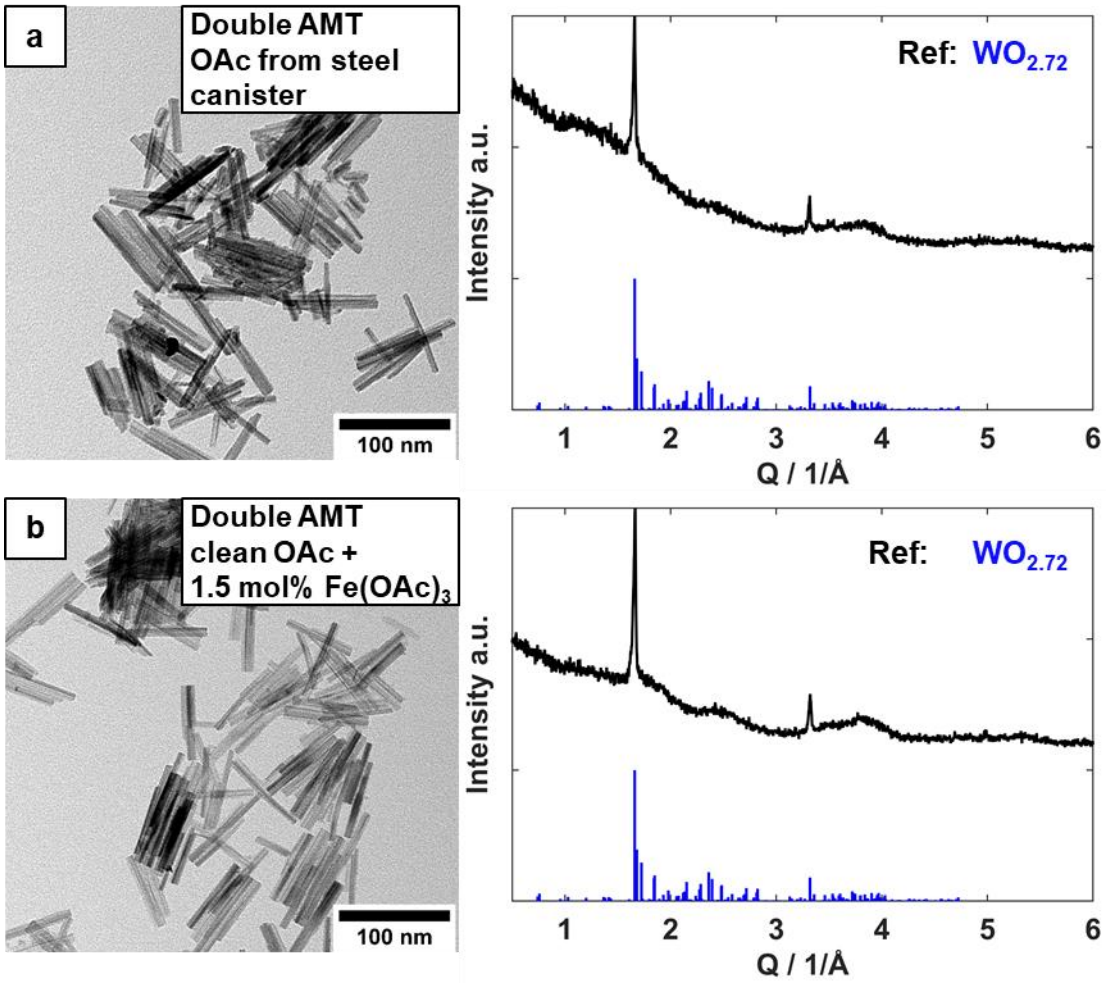

Figure S8.3.2. TEM images (left) and PXRD patterns (right) of a) WO_{3-x} NRs synthesized with oleic acid from the steel can and double amount AMT (0.24 mmol instead of 0.12 mmol) and b) addition of 1.5 mol% iron oleate to pure oleic acid and double amount AMT (0.24 mmol instead of 0.12 mmol). Reference: $WO_{2.72}$ (space group $P2/m$ (10), COD, Entry No.: 96-152-8167).

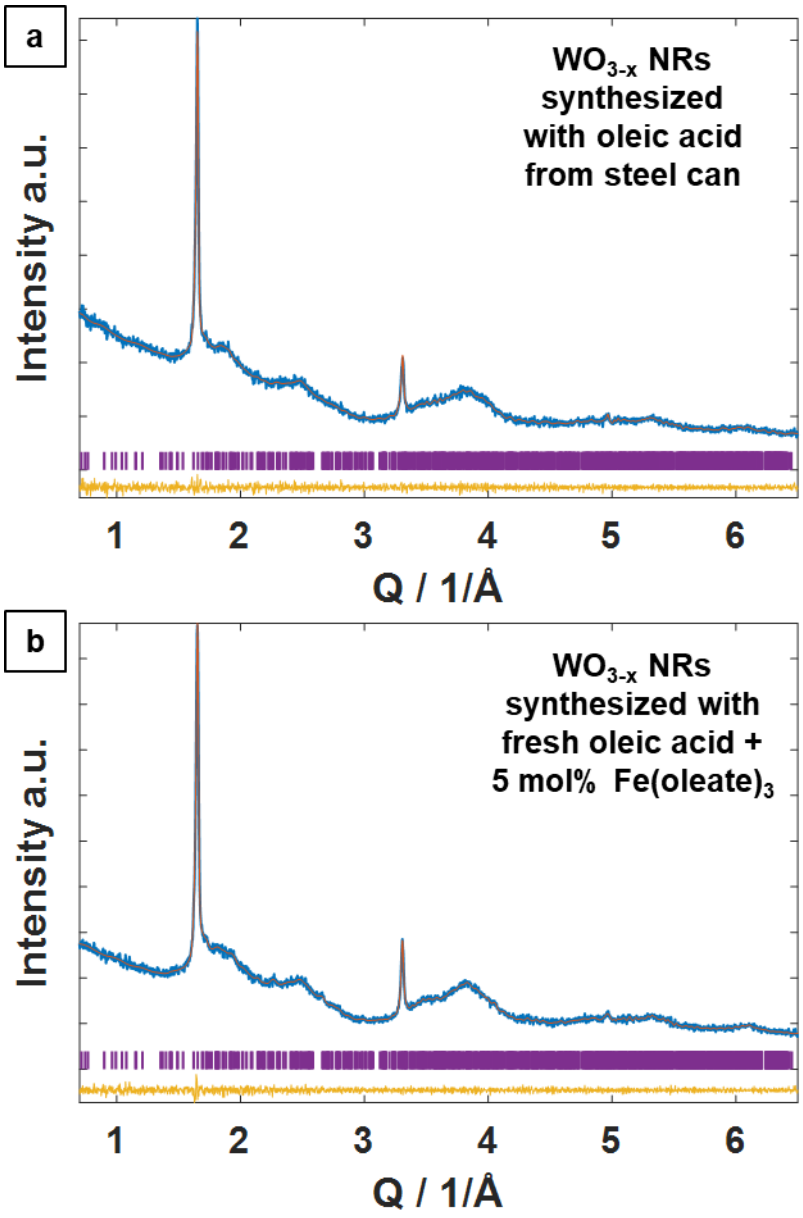

Figure S8.3.3. Pawley refinements of WO_{3-x} NRs based on space group $P2/m$ a) synthesized with oleic acid from steel canister with fit paramters a=18.103(217) Å, b=3.793(4) Å, c=13.992(129) Å, α=90 °, β=115.211 °, γ=90 °, rwp=2.98, goodness of fit =1.00, crystallite size =5.9(6)*67.1(7.6)*3.4(5) nm and b) synthesized with fresh oleic acid using 5 mol% $Fe(oleate)_3$ with fit paramters a=18.090(257) Å, b=3.798(4) Å, c=13.985(142) Å, α=90 °, β=115.211 °, γ=90 °, rwp=2.79, goodness of fit =1.00, crystallite size =6.7(7)*58.5(3.3)*3.6(5) nm.

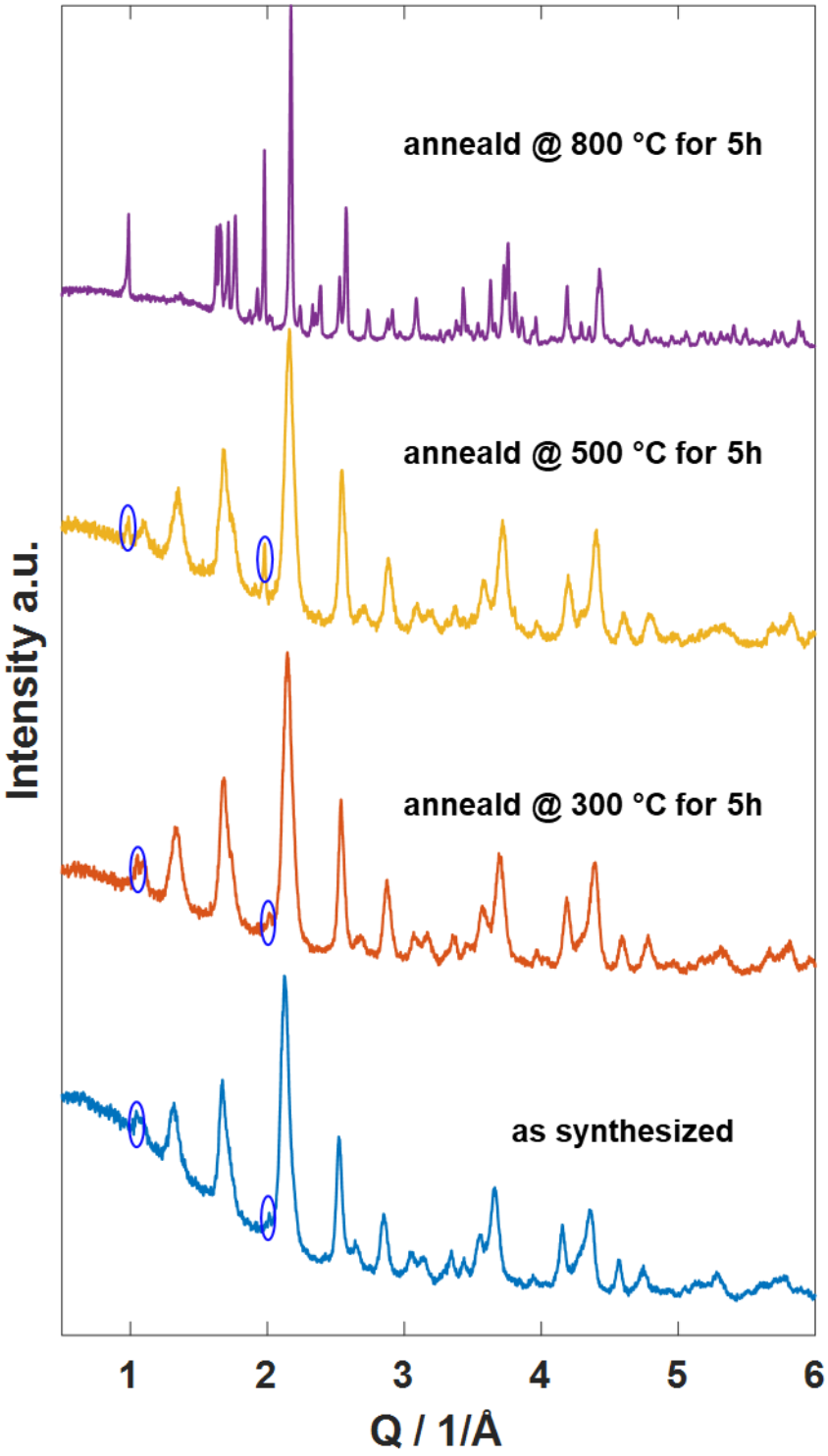

Figure S8.3.4. PXRD patterns of ferberite $FeWO_4$ NCs shown in Figure 4.2c annealed at different temperatures. Blue markings indicating hexagonal potassium tungsten bronze.

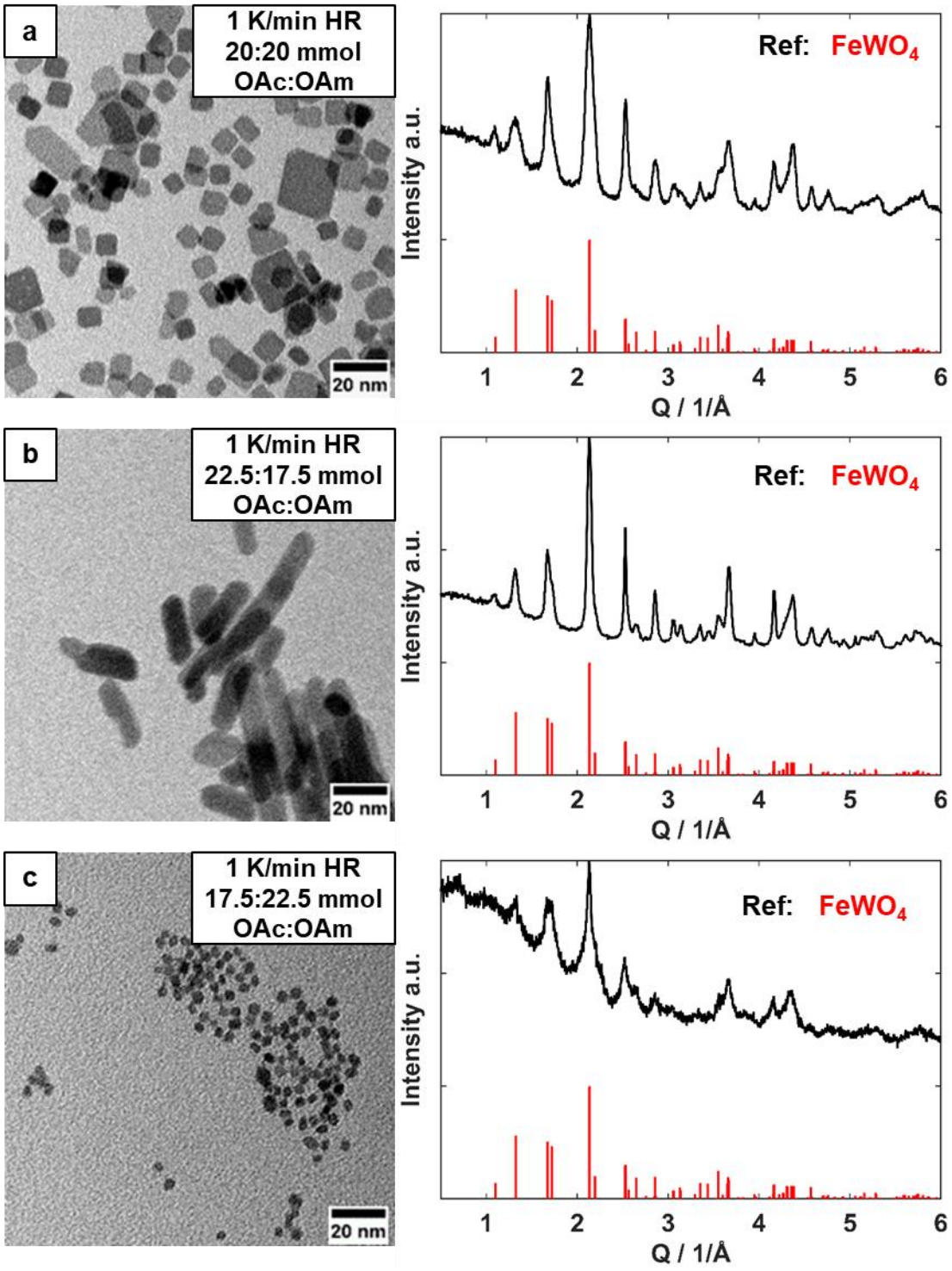

Figure S8.3.5. TEM images (left) and PXRD patterns (right) of ferberite $FeWO_4$ NCs synthesized with 1.43:1.43 mmol Fe:W, 1 K/min heating rate and a) OAc:OAm ratio of 20:20 mmol, b) OAc:OAm ratio of 22.5:17.5 mmol and c) OAc:OAm ratio of 17.5:22.5 mmol. References: $WO_{2.72}$ (space group $P2/m$ (13), COD, Entry No.: 96-152-8167). $FeWO_4$ (Ferberite, space group $P2/c$ (13), COD no. 96-900-8125).

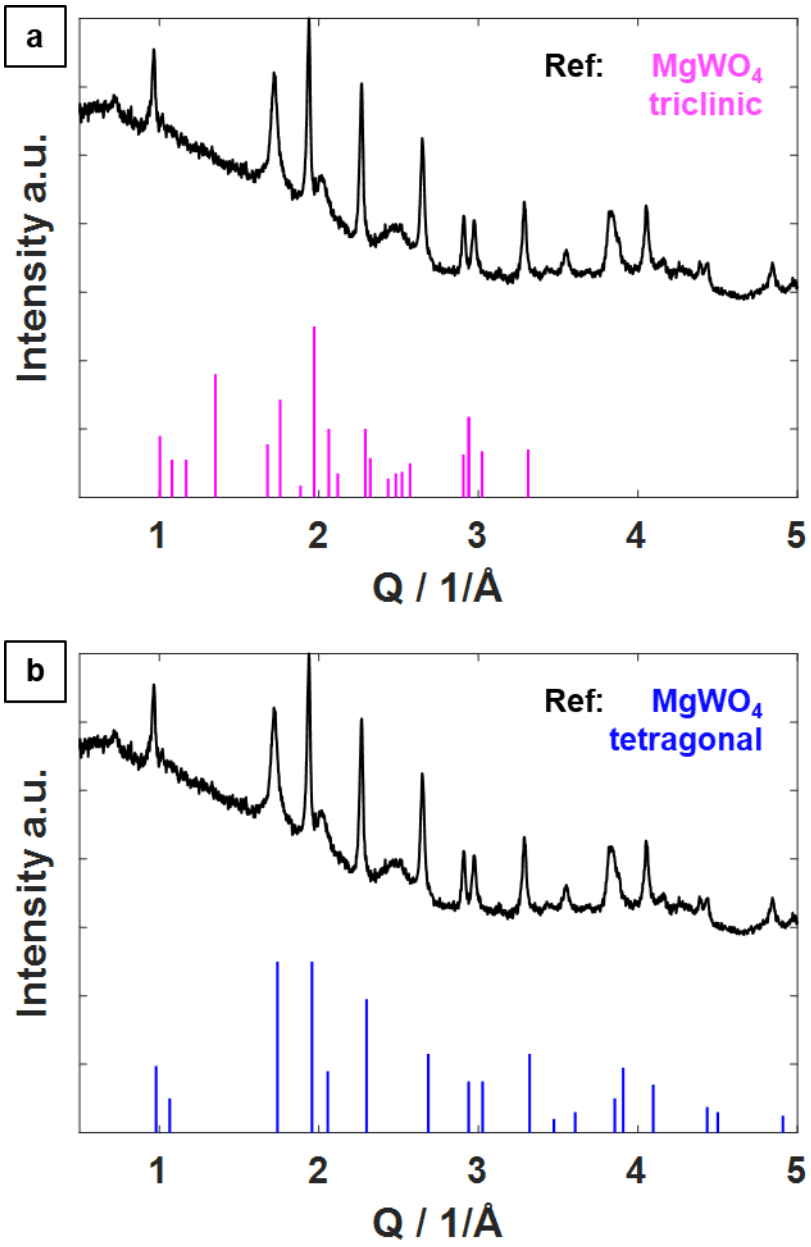

Figure S8.3.6. PXRD patterns of $FeWO_4$ NCs shown in Figure 4.2c with unknown structure. References: (a) $MgWO_4$ (triclinic, PDF, Entry No.: 00-045-0412) and (b) $MgWO_4$ (tetragonal, PDF, Entry No.: 00-052-0390).

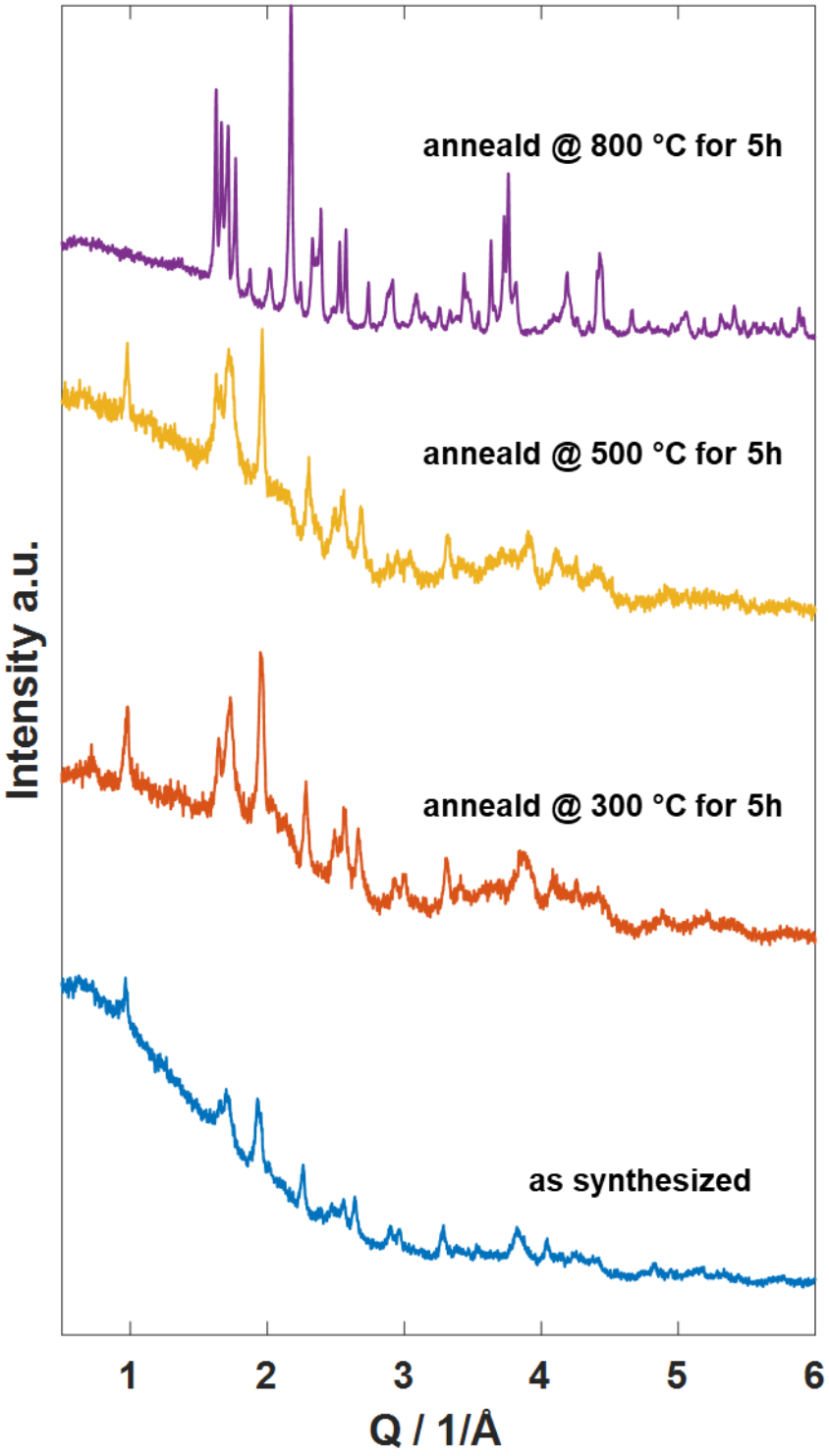

Figure S8.3.7. PXRD patterns of ferberite $FeWO_4$ NCs shown in Figure 4.3b annealed at different temperatures.

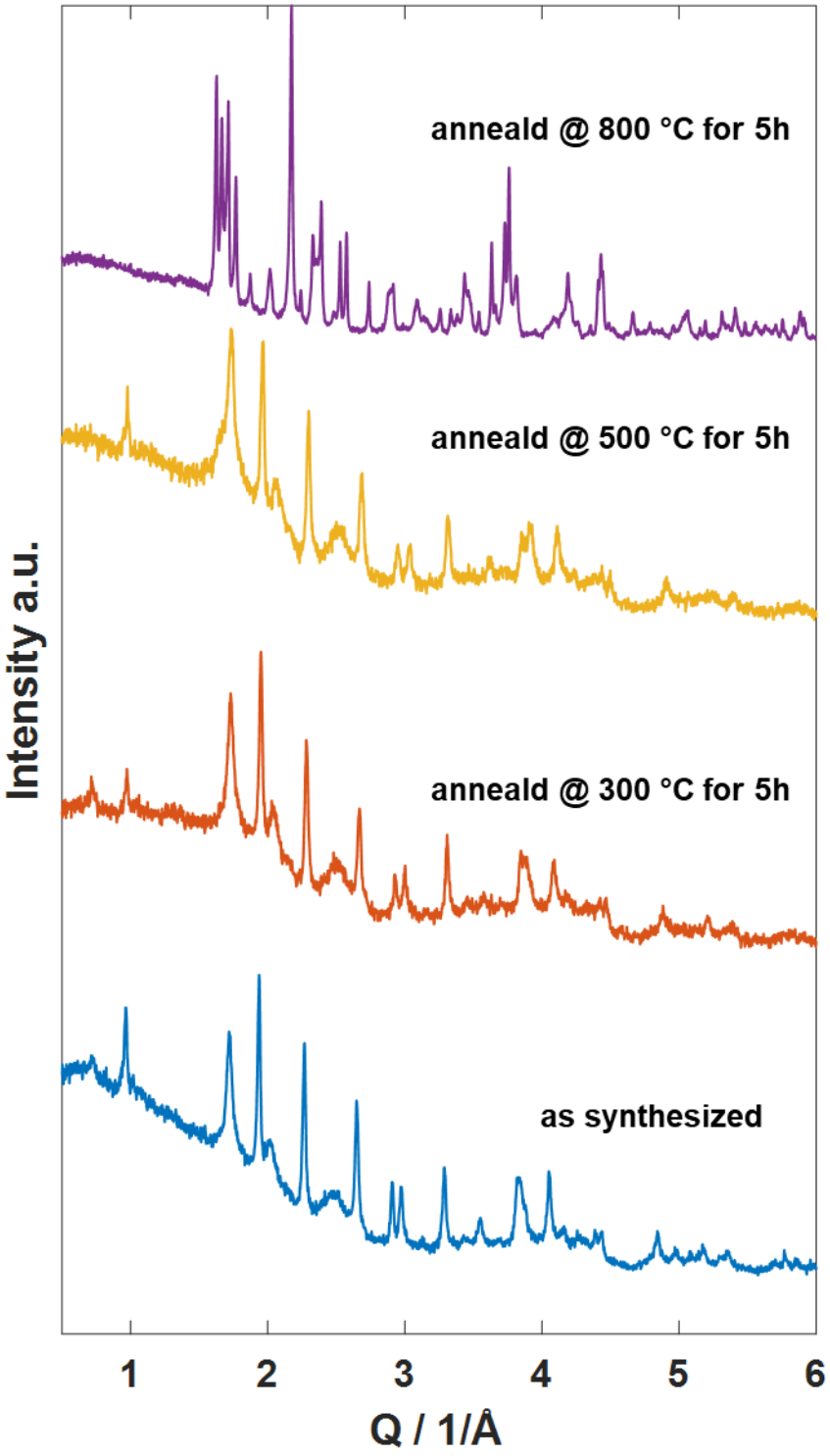

Figure S8.3.8. PXRD patterns of ferberite $FeWO_4$ NCs shown in Figure 4.3c annealed at different temperatures.

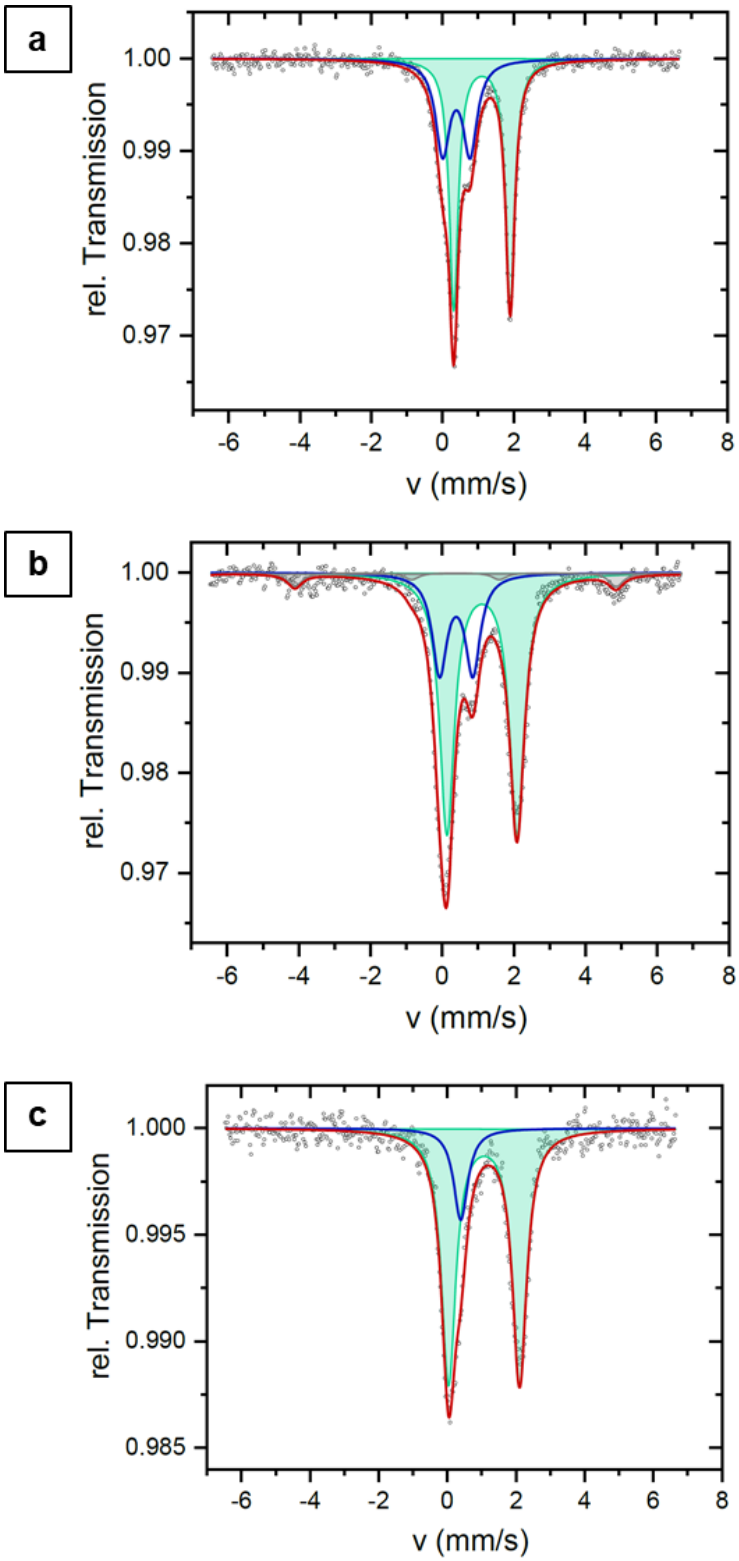

Figure S8.3.9. Mössbauer spectra of a) $FeWO_4$ NCs with ferberite structure shown in Figure 4.2c, b) of unknown $FeWO_4$ structure synthesized with $Fe(acac)_3$ in 20 mmol OAd, shown in Figure 4.3b and c) of unknown $FeWO_4$ structure synthesized with $Fe(oleate)_3$ in 20 mmol OAd, shown in Figure 4.3c. Fit parameters for Fe(II) and Fe(III) are found in Table 4.1.

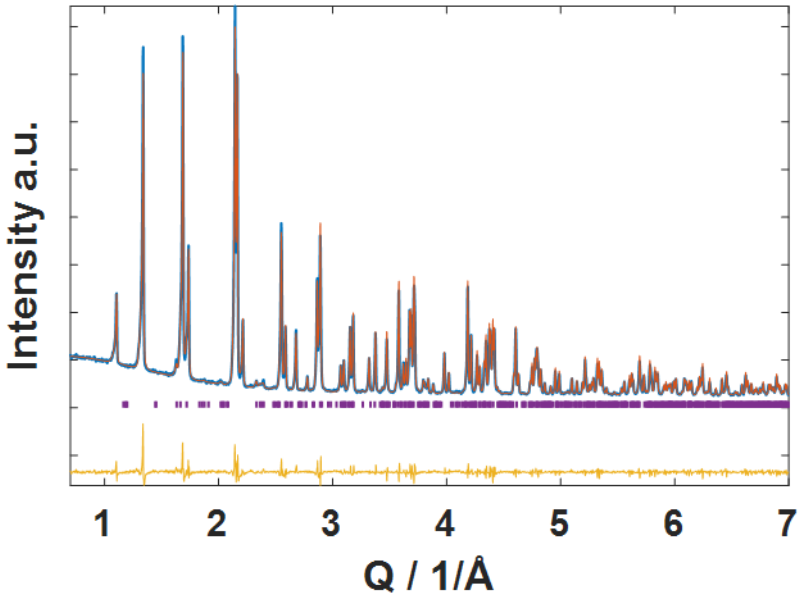

Figure S8.3.10. Rietveld refinements of $MgWO_4$ NCs annealed at 800 °C for 5 h in air using on monoclinic $MgWO_4$ (space group $P2/c$ (13)) and monoclinic WO_3 (space group $P2/n$ (14)) structures. Fit paramters for $MgWO_4$. a=4.689(0) Å, b=5.676(0) Å, c=4.929(0) Å, α=90 °, β=90.77(0) °, γ=90 ° weight percent=96.1(2) % and for WO_3: a=7.303(3) Å, b=7.542(3) Å, c=7.698(3) Å, α=90 °, β=90.73(5) °, γ=90 ° weight percent=3.9(2) %; rwp=5.14, goodness of fit =1.87.

8.4 Supporting Information for Chapter 5

8.4.1 Author Contributions

Conception and design of the study:

[redacted]

Preparation of samples and acquisition of data:

[redacted] – preparation of nanocrystals

[redacted] – biologic evaluations

[redacted] – halooperoxidase assays

[redacted] – leaching assay

[redacted] – TEM measurements

[redacted] – UV-Vis-NIR absorption and reflection spectroscopy

[redacted] – PXRD measurements

[redacted] – XPS measurements

[redacted] – ζ-potential measurements

Analysis and interpretation of data:

[redacted] – PXRD diffraction and refinements

[redacted] – TEM images

[redacted] – halooperoxidase data

[redacted] – biological data

[redacted] – XPS spectroscopy, ζ-potential

[redacted] – UV-Vis-NIR absorption and reflection spectroscopy

Drafting of the supporting information:

[redacted]

Revising the supporting information critically for important intellectual content:

[redacted]

Preparation of figures

[redacted]

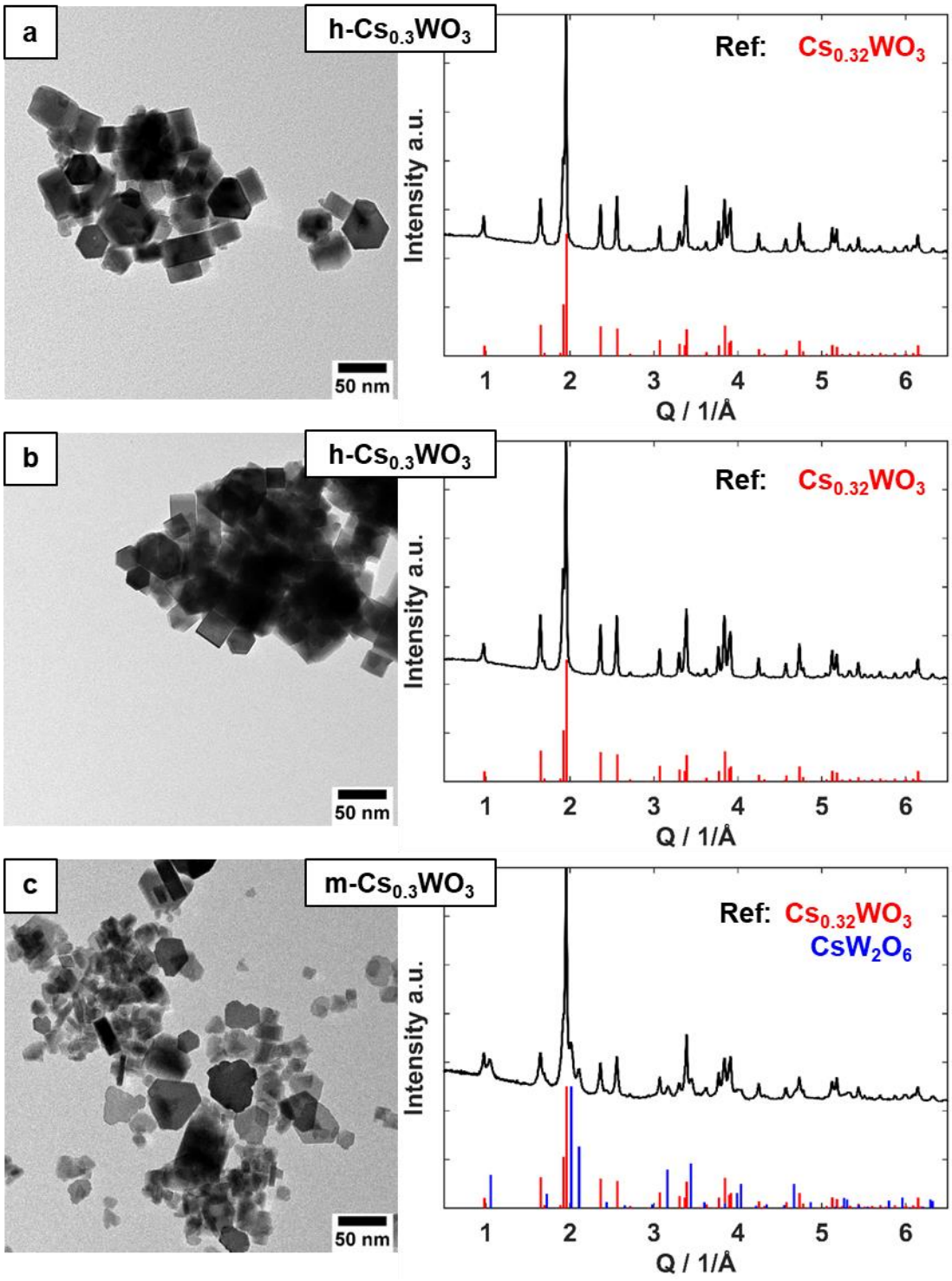

Figure S8.4.1. a) TEM image and PXRD pattern of hexagonal $Cs_{0.3}WO_3$ NCs synthesized with 22.5:17.5 mmol OAc:OAm and heating rate of 25 K/min, b) TEM image and PXRD pattern of hexagonal $Cs_{0.3}WO_3$ NCs synthesized with 20:20 mmol OAc:OAm and heating rate of 25 K/min and c) TEM image and PXRD pattern of mixed cubic/hexagonal $Cs_{0.3}WO_3$ NCs synthesized with 17.5:22.5 mmol OAc:OAm and heating rate of 25 K/min. PXRD references: $Cs_{0.32}WO_3$ (space group $P6_3/mcm$, ICSD no. 99-501-4972) and $CsW_{1.6}O_3$ (space group $Fd\bar{3}m$, ICSD no. 99-502-4816).

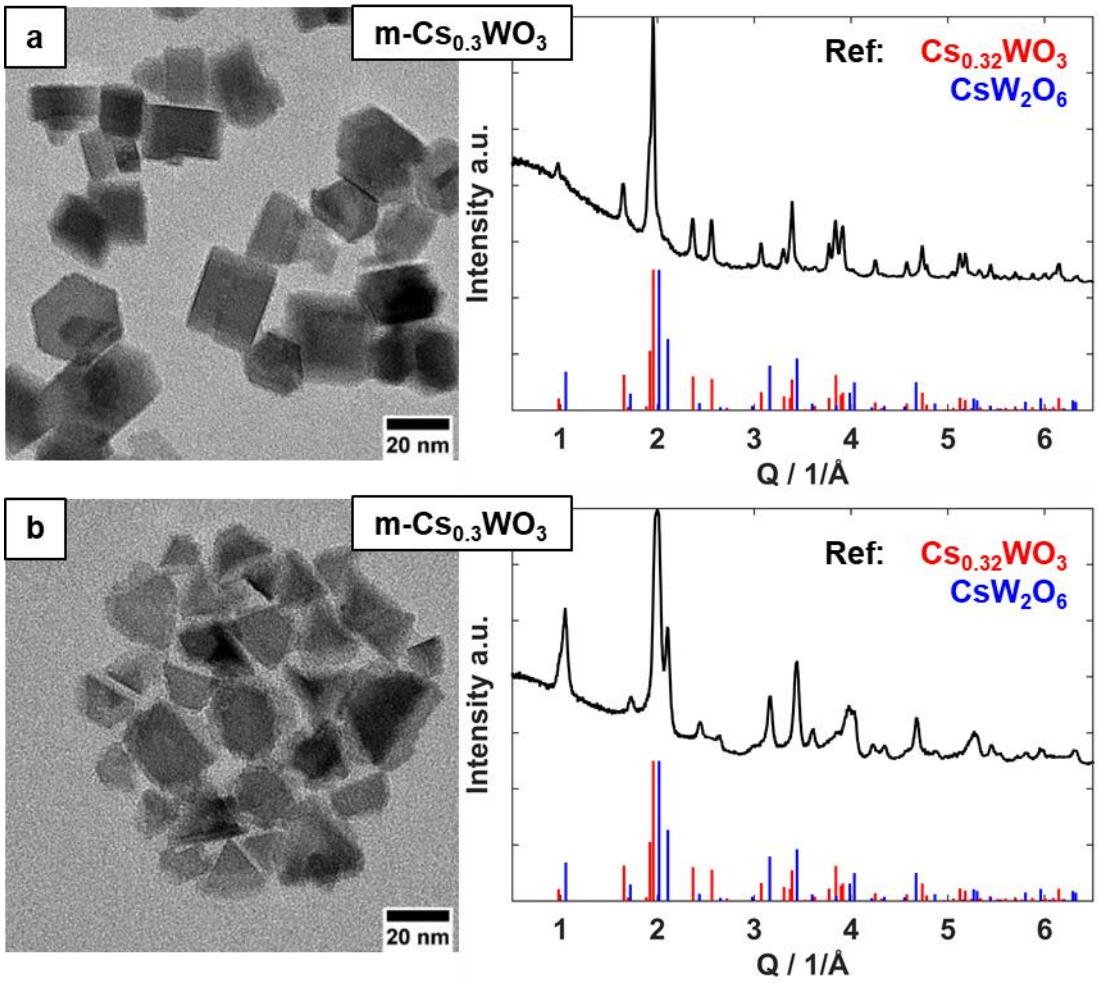

Figure S8.4.2. a) TEM image and PXRD pattern of mixed cubic/hexagonal $Cs_{0.3}WO_3$ NCs NCs synthesized with 19:21 mmol OAc:OAm and heating rate of 2.5 K/min and b) TEM image and PXRD pattern of mixed cubic/hexagonal $Cs_{0.3}WO_3$ NCs synthesized with 15:25 mmol OAc:OAm and heating rate of 2.5 K/min. PXRD references: $Cs_{0.32}WO_3$ (space group $P6_3/mcm$, ICSD no. 99-501-4972) and $CsW_{1.6}O_3$ (space group $Fd\bar{3}m$, ICSD no. 99-502-4816).

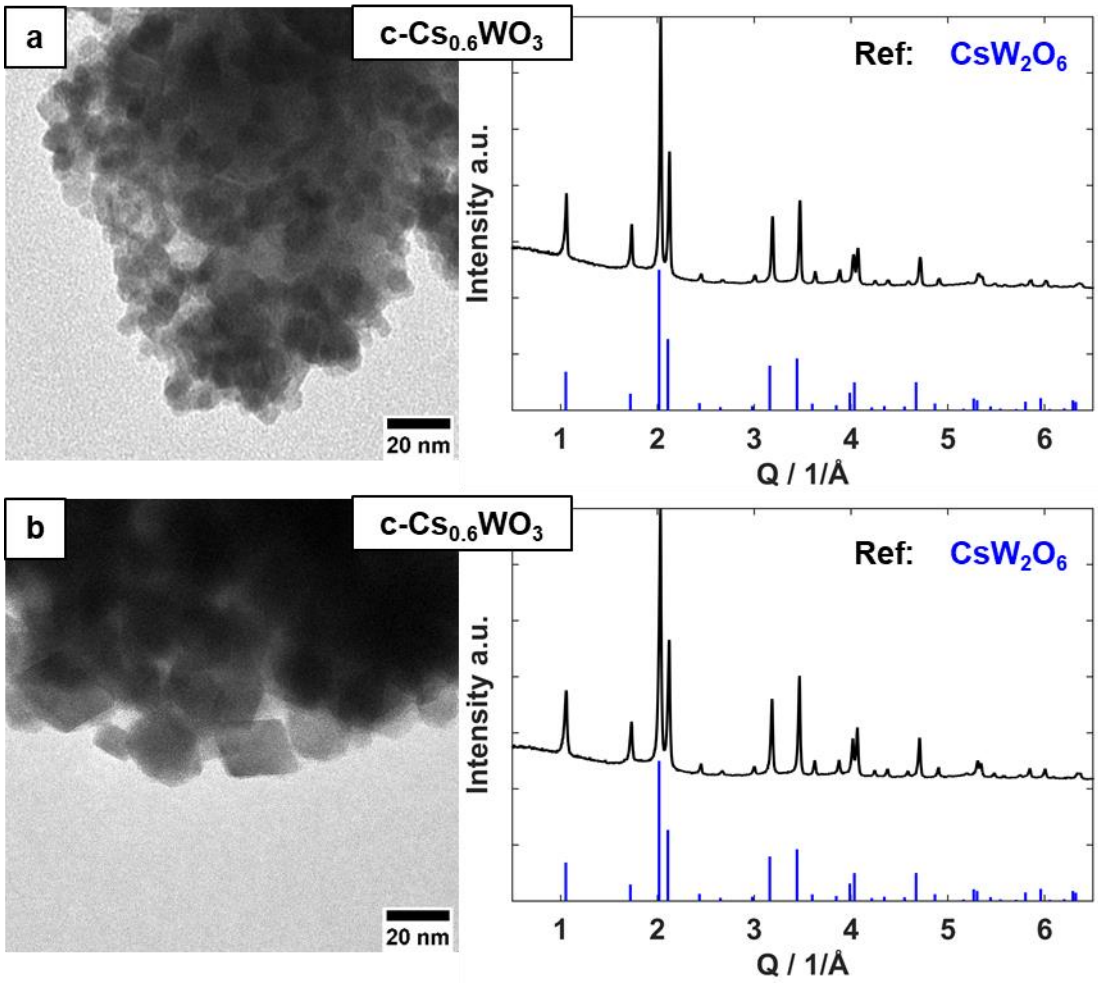

Figure S8.4.3. a) TEM image and PXRD pattern of cubic $Cs_{0.6}WO_3$ NCs synthesized with 20:20 mmol OAc:OAm and heating rate of 5 K/min and b) TEM image and PXRD pattern of cubic $Cs_{0.6}WO_3$ NCs synthesized with 23.5:17.5 mmol OAc:OAm and heating rate of 5 K/min. PXRD reference: $CsW_{1.6}O_3$ (space group $Fd\bar{3}m$, ICSD no. 99-502-4816).

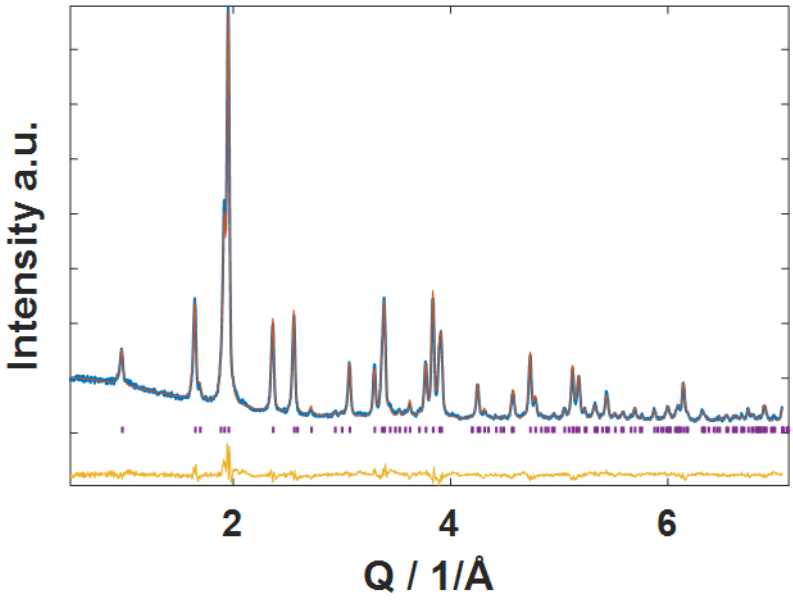

Figure S8.4.4. Rietveld refinement for h-$Cs_{0.3}WO_3$ synthesized with 20:20 mmol OAc:OAm and 5 K/min heating rate. Refinement performed using hexagonal $P6_3/mcm$ structure. Rwp: 5.90, gof: 1.45, a=7.406(0), b=7.407(5), c=7.610(0), CS=34.2(3) nm, Occ(Cs)=0.29(1).

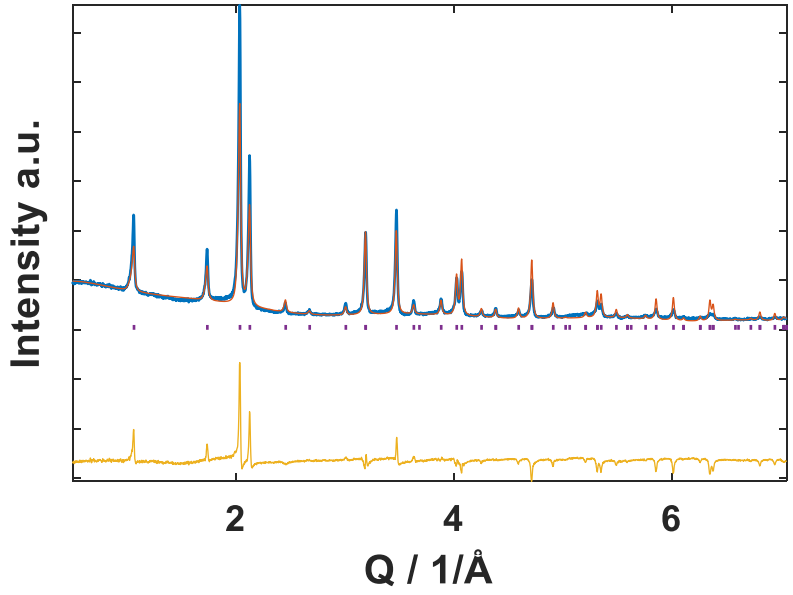

Figure S8.4.5. Rietveld refinement for c-$Cs_{0.6}WO_3$ synthesized with 17.5:22.5 mmol OAc:OAm and 5 K/min heating rate. Refinement performed using cubic $Fd\bar{3}m$ structure. Rwp: 12.33, gof: 3.89, a=b=c=10.235(0), CS=34.3(5) nm, Occ(Cs)=0.54(1).

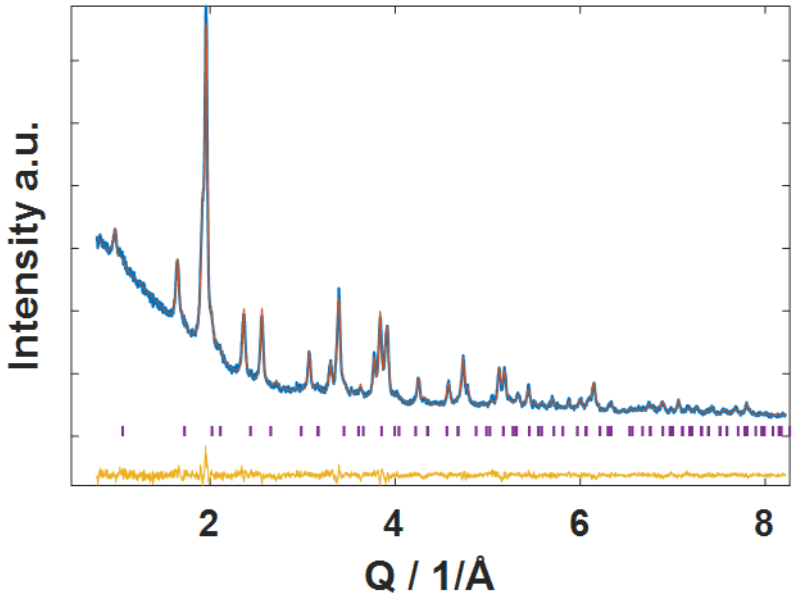

Figure S8.4.6. Rietveld refinement for m-$Cs_{0.3}WO_3$ synthesized with 19:21 mmol OAc:OAm and 2.5 K/min heating rate. Refinement performed using hexagonal $P6_3/mcm$ and cubic $Fd\bar{3}m$ structures. Rwp: 3.51, gof: 1.10; values of hexagonal phase: a=7.403(1), b=7.400(6), c=7.613(0), CS=25.4(3) nm, Occ(Cs)=0.29(0); values of cubic phase: a=b=c=10.312(3), CS=11.0(8) nm, Occ(Cs)=0.50(2); ratio h/c: 89.0(4):11.0(4).

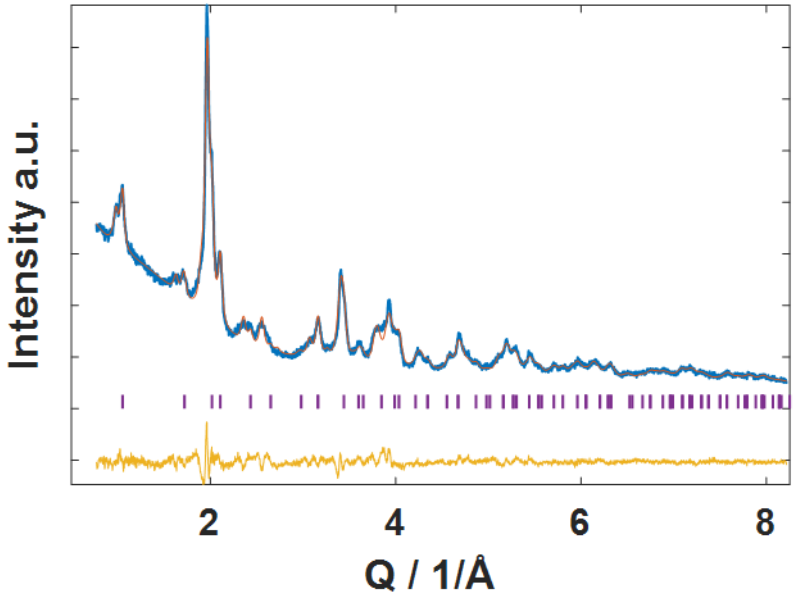

Figure S8.4.7. Rietveld refinement for m-$Cs_{0.3}WO_3$ synthesized with 17.5:22.5 mmol OAc:OAm and 2.5 K/min heating rate. Refinement performed using hexagonal $P6_3/mcm$ and cubic $Fd\bar{3}m$ structures. Rwp: 4.57, gof: 1.69; values of hexagonal phase: a=7.375(2), b=7.257(22), c=7.708(3), CS=15.9(4) nm, Occ(Cs)=0.27(0); values of cubic phase: a=b=c=10.327(2), CS=17.1(5) nm, Occ(Cs)=0.39(1); ratio h/c: 62.1(4):37.9(4).

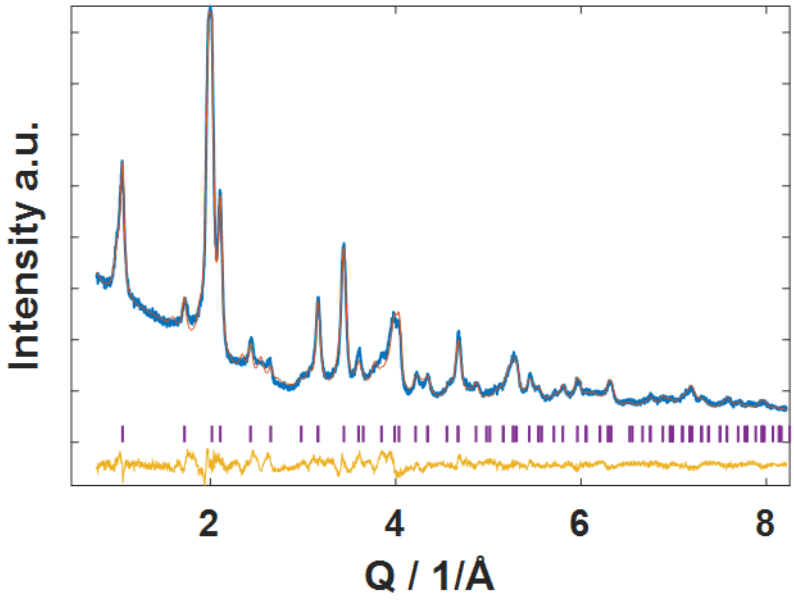

Figure S8.4.8. Rietveld refinement for m-$Cs_{0.3}WO_3$ synthesized with 15:25 mmol OAc:OAm and 2.5 K/min heating rate. Refinement performed using hexagonal $P6_3/mcm$ and cubic $Fd\bar{3}m$ structures. Rwp: 4.82, gof: 1.90; values of hexagonal phase: a=7.327(1), b=6.935(25), c=7.858(5), CS=12.6(3) nm, Occ(Cs)=0.27(0); values of cubic phase: a=b=c=10.328(1), CS=16.3(3) nm, Occ(Cs)=0.35(0); ratio h/c: 42.8(4):57.2(4).

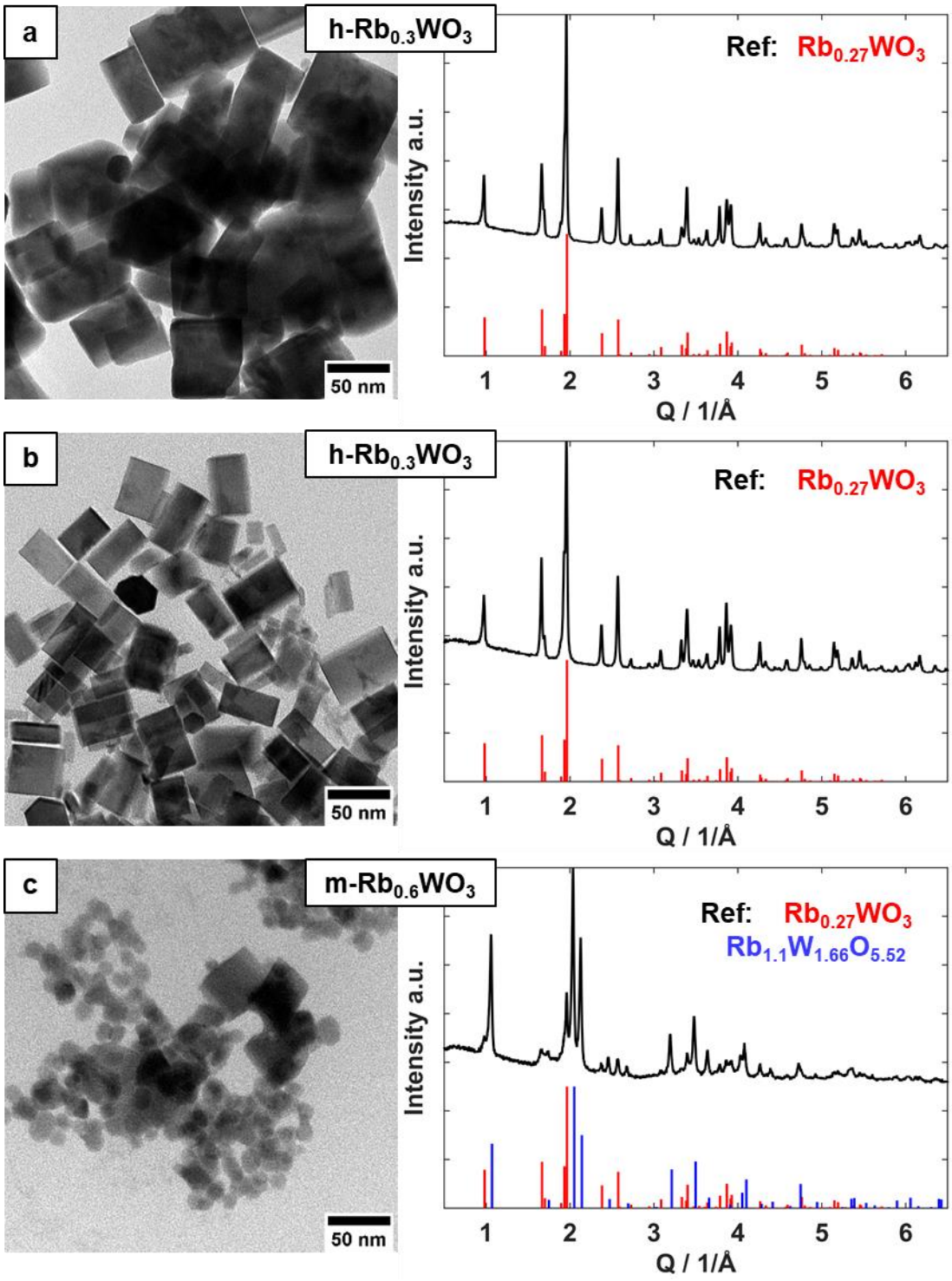

Figure S8.4.9. a) TEM image and PXRD pattern of hexagonal $Rb_{0.3}WO_3$ NCs synthesized with 20:20 mmol OAc:OAm and heating rate of 25 K/min, b) TEM image and PXRD pattern of hexagonal $Rb_{0.3}WO_3$ NCs synthesized with 17.5:22.5 mmol OAc:OAm and heating rate of 2.5 K/min and c) TEM image and PXRD pattern of mixed cubic/hexagonal $Rb_{0.6}WO_3$ NCs synthesized with 17.5:22.5 mmol OAc:OAm and heating rate of 2.5 K/min. PXRD references $Rb_{0.27}WO_3$ (space group $P6_3/mcm$, PDF no. 01-073-1549) and $Rb_{1.1}W_{1.66}O_{5.52}$ (space group $Fd\bar{3}m$, ICSD no. 99-502-7095).

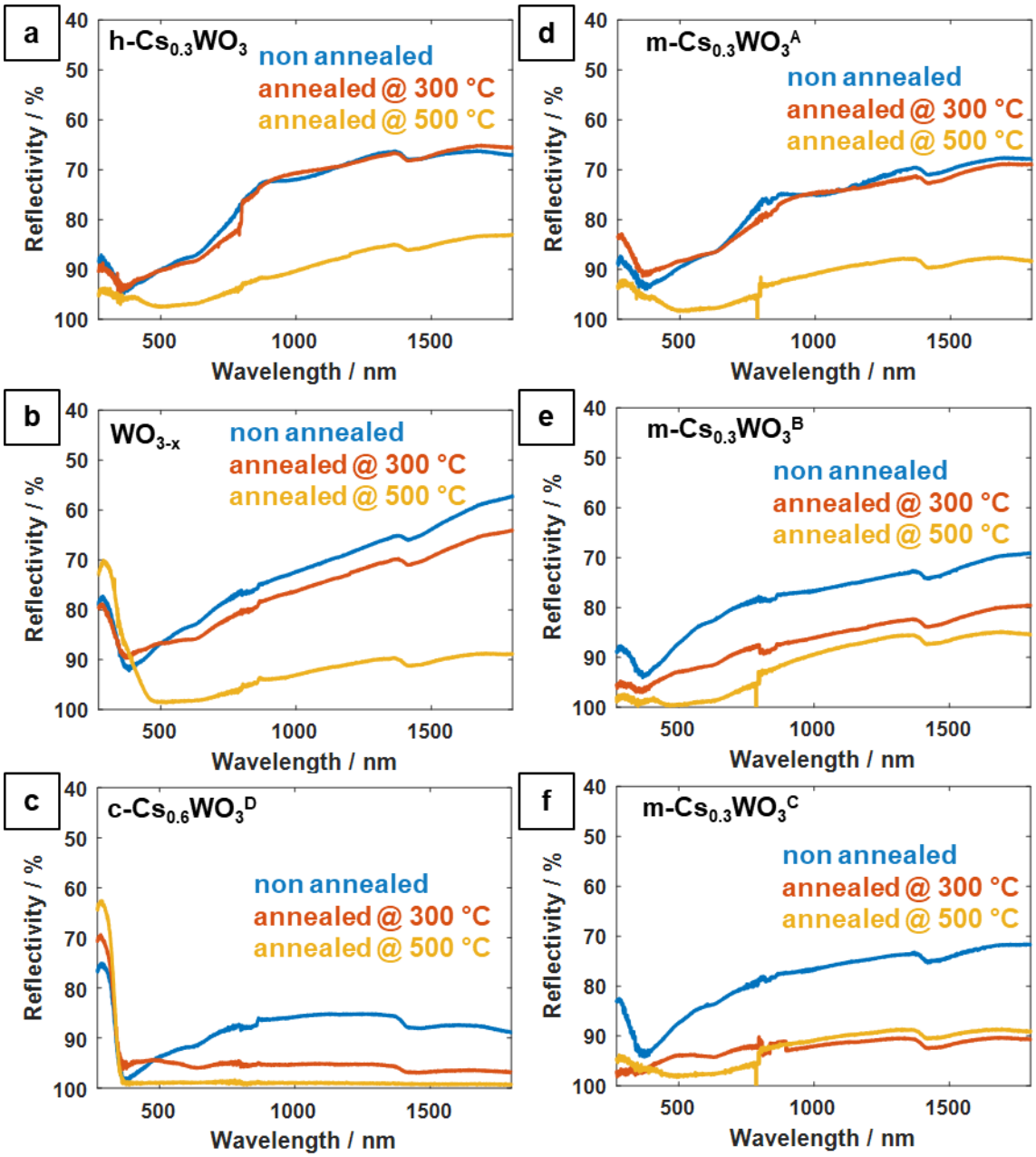

Figure S8.4.10. Diffuse reflectivity spectra of nanocrystals dried at 70 °C (blue), annealed at 300 °C (red) and annealed at 500 °C (yellow) for 5 h. a) h-$Cs_{0.3}WO_3$, b) WO_{3-x} NRs, c) c-$Cs_{0.6}WO_3$ synthesized with 17.5:22.5 mmol OAc:OAm, d) m-$Cs_{0.3}WO_3$ synthesized with 19:21 mmol OAc:OAm, e) m-$Cs_{0.3}WO_3$ synthesized with 17.5:22.5 mmol OAc:OAm and f) m-$Cs_{0.3}WO_3$ synthesized with 15:25 mmol OAc:OAm.

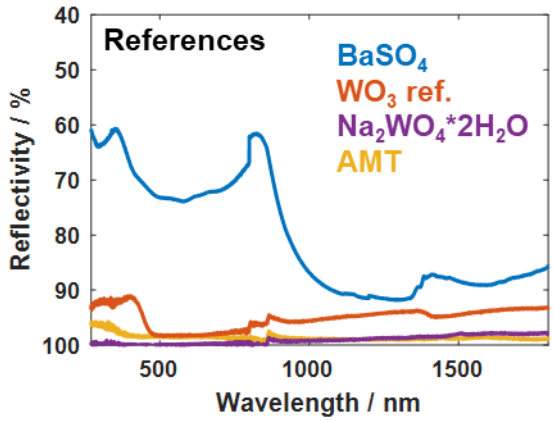

Figure S8.4.11. Diffuse reflectivity spectra of reference substances $BaSO_4$ (background), commercial WO_3, $Na_2WO_4*2H_2O$ and ammonium metatungstate (AMT)

Table S8.4.1. Additional HPO data measured for various samples.

Sample	Turnover rate / µM*min^{-1}	Turnover 24 h / µM	Lower limit / min	Upper limit / min
WO_{3-x}[a]	0.0448	41.87	500	750
WO_{3-x}[b]	0.0241	25.00	750	1400
h-ATB[a]	0.0088	8.80	800	1400
h-$Cs_{0.3}WO_3$[a]	0.0030	2.97	800	1400
h-$Cs_{0.3}WO_3$[b]	0.0050	4.33	1000	1400
m-$Cs_{0.3}WO_3$[a]	0.0098	11.49	600	1400
m-$Cs_{0.3}WO_3$[b]	0.0071	7.39	1000	1400
c-$Cs_{0.6}WO_3$[a]	0.0098	11.53	250	1000
c-$Cs_{0.6}WO_3$[b]	0.0978	34.90	50	130
h-$Rb_{0.3}WO_3$[a]	0.0093	10.54	750	1300
m-$Rb_{0.6}WO_3$[a]	0.0140	13.24	750	1400
WO_3	0.0078	7.60	1000	1400
AMT	0.0022	2.01	1000	1400
$Na_2WO_4*2H_2O$	0.0387	34.38	50	130

a. Annealed in air at 300 °C (5 h), b. annealed in air at 500 °C (5 h).

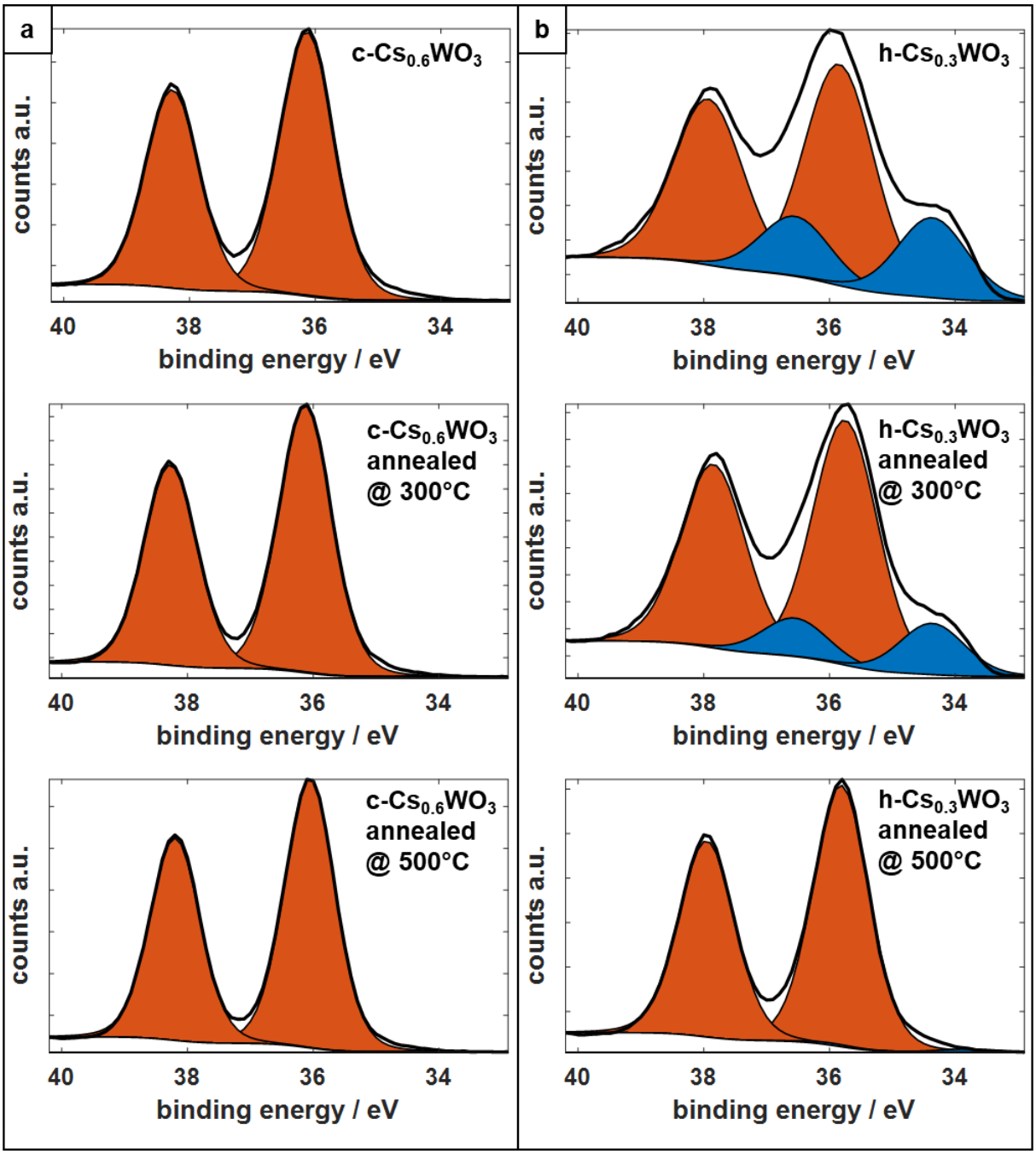

Figure S8.4.12. XPS spectra of 4f 5/2 and 3/2 core level of nanocrystals dried at 70 °C, annealed at 300 °C and annealed at 500 °C for 5 h of a) c-$Cs_{0.6}WO_3$ NCs and b) h-$Cs_{0.3}WO_3$ NCs.

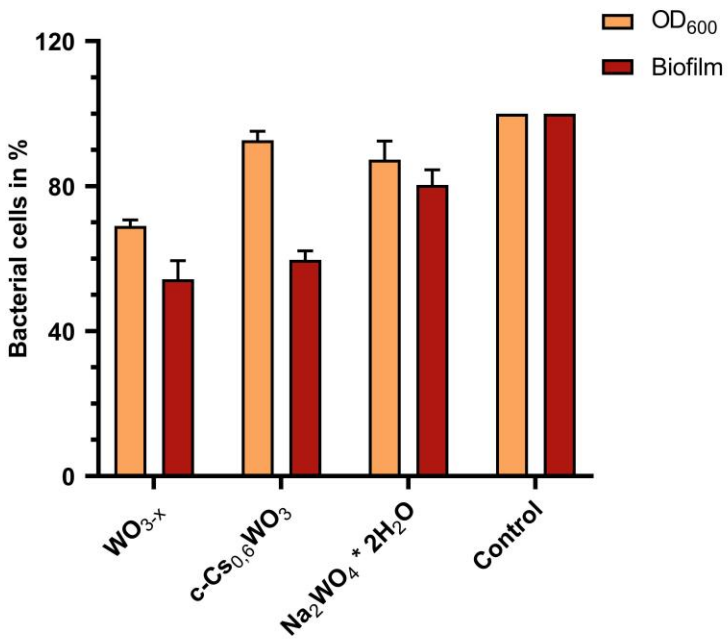

Figure S8.4.13. Comparison of *P. aeruginosa* bacterial cells treated with tungsten bronzes in planktonic and biofilm condition. The bacteria were cultivated in LB medium for 72 h at 30 °C in the presence of the referred tungsten bronzes. OD_{600} was then measured to observe the effect of the tungsten bronzes on the planktonic cells. After removing the planktonic cells, the attached cells i.e., biofilm were stained with crystal violet. After washing the unbound crystal violet, acetic acid was added for solubilization of the crystal violet. The absorbance at 575 nm was then measured to observe the effect of the tungsten bronzes on the biofilm.

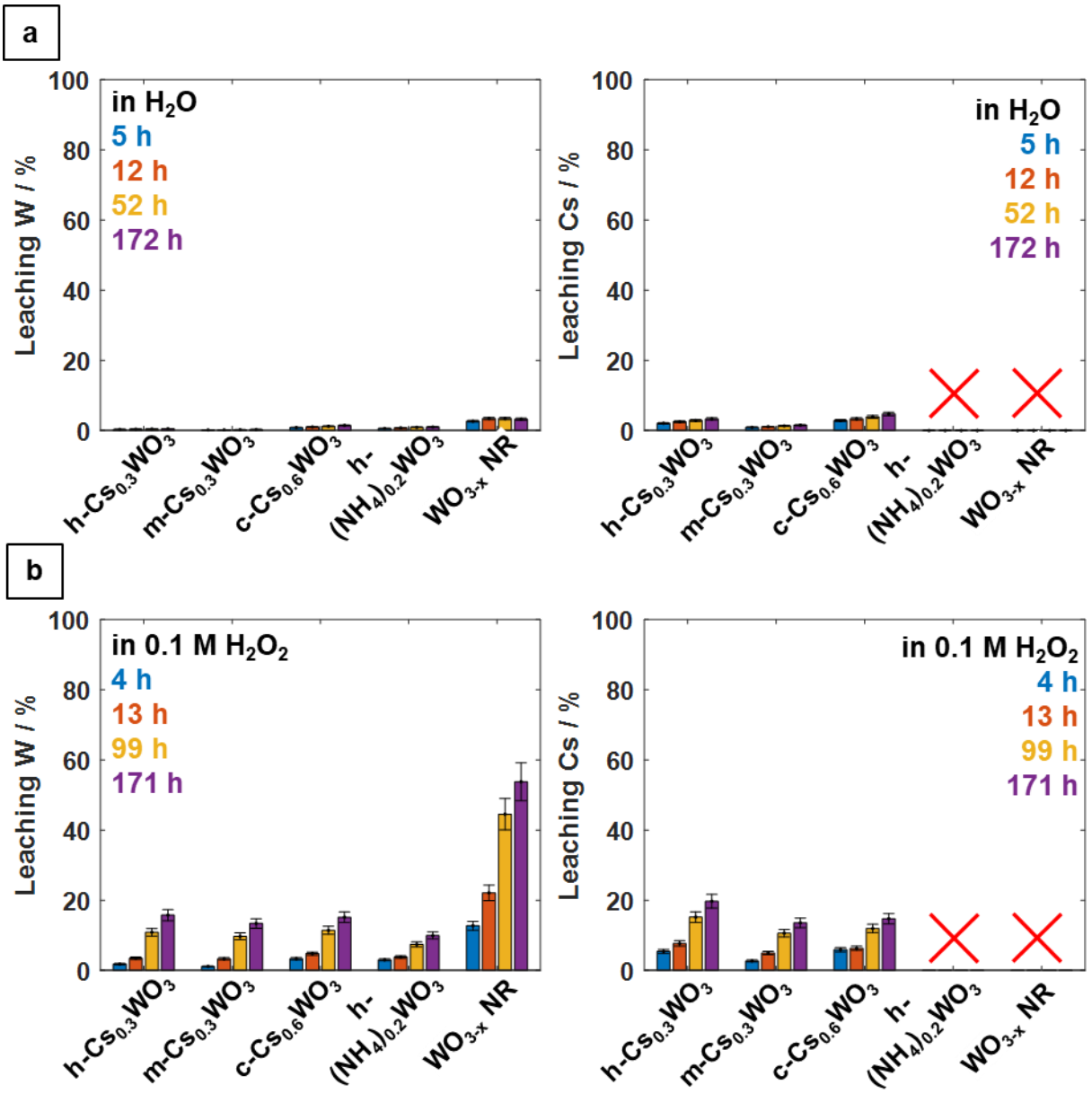

Figure S8.4.14. Leaching data of tungsten and cesium for h-$Cs_{0.3}WO_3$, m-$Cs_{0.3}WO_3$, c-$Cs_{0.6}WO_3$, h-ATB and WO_{3-x} a) in water and b) in 0.1 M H_2O_2.

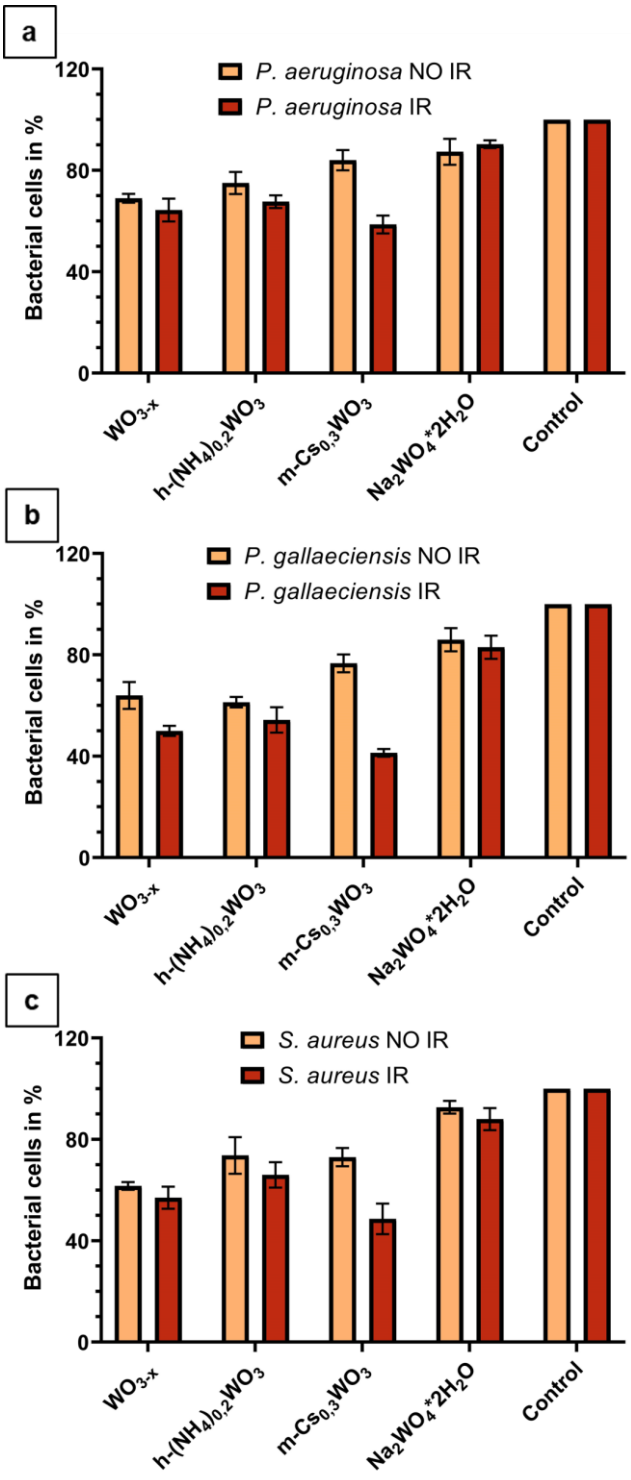

Figure S8.4.15. Comparison of the tungsten bronzes effect on *P. aeruginosa* a), *P. gallaeciensis* b) and *S. aureus* c) bacterial cells with IR irradiation and no irradiation at all. *S. aureus* and *P. aeruginosa* were grown at 30 °C in LB medium, *P. gallaeciensis* was grown at 30 °C in 2216 marine medium. The incubation of the bacteria was done for 72 h in 96-well plates in the absence or presence of tungsten bronzes and 950 nm IR irradiation. OD_{600} was then measured to observe the effect of the tungsten bronzes in combination with IR irradiation in comparison to no irradiation at all.

8.5 Supporting Information for Chapter 6

8.5.1 Author Contributions

Conception and design of the study:

[redacted]

Preparation of samples and acquisition of data:

[redacted] – preparation of nanocrystals

[redacted] – biologic evaluations

[redacted] – TEM measurements

[redacted] – PXRD measurements

[redacted] – CLSM measurements

Analysis and interpretation of data:

[redacted] – PXRD diffraction

[redacted] – TEM images

[redacted] – biological data

Drafting of the supporting information:

[redacted]

Revising the supporting information critically for important intellectual content:

[redacted]

Preparation of figures

[redacted]

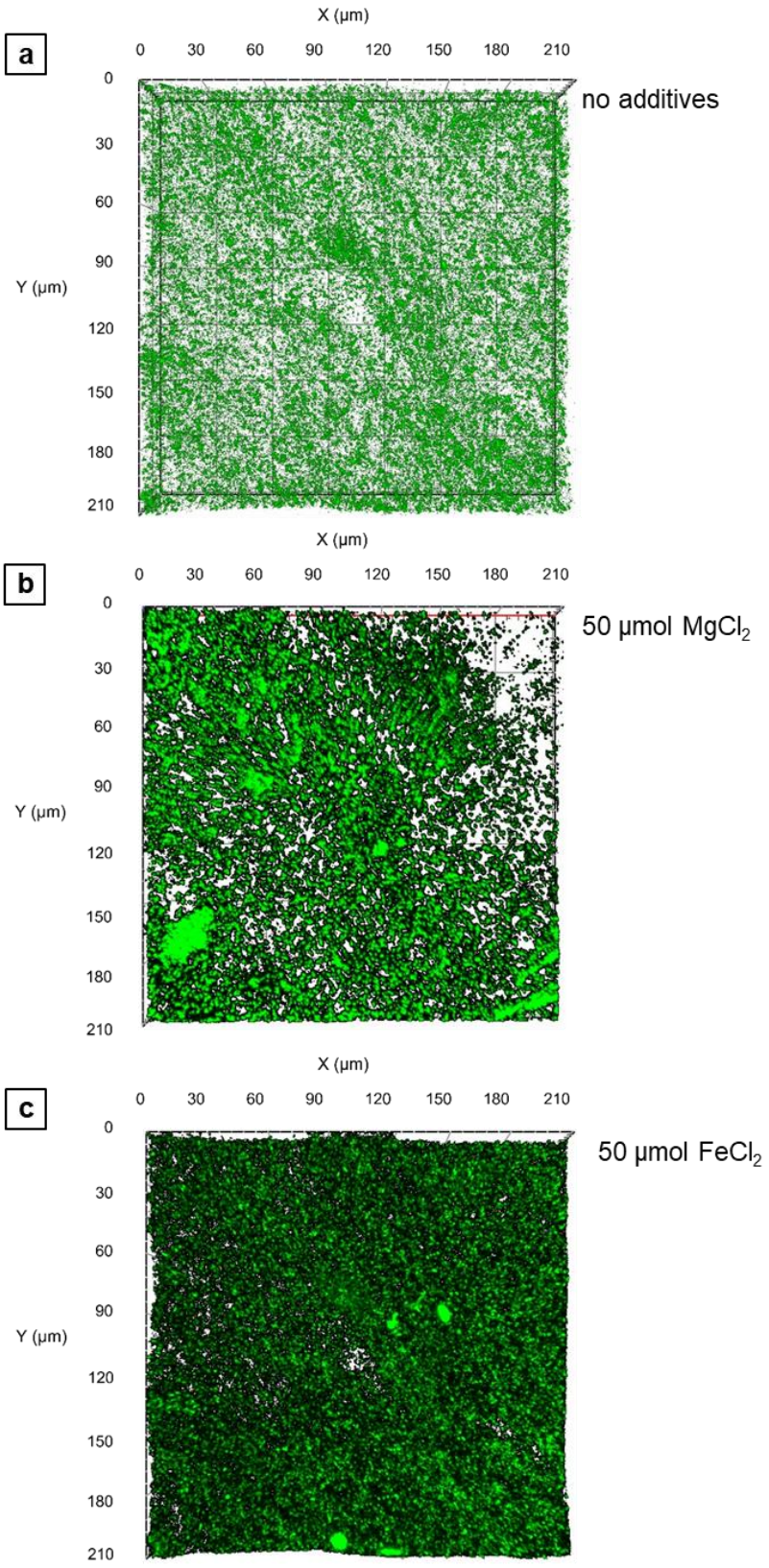

Figure S8.5.1. CLSM picture of *P. gallaeciensis* BF in a) control experiment without additives and 50 µM solution of b) $MnCl_2*4H_2O$ and c) $FeCl_2*4H_2O$.

Table S8.5.1. List of different tungstate nanocrystals with synthesis parameters as presented and discussed in this article.

Label Paper	**Metal precursor**	**Heating rate / K/min**	**Ratio oleic acid to oleylamine / mmol**	**Biologic properties found in**
$FeWO_4$	$Fe(oleat)_3$	2.5	20:20	Figure 6.3
$FeWO_4$[a]	$Fe(oleat)_3$	2.5	25:15	Figure S8.5.4
$FeWO_4$[a]	$Fe(oleat)_3$	2.5	15:25	Figure S8.5.4
$MnWO_4$[a]	$Mn(oleat)_2$	2.5	20:20	Figure 6.3
$MnWO_4$[a]	$Mn(oleat)_2$	2.5	21:19	Figure S8.5.6
$MnWO_4$[a]	$Mn(ac)_2*4H_2O$	2.5	21:19	Figure S8.5.6
$MnWO_4$[a]	$Mn(acac)_2$	2.5	21:19	Figure S8.5.6
$Mn_{0.5}Fe_{0.5}WO_4$[c]	$Fe(acac)_3$ + $Mn(ac)_2*4H_2O$	2.5	21:19	Figure 6.3
$CoWO_4$[a]	$CoCO_3$	5	20:20	Figure S8.5.8
$MgWO_4$[a]	$Mg(ac)_2$	2.5	20:20	Figure S8.5.8
$SrWO_4$[c]	$Sr(ac)_2$	5	20:20	Figure S8.5.8
$BaWO_4$[c]	$Ba(ac)_2$	5	20:20	Figure S8.5.8
$ZnWO_4$[a]	$Zn(acac)_2$	2.5	20:20	Figure S8.5.9
$ZnWO_4$[a]	$ZnCO_3*Zn(OH)_2$	5	20:20	Figure S8.5.9

a. 0.12 mmol AMT and 1.43 mmol metal precursor.

b. 0.12 mmol AMT and 0.72 mmol metal precursors each.

c. 0.24 mmol AMT and 2.86°mmol metal precursor

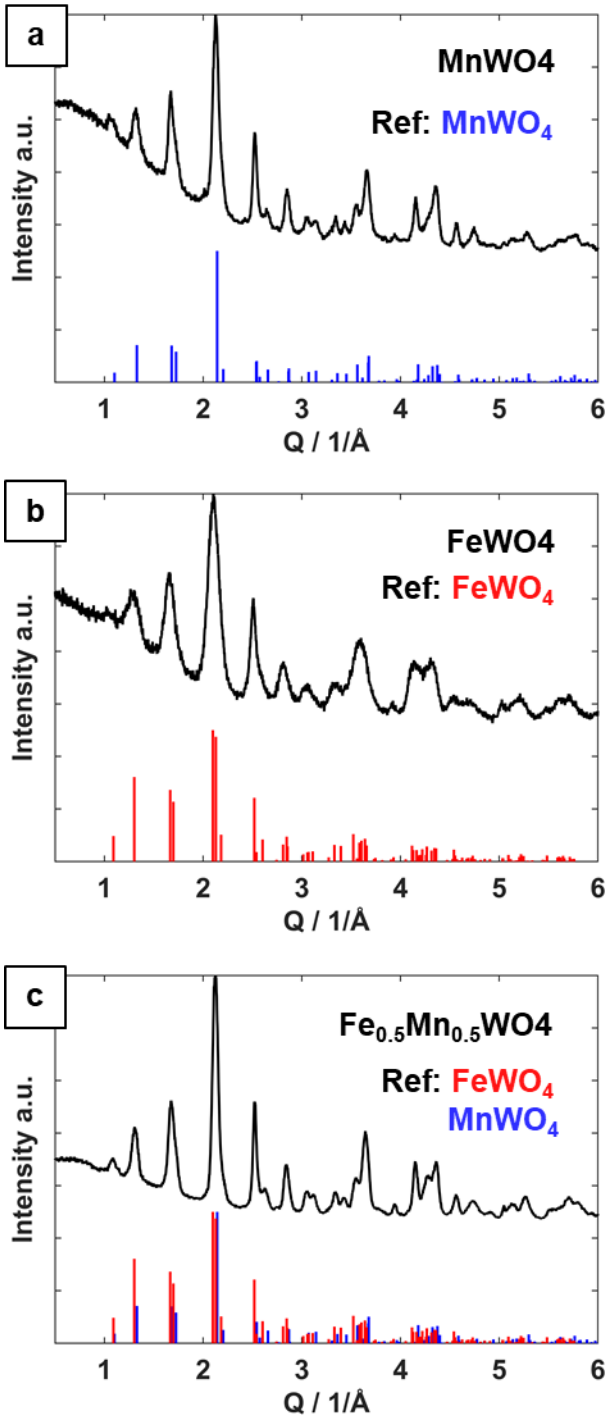

Figure S8.5.2. PXRD patterns of a) $MnWO_4$ NCs shown in Figure 6.3a, b) $FeWO_4$ NCs shown in Figure 6.3b and c) $Fe_{0.5}Mn_{0.5}WO_4$ NCs shown in Figure 6.3c. References: $MnWO_4$ (hüberite, space group $P2/c$ (13), PDF no. 01-080-0132) and $FeWO_4$ (Ferberite, space group $P2/c$ (13), COD no. 96-900-8125).

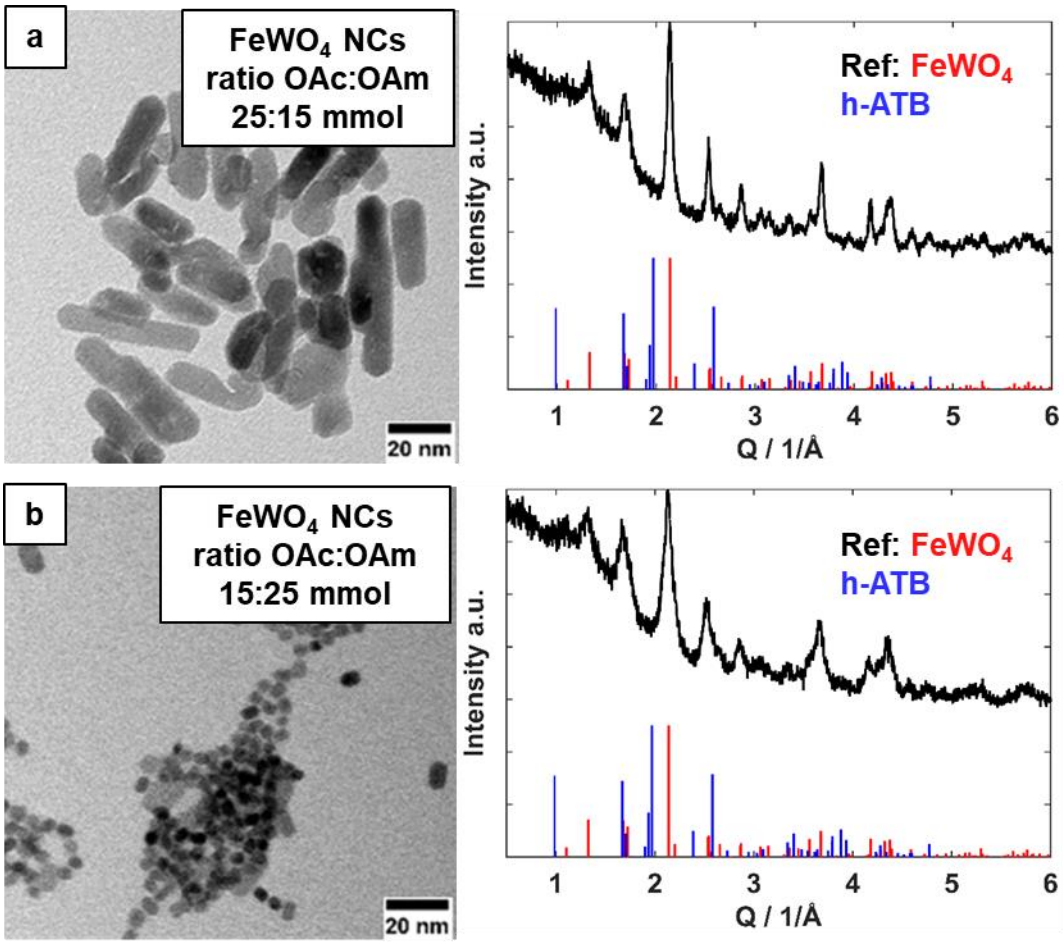

Figure S8.5.3. TEM images (left) and PXRD patterns (right) of $FeWO_4$ NCs synthesized with a) 25:15 mmol oleic acid : oleylamine and b) 15:25 mmol oleic acid : oleylamine. Reference: $FeWO_4$ (Ferberite, space group $P2/c$ (13), COD no. 96-900-8125).

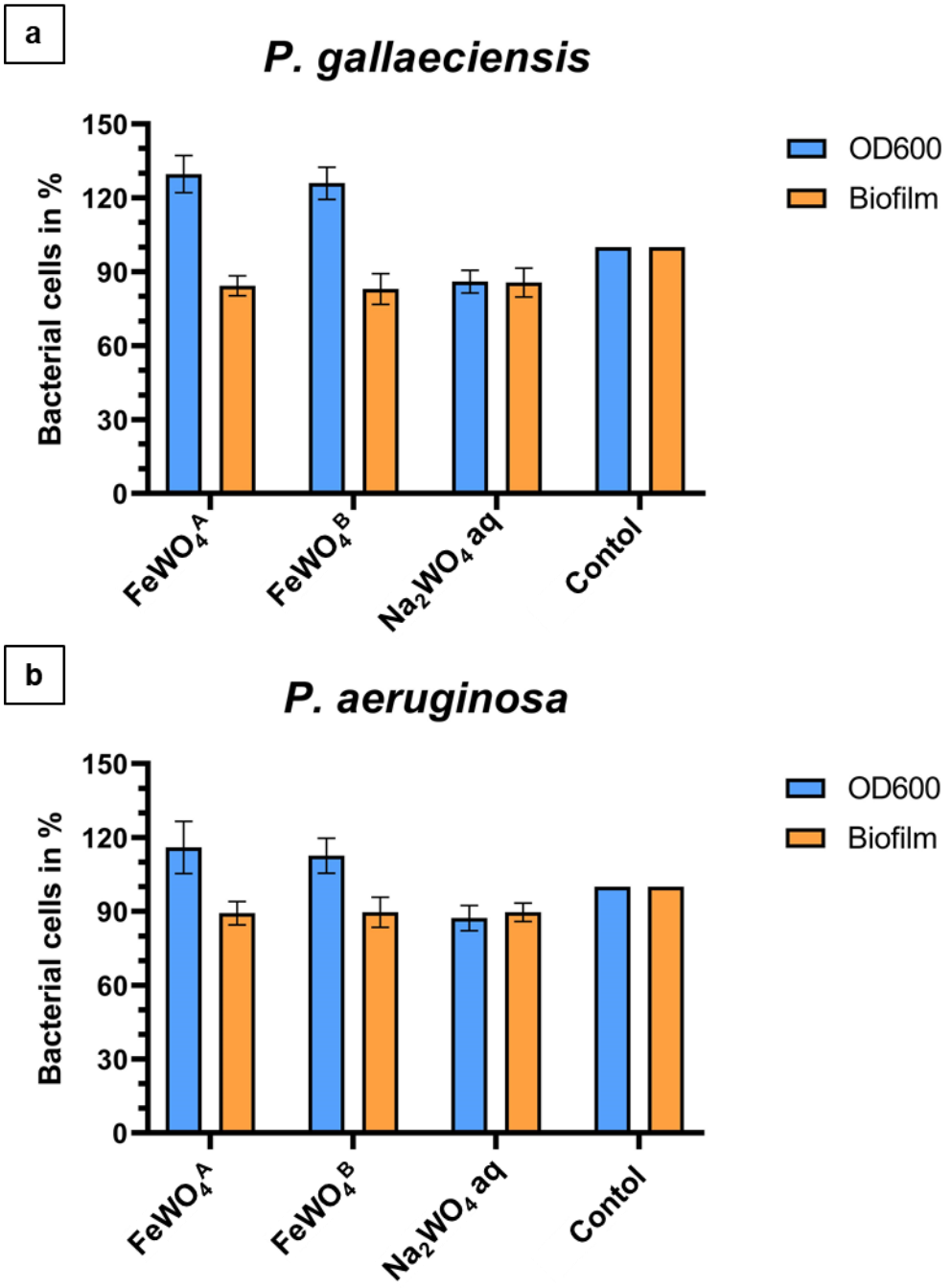

Figure S8.5.4. Biotests of additional $FeWO_4$ NCs shown in Figure S8.5.3 and $Na_2WO_4*2H_2O$ (0.1 mg/ml) towards Biofilm formation and planktonic cells of a) *P. gallaeciensis* and b) *P. aeruginosa*. Control without addition of NCs or salts.

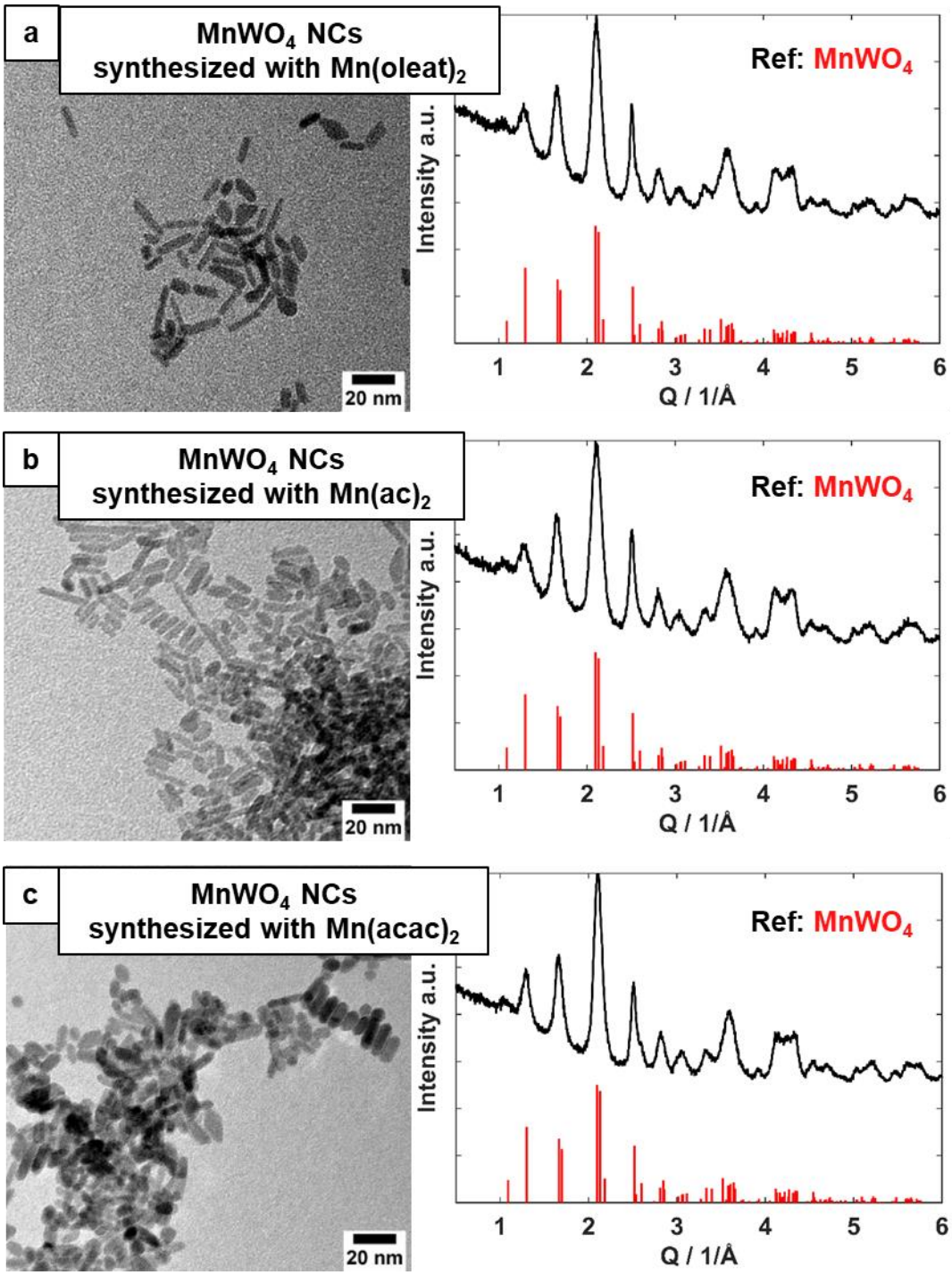

Figure S8.5.5. TEM images (left) and PXRD patterns (right) of $MnWO_4$ NCs synthesized using 21:19 mmol oleic acid:oleylamine with different precursors (1.43:1.43 mmol Mn:W), a) manganese oleate, b) manganese acetate and c) manganese acetylacetonate. Reference: $MnWO_4$ (hüberite, space group $P2/c$ (13), PDF no. 01-080-0132).

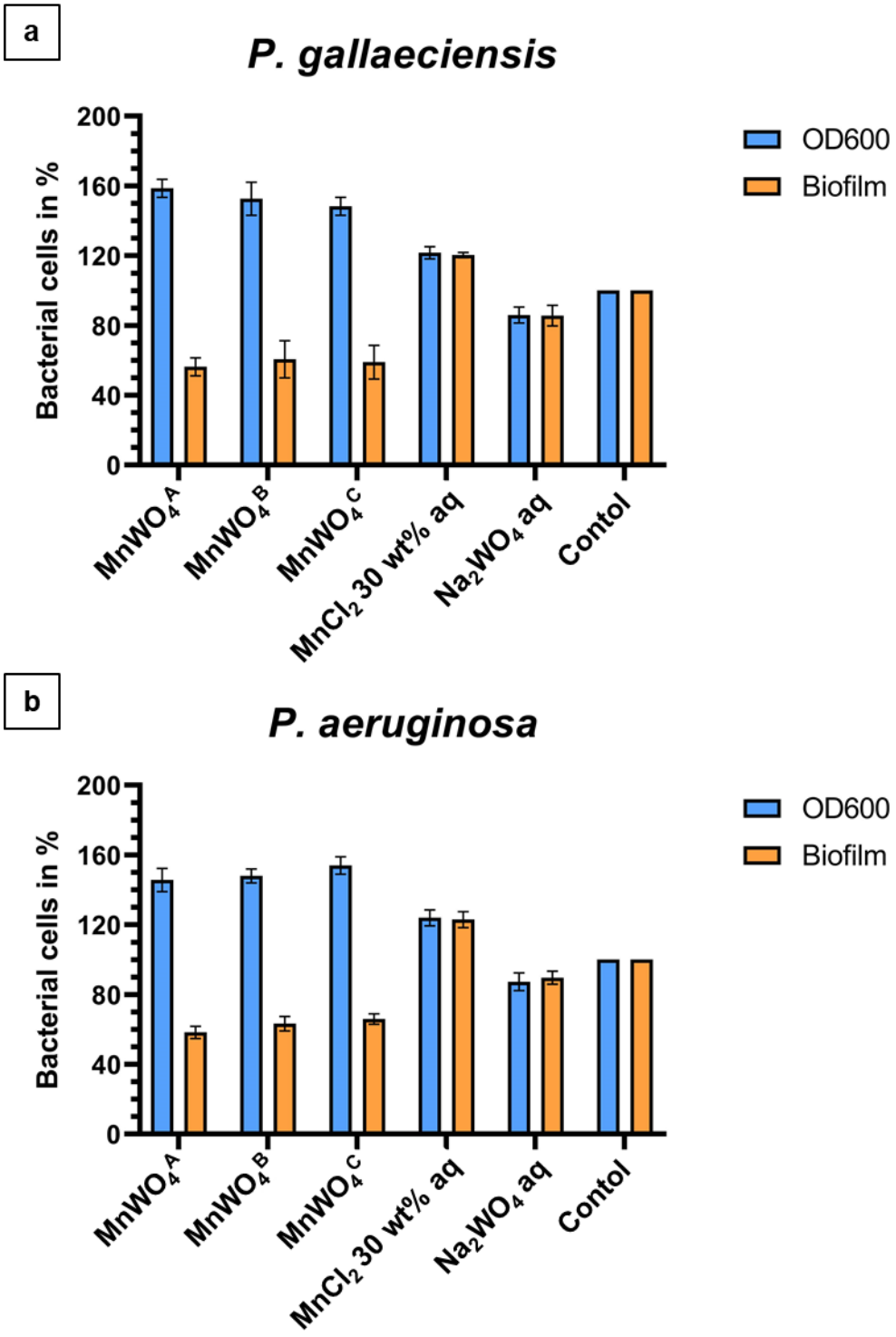

Figure S8.5.6. Biotests of $MnWO_4$ NCs shown in Figure S8.5.5 and $Na_2WO_4*2H_2O$ (0.1 mg/ml) and $MgCl_2*4H_2O$ (0.03 mg/ml) towards Biofilm formation and planktonic cells of a) *P. gallaeciensis* and b) *P. aeruginosa*. (0.1 mg/ml) as well as towards Biofilm formation and planktonic cells of a) *P. gallaeciensis* and b) *P. aeruginosa*. Control without addition of NCs or salts.

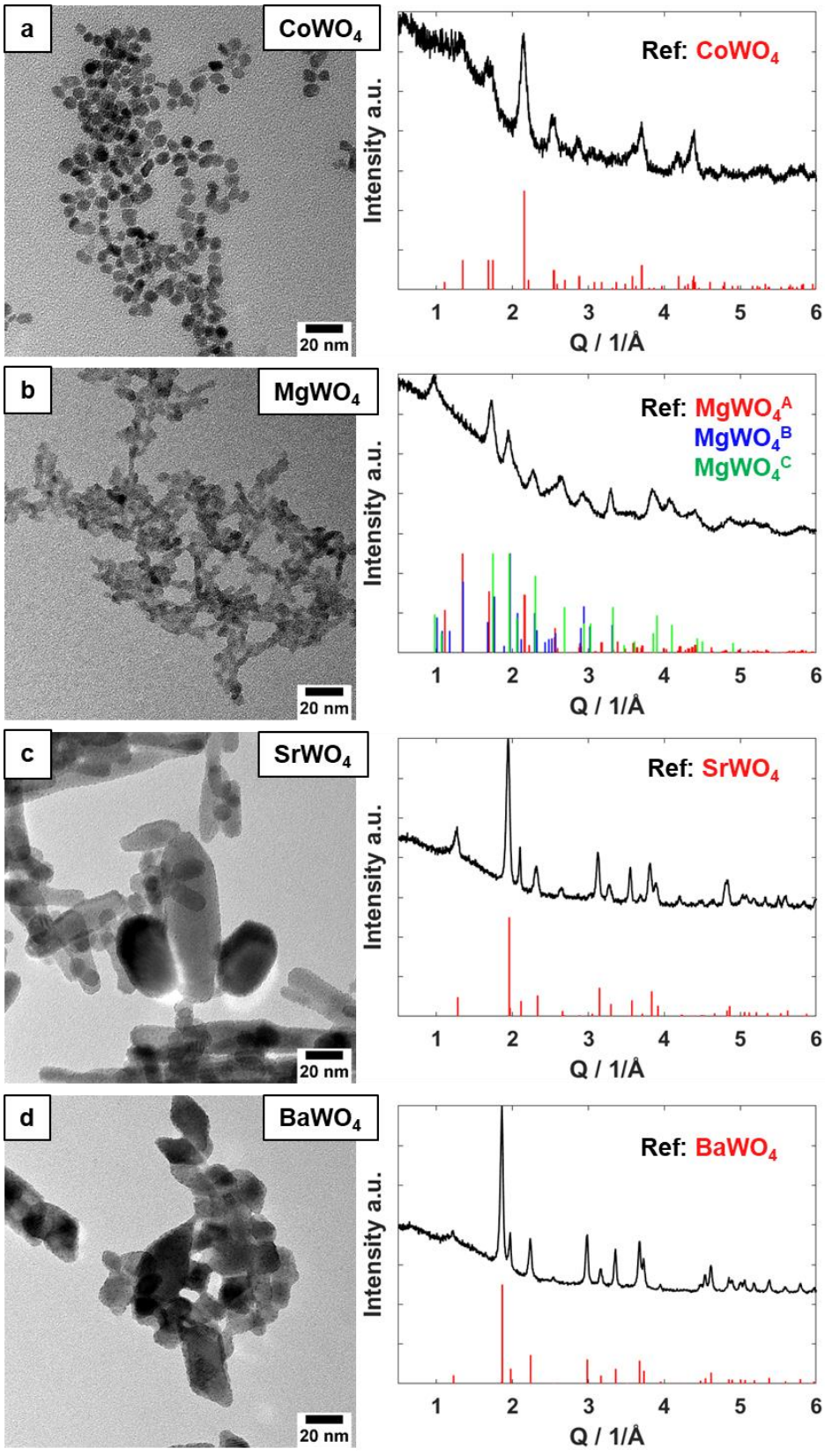

Figure S8.5.7. TEM images (left) and PXRD patterns (right) of a) $CoWO_4$ NCs, b) $MgWO_4$ NCs, c) $SrWO_4$ NCs and d) $BaWO_4$ NCs. References: $CoWO_4$ (space group $P2/c$ (13), PDF no. 00-015-0867), $MgWO_4{}^A$ (monoclinic, space group $P2/c$ (13), COD no. 99-501-2719), $MgWO_4{}^B$ (triclinic, PDF, Entry No.: 00-045-0412), $MgWO_4{}^C$ (tetragonal, PDF, Entry No.: 00-052-0390), $SrWO_4$ (space group $I4_1/a$ (88), COD no. 96-154-6037) and $BaWO_4$ (space group $I4_1/a$ (88), COD no. 96-152-7205). Synthesis parameters in Table S8.5.1.

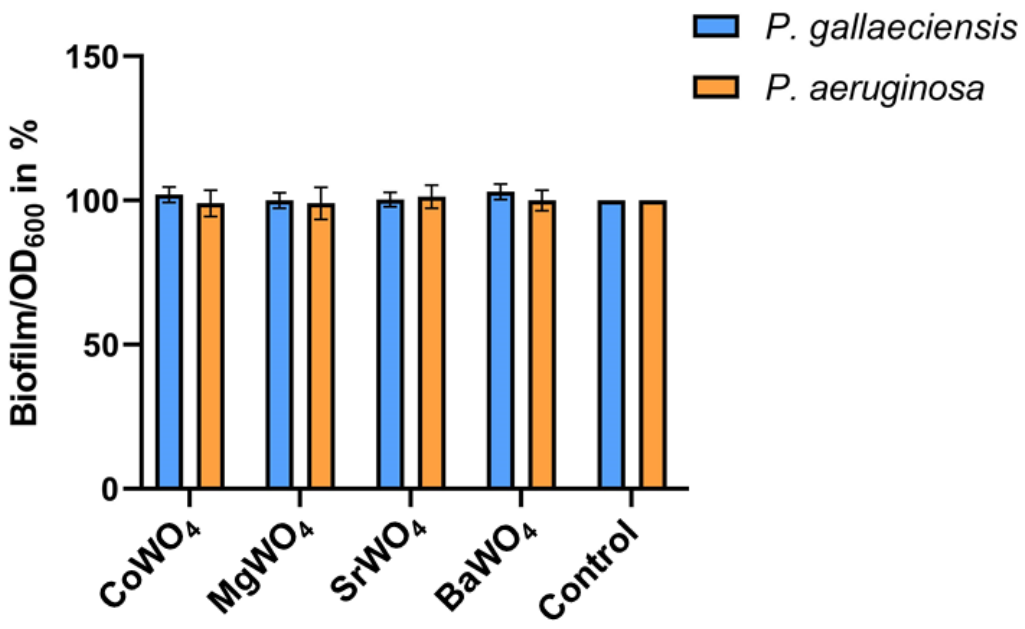

Figure S8.5.8. Influence of $CoWO_4$, $MgWO_4$, $BaWO_4$ and $SrWO_4$ (see Figure S8.5.7) (0.1 mg/ml each) towards biofilm formation of *P. gallaeciensis* and P. aeruginosa. In addition, a control experiment without NCs and $Na_2WO_4*2H_2O$ (0.1 mg/ml) as soluble reference material.

8.5.2 $ZnWO_4$ NCs show antibacterial and antifungal effects

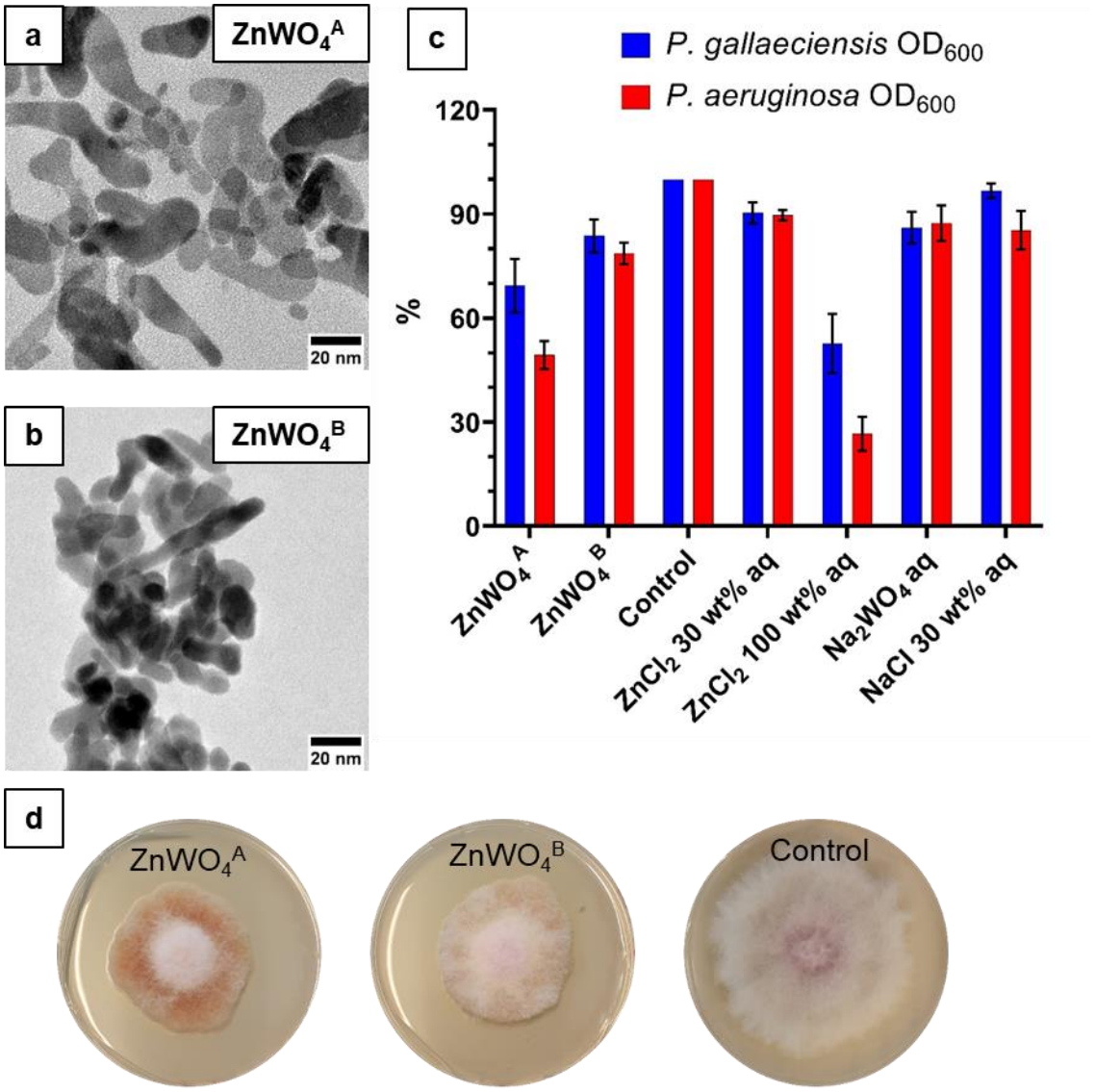

Figure S8.5.9. a) $ZnWO_4$ NCs synthesized with basic zinc carbonate ($ZnCO_3$*$Zn(OH)_2$, **A**) and b) zinc acetyl acetonate ($Zn(acac)_2$*$2H_2O$, **B**) as zinc precursor. c) Bacterial growth assay for *P. gallaeciensis* and *P. aeruginosa* with $ZnWO_4$ NCs (concentration 0.1 mg/ml), water soluble zinc chloride (30 wt%≈220 µM, 100 %≈750 µM), water soluble sodium tungstate and sodium chloride as reference compounds and a control (no additives). d) Growth test of *F. graminearum* in the presence of 0.1 mg/ml $ZnWO_4$ NCs.

Zinc cations have known inhibiting effect on bacterial growth,[1,2] and the antibacterial properties of zinc tungstate ($ZnWO_4$) on the growth of *P. gallaeciensis* and *P. aeruginosa* were also notable (Figure S8.5.9c). In contrast to iron and manganese tungstate, we observed no increased bacterial growth in any case compared to the control experiment. However, for $ZnWO_4$ synthesized with $ZnCO_3$*$Zn(OH)_2$ (Figure S8.5.9a), we observed a significant reduction of the bacterial growth of P. aeruginosa towards 49 %. The influence towards *P. gallaeciensis* was slightly less (69 %). $ZnWO_4$ NCs synthesized with zinc acetylacetonate (Figure S8.5.9b) showed less activity towards growth of both P.

aeruginosa (79 %) and P. gallaeciensis (84 %). The solubility of $ZnWO_4$ has been calculated as low (~10^{-9} at 298 °C, similar to $FeWO_4$ and $MnWO_4$)[3] we attribute the effect towards surface effects of the NCs. The Brønsted acidic properties of molybdenum and tungsten oxides have been discussed before[4,5] and may be the reason for their antibacterial properties. Additionally, cell penetration and membrane disruption may be responsible for cell death of bacteria.[6,7]

Additionally, we investigated the influence of $ZnWO_4$ NCs towards the growth of the fungus *F. graminearum*. Like *P. gallaeciensis* and *P. aeruginosa*, $ZnWO_4$ NCs synthesized with zinc carbonate showed a higher activity than those synthesized with zinc acetylacetonate. However, both nanocrystals reduce the fungal growth significantly with respect to the control experiment without additives. Additionally, the mycelium growth is reduced in both cases.

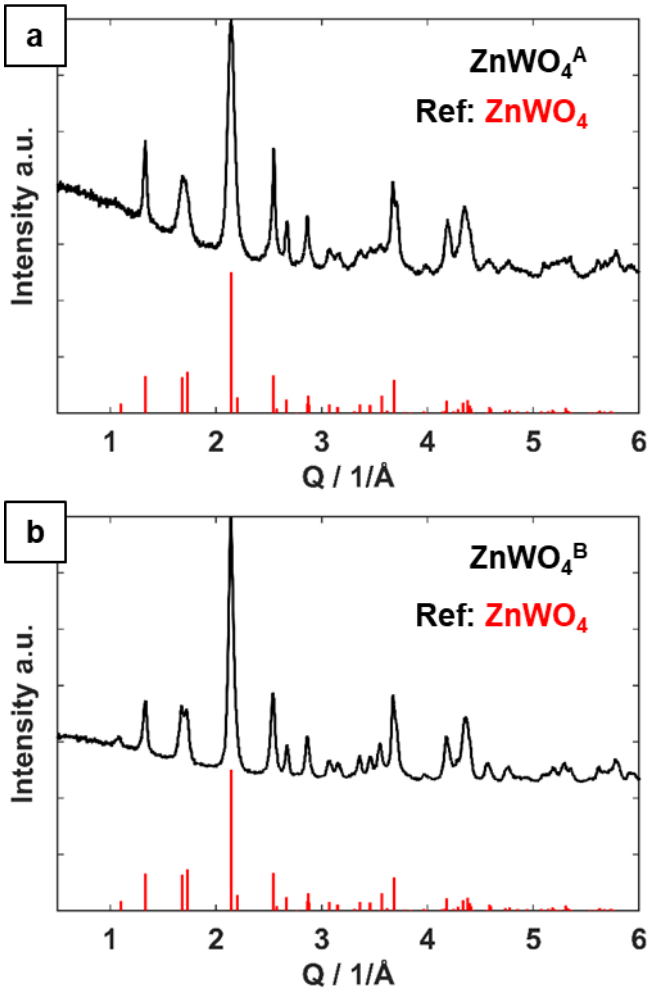

Figure S8.5.10. PXRD patterns of a) $ZnWO_4$ NCs shown in Figure S8.5.9a and b) $ZnWO_4$ NCs shown in Figure S8.5.9b. Reference: $ZnWO_4$ (sanmartinite, space group $P2/c$ (13), PDF no. 01-073-0554).

Fungal growth assays. To observe antifungal activity of the zinc tungstates, the NCs were added to the HMG medium at a final concentration of 0.1 mg/ml. After incubation of 6 h at RT, the agar was added, and the plates were poured. Then, an *F. graminearum* disc with a diameter of 1 cm was placed in the middle of the plate and was incubated for seven days at 26 °C. The plates were then photographed.

8.5.3 References

1 D. H. Nies, *Appl. Microbiol. Biotechnol.*, 1999, **51**, 730–750.

2 M. Mergeay, D. Nies, H. G. Schlegel, J. Gerits, P. Charles and F. van Gijsegem, *J. Bacteriol.*, 1985, **162**, 328–334.

3 J.-C. Buhl and A. Willgallis, *Chem. Geol.*, 1986, **56**, 271–279.

4 C. D. Baertsch, K. T. Komala, Y.-H. Chua and E. Iglesia, *J. Catal.*, 2002, **205**, 44–57.

5 F. Can, X. Courtois and D. Duprez, *Catalysts*, 2021, **11**, 703.

6 J. Jenkins, J. Mantell, C. Neal, A. Gholinia, P. Verkade, A. H. Nobbs and B. Su, *Nat. Commun.*, 2020, **11**, 1626.

7 G. Duan, L. Chen, Z. Jing, P. de Luna, L. Wen, L. Zhang, L. Zhao, J. Xu, Z. Li, Z. Yang and R. Zhou, *Chem. Res. Toxicol.*, 2019, **32**, 1357–1366.

8.6 List of Figures

Figure 1.1. *a) Nucleation curve according to LaMer[1], b) dependance of the r_{crit}. on surface and lattice energy c) Process of oriented attachment towards uniform nanocrystals according to the nonclassical nucleation theory. Inspired from [4] and [5].* 3

Figure 1.2. *Crystal structure of a) γ-WO_3 with monoclinic space group $P2_1/n$ and b) h-WO_3 with hexagonal space group $P6/mmm$, c) $W_{18}O_{49}$ ($WO_{2.72}$) Magnéli sub-oxide with monoclinic space group $P1$ and d) the iron tungstate $FeWO_4$ (Ferberite) with monoclinic space group $P2/c$. Structures visualized using VESTA 3.6.5.* 6

Figure 1.3. *Localized surface plasmon resonance and resulting absorption spectra of a) spherical and b) rod-like nanocrystals. Inspired by [46].* 8

Figure 2.1. *a) Overview scheme showing the reaction conditions leading to the formation of WO_{3-x} nanorods and h-ATB. b) Crystal structure of $W_{18}O_{49}$ (P2/m) (COD-ID: 1001678) and c) $(NH_4)_{0.2}WO_3$ ($P6_3$) according to the refinement of* ***ATB-13c*** *(Figure S8.1.2). d) Surface coordination of OAm and OAd for O^--terminated WO_{3-x} nanorods indicating steric effects of the ligands and resonance structure of OAd.* 18

Figure 2.2. *a) TEM image of WO_{3-x} nanorods obtained from the standard synthesis* ***NR-1*** *(T =350 °C, t = 30 min, heating rate = 5 °/min, HOAc/OAm = 20:20 mmol, AMT = 0.12 mmol), b) with HOAc/OAm ratio of 30:10 mmol (****NR-4****), c) with HOAc/OAm ratio of 10:30 mmol (****NR-8****), d) of a mixture of h-ATB and WO_{3-x} nanorods obtained from a synthesis with 0.24 mmol AMT (****ATB-1****) e) PXRD-diffractogram of* ***NR-1*** *(similar to* ***NR-4*** *and* ***NR-8****) with $WO_{2.72}$ Reference (COD, Entry No.: 96-152-8167). and f) PXRD-diffractogram of* ***ATB-1*** *with additional $(NH_4)_{0.25}WO_3$ Reference (ICDD, PDF Entry No.: 01-073-1084).* 19

Figure 2.3. *TEM and HR-TEM images of a, b) $WO_{2.72}$ NRs and c, d) h-ATB particles. Images taken from sample* ***NR-14****, containing both, NRs and h-ATB particles.* 20

Figure 2.4. *PXRD patterns of particles synthesized according to standard synthesis with 3-fold AMT (0.36 mmol) concentration before (****ATB-2****) and after (****ATB-2c****) purification (five times) with chloroform.* 21

Figure 2.5. *TEM images of WO_{3-x} / h-ATB particles from varied ATB-1 synthesis (fixed: 20:20 mmol HOAc/OAm, 0.24 mmol AMT, 350 °C for 30 min) with a) 10 °C/min (****ATB-7****), b) 2.5 °C/min heating rate (****ATB-8****), c) ~0 rpm and 10 °C/min (****ATB-9****), d) ~1000 rpm stirring speed and 10 °C/min (****ATB-11****) and e) corresponding PXRD-patterns for* ***ATB-7****,* ***ATB-8****,* ***ATB-9****, and* ***ATB-11****.* 22

Figure 2.6. *^{1}H-NMR spectra of final reaction solution (30 min at 350 °C, 1:1 HOAc/OAm) for* ***NR-1****,* ***ATB-12****,* ***Amide-2****,* ***Amide-4*** *and* ***Amide-5*** *particles. Areas shown for α-H shifts of HOAc, OAm and OAd as well as oleylammonium oleate salt*. HOAc and OAm form OAd quantitatively before cleavage at the final heating step (Figure S8.1.10).* 24

Figure 2.7. *a) Proposed reaction mechanism based on the oriented attachment of polyoxotungstates under the influence of polyoxotungstate concentration and surfactant concentration, b) particle from* ***ATB-2*** *reaction solution showing evidence for oriented attachment.* 27

Figure 2.8. *a) Solid state ^{1}H-NMR spectra of* ***ATB-13c*** *after annealing for 5 h at 70, 200, 300, 400, 500 °C in air. b) Solid state ^{1}H-NMR spectra of* ***ATB-13c*** *after annealing for 5 h at 70, 200, 300, 400, 500 °C under Ar. c) PXRD patterns of* ***ATB-13c*** *particles heated in air and d) PXRD pattern of* ***ATB-13c*** *particles heated under Ar. Marks indicate reflections changing after temperature treatment. Reference patterns of c) and d) are found in Figure S8.1.16 → Figure S8.1.24.* 30

Figure 2.9. *a) UV-Vis-NIR spectra of NR-1, NR-4, NR-8 and ATB-13 measured in TCE and b) energy-dependent.* 32

Figure 3.1. *a) Oxidation of thioanisole to MP-sulfoxide and MP-sulfon with H_2O_2 catalyzed by WO_{3-x} NRs, b) 3D-plot of an in situ kinetic catalysis under standard conditions (30 min, 0.04 mmol of thioanisole, 0.06 mmol of H_2O_2 (60%), 0.85 mg of WO_{3-x} NRs in 0.6 mL of methanol-d_4) and c) change of integrals for the reactant thioanisole (blue) and products MO-sulfoxide (green) and MP-sulfone (red) and conversion rate for thioanisol (dotted line) of the spectra in b).* 47

Figure 3.2. *a) TEM and HR-TEM image and b) powder X-ray diffractogram of WO_{3-x} NRs annealed at 300 °C with $W_{18}O_{49}$ reference (COD, entry no: 96-152-8167), a Pawley refinement is given in Figure S8.2.1. c) Structure of $W_{18}O_{49}$ projected along [010] and [101]. While the crystal structure of stoichiometric WO_3 contains an infinite 3D network of corner-sharing WO_6 octahedra, dense planar defects are regularly introduced in the parent WO_3 structure with a spacing dictated by the oxide deficiency. This leads to a shear-structure with corner- and edge-sharing octahedra forming pseudo-hexagonal channels in the $W_{18}O_{49}$ structure.* 49

Figure 3.3. *a) Effect of H_2O and D_2O on the oxidation of thioanisole with WO_{3-x} NRs (composition and exponential fit data provided in Table S8.2.1 and Table S8.2.2). b) Effect of annealing temperature of WO_{3-x} NRs on the conversion of thioanisole Powder X-ray diffractogram of annealed samples at different temperatures and the compositions of the reaction mixtures are given in Figure S8.2.2 and in Table* ***S8.2.3****. All experiments performed under standard conditions (0.04 mmol of thioanisole, 0.06 mmol of H_2O_2 (60%), 0.85 mg of WO_{3-x} NRs in methanol-d_4).* 51

Figure 3.4. *Sulfide oxidation capability of recycled WO_{3-x} NRs after a) 10 and b) 30 min.* 52

Figure 4.1. *Digital photographs of OAc used for particle syntheses. a) OAc from a steel canister, b) OAc from a glass bottle and c) OAc from a glass bottle mixed with ~1 wt% of iron oleate.* 68

Figure 4.2. *TEM images (left) and PXRD patterns (right) of a) WO_{3-x} NRs synthesized with oleic acid from the steel canister, b) addition of 20 mol% iron oleate to the standard synthesis and c) addition of 20 mol% iron oleate to the standard synthesis and a HR of 2.5 K/min. References: $WO_{2.72}$ (space group $P2/m$ (10), COD, Entry No.: 96-152-8167). $FeWO_4$ (Ferberite, space group $P2/c$ (13), COD no. 96-900-8125).* 69

Figure 4.3. *TEM images (left) and PXRD patterns (right) of $FeWO_4$ NCs synthesized with HR of 2.5 K/min and a) $Fe(acac)_3$ and 20:20 mmol OAc:OAm, blue markings indicate unknown structure, b) $Fe(acac)_3$ and 20 mmol OAd and c) $Fe(oleate)_3$ and 20 mmol OAd. Reference: $FeWO_4$ (Ferberite, space group $P2/c$ (13), COD no. 96-900-8125), not fitting the PXRD patterns in (b) and (c).* 71

Figure 4.4. *TEM images (left) and PXRD patterns (right) of $MgWO_4$ NCs synthesized with $Mg(acac)_2*2H_2O$ and HR of 2.5 K/min. a) as synthesized, b) annealed at 500 °C for 5 h and c) annealed at 800 °C for 5 h. References: $MgWO_4$ (triclinic, PDF, Entry No.: 00-045-0412), $MgWO_4$ (tetragonal, PDF, Entry No.: 00-052-0390), $MgWO_4$ (monoclinic, space group $P2/c$ (13), COD no. 99-501-2719) and WO_3 (monoclinic, space group $P2/n$ (14), COD no. 99-500-3824).* *74*

Figure 4.5. *Pawley refinements based triclinic (anorthic) space group $P1$ of a) $MgWO_4$ NCs annealed at 500 °C with fit parameters a=5.621(10) Å, b= 6.575(7) Å, c=8.829(11) Å, α=123.0(0) °, β=112.8(1) °, γ=101.7(1) °, rwp=2.41, goodness of fit=0.99, crystallite size=9.6(2) nm and b) unknown $FeWO_4$ synthesized using $Fe(oleate)_3$ with fit parameters a=5.713(3) Å, b=6.661(2) Å, c=8.960(3) Å, α=123.0(0) °, β=113.1(0) °, γ=101.4(0) °, rwp=3.41, goodness of fit =1.43, crystallite size =28.1(7) nm.* *75*

Figure 5.1. *a) TEM image and PXRD pattern of hexagonal $Cs_{0.3}WO_3$ NCs synthesized with 20:20 mmol OAc:OAm and heating rate of 5 K/min, b) TEM image and PXRD pattern of mixed cubic/hexagonal $Cs_{0.3}WO_3$ NCs synthesized with 17.5:22.5 mmol OAc:OAm and heating rate of 2.5 K/min and c) TEM image and PXRD pattern of cubic $Cs_{0.6}WO_3$ NCs synthesized with 17.5:22.5 mmol OAc:OAm and heating rate of 5 K/min. PXRD references: $Cs_{0.32}WO_3$ (space group $P63/mcm$, ICSD no. 99-501-4972) and $CsW_{1.6}O_3$ (space group $Fd3m$, ICSD no. 99-502-4816).* *87*

Figure 5.2. *Crystal structures of a) hexagonal cesium tungsten bronzes ($P63/mcm$) and b) cubic pyrochlore-type tungsten bronze ($Fd3m$) in polyhedral representations.* *88*

Figure 5.3. *Diffuse reflectance spectra of WO_{3-x} NRs, h-ATB, m-$Cs_{0.3}WO_3$, m-$Cs_{0.3}WO_3$ and c-$Cs_{0.6}WO_3$ a) dried at 70 °C and b) annealed at 300 °C for 5 h in air. *Discontinuities are caused by the background of the $BaSO_4$ white standard after the grating change.* *90*

Figure 5.4. *Evolution of TBPB concentration over the course of 24 h for WO_{3-x} NRs, h-$Cs_{0.3}WO_3$, m-$Cs_{0.3}WO_3$, c-$Cs_{0.6}WO_3$ and h-ATB NCs, as well as for soluble $Na_2WO_4*2H_2O$ reference.* *91*

Figure 5.5. *Effect of tungsten oxide bronze NCs on bacterial biofilm formation and quorum sensing. a) Crystal violet staining of P. aeruginosa grown in LB. The bacteria were cultivated for 72 h at 30 °C in the presence of the tungsten bronzes. After removing the planktonic cells, the attached cells i.e., biofilm were stained. b) X-Gal quantification with the biosensor A. tumefaciens A136. The AHL were incubated for 12 h at RT in presence and absence of the tungsten bronzes. The processed AHL were then added to the bacteria, which were cultivated for 8 h at 30 °C in LB medium, which was supplemented with X-Gal.* *94*

Figure 5.6. *Tungsten bronzes inhibit growth of Fusarium graminearum. a). The various NCs were added to the liquid HMG medium together with diluted H_2O_2 solution and incubated for 6 h at RT. The agar was then added and F. graminearum was placed in the middle of the plate. The results were then pictured after seven days of incubation. b) Effect of tungsten bronzes on the diameter of F. graminearum. The measurements were done with ImageJ.* *95*

Figure 5.7. *Effect of IR light (λ=950 nm) on the growth of S. aureus, P. aeruginosa and P. gallaeciensis. S. aureus and P. aeruginosa were grown at 30 °C in LB medium, P. gallaeciensis was grown at 30 °C in 2216 marine medium. The incubation of the bacteria was done for 72 h in 96-well plates in the absence or presence of tungsten bronzes and 950 nm IR irradiation. OD_{600} was then measured to observe the effect of the tungsten bronzes in combination with IR irradiation in comparison to no irradiation at all.* *96*

Figure 6.1. *a) Comparison of P. gallaeciensis BF formation on steel, laboratory glass and different polymer surfaces (polyethylene, PE; polyethylenterephthalat glycol, PETG; polystyrene, PS and polycarbonate, PC), referenced towards the glass surface. (b-e) Confocal laser scanning microscopy images of steel S235 b), glass c), PE d) and PC c) surfaces. The bacteria were cultivated for 72 h at 30 °C in the presence of steel, plastics and glass. The different materials were then rinsed with water to remove the planktonic cells. The remaining attached cells were then stained with crystal violet. For CLSM analysis the attached bacteria were stained with a combined SYTO9/propidium iodide solution. Inset showing the S235 steel surface after cultivation.* *112*

Figure 6.2. *Concentration dependent effect of metal cations on bacterial BF formation in P. gallaeciensis using solutions of chloride salts of Mn^{2+}, Fe^{2+}, Zn^{2+}, Cu^{2+}, Co^{2+} and Mg^{2+}. Concentrations used were 0, 50, 100, 500 and 1000 µM. For Fe^{2+} oxidation towards Fe^{3+} can be assumed.* *113*

Figure 6.3. *TEM images of a) $MnWO_4$, b) $FeWO_4$ and c) $(Fe_{0.5}Mn_{0.5})WO_3$ nanocrystals. BF formation and bacterial growth for d) P. gallaeciensis and e) P. aeruginosa as a function of nanocrystal composition ($MnWO_4$, $FeWO_4$ and $(Fe_{0.5}Mn_{0.5})WO_3$, 0.1 mg/ml each) and $MnCl_2$ (30 wt%, 150 µM) $Na_2WO_4*2H_2O$ (0.1 mg/ml, 303 µM) as water soluble reference compounds.* *116*

Figure S8.1.1. *Length (left), width (mid) and AR (right) histograms for a) **NR-1**, b) **NR-4**, c) **NR-8**, d) **ATB-13** and e) **ODE-3** particles. Corresponding average values are given in Table 2.2.* *134*

Figure S8.1.2. *a) Pawley Refinement of **NR-1** (WO_{3-x} nanorods) using space group P2/m, angles α=β=90 °, γ=115.21 ° and an anisotropic shape description for the crystallite size and b) Rietveld refinement of **ATB-13c** (h-ATB) based on $K_{0.26}WO_3$ with space group $P6_3$ and angles α=β=90 °, γ=120 °, preferred orientation along [020]. NH_4^+ content was fixed at 0.2 per tungsten. Potential impurities due to WO_{3-x} cannot be ruled out. Lattice parameters are compiled in Table S3.* *135*

Figure S8.1.3. *TEM images of the reaction solution for **ATB-1** at different temperature steps as well as at different points of time of the final temperature of 350 °C. HR-TEM image of rods found at 250 °C with size of selected particles.* *138*

Figure S8.1.4. *TEM images of WO_{3-x} nanorods based on the standard synthesis (**NR-1**) with different HOAc:OAm ratios a) 22.5:17.5 mmol (**NR-2**), b) 25:15 mmol (**NR-3**), c) 40:0 mmol (**NR-5**), d) 17.5:22.5 mmol (**NR-6**), e) 15:25 mmol (**NR-7**) and f) 0:40 mmol (**NR-9**) as well as 20:20 mmol HOAc:OAm with heating rate of g) 2.5 K/min (**NR-10**), h) 10 K/min (**NR-11**), i) 15 min at 350 °C (**NR-12**) and j) 60 min at 350 °C (**NR-13**).* *139*

Figure S8.1.5. *TEM images of particles with according to* ***ATB-1*** *standard synthesis (Table S8.1.1) with different HOAc/OAm ratios. a) 22.5:17.5 mmol (**ATB-3**), b) 25:15 mmol (**ATB-4**), c) 17.5:22.5 mmol (**ATB-5**), d) 15:25 mmol (**ATB-6**) and e) the corresponding PXRD-patterns of (a-d)..... 140*

Figure S8.1.6. *TEM images of upscaled synthesis a) **NR-15**, b) **NR-16**, c) **ATB-12**, d) **ATB-13** and e) corresponding PXRD patterns. 140*

Figure S8.1.7. *TEM images of particles with according to optimized bronze synthesis (**ATB-12)** with different HOAc/OAm ratios a) 15:25 mmol (**ATB-16**), b) 25:15 mmol (**ATB-17**) and c) the corresponding PXRD-patterns of a) and b). 141*

Figure S8.1.8. *XPS Spectra of (a-d) WO_{3-x} (**NR-1**) particles (e-f) and h-ATB (**ATB-15c**) particles, showing overview spectra, O 1s, N 1s and W 4f core level. 142*

Figure S8.1.9. *Reaction of oleic acid and oleylamine to oleylammoniumoleat and condensation towards oleyl oleamide with respective ^{1}H-NMR spectra measured in $CDCl_3$. 143*

Figure S8.1.10. *^{1}H-NMR kinetics of a reaction solution according to **NR-1** at different temperatures a) without and b) with AMT. In both cases the immediate formation of oleylammoniumoleate (salt*) from HOAc and OAm is observed, as well as the progressing formation of oleyl oleamide (OAd). For (b) we observe free HOAc at the end of the reaction although all HOAc/OAm was bound as OAd before, indicating cleavage of the amide by WO_{3-x} NRs. 144*

Figure S8.1.11. *a) ^{1}H-NMR spectra of **NR-1** particles dissolved in 6.7 M NaOD and extracted with 0.5 ml $CDCL_3$ (maroon) after acidification of the NaOD solution with DCl and then again extracted with 0.5 ml $CDCl_3$ (green) and b) COSY spectra of basic extraction. All spectra show peaks of OAd and OAm, as well as small amounts of undefined byproducts, but no traces of HOAc. 145*

Figure S8.1.12. *Particles synthesized with oleyl oleamide instead of the HOAc/OAm couple, a) using **NR-1** conditions (**Amide-1**), b) with threefold (0.36 mmol) AMT **(Amide-2)**, c) using **ATB-12** conditions (**Amide-3**) and synthesis reusing **NR-1** reaction solution d) under **NR-1** conditions (**Amide-4**), e) with addition of OAm under **NR-1** conditions (**Amide-5**), f) with addition of OAm under **ATB-12** conditions (**Amide-6)** and g) PXRD patterns of the particles shown in (a-f). 146*

Figure S8.1.13. *TEM images of particles with according to optimized bronze synthesis (**ATB-12)** with addition of different sodium salts (0.3:1 Na:W) a) disodium carbonate, b) sodium oleate, c) sodium hydrogen carbonate, d), sodium acetate trihydrate, e) sodium acetate trihydrate in OAd f) the corresponding PXRD-patterns of (a-e). 147*

Figure S8.1.14. *MAS ^{1}H-NMR spectra of **ATB 13-c** particles after 3 h at 300 °C in air, (directly measured, maroon), after 23 h in air and after additional annealing at 300 °C (air) for 21 h. 148*

Figure S8.1.15. *Deconvolution of NH_4^+ signal of a) ATB-14c for 5 h at 200 °C and b) ATB-14c for 5 h at 300 °C and c) ^{1}H-NMR spectra of adamantane. Samples measured with the same receiver gain, rotor and referenced towards external adamantane standard. Sample weights were taken into account. 149*

Figure S8.1.16. *PXRD pattern of* ***ATB-13c*** *70 °C with $(NH_4)_{0.25}WO_3$ Reference ($P6_3/mcm$, ICDD, PDF Entry No.: 01-073-1084).* *150*

Figure S8.1.17. *PXRD pattern of* ***ATB-13c*** *200 °C (Air) with $(NH_4)_{0.25}WO_3$ reference ($P6_3/mcm$, ICDD, PDF Entry No.: 01-073-1084).* *150*

Figure S8.1.18. *PXRD pattern of* ***ATB-13c*** *300 °C (Air) with hexagonal WO_3 reference ($P6_3/mcm$, ICSD, Entry No.: 99-503-1860).* *151*

Figure S8.1.19. *PXRD pattern of* ***ATB-13c*** *400 °C (Air) with hexagonal WO_3 reference (P6/mmm, ICSD, Entry No.: 99-501-1286).* *151*

Figure S8.1.20. *PXRD pattern of* ***ATB-13c*** *500 °C (Air) with monoclinic WO_3 reference ($P2_1/n$, COD, Entry No.: 96-152-8916.* *152*

Figure S8.1.21. *PXRD pattern of* ***ATB-13c*** *200 °C (Ar) with $(NH_4)_{0.25}WO_3$ reference ($P6_3/mcm$, ICDD, PDF Entry No.: 01-073-1084).* *152*

Figure S8.1.22. *PXRD pattern of* ***ATB-13c*** *300 °C (Ar) with $(NH_4)_{0.25}WO_3$ reference ($P6_3/mcm$, ICDD, PDF Entry No.: 01-073-1084).* *153*

Figure S8.1.23. *PXRD pattern of* ***ATB-13c*** *400 °C (Ar) with hexagonal WO_3 reference ($P6_3/mcm$, ICSD, Entry No.: 99-503-1860).* *153*

Figure S8.1.24. *PXRD pattern of* ***ATB-13c*** *500 °C (Ar) with hexagonal WO_3 reference ($P6_3/mcm$, ICSD, Entry No.: 99-503-1860).* *154*

Figure S8.1.25. *PXRD pattern of* ***ATB-13c*** *600 °C (Ar) with monoclinic WO_3 reference ($P2_1/n$, COD, Entry No.: 96-152-8916).* *154*

Figure S8.1.26. *a) UV-Vis-NIR spectra of* ***NR-1***, ***ATB-1*** *and* ***ATB-13*** *measured in TCE and b) Energy dependent absorption of the respective particles.* *155*

Figure S8.1.27. *^{13}C-NMR spectra of oleyl oleamide.* *155*

Figure S8.1.28. *Effect of replacing HOAc/OAm (ratio still 1:1) with different amounts of ODE. a) 20 mmol ODE, 10 mmol HOAc, 10 mmol OAm (**ODE-1**), b) 30 mmol ODE, 5 mmol HOAc, 5 mmol OAm (**ODE-2**), c) 35 mmol ODE, 2.5 mmol HOAc, 2.5 mmol OAm (**ODE-3**), d) 40 mmol ODE, no HOAc/OAm (**ODE-4**), e) PXRD patterns and f) UV-Vis-NIR spectra of the shown particles (a-d).* *157*

Figure S8.2.1. *Pawley refinements of WO_{3-x} NRs annealed at 300°C using space group P2/m and a quadratic form to compensate the anisotropy.[1] Refined parameters are: R_{wp}: 2.23, GOF: 1.08, crystal size (a*b*c): 4.1*72.6*4.3 nm. Lattice parameters: a=18.196 Å, b=3.794 Å and c= 14.000 Å.* *162*

Figure S8.2.2. *TEM images of WO_{3-x} nanorods annealed at a) 300 °C, b) 400 °C, c) 500 °C and d) after six reaction cycles. e) P-XRD patterns of annealed WO_{3-x} nanorods up to 500 °C and f) after five reaction cycles. References: $W_{18}O_{49}$ ($WO_{2.72}$, COD, Entry No.: 96-152-8167), WO_3 (monoclinic, COD, Entry No.: 96-152-8916).* *163*

Figure S8.2.3. *a) TEM image and b) P-XRD pattern of CeO_2 nanoparticles. Reference: Cerianite (CeO_2), COD, Entry No.: 96-900-9009).* *164*

Figure S8.2.4. *a) ^{1}H-NMR spectra of a standard catalysis (0.04 mmol thioanisole, 0.06 mmol H_2O_2 (60 %), 0.85 mg WO_{3-x} nanorods in 0.6 mL of methanol-d4) after 10 and 30 min, x marking the peaks used for integration. b) Time dependent composition during the catalysis based on ^{1}H-NMR data.* *166*

Figure S8.2.5. *a) ^{1}H-NMR spectra of a catalysis with double amounts (0.08 mmol thioanisole, 0.12 mmol H_2O_2 (60 %), 1.7 mg WO_{3-x} nanorods in 0.6 mL of methanol-d_4) after 10 and 30 min, **x** marking the peaks used for integration. b) Time dependent composition during the catalysis based on ^{1}H-NMR data.* *167*

Figure S8.2.6. *a) ^{1}H-NMR spectra of a catalysis with water influence (0.04 mmol thioanisole, 0.06 mmol H_2O_2 (60 %), 0.85 mg WO_{3-x} nanorods in 0.4 mL of methanol-d_4 and 0.2 ml D_2O) after 10 and 30 min, **x** marking the peaks used for integration. b) Time-dependent composition during the catalysis based on ^{1}H-NMR data.*..... *168*

Figure S8.2.7. *^{1}H-NMR spectra of a standard catalysis (0.04 mmol thioanisole, 0.12 mmol H_2O_2 (60 %), 0.85 mg WO_{3-x} nanorods in 0.6 mL of methanol-d_4) after 10 min, 30 min, 22h and 13 d, **x** marking the peaks used for integration.* *169*

Figure S8.2.8. *a) ^{1}H-NMR spectra of an oxidation catalysis using sulfoxides (0.04 mmol MP-sulfone, 0.06 mmol H_2O_2 (60 %), 0.85 mg WO_{3-x} nanorods in 0.6 mL of methanol-d_4) after 10 and 30 min, **x** marking the peaks used for integration. b) Time-dependent composition during the catalysis based on ^{1}H-NMR data.* *170*

Figure S8.2.9. *a) ^{1}H-NMR spectra of a standard oxidation catalysis (0.04 mmol thioanisole, 0.06 mmol H_2O_2 (60 %), 0.85 mg Na_2WO_4 * $2H_2O$ in 0.6 mL of methanol-d_4) after 10 and 30 min, **x** marking the peaks used for integration. b) Time-dependent composition during the catalysis based on ^{1}H-NMR data.* *171*

Figure S8.2.10. *a) ^{1}H-NMR spectra of a standard catalysis (0.04 mmol thioanisole, 0.06 mmol H_2O_2 (60 %), 0.85 mg CeO_2 nanoparticles in 0.6 mL of methanol-d_4) after 10 and 30 min, **x** marking the peaks used for integration. b) Time-dependent composition during the catalysis based on ^{1}H-NMR data.* *172*

Figure S8.2.11. *a) ^{1}H-NMR spectra of a catalysis using sulfoxide (0.04 mmol MP-sulfoxide, 0.06 mmol H_2O_2 (60 %), 0.85 mg CeO_2 nanoparticles in 0.6 mL of methanol-d_4) after 10 and 30 min, **x** marking the peaks used for integration. b) Time-dependent composition during the catalysis based on ^{1}H-NMR data.* *173*

Figure S8.2.12. *a) ^{1}H-NMR spectra of a standard catalysis (0.04 mmol di-n-propyl sulfide, 0.06 mmol H_2O_2 (60 %), 0.85 mg WO_{3-x} nanorods in 0.6 mL of methanol-d_4) after 10 and 30 min, **x** marking the peaks used for integration. b) Time-dependent composition during the catalysis based on ^{1}H-NMR data.* *175*

Figure S8.2.13. *a) ^{1}H-NMR spectra of a standard catalysis (0.04 mmol di-tert-butyl sulfide, 0.06 mmol H_2O_2 (60 %), 0.85 mg WO_{3-x} nanorods in 0.6 mL of methanol-d_4) after 10 and 30 min, **x** marking the peaks used for integration. b) Time-dependent composition during the catalysis based on ^{1}H-NMR data.* *177*

Figure S8.2.14. *a) ^{1}H-NMR spectra of a standard catalysis (0.04 mmol diphenyl sulfide, 0.06 mmol H_2O_2 (60 %), 0.85 mg WO_{3-x} nanorods in 0.6 mL of methanol-d_4) after 10 and 30 min,* ***x*** *marking the peaks used for integration. b) Time-dependent composition during the catalysis based on ^{1}H-NMR data..... 179*

Figure S8.2.15. *a) ^{1}H-NMR spectra of a standard catalysis (0.04 mmol dibenzyl sulfide, 0.06 mmol H_2O_2 (60 %), 0.85 mg WO_{3-x} nanorods in 0.6 mL of methanol-d_4) after 10 and 30 min,* ***x*** *marking the peaks used for integration. b) Time-dependent composition during the catalysis based on ^{1}H-NMR data..... 181*

Figure S8.2.16. *a) ^{1}H-NMR spectra of a standard catalysis (0.04 mmol 4-nitrophenyl methyl sulfide, 0.06 mmol H_2O_2 (60 %), 0.85 mg WO_{3-x} nanorods in 0.6 mL of methanol-d_4) after 10 and 30 min,* ***x*** *marking the peaks used for integration. b) Time-dependent composition during the catalysis based on ^{1}H-NMR data. 183*

Figure S8.2.17. *a) ^{1}H-NMR spectra of a standard catalysis (0.04 mmol 4-methoxyphenyl methyl sulfide, 0.06 mmol H_2O_2 (60 %), 0.85 mg WO_{3-x} nanorods in 0.6 mL of methanol-d_4) after 10 and 30 min,* ***x*** *marking the peaks used for integration. b) Time-dependent composition during the catalysis based on ^{1}H-NMR data..... 185*

Figure S8.2.18. *a) ^{1}H-NMR spectra of a standard catalysis (0.04 mmol 4-aminophenyl methyl sulfide, 0.06 mmol H_2O_2 (60 %), 0.85 mg WO_{3-x} nanorods in 0.6 mL of methanol-d_4) after 10 and 30 min,* ***x*** *marking the peaks used for integration. b) Time-dependent composition during the catalysis based on ^{1}H-NMR data. 187*

Figure S8.2.19. *a) ^{1}H-NMR spectra of a catalysis using sulfoxides (0.04 mmol DMSO, 0.06 mmol H_2O_2 (60 %), 0.85 mg WO_{3-x} nanorods in 0.6 mL of methanol-d_4) after 10 and 30 min,* ***x*** *marking the peaks used for integration. b) Time-dependent composition during the catalysis based on ^{1}H-NMR data..... 189*

Figure S8.2.20. *a) ^{1}H-NMR spectra of a standard catalysis (0.04 mmol dibenzothiophen, 0.06 mmol H_2O_2 (60 %), 0.85 mg WO_{3-x} nanorods in 0.6 mL of methanol-d_4) after 10 and 30 min. b) ^{1}H-NMR spectra of an ex situ catalysis (0.04 mmol dibenzothiophen, 0.06 mmol H_2O_2 (60 %), 8.5 mg WO_{3-x} nanorods in 1 mL of methanol-d_4) after 10 and 30 min.* ***x*** *marking the peaks used for integration..... 191*

Figure S8.3.1. *TEM images (left) and PXRD patterns (right) of a) WO_{3-x} NRs synthesized with oleic acid from the steel can, b) addition of 20 mol% iron oleate to the standard synthesis and c) addition of 20 mol% iron oleate to the standard synthesis and a HR of 2.5 K/min. References: $WO_{2.72}$ (space group $P2/m$ (10), COD, Entry No.: 96-152-8167). $FeWO_4$ (Ferberite, space group $P2/c$ (13), COD no. 96-900-8125) and $K_{0.26}WO_3$ (hexagonal, space group $P63$ (173), ICSD no. 99-501-7632). 194*

Figure S8.3.2. *TEM images (left) and PXRD patterns (right) of a) WO_{3-x} NRs synthesized with oleic acid from the steel can and double amount AMT (0.24 mmol instead of 0.12 mmol) and b) addition of 1.5 mol% iron oleate to pure oleic acid and double amount AMT (0.24 mmol instead of 0.12 mmol). Reference: $WO_{2.72}$ (space group $P2/m$ (10), COD, Entry No.: 96-152-8167)..... 195*

Figure S8.3.3. *Pawley refinements of WO_{3-x} NRs based on space group $P2/m$ a) synthesized with oleic acid from steel canister with fit paramters a=18.103(217) Å, b=3.793(4) Å, c=13.992(129) Å, α=90 °, β=115.211 °, γ=90 °, rwp=2.98, goodness of fit =1.00, crystallite size =5.9(6)*67.1(7.6)*3.4(5) nm and b) synthesized with fresh oleic*

*acid using 5 mol% Fe(oleate)$_3$ with fit paramters a=18.090(257) Å, b=3.798(4) Å, c=13.985(142) Å, α=90 °, β=115.211 °, γ=90 °, rwp=2.79, goodness of fit =1.00, crystallite size =6.7(7)*58.5(3.3)*3.6(5) nm. 196*

Figure S8.3.4. *PXRD patterns of ferberite FeWO$_4$ NCs shown in Figure 4.2c annealed at different temperatures. Blue markings indicating hexagonal potassium tungsten bronze. 197*

Figure S8.3.5*. TEM images (left) and PXRD patterns (right) of ferberite FeWO$_4$ NCs synthesized with 1.43:1.43 mmol Fe:W, 1 K/min heating rate and a) OAc:OAm ratio of 20:20 mmol, b) OAc:OAm ratio of 22.5:17.5 mmol and c) OAc:OAm ratio of 17.5:22.5 mmol. References: WO$_{2.72}$ (space group $P2/m$ (13), COD, Entry No.: 96-152-8167). FeWO$_4$ (Ferberite, space group $P2/c$ (13), COD no. 96-900-8125). 198*

Figure S8.3.6. *PXRD patterns of FeWO$_4$ NCs shown in Figure 4.2c with unknown structure. References: (a) MgWO$_4$ (triclinic, PDF, Entry No.: 00-045-0412) and (b) MgWO$_4$ (tetragonal, PDF, Entry No.: 00-052-0390). .. 199*

Figure S8.3.7*. PXRD patterns of ferberite FeWO$_4$ NCs shown in Figure 4.3b annealed at different temperatures. 200*

Figure S8.3.8. *PXRD patterns of ferberite FeWO$_4$ NCs shown in Figure 4.3c annealed at different temperatures. 201*

Figure S8.3.9. *Mössbauer spectra of a) FeWO$_4$ NCs with ferberite structure shown in Figure 4.2c, b) of unknown FeWO$_4$ structure synthesized with Fe(acac)$_3$ in 20 mmol OAd, shown in Figure 4.3b and c) of unknown FeWO$_4$ structure synthesized with Fe(oleate)$_3$ in 20 mmol OAd, shown in Figure 4.3c. Fit parameters for Fe(II) and Fe(III) are found in Table 4.1. ..... 202*

Figure S8.3.10. *Rietveld refinements of MgWO$_4$ NCs annealed at 800 °C for 5 h in air using on monoclinic MgWO$_4$ (space group $P2/c$ (13)) and monoclinic WO$_3$ (space group $P2/n$ (14)) structures. Fit paramters for MgWO$_4$. a=4.689(0) Å, b=5.676(0) Å, c=4.929(0) Å, α=90 °, β=90.77(0) °, γ=90 ° weight percent=96.1(2) % and for WO$_3$: a=7.303(3) Å, b=7.542(3) Å, c=7.698(3) Å, α=90 °, β=90.73(5) °, γ=90 ° weight percent=3.9(2) %; rwp=5.14, goodness of fit =1.87. ..... 203*

Figure S8.4.1. *a) TEM image and PXRD pattern of hexagonal Cs$_{0.3}$WO$_3$ NCs synthesized with 22.5:17.5 mmol OAc:OAm and heating rate of 25 K/min, b) TEM image and PXRD pattern of hexagonal Cs$_{0.3}$WO$_3$ NCs synthesized with 20:20 mmol OAc:OAm and heating rate of 25 K/min and c) TEM image and PXRD pattern of mixed cubic/hexagonal Cs$_{0.3}$WO$_3$ NCs synthesized with 17.5:22.5 mmol OAc:OAm and heating rate of 25 K/min. PXRD references: Cs$_{0.32}$WO$_3$ (space group $P63/mcm$, ICSD no. 99-501-4972) and CsW$_{1.6}$O$_3$ (space group $Fd3m$, ICSD no. 99-502-4816). 205*

Figure S8.4.2. *a) TEM image and PXRD pattern of mixed cubic/hexagonal Cs$_{0.3}$WO$_3$ NCs NCs synthesized with 19:21 mmol OAc:OAm and heating rate of 2.5 K/min and b) TEM image and PXRD pattern of mixed cubic/hexagonal Cs$_{0.3}$WO$_3$ NCs synthesized with 15:25 mmol OAc:OAm and heating rate of 2.5 K/min. PXRD references: Cs$_{0.32}$WO$_3$ (space group $P63/mcm$, ICSD no. 99-501-4972) and CsW$_{1.6}$O$_3$ (space group $Fd3m$, ICSD no. 99-502-4816). 206*

Figure S8.4.3. *a) TEM image and PXRD pattern of cubic $Cs_{0.6}WO_3$ NCs synthesized with 20:20 mmol OAc:OAm and heating rate of 5 K/min and b) TEM image and PXRD pattern of cubic $Cs_{0.6}WO_3$ NCs synthesized with 23.5:17.5 mmol OAc:OAm and heating rate of 5 K/min. PXRD reference: $CsW_{1.6}O_3$ (space group $Fd\bar{3}m$, ICSD no. 99-502-4816).* *207*

Figure S8.4.4. *Rietveld refinement for h-$Cs_{0.3}WO_3$ synthesized with 20:20 mmol OAc:OAm and 5 K/min heating rate. Refinement performed using hexagonal $P6\bar{3}/mcm$ structure. Rwp: 5.90, gof: 1.45, a=7.406(0), b=7.407(5), c=7.610(0), CS=34.2(3) nm, Occ(Cs)=0.29(1).* *208*

Figure S8.4.5. *Rietveld refinement for c-$Cs_{0.6}WO_3$ synthesized with 17.5:22.5 mmol OAc:OAm and 5 K/min heating rate. Refinement performed using cubic $Fd\bar{3}m$ structure. Rwp: 12.33, gof: 3.89, a=b=c=10.235(0), CS=34.3(5) nm, Occ(Cs)=0.54(1).* *208*

Figure S8.4.6. *Rietveld refinement for m-$Cs_{0.3}WO_3$ synthesized with 19:21 mmol OAc:OAm and 2.5 K/min heating rate. Refinement performed using hexagonal $P6\bar{3}/mcm$ and cubic $Fd\bar{3}m$ structures. Rwp: 3.51, gof: 1.10; values of hexagonal phase: a=7.403(1), b=7.400(6), c=7.613(0), CS=25.4(3) nm, Occ(Cs)=0.29(0); values of cubic phase: a=b=c=10.312(3), CS=11.0(8) nm, Occ(Cs)=0.50(2); ratio h/c: 89.0(4):11.0(4).* *209*

Figure S8.4.7. *Rietveld refinement for m-$Cs_{0.3}WO_3$ synthesized with 17.5:22.5 mmol OAc:OAm and 2.5 K/min heating rate. Refinement performed using hexagonal $P6\bar{3}/mcm$ and cubic $Fd\bar{3}m$ structures. Rwp: 4.57, gof: 1.69; values of hexagonal phase: a=7.375(2), b=7.257(22), c=7.708(3), CS=15.9(4) nm, Occ(Cs)=0.27(0); values of cubic phase: a=b=c=10.327(2), CS=17.1(5) nm, Occ(Cs)=0.39(1); ratio h/c: 62.1(4):37.9(4).* *209*

Figure S8.4.8. *Rietveld refinement for m-$Cs_{0.3}WO_3$ synthesized with 15:25 mmol OAc:OAm and 2.5 K/min heating rate. Refinement performed using hexagonal $P6\bar{3}/mcm$ and cubic $Fd\bar{3}m$ structures. Rwp: 4.82, gof: 1.90; values of hexagonal phase: a=7.327(1), b=6.935(25), c=7.858(5), CS=12.6(3) nm, Occ(Cs)=0.27(0); values of cubic phase: a=b=c=10.328(1), CS=16.3(3) nm, Occ(Cs)=0.35(0); ratio h/c: 42.8(4):57.2(4).* *210*

Figure S8.4.9. *a) TEM image and PXRD pattern of hexagonal $Rb_{0.3}WO_3$ NCs synthesized with 20:20 mmol OAc:OAm and heating rate of 25 K/min, b) TEM image and PXRD pattern of hexagonal $Rb_{0.3}WO_3$ NCs synthesized with 17.5:22.5 mmol OAc:OAm and heating rate of 2.5 K/min and c) TEM image and PXRD pattern of mixed cubic/hexagonal $Rb_{0.6}WO_3$ NCs synthesized with 17.5:22.5 mmol OAc:OAm and heating rate of 2.5 K/min. PXRD references $Rb_{0.27}WO_3$ (space group $P6\bar{3}/mcm$, PDF no. 01-073-1549) and $Rb_{1.1}W_{1.66}O_{5.52}$ (space group $Fd\bar{3}m$, ICSD no. 99-502-7095).* *211*

Figure S8.4.10. *Diffuse reflectivity spectra of nanocrystals dried at 70 °C (blue), annealed at 300 °C (red) and annealed at 500 °C (yellow) for 5 h. a) h-$Cs_{0.3}WO_3$, b) WO_{3-x} NRs, c) c-$Cs_{0.6}WO_3$ synthesized with 17.5:22.5 mmol OAc:OAm, d) m-$Cs_{0.3}WO_3$ synthesized with 19:21 mmol OAc:OAm, e) m-$Cs_{0.3}WO_3$ synthesized with 17.5:22.5 mmol OAc:OAm and f) m-$Cs_{0.3}WO_3$ synthesized with 15:25 mmol OAc:OAm.* *212*

Figure S8.4.11. *Diffuse reflectivity spectra of reference substances $BaSO_4$ (background), commercial WO_3, $Na_2WO_4*2H_2O$ and ammonium metatungstate (AMT).* *213*

Figure S8.4.12. *XPS spectra of 4f 5/2 and 3/2 core level of nanocrystals dried at 70 °C, annealed at 300 °C and annealed at 500 °C for 5 h of a) c-$Cs_{0.6}WO_3$ NCs and b) h-$Cs_{0.3}WO_3$ NCs. 214*

Figure S8.4.13. *Comparison of P. aeruginosa bacterial cells treated with tungsten bronzes in planktonic and biofilm condition. The bacteria were cultivated in LB medium for 72 h at 30 °C in the presence of the referred tungsten bronzes. OD_{600} was then measured to observe the effect of the tungsten bronzes on the planktonic cells. After removing the planktonic cells, the attached cells i.e., biofilm were stained with crystal violet. After washing the unbound crystal violet, acetic acid was added for solubilization of the crystal violet. The absorbance at 575 nm was then measured to observe the effect of the tungsten bronzes on the biofilm. 215*

Figure S8.4.14. *Leaching data of tungsten and cesium for h-$Cs_{0.3}WO_3$, m-$Cs_{0.3}WO_3$, c-$Cs_{0.6}WO_3$, h-ATB and WO_{3-x} a) in water and b) in 0.1 M H_2O_2. ..... 216*

Figure S8.4.15. *Comparison of the tungsten bronzes effect on P. aeruginosa a), P. gallaeciensis b) and S. aureus c) bacterial cells with IR irradiation and no irradiation at all. S. aureus and P. aeruginosa were grown at 30 °C in LB medium, P. gallaeciensis was grown at 30 °C in 2216 marine medium. The incubation of the bacteria was done for 72 h in 96-well plates in the absence or presence of tungsten bronzes and 950 nm IR irradiation. OD_{600} was then measured to observe the effect of the tungsten bronzes in combination with IR irradiation in comparison to no irradiation at all. 217*

Figure S8.5.1. *CLSM picture of P. gallaeciensis BF in a) control experiment without additives and 50 µM solution of b) $MnCl_2*4H_2O$ and c) $FeCl_2*4H_2O$. 219*

Figure S8.5.2. *PXRD patterns of a) $MnWO_4$ NCs shown in Figure 6.3a, b) $FeWO_4$ NCs shown in Figure 6.3b and c) $Fe_{0.5}Mn_{0.5}WO_4$ NCs shown in Figure 6.3c. References: $MnWO_4$ (hüberite, space group $P2/c$ (13), PDF no. 01-080-0132) and $FeWO_4$ (Ferberite, space group $P2/c$ (13), COD no. 96-900-8125). 221*

Figure S8.5.3. *TEM images (left) and PXRD patterns (right) of $FeWO_4$ NCs synthesized with a) 25:15 mmol oleic acid : oleylamine and b) 15:25 mmol oleic acid : oleylamine. Reference: $FeWO_4$ (Ferberite, space group $P2/c$ (13), COD no. 96-900-8125). 222*

Figure S8.5.4. *Biotests of additional $FeWO_4$ NCs shown in Figure S8.5.3 and $Na_2WO_4*2H_2O$ (0.1 mg/ml) towards Biofilm formation and planktonic cells of a) P. gallaeciensis and b) P. aeruginosa. Control without addition of NCs or salts. 223*

Figure S8.5.5. *TEM images (left) and PXRD patterns (right) of $MnWO_4$ NCs synthesized using 21:19 mmol oleic acid:oleylamine with different precursors (1.43:1.43 mmol Mn:W), a) manganese oleate, b) manganese acetate and c) manganese acetylacetonate. Reference: $MnWO_4$ (hüberite, space group $P2/c$ (13), PDF no. 01-080-0132). 224*

Figure S8.5.6. *Biotests of $MnWO_4$ NCs shown in Figure S8.5.5 and $Na_2WO_4*2H_2O$ (0.1 mg/ml) and $MgCl_2*4H_2O$ (0.03 mg/ml) towards Biofilm formation and planktonic cells of a) P. gallaeciensis and b) P. aeruginosa. (0.1 mg/ml) as well as towards Biofilm formation and planktonic cells of a) P. gallaeciensis and b) P. aeruginosa. Control without addition of NCs or salts. 225*

Figure S8.5.7. *TEM images (left) and PXRD patterns (right) of a) $CoWO_4$ NCs, b) $MgWO_4$ NCs, c) $SrWO_4$ NCs and d) $BaWO_4$ NCs. References: $CoWO_4$ (space group $P2/c$ (13), PDF no. 00-015-0867), $MgWO_4^A$ (monoclinic, space group $P2/c$ (13), COD no. 99-501-2719), $MgWO_4^B$ (triclinic, PDF, Entry No.: 00-045-0412), $MgWO_4^C$ (tetragonal, PDF, Entry No.: 00-052-0390), $SrWO_4$ (space group $I41/a$ (88), COD no. 96-154-6037) and $BaWO_4$ (space group $I41/a$ (88), COD no. 96-152-7205). Synthesis parameters in Table S8.5.1.* *226*

Figure S8.5.8. *Influence of $CoWO_4$, $MgWO_4$, $BaWO_4$ and $SrWO_4$ (see Figure S8.5.7) (0.1 mg/ml each) towards biofilm formation of P. gallaeciensis and P. aeruginosa. In addition, a control experiment without NCs and $Na_2WO_4*2H_2O$ (0.1 mg/ml) as soluble reference material.* *227*

Figure S8.5.9. *a) $ZnWO_4$ NCs synthesized with basic zinc carbonate ($ZnCO_3*Zn(OH)_2$, **A**) and b) zinc acetyl acetonate ($Zn(acac)_2*2H_2O$, **B**) as zinc precursor. c) Bacterial growth assay for P. gallaeciensis and P. aeruginosa with $ZnWO_4$ NCs (concentration 0.1 mg/ml), water soluble zinc chloride (30 wt%≈220 µM, 100 %≈750 µM), water soluble sodium tungstate and sodium chloride as reference compounds and a control (no additives). d) Growth test of F. graminearum in the presence of 0.1 mg/ml $ZnWO_4$ NCs.* *228*

Figure S8.5.10. *PXRD patterns of a) $ZnWO_4$ NCs shown in Figure S8.5.9a and b) $ZnWO_4$ NCs shown in Figure S8.5.9b. Reference: $ZnWO_4$ (sanmartinite, space group $P2/c$ (13), PDF no. 01-073-0554).* *229*

8.7 List of Tables

Table 2.1. *Overview of syntheses for nanorods (**NR-X**), h-ATB (**ATB-X**), with oleyl oleamide (**Amide-X**) with reaction conditions and estimated ratio of WO_{3-x} and h-ATB. Complete table: Table S8.1.1 (c) purified particles. 17*

Table 2.2. *Particle sizes including length, width, aspect ratio and number of particles of WO_{3-x} nanorods for selected syntheses. The corresponding histograms are provided in Figure S8.1.1. 19*

Table 2.3. *Chemical shifts of different ^1H signals in ^1H- MAS-NMR spectra for h-ATB together with chemical shift of h-ATB and several reference[71] samples. 31*

Table 3.1. *Composition of the reaction solution after 10 and 30 min during the in situ oxidation of thioanisole using WO_{3-x} NRs in 0.6 mL of methanol-d_4 as catalyst and the substrate thioanisole and the oxidant H_2O_2 in variable concentrations. 50*

Table 3.2. *Composition for in situ oxidation reaction after 10 and 30 min for different sulfides and sulfoxides under standard conditions (0.85 mg WO_{3-x} catalyst, 0.04 mmol substrate, 0.06 mmol H_2O_2 (60%) in 0.6 ml methanol-d_4). 54*

Table 3.3. *Screening of different compounds for their potential in oxidation catalysis for the oxidation of thioanisole. 56*

Table 4.1. *Fit data for the Mössbauer spectra of ferberite $FeWO_4$ NCs (Figure S8.3.5c) and of $FeWO_4$ with unknown structure (Figure 4.3b, c) 72*

Table 5.1. *Turnover rates, maximum turnovers after 24 h and suitable fitting limits for different tungsten oxide bronzes and reference materials derived from HPO assays. Additional information is supplied in Table S8.4.1. 92*

Table S8.1.1. *Overview of synthesis for nanorods (**NR-X**), HATB (**ATB-X**), synthesis with ODE (**ODE-X**) and oleyl oleamide (**Amid-X**) with reaction conditions and estimated ratio of WO_{3-x} and HATB. (c) indicates cleaned particles. 132*

Table S8.1.2. *Refinement data for different pure samples from Rietveld and Pawley refinements. 136*

Table S8.1.3. *Assignment of Miller-Indices from HATB/$WO_{2.72}$ references towards phase mixture of sample **ATB-1** ($WO_{2.72}$: COD, Entry No.: 96-152-8167, $(NH_4)_{0.25}WO_3$: ICDD, PDF Entry No.: 01-073-1084, $(NH_4)_{0.33}WO_3$: ICDD, PDF Entry No.: 00-042-0452)..... 137*

Table S8.2.1. *Product composition with additional water to standard in situ experiment (0.85 mg WO_{3-x} nanorods, 0.04 mmol thioanisole, 0.06 mmol H_2O_2 (60 %) in 0.6 ml methanol-d_4). 160*

Table S8.2.2. *Fit parameters for water curves according to the equation above. 160*

Table S8.2.3. *Product composition after annealing at different temperatures for standard in situ experiment (0.85 mg WO_{3-x} nanorods, 0.04 mmol thioanisole, 0.06 mmol H_2O_2 (60 %) in 0.6 ml methanol-d_4). 161*

Table S8.2.4. *BET surface area and ζ – potential of nanoparticles used for sulfide oxidation..... 161*

Table S8.4.1. *Additional HPO data measured for various samples..... 213*

Table S8.5.1. *List of different tungstate nanocrystals with synthesis parameters as presented and discussed in this article..... 220*

8.8 List of Abbreviations

a, *b*, *c*	Lattice parameters
AHL	N-Acyl homoserine lactone
AMT	Ammonium metatungstate
AR	Aspect ratio
BET	Brunauer-Emmet-Teller method fir surface analysis
BF	Biofilm
c	Concentration
c_{crit}	Critical saturation concentration
c_S	Saturation concentration
CLSM	Confocal laser scanning microscopy
COD	Crystallography Open Database
COSY	Correlation Spectroscopy
CS	Crystallite size
δ	Chemical Shift
Eq.	Equation
ΔG_N	Free energy of nucleation
ΔG_v	Lattice energy
γ	Surface energy
gof	goodness of fit
h-ATB	hexagonal ammonium tungsten bronze
HMG	Medium for fungal growth
HOAc	Oleic acid
HPO	Haloperoxidase
HR	Heating rate
HR-TEM	High resolution transition electron microscopy
ICDD	International Centre for Diffraction Data

ICSD	Inorganic Crystal Structure Database
LB	Medium for bacterial growth
LSPR	Localized surface plasmon resonance
MAS	Magic-Angle spinning
MoKα	Molybdenum Kα Radiation
MP-sulfone	Methyl phenyl sulfone
MP-sulfoxide	Methyl phenyl sulfoxide
NC	Nanocrystals
NIR	Near-infrared light
NMR	Nuclear Magnetic Resonance
NP	Nanoparticles
NR	Nanorods
OAc	Oleic acid
OAd	Oleyl oleamide
OAm	Oleylamine
Occ	Elemental Occupancy
OD	Optical density
ODE	Octadecene
PC	Polycarbonate
PDF	Powder diffraction file
PE	Polyethylene
PETG	Polyethylene terephthalate glycol
PR	Phenol red
PS	Polystyrene
PXRD	Powder X-ray diffraction
Q	scattering vector
QQ	Quorum quenching
QS	Quorum sensing

r	radius
r_{crit}	critical radius
RT	Room temperature
Rwp	Weighted Profile R-Value
S	Supersaturation
TBPB	Tetrabromphenol blue
TEM	Transition electron microscopy
UV	Ultraviolet light
Vis	Visible light
wt%	Weight-percent
X-gal	5-bromo-4-chloro-3-indolyl-β-D-galactopyranoside
XPS	X-ray photoelectron spectroscopy